Search for very-high-energy gamma and neutrino emission from microquasars with HESS and ANTARES/KM3NeT

Sébastien Le Stum

Aix*Marseille université
Socialement engagée

NNT:2023AIXM0554

THÈSE DE DOCTORAT

Soutenue à Aix-Marseille Université
le 15 décembre 2023 par

Sébastien LE STUM

Recherche d'émission gamma de très haute énergie et de neutrinos provenant de microquasars avec HESS et ANTARES/KM3NeT

Search for very-high-energy gamma and neutrino emission from microquasars with HESS and ANTARES/KM3NeT

Discipline
Physique et Sciences de la Matière

Spécialité
Physique des Particules et Astroparticules

École doctorale
Physique et Sciences de la Matière (ED352)

Laboratoire
Centre de Physique des Particules de Marseille

Composition du jury

Catherine BOISSON Astronome Observatoire de Paris, LUTH	Rapporteure
Rosa CONIGLIONE Chercheur INFN INFN Catania, LNS	Rapporteure
Alexis COLEIRO Maître de conférences Université Paris Cité, APC	Examinateur
Cristinel DIACONU Directeur de recherche Aix-Marseille Université, CPPM	Président du jury
Jean-Pierre ERNENWEIN Professeur des Universités Aix-Marseille Université, CPPM	Directeur de thèse
Damien DORNIC Chargé de recherche Aix-Marseille Université, CPPM	Co-Directeur de thèse

CENTRE DE PHYSIQUE DES PARTICULES DE MARSEILLE
CPPM

Affidavit

Je soussigné, Sébastien Le Stum, déclare par la présente que le travail présenté dans ce manuscrit est mon propre travail, réalisé sous la direction scientifique de Jean-Pierre Ernenwein et Damien Dornic dans le respect des principes d'honnêteté, d'intégrité et de responsabilité inhérents à la mission de recherche. Les travaux de recherche et la rédaction de ce manuscrit ont été réalisés dans le respect à la fois de la charte nationale de déontologie des métiers de la recherche et de la charte d'Aix-Marseille Université relative à la lutte contre le plagiat.

Ce travail n'a pas été précédemment soumis en France ou à l'étranger dans une version identique ou similaire à un organisme examinateur.

Fait à Marseille le 20 octobre 2023

Liste de publications et participation aux conférences

Liste des publications réalisées dans le cadre du projet de thèse:

1. Gamma-ray observations of MAXI J1820+070 during the 2018 outburst, MAGIC-HESS-VERITAS Collaborations. Monthly Notices of the Royal Astronomical Society 517.4 (Sept. 2022), pp. 4736–4751. *Corresponding Author*. Referred in the text as [1]. https://doi.org/10.1093/mnras/stac2686

2. Searches for neutrino counterparts of gravitational waves from the LIGO/Virgo third observing run with KM3NeT, KM3NeT Collaboration. *Corresponding Author*. (Accepted to JCAP [2])

Participation aux conférences et écoles d'été au cours de la période de thèse:

1. The XXX International Conference on Neutrino Physics and Astrophysics, *Neutrino2022*, Seoul, South Korea, May 30 to June 4, 2022:
   a) First search for neutrino counterparts from gravitational wave sources with KM3NeT, *Poster, presenter*, https://indico.kps.or.kr/event/30/contributions/435/
   b) Online Multi-Messenger Program of KM3NeT, *Poster, co-author*, https://indico.kps.or.kr/event/30/contributions/248/
   c) Follow-up of IceCube alerts with KM3NeT ARCA and ORCA, *Poster, co-author*, https://indico.kps.or.kr/event/30/contributions/440/

2. KM3NeT Town Hall Meeting, 20–22 September 2022, Catania, Italy: "Real-time correlation analysis with KM3NeT", *Oral presentation* . https://indico.cern.ch/event/1132669/

3. 10th Microquasar Workshop, 22-26 May 2023, Crete, Greece: "Searching for neutrinos from microquasar flares with ANTARES", *Oral presentation*. https://sites.google.com/view/microquasar-workshop2023/home

4. 38th International Cosmic Ray Conference, *ICRC2023*, Nagoya, Japan, July 26 to Aug 3, 2023:

a) Searching for neutrinos from microquasar flares with ANTARES and KM3NeT, *Poster, presenter*, https://doi.org/10.22323/1.444.1505

b) Follow-up of multi-messenger alerts with the KM3NeT ARCA and ORCA detectors", *Poster, co-author*, https://doi.org/10.22323/1.444.1521

c) Refined neutrino follow-up analysis of GRB 221009A with KM3NeT ARCA and ORCA detectors", *Poster, co-author*, https://doi.org/10.22323/1.444.1503

d) The Real-time Analysis Platform of KM3NeT and its first results, *Poster, co-author*, https://doi.org/10.22323/1.444.1125

e) Follow-up of O3 gravitational wave events with neutrinos in ANTARES and KM3NeT telescopes, *Poster, co-author*, https://doi.org/10.22323/1.444.1506

"These messengers will not be hindered from accomplishing at their best speed the distance which they have to go, either by snow, or rain, or heat, or by the darkness of night."

— Herodotus

Résumé

Le travail présenté dans cette thèse porte sur un ensemble d'études réalisées dans le cadre de l'astronomie multimessager. Ainsi, nous nous basons principalement sur les données récoltées par le télescope à rayons gamma de très haute énergie HESS et par les télescopes sous-marins à neutrinos ANTARES et KM3NeT. Les objets principaux de cette étude sont les microquasars, des systèmes binaires galactiques comportant un objet compact, trou noir ou étoile à neutron, et une étoile compagnon. Ces systèmes présentent des phénomènes d'accrétion-éjection et sont particulièrement visibles dans le domaine des rayons X et des ondes radio pendant des phases d'éruption intense et transitoires. En nous concentrant sur ces phases d'activité, nous recherchons des émissions de rayons gamma et de neutrinos pouvant être marqueurs de l'accélération de particules à très haute énergie dans ces systèmes. Aucun signal significatif n'ayant pu être mis en évidence, les résultats de cette étude sont un ensemble de limites supérieures que nous plaçons sur des distributions spectrales en énergie. Une autre partie de la thèse se place dans le cadre plus large de l'astronomie temps-réel, avec le développement de méthodes d'analyse pour la recherche de signaux neutrinos avec le télescope KM3NeT/ORCA en coïncidence avec des alertes de phénomènes transitoires lancées à la communauté. Ces méthodes sont appliquées à la recherche de corrélation avec des neutrinos de haute énergie détectés par le télescope IceCube, au sursaut gamma GRB221009A et aux détections d'ondes gravitationnelles. Enfin, l'application de ces méthodes à l'analyse de données en temps-réel de KM3NeT est discutée.

Mots clés: microquasars, rayons gamma, HESS, neutrino, ANTARES, KM3NeT, astronomie multimessager

Abstract

The work presented in this thesis covers a range of studies performed in the context of multi-messenger astronomy. We mainly rely on data collected by the Very-High-Energy gamma-ray telescope HESS and the deep-sea neutrino telescopes ANTARES and KM3NeT. The main objects of this work are microquasars, galactic binary systems including a compact object, black hole or neutron star, and a companion star. These systems exhibit accretion-ejection phenomena and are particularly visible in X-ray and radio during intense transient outbursts. Focusing on these flaring periods, we search for gamma-rays and neutrinos that could be emitted by particles accelerated to very high energy in these systems. No significant signal could be detected, and the results of this study are upper limits that we put on spectral energy distributions. Another part of this thesis presents the work done in the broader context of time domain astronomy, with the development of analysis methods for the search of neutrino signals in the telescope KM3NeT/ORCA in coincidence with alerts of transient phenomena sent to the community. These methods are applied for the search of a coincident signal to several high-energy neutrinos detected by the IceCube telescope, to the gamma-ray burst GRB221009A, and to gravitational wave detections. Finally, the application of these methods to the analysis of real-time data from KM3NeT is discussed.

Keywords: microquasars, gamma-rays, HESS, neutrino, ANTARES, KM3NeT, multi-messenger astronomy

Résumé étendu

L'astronomie multimessager est l'étude conjointe de plusieurs transporteurs d'informations provenant de sources astrophysiques. Ces dernières années, ce domaine a connu un intérêt croissant par la construction de télescopes capables de détecter des signaux d'ondes gravitationnelles ou des neutrinos cosmiques. Ces équipements sont particulièrement sensibles aux phénomènes cosmiques de très haute énergie, faisant de l'astronomie multimessager un outil particulièrement performant pour l'étude des processus les plus intenses de l'Univers.

Dans ce contexte, nous nous intéressons aux microquasars. Ces objets sont des systèmes binaires galactiques comportant un objet compact (trou noir ou étoile à neutron) gravitationnellement lié avec une étoile dite compagnon. Des phénomènes de transfert de masse ont lieu depuis l'étoile compagnon vers l'objet compact avec formation d'un disque d'accrétion. De la matière est dans le même temps ejectée et forme un jet similaire à ceux observés dans les quasars, ce qui a valu aux microquasars leur dénomination. Ces processus d'accretion-ejection ont lieu de manière transitoire lors de périodes d'éruption intenses. Plusieurs contributions au spectre électromagnétique peuvent y être identifiées. La composante la plus évidente est le flux en rayons X, qui trouve son origine d'une part dans le disque d'accrétion caractérisé par une émission thermique, et d'autre part dans de la matière coronale caractérisée par une émission de plus haute énergie en forme de loi de puissance traduisant la présence de particules accélérées. Le jet quant à lui, bien qu'il puisse aussi contribuer aux émissions en rayons X depuis sa base au plus proche de l'objet compact, est principalement caractérisé par son spectre d'émission dans le domaine radio. Lorsque l'on trace l'évolution du spectre de rayons X d'un microquasar lors d'une période d'activité sur un diagramme dureté-intensité [1], il est courant de constater qu'il suit régulièrement le même chemin, et ce d'une source à l'autre. Ainsi, le système commence son éruption dans un état dur, dominé par sa composante non-thermique, dans lequel il va augmenter en intensité. Il s'ensuit une transition d'état pendant laquelle la composante thermique du spectre va devenir dominante. Le système sera ensuite dans un état mou où il perd progressivement en intensité avant d'effectuer une nouvelle transition vers l'état dur et perdre encore en intensité. Des études de corrélations entre l'état du spectre de rayons X et les mesures radio trouvent des émissions discrètes de matières à des vitesses relativistes pendant les transitions d'état, et une disparition du jet dans l'état mou. Comme illustré sur la Figure 1, ce comportement peut s'expliquer par une évolution de la configuration du système.

[1] La dureté représentant la forme du spectre, avec un spectre plus dur ayant une plus grande contribu-

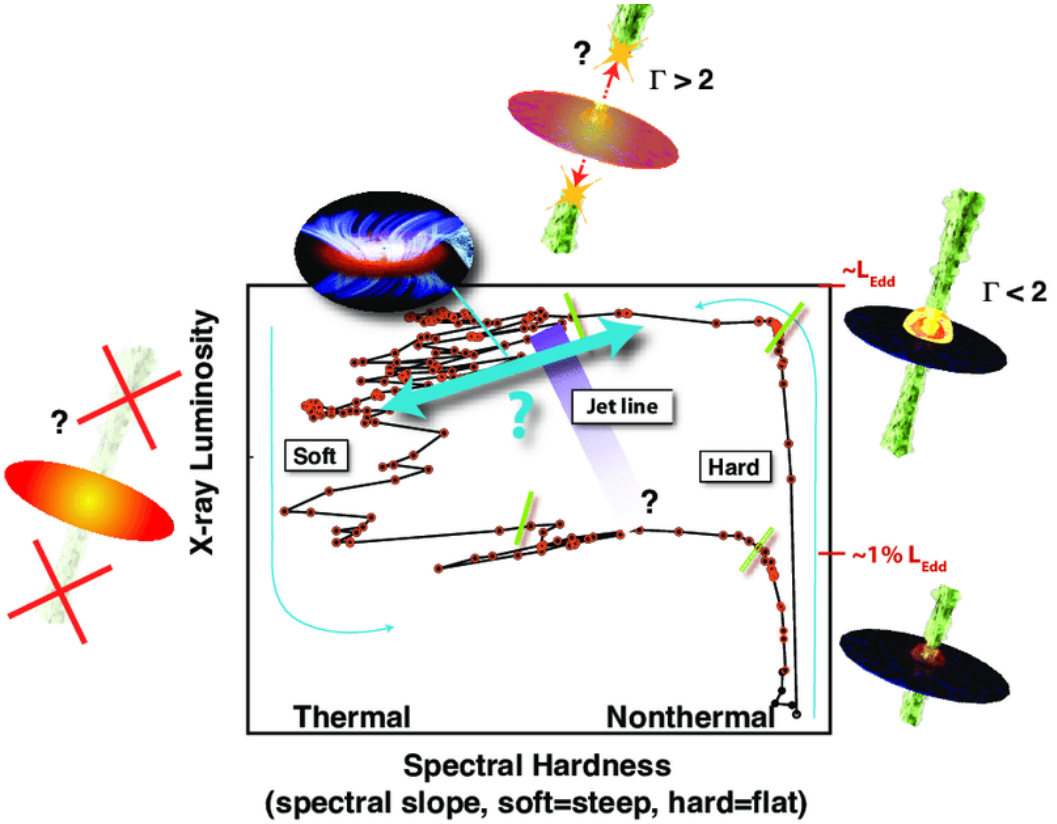

Figure 1.: Exemple d'un trajet typique de l'émission en rayons X d'une éruption de GX339-4. Des schémas de la configuration du système disque-jet sont représentés. L_{Edd} est la luminosité d'Eddington. Γ est le facteur de Lorentz de la masse éjectée. Figure tirée de [3].

Astronomie γ et neutrino

H.E.S.S. (pour High Energy Stereoscopic System) est un réseau de télescopes à imagerie atmosphérique situé en Namibie. Cette technologie permet l'observation du rayonnement Tcherenkov induit par des gerbes de particules générées par l'interaction de photons γ dans l'atmosphère, comme schématisé sur la Figure 2. L'étude des images capturées par ces télescopes permet de reconstruire la direction et l'énergie du photon primaire, indispensable pour de l'astronomie. Ces rayons γ nécessitent néanmoins une énergie suffisamment importante pour générer des gerbes atmosphériques, plaçant HESS dans le domaine de l'astronomie de très haute énergie, généralement prise entre 100 GeV et 100 TeV.

L'astronomie neutrino de haute énergie repose sur des principes similaires. Cette fois, les instruments sont situés dans les fonds marins, ce qui permet de tirer profit d'un environnement sans lumière et protégé de la majorité du rayonnement cosmique. Cela permet ainsi d'isoler les neutrinos, seules particules capables de traverser le di-

tion de la partie non-thermique.

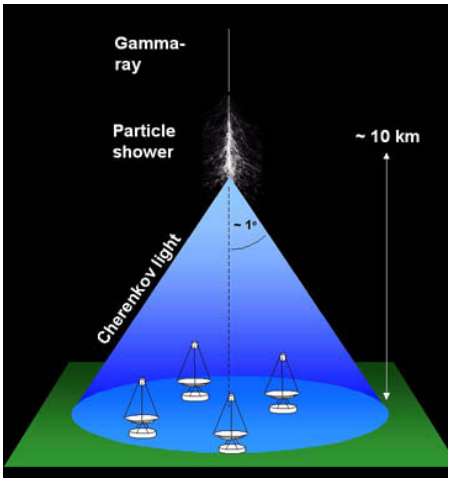

Figure 2.: Schéma d'un cône de lumière constitué par la lumière Tcherenkov d'une gerbe atmosphérique électromagnétique et atteignant un réseau de détecteur au sol.

amètre terrestre sans diminution significative de leur flux. Ces neutrinos, à condition d'avoir une énergie suffisante ($\gtrsim$ GeV) induisent deux topologies pouvant être distinguées selon leur saveurs, comme schématisé Figure 3. Ainsi les neutrinos muoniques peuvent générer la production de muons qui se propagent dans l'eau de manière rectiligne sur de grande distance, et leur rayonnement Tcherenkov prend la forme d'un cône. La direction du muon pouvant être reconstruite de façon précise et reliée à la direction du neutrino primaire, c'est cette topologie qui est la plus intéressante pour l'astronomie. Les autres saveurs de neutrinos génèrent des gerbes localisées proche de leur lieu d'interaction. Les télescopes à neutrinos sur lesquels reposent les travaux de cette thèse sont ANTARES, ayant fonctionné de mars 2006 à février 2022 à 2500 mètres au fond de la mer Méditerrannée au large de Toulon, et son successeur KM3NeT en construction sur deux sites: ORCA, lui aussi au large de Toulon, et ARCA, au large de la Sicile. Alors qu'ANTARES était optimisé pour la détection de neutrinos avec des énergies allant de quelques centaines de GeV à quelques PeV, les deux sites de KM3NeT couvrent des gammes d'énergies complémentaires avec ORCA étant optimisé pour des neutrinos de quelques GeV à quelques TeV et ARCA du TeV au PeV.

Recherche d'émission de haute énergie provenant de périodes d'activité de microquasars

Cette étude est une recherche multimessager et multi-longueurs d'onde de marqueurs d'accélération de particules de très haute énergie dans les microquasars. Dans la mesure où ces sources présentent des périodes d'activité intenses entrecoupant des périodes d'inactivité, nous considérons que cette accélération a lieu pendant les périodes d'éruption, où un flux important de rayons X témoigne d'un échauffement

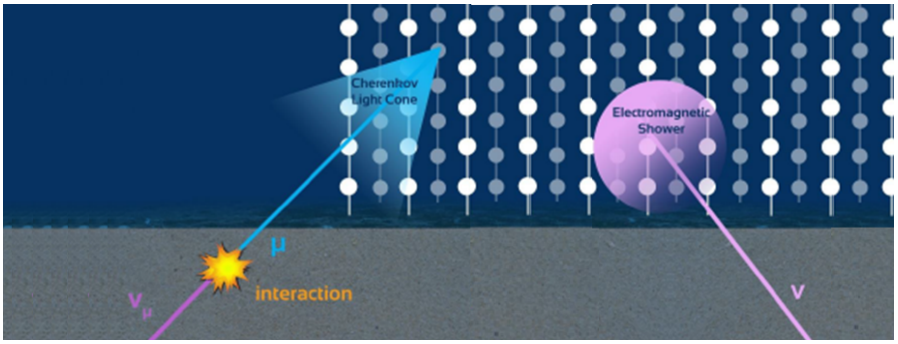

Figure 3.: Schéma des deux principales topologies des évènements dans un détecteur de neutrinos de haute énergie. Gauche : ν_μ interagissant en dehors du volume du détecteur et produisant un muon qui se propage jusqu'à lui et induisant l'émission d'un cône Tcherenkov. Droite : ν_e interagissant à l'intérieur du volume du détecteur et produisant une gerbe électromagnétique induisant elle-même une émission de lumière Tcherenkov. Figure tirée de [4].

intense au voisinage de l'objet compact, et où l'éjection de matière qui s'en suit créé un environnement propice à l'apparition de chocs. Ainsi, notre recherche se concentre dans des fenêtres temporelles marquées par la présence significative d'un flux de rayons X. Ignorer de la sorte les périodes d'inactivité des sources permet de limiter les contributions du bruit de fond dans les diverses analyses.

La détermination de ces périodes de recherche est effectué grâce à l'étude de courbes de lumière mises à disposition par plusieurs télescopes à rayons X à grands champs de vue: RXTE/ASM, Swift/BAT et MAXI/GSC. Ces télescopes permettent le suivi à long terme d'un nombre de sources transitoires avec des fréquences de mesures de plusieurs fois par jour. Un exemple de ces périodes est présenté sur la Figure 4 où nous pouvons constater les périodes d'activité en rayons X du microquasar GX339-4.

L'étude des données provenant des observations HESS se fait en deux temps. Premièrement, nous nous intéressons à l'ensemble des observations incluant un microquasar dans le champ de vue du télescope, que la source soit la cible de l'observation ou non. Aucun excès significatif n'a pu être détecté, et un excès marginal à 2.6 σ du microquasar GRS1915+105 ressort de l'analyse, sans pouvoir être formellement attribué à la source. Dans un second temps, nous nous concentrons sur les observations effectuées pendant les périodes d'activité en rayons X. Les résultats de cette étude sont données dans la Table 1. Bien qu'aucun signal significatif n'ait pu être observé, cette étude permet de placer des limites supérieures sur une distribution spectrale d'énergie pour chaque source de manière cohérente dans la mesure où le flux multi-longueurs d'onde est moins variable d'une observation à l'autre que dans le premier cas. Pour cette même raison, nous séparons les observations de GX339-4 en trois périodes correspondant à trois états spectraux bien définis.

Une étude est aussi effectuée dans le domaine des rayons γ de haute énergie, c'est-à-dire entre 100 MeV et 100 GeV, provenant du télescope spatial Fermi/LAT, grâce aux

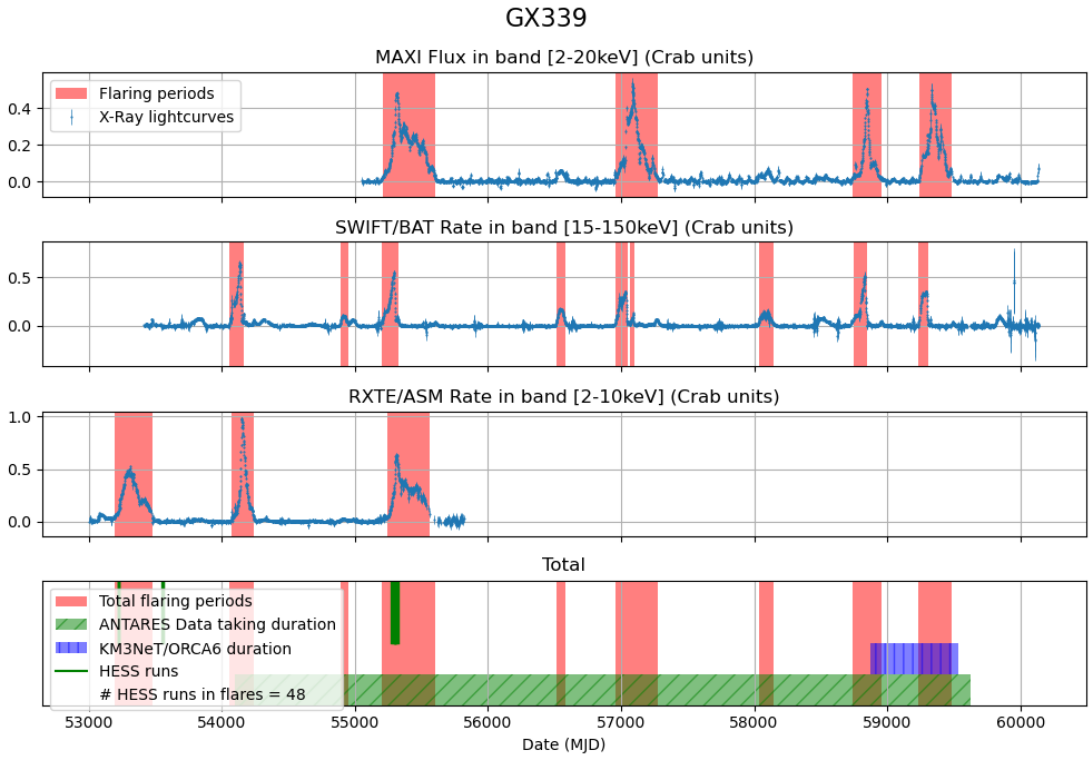

Figure 4.: Courbes de lumière en rayons X de GX339-4, mesurées par les télescopes MAXI/GSC, Swift/BAT et RXTE/ASM. Les périodes d'activité sont notées en rouge. La durée de prise de données de ANTARES est représentée par une bande verte et la période KM3NeT/ORCA6 par une bande bleue. Les dates d'observations HESS sont marquées par des lignes verticales vertes.

Source	Temps d'obs. (h)	Significativité	Seuil (TeV)	U.L.
GRS 1915+105	10.9	1.9	0.38	1.4
MAXI J1535-571	5.3	-0.5	0.62	1.4
MAXI J1348-630	4.2	-1.2	0.28	0.82
GRS1716-249	1.3	0.0	0.19	2.4
GX339-4 (All flare)	19.1	-0.6	0.31	1.5
GX339-4 (HS)	2.0	-0.2	0.31	5.2
GX339-4 (ST)	8.2	-0.3	0.31	2.1
GX339-4 (SS)	8.9	-0.6	0.31	1.1

Table 1.: Résultats des analyses de données provenant d'observations HESS de micro-quasars en éruption. Les limites supérieures intégrales (notées U.L.) sont données en unitées de 10^{-8}ph/m^2/s et sont calculées au-dessus de leur seuil en énergie respectifs.

données et outils d'analyse publics mis à disposition.

Nous procedons de même à l'analyse dans le domaine des neutrinos. Nous recherchons une corrélation entre la détection de neutrinos autour de nos microquasars pendant leurs périodes d'activité dans les données d'ANTARES et de KM3NeT/ORCA. Les données d'ANTARES couvrent une période allant de janvier 2007 à février 2022 et celles de ORCA ont été prises dans sa configuration à 6 lignes (ORCA6), de janvier 2020 à novembre 2021. Des limites sur la fluence, c'est-à-dire sur la quantité d'énergie émise en neutrinos sont présentées sur la Figure 5. Trois sources présentent des périodes d'activité pendant la prise de données ORCA6, et les limites sur leurs flux dans le domaine en énergie des deux détecteurs sont présentées sur la Figure 6.

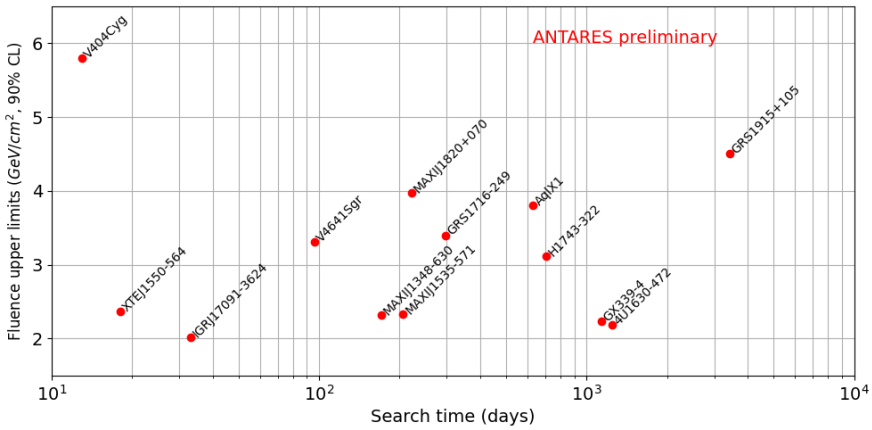

Figure 5.: Limite supérieure de fluence neutrino avec ANTARES en fonction de la durée de la fenêtre de recherche. Cette durée correspond à la période d'activité observée dans de bonnes conditions de prise de données.

Avec l'addition de mesures multi-longueur d'onde provenant de la littérature, nous procédons à une modélisation des paramètres de deux systèmes à partir de leurs distributions spectrales d'énergie, comme illustré sur la Figure 7.

Afin de maximiser les chances d'une future découverte d'un signal neutrino ou γ, un système de monitorage automatique se basant sur les mêmes méthodes d'analyses que celles utilisées plus haut a été mis en place. Ce système, schématisé sur la figure Figure 8, recherche dans les données publiques, mises à jour plusieurs fois par jour, des télescopes MAXI/GSC et Swift/BAT pour détecter au plus tôt de nouvelles périodes d'activité. Si un flux significatif ou une transition d'état spectral est détectée, une analyse de données Fermi/LAT est lancée dans une fenêtre de 1 jour avant la détection jusqu'aux dernières données disponibles, celles-ci étant accessibles quelques heures après leur collection. Dans le même temps, une analyse des données temps-réel de KM3NeT (ORCA et ARCA) est lancée. Ces mesures entrent dans la stratégie d'observation de HESS, car la détection d'un signal dans les données Fermi/LAT ou KM3NeT déclencherait des observations de la source en question.

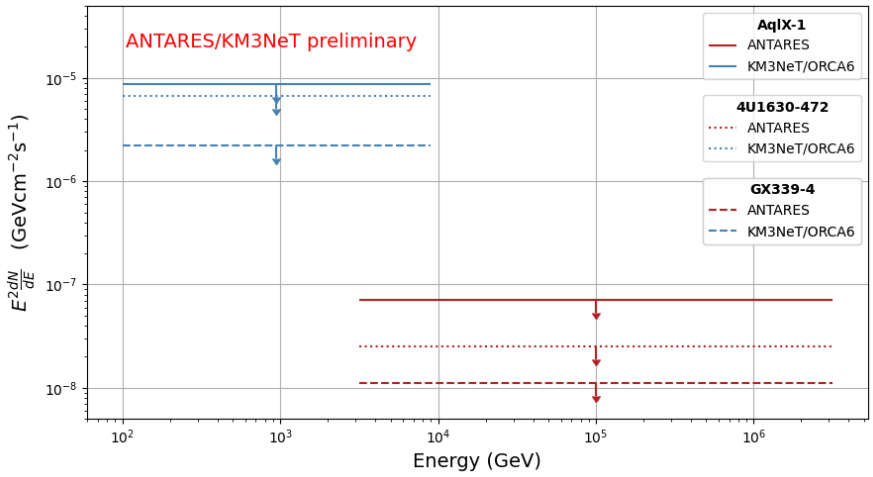

Figure 6.: Limites supérieures sur le flux neutrino de AqlX-1 (ligne pleine), 4U1630-472 (pointillée) and GX339-4 (tiretée) de KM3NeT/ORCA (bleu) et ANTARES (rouge). Les limites sont données $E^2\frac{dN}{dE}$, (en GeVcm^{-2}s^{-1}), en supposant un flux de neutrino avec un spectre en énergie de la forme ϕ(E) $\propto$ E^{-2}.

Recherches de corrélation neutrino en suivi d'alertes multimessagers

L'astronomie temps-réel nécessite un traitement rapide des données et la communication d'alertes entre les différents observatoires dans les délais les plus brefs possibles afin de déclencher des observations de phénomènes transitoires par l'ensemble de la communauté. Dans ce contexte, des travaux ont été réalisés afin de développer les méthodes d'analyse pour le suivi d'alertes multimessagers avec ORCA. Notamment, des recherches de signaux en coïncidence avec des évènements neutrinos de haute énergie du télescope IceCube ont été effectuées. Ces évènements IceCube ont des directions coïncidentes avec les positions de blazars (à savoir PKS0735+17, PKS1741-03, PKS0215+015 et TXS0310+222), ce qui ajoute à la pertinence de l'étude. Un autre évènement, le sursaut gamma particulièrement intense GRB221009A, a lui aussi fait l'objet d'un suivi avec KM3NeT. Les résultats de cette étude sont présentés sur la Figure 9 aux côtés de mesures d'autres télescopes. Enfin, une recherche de corrélations dans les données de ORCA avec les détections d'ondes gravitationnelles provenant de la période d'observation O3 des interféromètres LIGO et Virgo a été effectuée.

Afin de permettre le suivi d'alertes émises par la communauté de manière fiable et rapide, un système de reconstruction et de classification des évènements directement depuis l'acquisition des données de KM3NeT a été mis en place. Ainsi, avec l'aide d'une implémentation permettant la réception et le filtrage des alertes émises automatiquement par divers télescopes, des recherches de corrélation entre ces alertes et les données de KM3NeT peuvent être effectuées. Les méthodes d'analyses développées pour les précédentes études ont ainsi été implémentée dans ce système de suivi

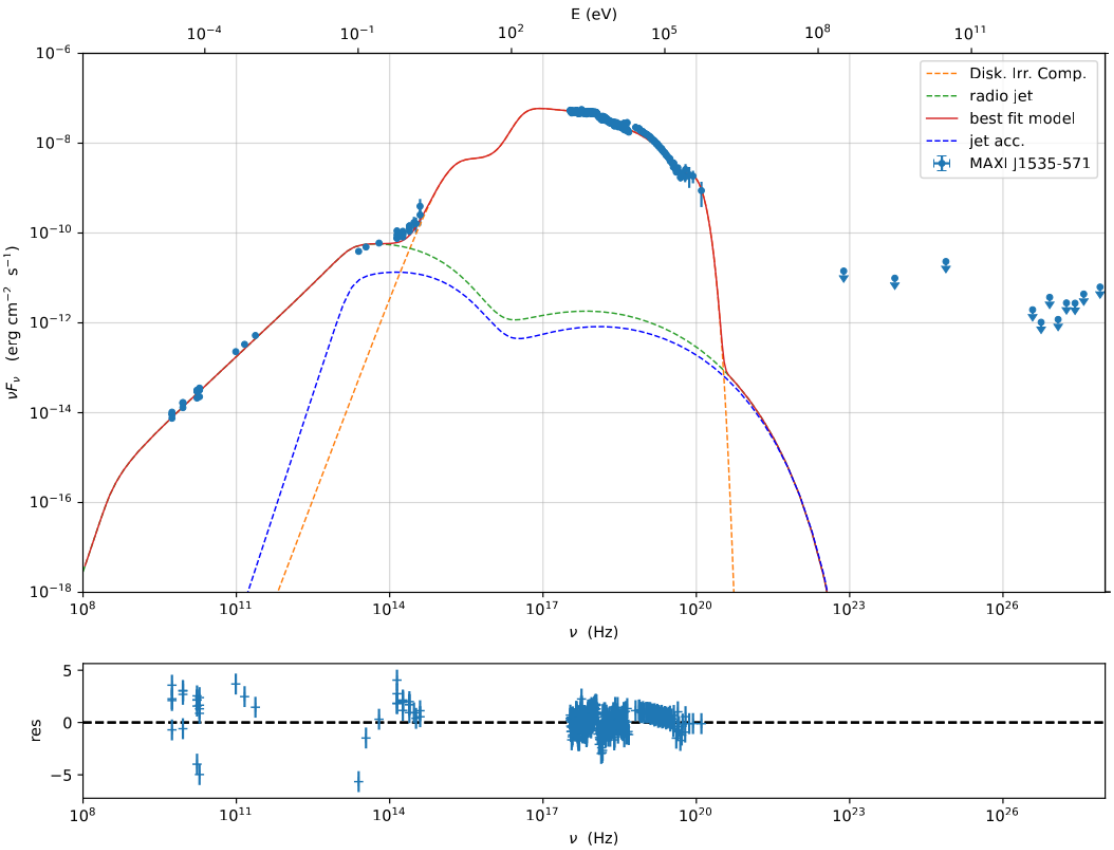

Figure 7.: Modélisation d'un état de transition pendant l'éruption du microquasar MAXIJ1535-571. Les mesures de diverses télescopes sont notées en bleu. Les contributions des diverses composantes du système à la distribution spectrale d'énergie modélisée sont notées par différentes couleurs. Les résidus de la modélisation sont notés sur le panneau du bas.

d'alertes en temps-réel. Cela permet à KM3NeT d'effectuer des recherches de neutrinos provenant de microquasars, mais aussi d'autres sources transitoires détectées dans plusieurs messagers tels que les sursauts gamma ou les coalescences d'objets compacts détectées par ondes gravitationelles.

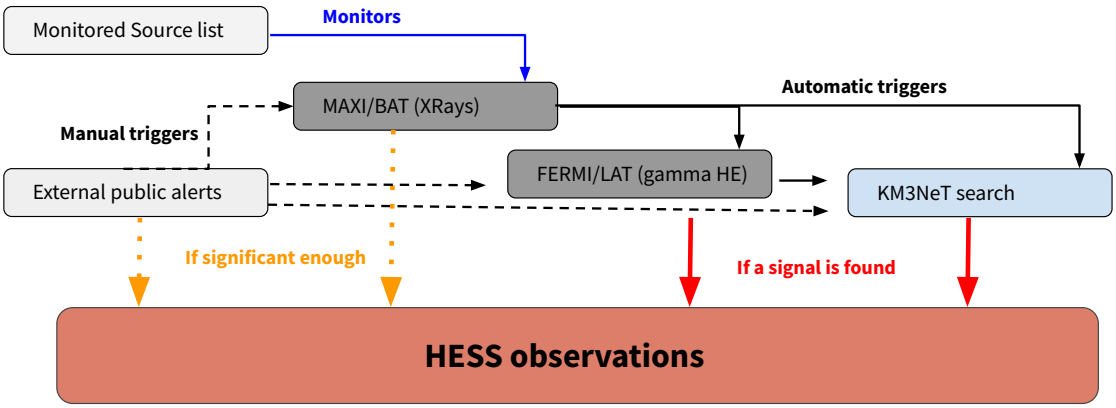

Figure 8.: Diagramme résumant le moniteur multimessagers de microquasars.

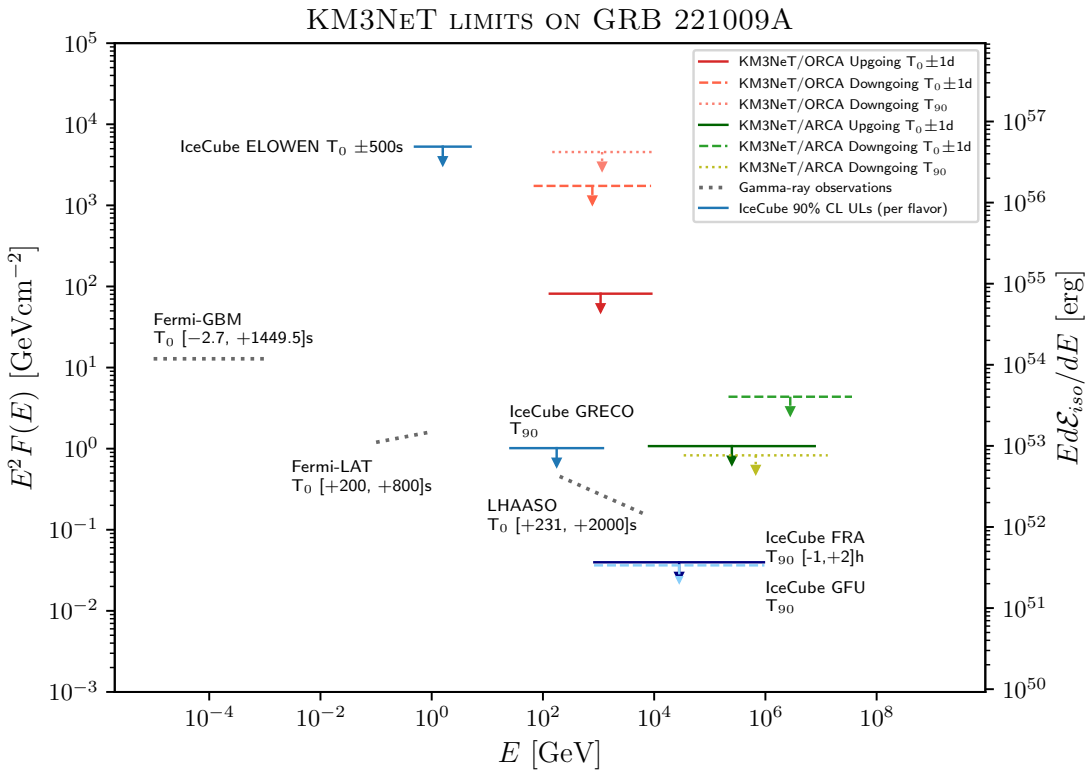

Figure 9.: Comparaison des limites supérieures par les téléscopes à neutrinos IceCube et KM3NeT sur la fluence neutrino du sursaut gamma GRB221009A, avec les mesures de plusieurs observatoires gamma [5].

Contents

Preface

Multi-messenger astronomy is the study of multiple conveyors of information from astrophysical sources. This field has been expanding in the last few years with the construction of facilities dedicated to the detection of gravitational waves or astrophysical neutrinos. Such facilities are sensitive to very high-energy phenomena, making multi-messenger astronomy a particularly good tool for probing the most intense processes in the Universe, and are especially efficient working together, in real-time, with photon telescopes. Microquasars are binary systems of a compact object and a star, exhibiting processes of mass accretion from the star to the compact object, and ejection of matter through a jet. These sources display phases of intense outbursts, primarily detected in X-ray. The high energy, transient nature of these sources make them interesting subjects for a study through a multi-messenger lens. The work presented in this thesis then consists of searching for very high energy emissions, in γ-rays or neutrinos, from microquasars. We can divide this work into 2 topics, the first being a search based on data from past observations, and the second being strategy and preparation for future observations.

This manuscript is separated into 3 parts. Part I is dedicated to introducing the context and the tools of the work developed in this thesis. A brief introduction to astronomy in the Very High Energy domain is given in chapter 1, while the mechanisms involved in the emission of photons and neutrinos from astrophysical sources are presented in chapter 2. Microquasars, the main sources of interest for this work, is the topic of chapter 3 where their phenomenology and multiwavelength behavior are described. Then, chapter 4 contains descriptions of the observatories from which this work is based, mainly the H.E.S.S. telescope array for Very High Energy γ-ray astronomy and the deep-sea neutrino telescopes ANTARES and KM3NeT. For each facility, a description of the detection principle is given, followed by generalities on the calibration, selection, and initial data reduction routinely used in the respective collaborations.

The central work of this thesis, a search for γ-rays and neutrinos from microquasars, is developed in Part II. After an introduction to the studied systems in chapter 5, the method to derive the periods of interest for the analysis from the X-ray activity of those sources is described in chapter 6. Analysis results from H.E.S.S. observations are then shown in chapter 7. An analysis is also performed from Fermi/LAT data, described in chapter 8. The specific data analysis methods from neutrino telescopes performed in this thesis and their results are detailed in chapter 9. Results obtained in Part II are combined in chapter 10 as spectral energy distributions, with modeling performed on selected sources. To close this part, and to transition from archival data analysis to real-time astronomy, chapter 11 describes the implementation of an automatic

monitor and alert broker for microquasar activity.

Finally, Part III focuses on the development of the alert follow-up capabilities of KM3NeT. The strategy for automatic executions, in real-time data, of neutrino signal searches in coincidence with external alerts is described in chapter 13. This chapter then describes the analysis methods for these follow-up searches for several types of alerts. Neutrino searches in one of KM3NeT detector, ORCA, in correlation to several multi-messenger signals are developed in chapter 12, namely high-energy neutrinos coincident with blazars detected by the IceCube Neutrino Telescope, Gravitational Waves from mergers detected by the LIGO/Virgo interferometers, and the Gamma Ray Burst (GRB)221009A.

Part I.

Context: multi-messenger astronomy, microquasars, and methods for high-energy astronomy.

Contents

1. A Multi-Messenger Astronomy

1.1. Introduction

Since the discovery of cosmic rays by Victor Hess in the early 20th century, the existence of a high-energy particle population in the Universe has been studied. Following experiments led by Pierre Auger [6] revealed that the cosmic rays discovered by Hess were actually secondary particles induced by even higher energy particles interacting in the upper atmosphere.

As seen in Figure 1.1, the spectrum of cosmic rays has been extensively studied in a broad energy range and exhibits some particular features. Below $\sim 10^{10}$ eV, the flux is dominated by charged particles from the Sun, and cosmic rays from beyond the Solar system are modulated by solar activity. Above this energy, the cosmic ray spectrum follows a power law. Around $\sim 10^{15}$ eV and $\sim 10^{17}$ eV are softenings of the particle spectrum, features known as the first and second *knees*. Below the second knee, the particles are thought to originate from our galaxy. An *ankle*, corresponding to the hardening of the spectrum, can be seen around $\sim 10^{19}$ eV above which the particles are thought to be of extra-galactic origin. Above $\sim 5 \times 10^{19}$ eV, the propagation of protons is limited by their interaction with photons from the Cosmic Microwave Background radiation, resulting in what is known as the Greisen–Zatsepin–Kuzmin (GZK) effect.

As charged particles are deflected by magnetic fields in their travel from their source to us, it is impossible to trace them back to their sources of origin, except in the extremely high energy range where the deflection angle can be bigger than the distance to the source. Astronomy, in the strict sense, is mostly impossible from cosmic rays. Thus, in order to unveil the sources of origin of these particles and study the high-energy phenomena that produce and release them in the Universe, observations of other *messengers*, conveyers of information, are necessary.

We should turn toward the first messenger: the photon. In addition to the traditional astronomy that used visible light for millennia, our visibility was improved with the use of increasingly sensitive telescopes as well as broadened by the observation across the electromagnetic spectrum brought by multi-wavelength detection facilities. Today, astronomy is a multi-messenger astronomy with the detection of messengers beyond photons. Gravitational Wave (GW) detectors allowed for example the detection of the merger between two neutron stars [8] which have also been detected with photons in a broad range of energy. As seen in Figure 1.2, the use of multiple messengers was a necessary condition for establishing this discovery. The other new messenger is the neutrino, and neutrino astronomy will be a central part of this thesis.

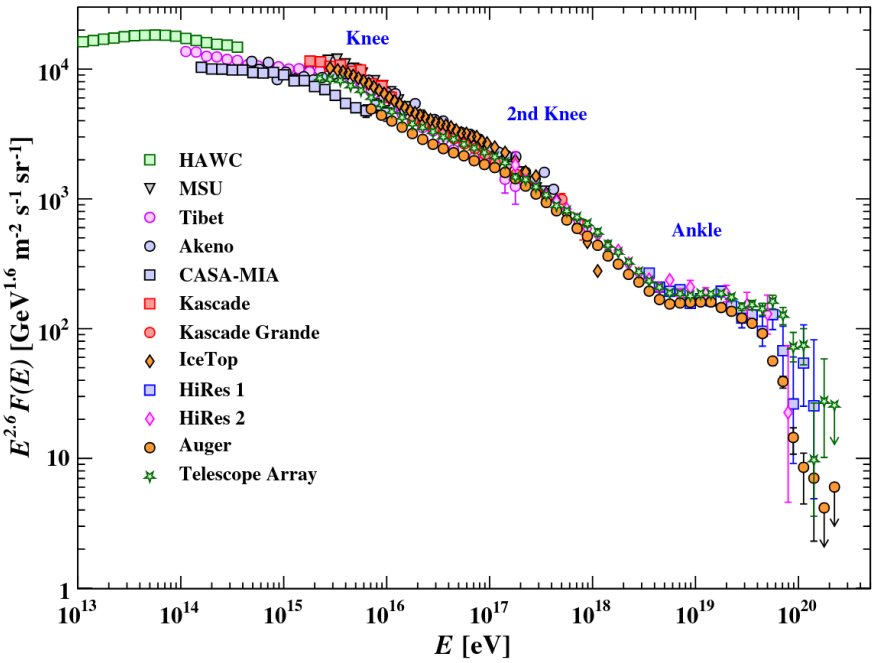

Figure 1.1.: All-particle cosmic-ray spectrum as a function of the energy per nucleus E from air shower measurements. The flux is scaled by $E^{2.6}$ for clarity. Figure from [7].

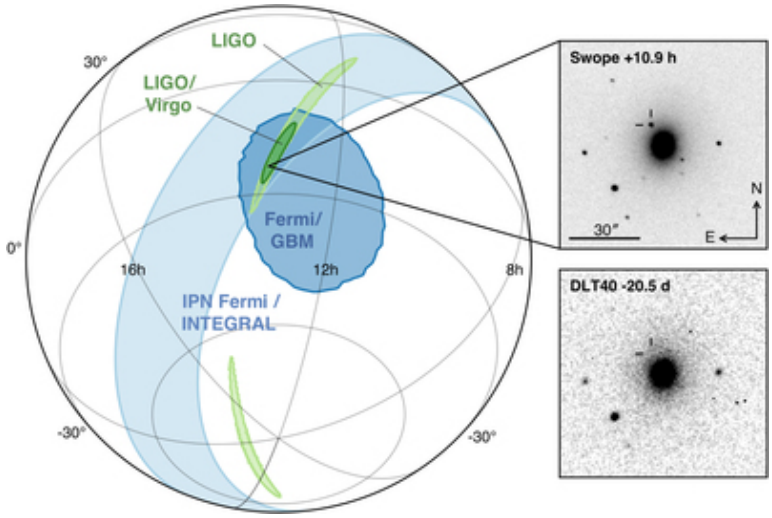

Figure 1.2.: Localization of GW170817 multiple telescopes. Localization from GW detectors LIGO and Virgo in green (LIGO in light green, LIGO+Virgo in dark green). X-ray/γ-ray detector Fermi/GBM in dark blue, and localization from the timing between Fermi and INTEGRAL telescopes in light blue. Images from optical telescopes DLT40 and Swope taken respectively 20.5 days before and 10.9 hours after the event are inset. From [8].

High-energy astronomy is the domain that is the most susceptible to gain from the use of multiple messengers. Indeed, the phenomena at play are often transient, with extreme amounts of energy being released from explosive events. Contrary to most telescopes in the electromagnetic spectrum, neutrino and GW detectors are able to detect events from a large part of the sky at any given time, which makes them particularly efficient at detecting those high-energy transient events. Time-domain astronomy to study the temporal evolution of these events necessitates follow-up observations with electromagnetic telescopes to be performed as quickly as possible. This is made possible by the elaboration of networks of alert systems working automatically between different telescopes and observatories in all messengers and electromagnetic wavelengths. The overlap between high-energy, time-domain, and multi-messenger astronomy is then natural.

1.2. The γ-ray sky

γ-ray is a generic term covering the high end of the electromagnetic spectrum. It however covers a large range, multiple orders of magnitudes, of energy. To distinguish energy domains that are each characterized by their own detection methods, the following naming convention is commonly adopted: High Energy (HE) γ-rays refer to photon energy between 100 MeV and 100 GeV and are detected above the atmosphere by space telescopes, while Very High Energy (VHE) refers to photon energy between 100 GeV and 100 TeV that are capable of initiating a particle shower in the atmosphere detectable from ground-based observatories. Higher energies, Ultra High Energy (UHE) above 100 TeV, necessitate the use of detectors with large areas of collection, which can be achieved by a high-altitude water Cherenkov detector.

Figure 1.3 shows the number of discovered sources per year in the X-ray, HE and VHE bands and highlights some of the telescopes responsible for these discoveries.

In HE, the more complete catalog to this day is given by the Fermi/LAT telescope and includes around 5000 sources [9], galactic and extra-galactic, on top of a diffuse flux with a galactic component correlated with the distribution of matter density in the galactic plane, and an isotropic flux of extra-galactic origin. In the VHE domain, the first source detected was the Crab Nebula by the Whipple Observatory in 1989 [10]. Today, more than 200 sources have been detected in this energy range [11] and could be identified to galactic or extra-galactic objects.

Galactic VHE emitters are often extended sources, such as Supernova Remnant (SNR) that are features created when matter ejected from a supernova forms a powerful outward-moving shock in the Interstellar medium (ISM), or Pulsar Wind Nebula (PWN) which are relativistic plasma powered by the outflow of a pulsar. Emission in the VHE range was also observed coming from close to the pulsar itself, characterized by a pulsating flux of γ-rays. Some binary systems are also detected in this energy range and are thus known as γ-ray binaries. Extra-galactic sources, on the other hand, are identified as Active Galactic Nuclei (AGN), where accretion of matter around supermassive black holes leads to bright emissions, or as starburst galaxies, characterized

by high formation rates of massive stars and high rates of subsequent supernovae. Transient events have been detected as well in VHE, such as the Gamma-Ray Burst (GRB) 190829A [12] or the galactic recurrent nova RS Ophichui [13].

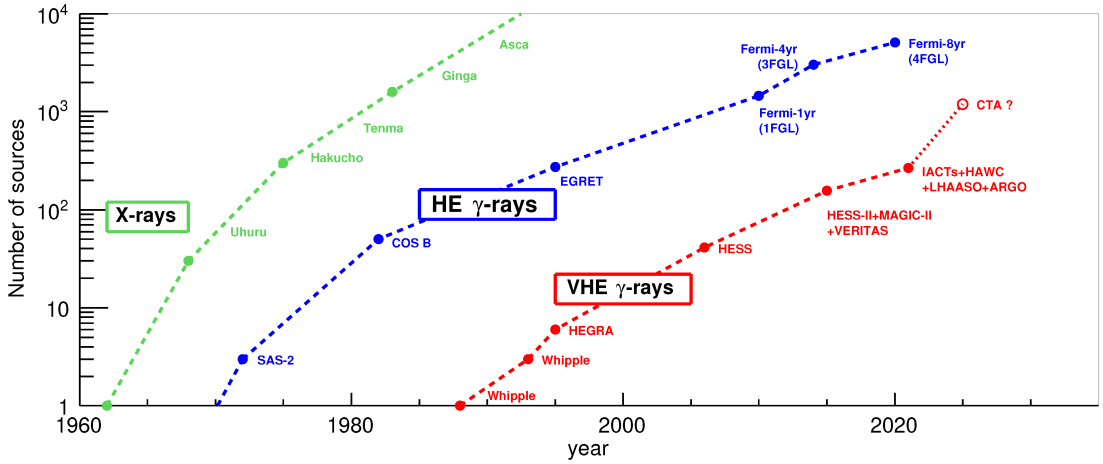

Figure 1.3.: Number of discovered sources as a function of time, in 3 energy bands. Observatories contributing to the discoveries are indicated. Figure taken from [14].

In the UHE range, the LHAASO observatory reported in 2021 the detection of photons originating from 12 galactic sources [15]. Since the production of photons in this energy range may require acceleration of particles to the PeV energy range, these sources are referred to as *PeVatrons*.

1.3. Neutrinos sources

The first neutrino source detected beyond the solar system was actually an event: the supernova SN1987A [16], at a distance of 50 kpc in the Large Magellanic Cloud. A total of 20 neutrinos have been detected in a few seconds by the Kamiokande and IMB water Cherenkov detectors, and an additional 5 from the Baksan scintillator detector [17]. The average energy of these neutrinos was estimated to be ~ 15 MeV. These detections, in a multi-messenger setting with observations of Multi-Wavelength (MWL) light, allowed a further understanding of the mechanisms of core-collapse as well as an exploration of the neutrino mass and magnetic moment [18].

At higher energy, above ~ 100 TeV, the IceCube neutrino telescope discovered a diffuse flux of neutrinos of astrophysical origin [19] which is reaching the PeV energy range, as seen on Figure 1.4. This flux is consistent with an isotropic distribution, and its origin is debated, but further neutrino detections in the next years will bring more light to this question.

On top of this isotropic flux, an excess of neutrino was detected as originating from the galactic plane at a 4.5σ level with 10 years of IceCube data [20] and at 2.2σ level with 13 years of ANTARES data [21]. The possibility remains that the isotropic and galactic

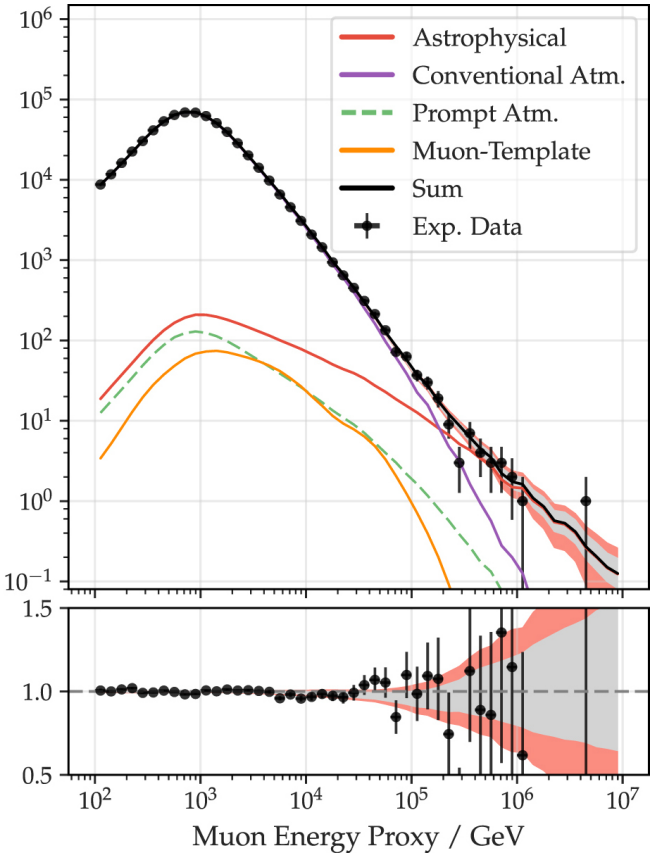

Figure 1.4.: Distribution of the muon energy, serving as proxy to ν_μ energy in the IceCube detector. The experimental data (black dots) are shown with the best-fit expectation from simulations of different contributions to the overall flux. The ratio of data to simulations is shown in the bottom plot. The fitted flux from astrophysical neutrinos is shown in red and dominates the flux above 100 TeV, over the atmospheric contributions in purple (conventional), green (prompt), and yellow (muons). Taken from [19].

diffuse fluxes originate from a population of unresolved point sources, as so far, 2 high-energy neutrino sources have been detected. The first one is the blazar TXS 0506+056 [22], with a 290 TeV neutrino detected in 2017 that could be significantly correlated in space with its coordinates and in time with an increase of its γ-ray flux. Following this measurement, an additional search of neutrinos from this source was performed. It considered lower energy neutrinos in 10 years of IceCube data and independently found a 3.5σ evidence of a neutrino flaring period from the blazar in a $\sim$ 6-month window between September 2014 and March 2015, which places blazars as neutrino emitters. IceCube announced more recently, in 2022, the discovery of an excess from background expectation with a 4.2σ significance coincident with the position of the active galaxy NGC1068 [23]. Around 80 neutrinos of energy between 1.5 TeV and 15 TeV are then attributed to the source in the close to 10 years of data. Interestingly, this

later source is found to be a steady neutrino emitter, as opposed to the flaring behavior of TXS 0506+056. The neutrino flux can be identified as originating from the AGN of NGC1068, heavily obscured by its surrounding medium. This is supported by the fact that no VHE γ-rays were observed for this source, even if the neutrino emission processes also generate photons in a similar energy range, as described in chapter 2.

2. γ-ray and neutrino productions

2.1. Charged particle acceleration mechanisms

To explain the cosmic ray spectrum that was observed at Earth which follows a power-law, Enrico Fermi proposed in 1949 [24] a simple model where a charged particle of initial energy E would, in the interstellar medium, collision heads-on a magnetic cloud of turbulent low-energy medium. The average energy gained by such a particle per collision ΔE is given by:

$$\left\langle \frac{\Delta E}{E} \right\rangle = \frac{4}{3}\left(\frac{V}{c}\right)^2 \tag{2.1}$$

with V the speed of the particle with respect to the cloud and c the speed of light. We note the second order of the energy gain with respect to V/c. This acceleration mechanism is known as the *second-order* Fermi acceleration.

The second order of the mechanism initially proposed by Fermi meant that its efficiency was low and insufficient to explain the cosmic ray spectrum. Later developments consider charged particles moving back and forth across a shock front [25]. This mechanism, known as diffusive shock acceleration [26], yields for a particle an average energy gain at every back-and-forth shock crossing:

$$\left\langle \frac{\Delta E}{E} \right\rangle = \frac{4}{3}\left(\frac{V}{c}\right) \tag{2.2}$$

with V being this time the velocity of the particle with respect to the matter flow downstream of the shock. This time, the average energy gain is of first order with respect to V/c, and this mechanism is commonly known as the *first order* Fermi acceleration.

If a strong, collisionless, non-relativistic shock is assumed, the accelerated particle energy spectrum can be computed as a power-law with index -2 [27]:

$$N(E)dE \propto E^{-2}dE \tag{2.3}$$

The diffusive shock acceleration is the central mechanism in contemporary high-energy astrophysics as it is the preferred explanation for populations of accelerated particles.

2.2. Leptonic radiative processes

Once accelerated, charged particles can escape the systems that lead to their acceleration and travel through the interstellar medium. But, more interestingly for the study of the high-energy mechanisms in said systems, the interaction of high-energy particles can result in photon or neutrino production close to their acceleration sites. The secondary particles, neutral, can travel the interstellar medium in straight lines and can be traced back to their source. This is the leading principle behind high-energy astronomy. The following section overviews the radiative mechanisms of high-energy electrons and protons.

2.2.1. Synchrotron emission

Charged particles in a magnetic field B emit photons. When these particles are relativistic, the emission mechanism is known as the synchrotron radiation.

The average energy loss of such an electron from a population of isotropically distributed velocities is given by [28]:

$$\frac{dE}{dt} = -\frac{4}{3}\sigma_T c\gamma^2\beta^2\left(\frac{B^2}{8\pi}\right) \tag{2.4}$$

with σ_T the Thomson interaction cross-section, γ the particle Lorentz factor and $\beta = v/c$. $\left(B^2/8\pi\right)$ is the energy density of the magnetic field.

We can notice from Equation 2.4 that the power emitted by relativistic electrons is greatly (>10^6) higher than protons of similar γ, due to their lower mass. Indeed, the interaction cross-section between a photon and a charged particle of mass m is $\sigma \propto 1/m^2$. The synchrotron radiation is then dominated by the electron population and is considered a leptonic process.

From a power law distribution $N(E)dE = \kappa E^{-p}dE$ of electrons in a magnetic field B [27] the emitted flux density as a function of frequency $J(\nu)$ can be directly linked to the magnetic field intensity and the spectral index p of the electrons as:

$$J(\nu) \propto B^{\frac{(p+1)}{2}}\nu^{\frac{-(p-1)}{2}} \tag{2.5}$$

This flux is directly observed at Earth if the synchrotron emission is not absorbed. The population of synchrotron-emitting electrons can however scatter or absorb photons in a *synchrotron self-absorption*. This relation then holds in the optically thin case, meaning that the mean free path of the photons is larger than the source size. This results in a low-frequency cutoff of the observed spectrum.

2.2.2. Inverse Compton process

A high-energy charged particle, when interacting with a lower-energy photon, transmits a fraction of its energy to it via an Inverse Compton scattering.

The cross-section of this interaction is given by the Thomson cross-section σ_T if the photon energy before scattering in the reference frame of the electron E'_i is lower than the electron rest mass energy $m_e c^2$. Otherwise, quantum electrodynamic corrections are applied to the cross-section, then given by the Klein-Nishina formula (initially published in [29]), which at high photon energy in the electron rest frame can be expressed after averaging over the direction as :

$$\sigma_{KN} \approx \frac{3}{8}\sigma_T \frac{m_e c^2}{E'_i}\left(\ln\left(\frac{E'_i}{2m_e c^2}\right) + \frac{1}{2}\right) \tag{2.6}$$

Two interaction regimes are defined depending on the interaction cross-section: the Thomson and the Klein-Nishina regimes. The interaction efficiency is lower in the latter than in the former as the cross-section becomes inversely proportional to the interaction energy in the high-energy limit [18].

In the Thomson region, the formula describing the energy loss of a particle of Lorentz factor γ is very similar to the one in the synchrotron radiation case:

$$\frac{dE}{dt} = -\frac{4}{3}\sigma_T c\gamma^2\beta^2 U_r \tag{2.7}$$

with U_r the radiation energy density before scattering:

$$U_r = \int \epsilon n(\epsilon) d\epsilon \tag{2.8}$$

$n(\epsilon)$ being the photon density.

In the Thomson regime, the average energy transfer can be given with respect to the electron Lorentz factor as:

$$\langle E_1 \rangle = \frac{4}{3}\gamma^2 E_0 \tag{2.9}$$

where E_0 is the energy of the incoming photon from an isotropic distribution and $\langle E_1 \rangle$ is the average energy of the outgoing photon.

On the other hand, in the high-energy limit of the Klein-Nishina regime, the average scattered photon energy is half the average electron energy:

$$\langle E_1 \rangle = \frac{1}{2}\langle E_e \rangle \tag{2.10}$$

The Inverse Compton interaction can take place between photons emitted through synchrotron radiation and the radiating electrons themselves. This process is known as the Synchrotron Self-Compton (SSC). As quoted in [30], *electrons work twice* in this mechanism. We note that in this case, if the emission is in the Thomson regime, the spectrum of the SSC will mirror the synchrotron spectrum [31].

The term Comptonization is commonly used to denote the spectrum shift of an initial photon population through a cloud of accelerated electrons.

2.2.3. Bremsstrahlung radiation

Braking, or Bremsstrahlung, radiation takes place when a charged particle moves through a Coulomb field. The resulting photon spectrum from a power-law electron is also a power-law, with a similar spectral index.

The intensity of this radiation mostly depends on the density of the medium in which the particles evolve as it requires electric field interaction. The characteristic energy loss time in a neutral medium of density n is given by:

$$\tau \approx 4 \times 10^7 \left(\frac{n}{1\text{cm}^{-3}}\right)^{-1} \text{year} \tag{2.11}$$

With $n < 1\text{cm}^{-3}$ in the ISM, and $n \sim 100\text{cm}^{-3}$ up to $n \sim 10^5\text{cm}^{-3}$ in molecular clouds. Bremsstrahlung is then expected to be sub-dominant with respect to synchrotron or inverse Compton in most astrophysical settings. This process however is significant in dense media and is particularly involved in the development of particle cascades observed by detectors described in chapter 4.

2.3. Hadronic processes

Let us now describe phenomena exclusive to high-energy hadrons, which are dominated by protons in our case. Accelerated protons p_{HE} can interact either with a low-energy photon γ_{LE} or with a low-energy proton p_{LE} from the surrounding medium.

Hadron-photon or photohadronic interactions are dominated in the high-energy regime by the resonant Δ^+ production which quickly decays into pions [32] :

$$p_{HE} + \gamma_{LE} \rightarrow \Delta^+ \rightarrow \begin{cases} n + \pi^+ & 1/3 \text{ of cases} \\ p + \pi^0 & 2/3 \text{ of cases} \end{cases}$$

However non-resonant processes, such as multi-pion production:

$$p_{HE} + \gamma_{LE} \rightarrow \begin{cases} p + a\pi^0 + b(\pi^+ + \pi^-) \\ n + \pi^+ + a\pi^0 + b(\pi^+ + \pi^-) \end{cases}$$

or other meson resonances:

$$p_{HE} + \gamma_{LE} \rightarrow \eta, K, ... \rightarrow \{\pi^0, \pi^\pm, \nu, \mu\}$$

bring the quantity of π^+ to be approximately equal the π_0 [33].

Hadron-hadron interactions on low-energy protons or nucleons in the medium [34] also lead to the production of pions:

$$\left.\begin{matrix} p_{HE} + p_{LE} \\ p_{HE} + N \end{matrix}\right\} \rightarrow H + \{\pi^0, \pi^\pm\}$$

However, the hadron-hadron interactions are expected to be subdominant with respect to the photohadronic interaction if the matter density is lower than the radiation density, which is expected in most astrophysical settings.

The charged pions produced in hadronic interaction decay into muons and neutrinos:

$$\begin{cases} \pi^+ \rightarrow \mu^+ + \nu_\mu \\ \pi^- \rightarrow \mu^- + \bar{\nu}_\mu \end{cases}$$

The muons in turn decay into electrons and neutrinos:

$$\begin{cases} \mu^+ \rightarrow e^+ + \nu_e + \bar{\nu}_\mu \\ \mu^- \rightarrow e^- + \bar{\nu}_e + \nu_\mu \end{cases}$$

Neutral pions, on the other hand, mostly decay into photons:

$$\pi^0 \rightarrow \begin{cases} 2\gamma & \sim 99\% \text{ of cases} \\ \gamma + e^- + e^+ & \sim 1\% \text{ of cases} \end{cases}$$

Finally, the resulting high-energy electrons can radiate through synchrotron or inverse Compton.

In the dominant Δ^+ photohadronic production, the interactions on average produce 1.3 photons with energy 10% of the initial proton energy and 1 neutrino with 5% of the initial proton energy. As the energy of the radiated particles can be averaged as a fraction of the proton energy in any hadronic interaction, the resulting γ-ray spectrum has a shape similar to the proton energy distribution, above the interaction threshold.

2.4. Example spectra from multiple emission processes

To illustrate the multiple contributions from the different emission processes, the modeled Spectral Energy Distribution (SED) of the SNR SN 1006 from [35] is shown in Figure 2.1. In this figure, two SED are shown to interpret measurements from the HESS Cherenkov telescope array in the VHE range either as coming from inverse Compton of accelerated electrons on the Cosmic Microwave Background or from the decay of π_0 generated from a population of accelerated protons interacting with cold protons. In this example, no interpretation is preferred over the other, or over a combination of the two.

2.5. Joint observations of photons and neutrinos

High-energy hadronic processes emit neutrinos in addition to γ-rays. The former, however, can travel unaffected to the observer while photons might be absorbed in

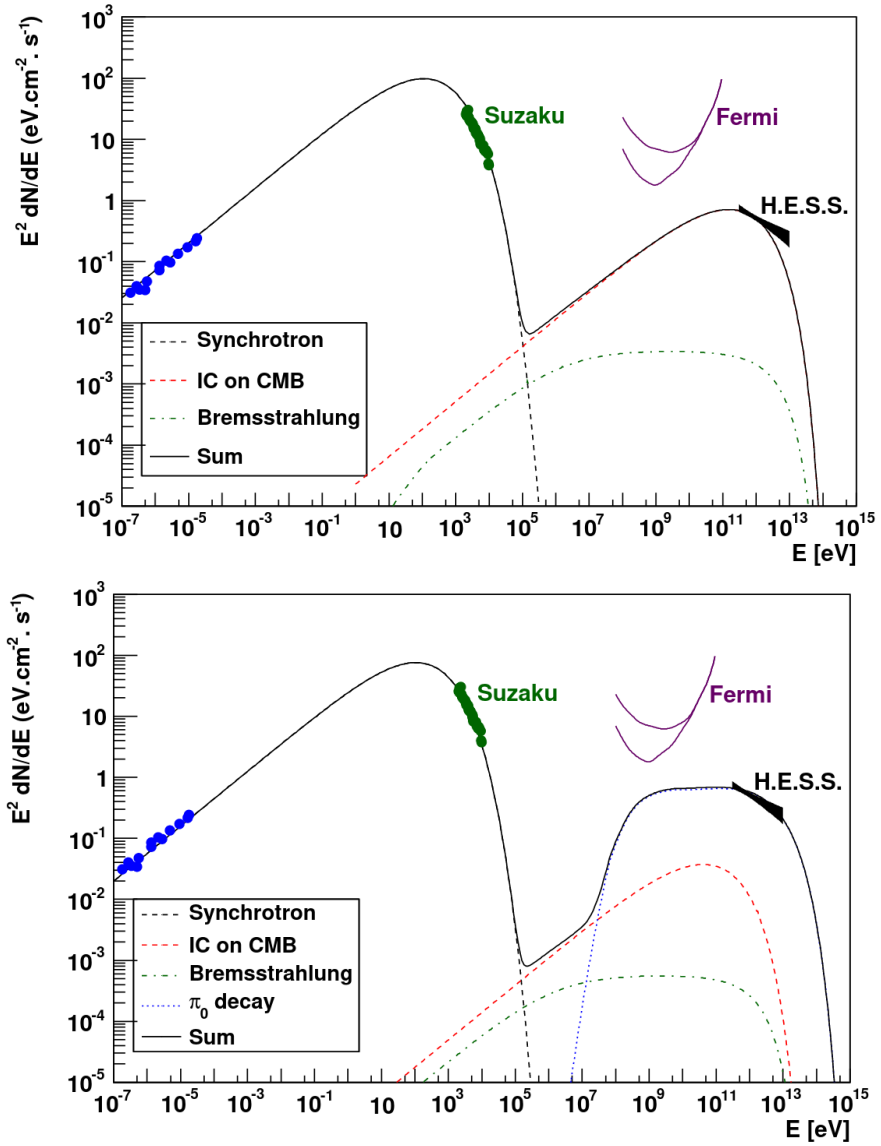

Figure 2.1.: Broadband SED of SN 1006 modeled from radio observations (blue dots), X-ray from Suzaku (green dots), and VHE γ-ray spectrum with HESS (black dots). The emissions from different processes are synchrotron radiation in dashed black lines, inverse Compton in dotted red lines, bremsstrahlung in dot-dashed green lines, and decay of π_0 from proton-proton interactions in dotted blue lines. Top: no hadronic interaction is considered in the model, the inverse Compton process is responsible for the spectrum observed with HESS. Bottom: A power-law proton population of index = -2 is introduced and HESS observations are modeled with a π_0 decay spectrum.

the source or in the interstellar medium. On the other hand, leptonic processes do not emit neutrinos.

Several studies have been conducted to link the γ-ray and neutrino fluxes from their common hadronic origin [36, 37]. Among them, [38] computed the expected γ-ray and neutrino fluxes from a population of proton following a power law with an exponential cut-off:

$$\frac{dN_p}{dE_p} = k_p \left(\frac{E_p}{1\text{TeV}}\right)^{-\alpha} \exp\left(-\frac{E_p}{\epsilon_p}\right) \tag{2.12}$$

by the following parametrization:

$$\frac{dN_{\gamma/\nu}}{dE_{\gamma/\nu}} \approx k_{\gamma/\nu} \left(\frac{E_{\gamma/\nu}}{1\text{TeV}}\right)^{-\Gamma_{\gamma/\nu}} \exp\left(-\sqrt{\frac{E_{\gamma/\nu}}{\epsilon_{\gamma/\nu}}}\right) \tag{2.13}$$

with the parameters:

$$k_\nu \approx (0.71 - 0.16\alpha) k_\gamma$$

$$\Gamma_\nu \approx \Gamma_\gamma \approx \alpha - 0.1$$

$$\epsilon_\nu \approx 0.59\epsilon_\gamma \approx \epsilon_p/40$$

Authors in [38] point out that this relation holds under a few conditions, i.e. that the observed γ-ray flux is only due to hadronic emission, that no efficient γ-ray absorption takes place in the emitting source, or that the magnetic field is low enough to disregard energy losses from synchrotron emission of muons from π_0 decay. However, a significant deviation between these relationships and any detected γ-ray and neutrino fluxes could serve as a probe to the aforementioned mechanisms.

The effect of absorption of γ-rays from microquasars was studied in [39] which found an important opacity to TeV photons due to infrared photons emitted by synchrotron radiation. The attenuation of the γ-ray flux is then directly linked to the intensity of the magnetic field and to the density of synchrotron-emitting electrons. Since neutrinos are not affected by such absorption the γ-ray opacity can be quantified from the measured γ-ray flux and the one derived from the neutrino flux.

Multi-messenger observations of astrophysical sources [40] can then reveal the density and the composition of the medium. For example, the discovery of galactic neutrinos [20] in conjunction with observations of the galactic gamma-ray flux allows to study the distribution of cosmic rays in the galactic center [41] or the contribution of galactic sources to the neutrino flux [42].

3. Microquasars

3.1. History

The first X-ray source beyond the solar system was discovered in 1962 using a set of Geiger counters mounted onto a rocket launched above the atmosphere [43]. While initially planned for the study of X-ray fluorescence of the lunar surface, this experiment detected a signal that was not compatible with the Moon's location. The discovered source was named Scorpius X-1. This discovery marked the beginning of X-ray astronomy. In the years that followed other rocket or balloon experiments were launched, which led to the discovery of other sources, suggesting the existence of a population of galactic objects exhibiting high-energy phenomena. Radio observations and optical spectroscopy of one of these sources, Cygnus X-1 discovered in 1964, suggested it was a binary system [44]. Indeed, velocity measurements of the optical counterpart to the X-ray emission found a periodicity that was compatible with an orbital motion. An accretion disk was soon after proposed as responsible for the X-ray emission [45], as the star in this system seemed not able to emit enough X-ray to explain the observed flux. Moreover, the study of the orbital parameters of the system allowed to determine the properties of the object in orbit with the star, which constituted the first object confirmed to be a Black Hole [46], that until then was only postulated from General Relativity.

Spectroscopic observations in visible light of SS 433 [47] revealed a spectrum that could not be explained with a simple star, with emission lines exhibiting aperiodical variability in wavelength and intensity. It was postulated that these features were compatible with the presence of matter ejected at an irregular rate, the emission lines variability being explained by rapidly changing Doppler-shifting of the emission [48]. This fact was later confirmed by radio observations that were consistent with matter traveling away from a central source in a double-sided jet [49]. Additional radio observations of the jet matter proper motion measured a velocity of $0.26c$ [50]. More radio searches around X-ray sources were performed to determine the presence of jets and find other objects similar to SS 433. This is what led Scorpius X-1 to be referred to as *microquasar* in 1989 [51], even if the radio source was later found to be unrelated to the object [52]. That denomination was given in comparison to quasars (for quasi-stellar objects), active galactic nuclei where jets of relativistic ejections were observed.

The first confirmed microquasar to be given that classification was 1E 1740.7-2642[1]

[1]Also known as "The Great Annihilator" due to its emission in the 511 keV positron annihilation emission line.

in 1992 [53], by associating X-Ray and γ observations (300 to 600 keV) with Granat and radio observations with VLA. This source exhibits two collimated jets launched from an X-ray source that was found to be a binary system. In 1994, an apparently superluminal ejection was discovered coming from another microquasar, GRS 1915+105 [54], with velocities up to $0.92c$. The superluminal appearance of the motion is a geometric projection effect of the relativistic motion to the line of sight. This behavior was until then only observed in ejections from radio galaxies, confirming the analogy between quasars and microquasars.

3.2. General properties of the microquasar system

Microquasars are binary systems of a compact object (Black Hole or Neutron Star) and a companion star. As they are mostly detected from their X-ray emission, a microquasar is a subclass of X-Ray Binary (XRB). Their particularity resides in the accretion/ejection mechanisms they exhibit. Matter from the star is accreted to the compact object, and is ejected from the vicinity of the compact object in a jet. This section describes the general phenomenology of the microquasar system and introduces its mechanisms. Figure 3.1 shows a schematic representation of the microquasar, and its comparison to the quasar. It should be noted that while the presence of a Black Hole could be deemed necessary for the system to be classified as a microquasar, sources exhibiting similar phenomena of accretion-ejection from a Neutron Star can also fall into this category.

This section presents an overview of the main components of the system and the physical processes involved in mass transfer, accretion, and ejection.

Roche Lobe overflow As seen on Figure 3.2, two main categories of XRB can be drawn depending on the mass of the companion star: if it is a high-mass star (more than a few solar masses), typically of spectral types O or B for main sequence stars, the system is a High-Mass X-Ray Binary (HMXB) and the mass transfer from the companion is dominated by winds that are caught in the gravitational potential of the compact object. On the other hand, companion stars with low masses (solar mass or lower), are found in a Low-Mass X-Ray Binary (LMXB). These stars do not typically show strong winds and the matter transfer is done via Roche-Lobe overflow. The phenomenon happens when matter from the atmosphere of the companion star crosses the Lagrange point L1 of the binary system, typically through a combination of tidal deformation of the star from the compact object and convective movements in the star envelope. This overflow drives an accretion toward the compact object via an accretion disk. It should be noted that an HMXB can also exhibit mass transfer through Roche-lobe overflow.

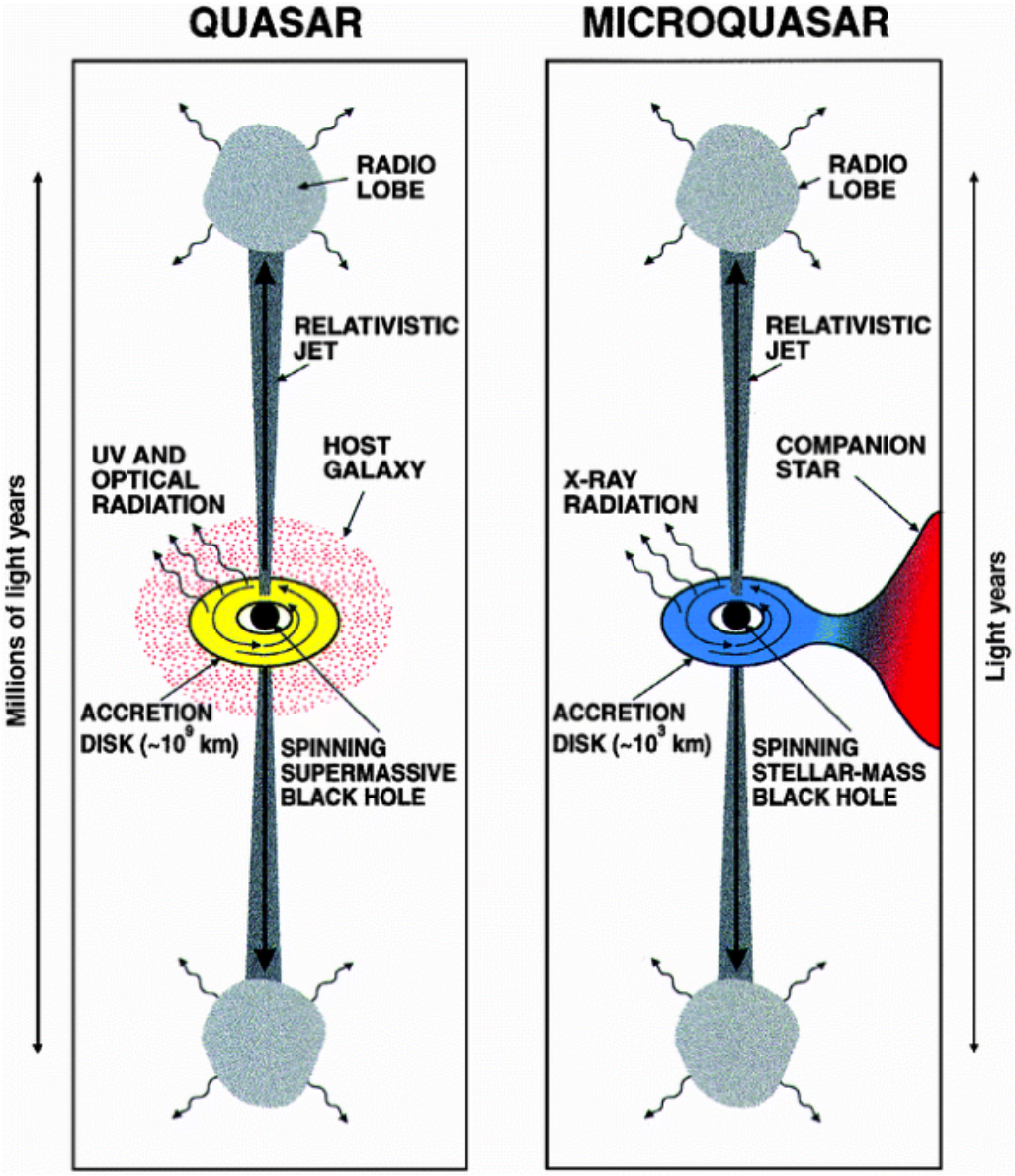

Figure 3.1.: Sketch illustrating the similarities between a quasar (left) and a microquasar (right). In both systems, a compact object accretes matter from a disk and ejects matter in a relativistic jet. Differences come from the scales involved, with a supermassive black hole with 10^6 lightyear jet scales in a quasar and a stellar-mass compact object with jets on the scale of a few lightyears. Furthermore, the disk of a quasar comes from matter in the host galaxy and is detected mostly in ultraviolet and optical light, while the disk in a microquasar is filled by matter from a companion star and is detected in X-ray. Figure from [55].

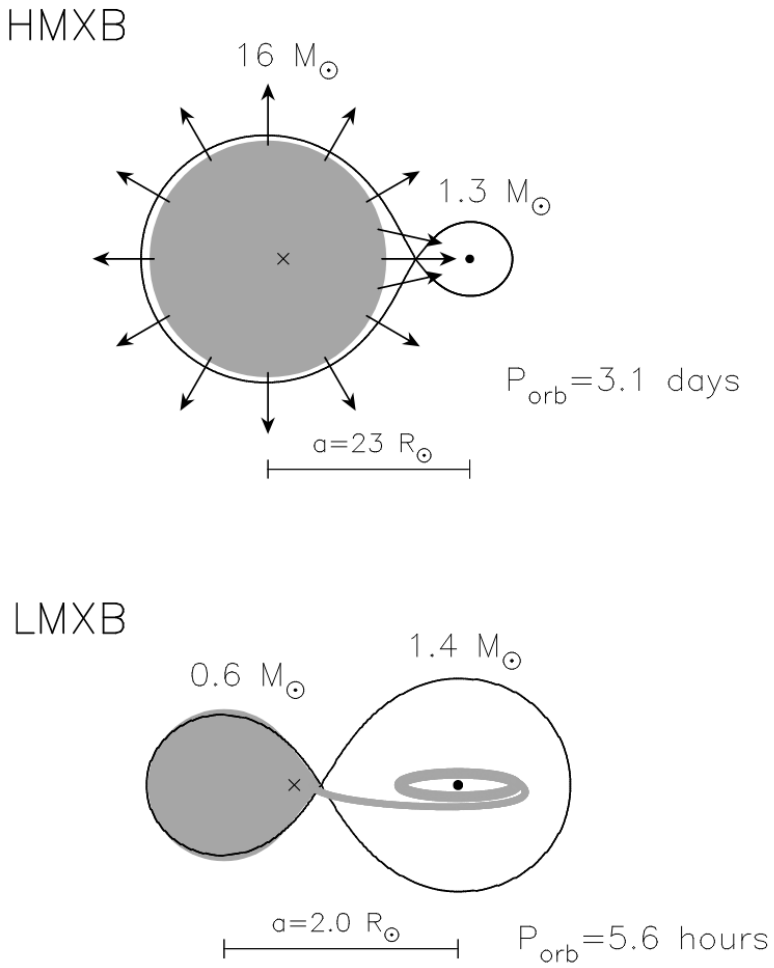

Figure 3.2.: Typical picture of mass transfer in binary systems from [56]. Examples of masses and orbital parameters from a HMXB and LMXB, and a neutron-star compact object are given. In the HMXB the arrows represent mass transfer through stellar winds, and in the LMXB an accretion disk is represented. The closed loop indicates an equipotential line, with its crossing point being the Lagrange L1 point of the binary system.

Accretion disk The standard picture of the accretion disk around a black hole was given by Shakura and Sunyaev[57]. It is an optically thick, geometrically thin disk characterized by a multi-blackbody spectrum, coming from the fact that the temperature of matter at distance R from the compact object is given by:

$$T(R) = \left(\frac{3GM\dot{M}}{8\pi R^3 \sigma} \left[1 - \left(\frac{R_*}{R} \right)^{1/2} \right] \right)^{\frac{1}{4}} \text{K} \tag{3.1}$$

with M the black hole mass, $\dot{M}$ the mass transfer rate, σ Stefan-Boltzmann constant

and R_* the internal radius of the disk. The temperature evolves for large radii as $T(R) \propto R^{-\frac{3}{4}}$.

The luminosity of a source is often expressed as a fraction of the *Eddington luminosity*, the luminosity at which the outward radiation pressure acting on the accreting matter is equal to the inward gravitational pull [28]. It is given for a hydrogen plasma as:

$$L_{\text{Edd}} = \frac{4\pi G M m_p c}{\sigma_T} \approx 1.26 \times 10^{38} \left(\frac{M}{M_\odot}\right) \text{erg/s} \tag{3.2}$$

This puts a limit on the accretion rate if it is assumed that this rate cannot exceed L_{Edd}. The temperature of matter accreting at this Eddington limit at a black hole Innermost Stable Circular Orbit (ISCO) can be approximated by [58]:

$$T \sim 2 \times 10^7 \left(\frac{M}{M_\odot}\right)^{-1/4} \text{K} \tag{3.3}$$

where $M_\odot$ is the mass of the Sun. Noting that this temperature is higher in a less massive black hole, this relation explains why accretion disks from AGN are detected in visible and ultraviolet light while stellar-mass black holes in binary systems are luminous X-Ray emitters.

In order to accrete toward the compact object, particles from the disk need to transfer their angular momentum. This transfer is modeled as energy dissipation through magnetic viscosity induced by turbulence in the matter of the disk.

Corona Observations of a non-thermal component in the X-ray spectrum in the shape of a power-law indicate the existence of an optically thin plasma cloud containing populations of accelerated particles. This cloud is commonly referred to as the *corona*, in comparison to the corona of the Sun which exhibits similar properties, albeit at lower energy. The geometry and the nature of the corona in the system are still debated, but the accepted explanation is that the observed non-thermal X-ray spectrum comes from the Comptonization of soft X-ray from the disk onto the accelerated electrons in the corona [59]. Furthermore, the presence of the Fe K α line at 6.4 keV in the X-ray spectrum is interpreted as photons coming from the corona reflected on the disk, which indicates an irradiation that gives us hints on the geometry of the system. Thus, multiple models have been proposed to explain this reflection. Among them, the so-called "lamppost" corona[60] is placed above the compact object, at the base of the jet; the corona can also be interpreted as enclosing the standard accretion disk[61]; or as the boundary region between the disk and the jet, as a Jet-Emitting Disk [62].

Truncated disk The most commonly accepted disk-corona scheme relies on the configuration of a standard disk, truncated at some distance from the compact object [63]. The corona is then the location of a hot accretion flow from the disk to the compact object, inside which electrons are accelerated. This model takes into account

the MWL variability of the source described in section 3.3. A schematic representation of 2 configurations of the system in this model is given on Figure 3.3.

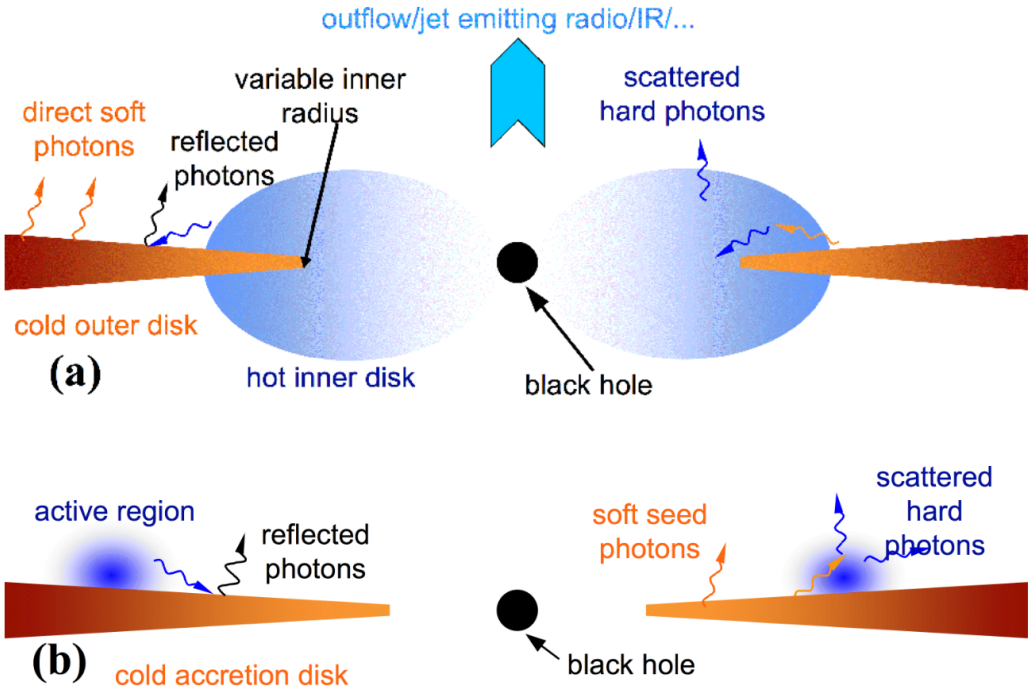

Figure 3.3.: Schematic of two system configurations in the truncated disk model from [64]. (a) shows a hot accretion flow acting as a corona, surrounded by an optically thick standard disk truncated far from the ISCO and overlapping with the hot flow. Soft thermal photons from the disk are Comptonized in the hot flow and partly reflected on the disk. (b) shows an optically thick disk reaching the ISCO.

Compact jet Far from being limited to microquasars or AGN, jets are observed along accreting systems from young stellar objects [65] to cataclysmic variables [66]. Despite that fact, jet launching mechanisms are still debated. The current understanding of the formation of relativistic jets relies mainly on two hypotheses. In a Blandford-Znajek jet [67], energy is extracted from a Kerr black hole spin via poloidal magnetic field lines generated by the disk threading its ergosphere. Alternatively, in a Blandford-Payne jet [68], the jet is launched directly from poloidal magnetic field lines arising from the disk. The jet power is then extracted from the disk as matter moving along co-rotating magnetic field lines is ejected by magnetocentrifugal force.

As the computational power allowed simulations of more complex systems, the understanding of jet launching mechanisms from MagnetoHydroDynamic (MHD) simulations has been improved. We can see for example in Figure 3.4 a sketch of the magnetic field geometry discussed in [69]. In this work, authors find from MHD

simulation that jets can be propelled by the magnetic coil effect induced by differential rotation of the accreting material.

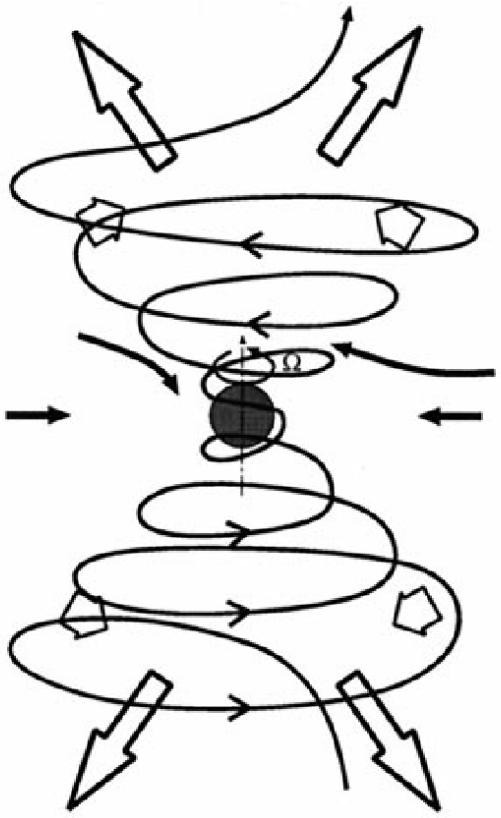

Figure 3.4.: Schematic of a MHD jet model from [69]. Solid black arrows represent magnetized inflow toward the compact object. This inflow rotates and drives the magnetic field lines into a rotating helical coil. Matter is expelled along the magnetic field lines through magnetocentrifugal forces. Short open arrows represent the magnetic pressure that lifts the matter into a jet, represented by long open arrows.

Compact jets are characterized by their radio spectrum, which appears flat in their flux density. This shape is easily explained by the superposition of multiple self-absorbed synchrotron spectra [27]. Each spectrum is emitted at a different jet height from the compact object, as shown in Figure 3.5. This behavior is due to the lateral expansion of the jet with its distance from the compact object, as the electron density and magnetic field density decrease.

The maximum frequency before a change of the spectrum slope, as noted $\nu_{\max}$ on Figure 3.5, depends in this picture on the magnetic field density at the base of the jet.

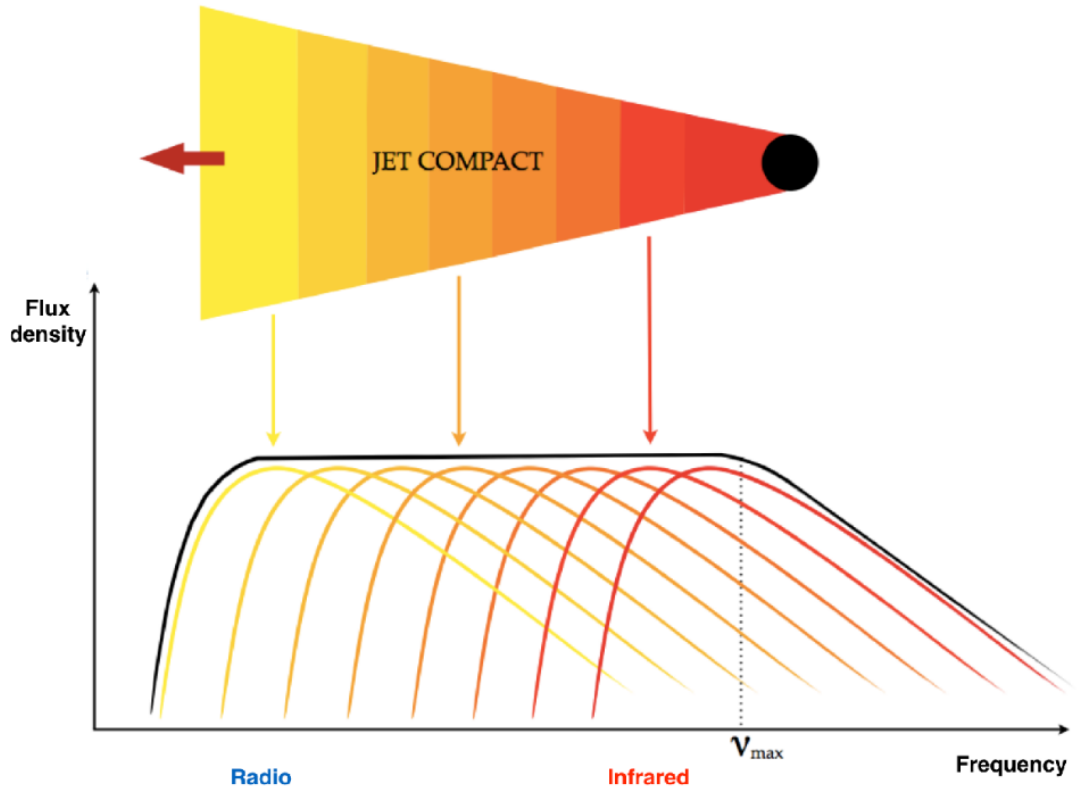

Figure 3.5.: Schematic representation of the compact jet and the associated flux density spectrum [70]. The overall spectrum, in black, is the superposition of the emissions of spectra from multiple slices of the jet, represented as a gradient.

3.3. Multiwavelength variability during microquasar flares

3.3.1. X-Ray spectral states

A usual indicator of the spectral evolution of a source is the hardness ratio, defined as an X-ray flux (or photon rate) ratio between two successive energy bands. When represented against the luminosity of this source on a Hardness Intensity Diagram (HID), it was observed that the X-ray spectra of LMXB microquasars during outbursts take a usual q-shaped path in the diagram [71, 72]. On Figure 3.6 is an HID of an outburst of GX 399-4 given as an example, with representations of the disk-jet system configurations during a flare described in this section.

The regularity of this path, from one flare to another and even from one source to another, allows us to draw canonical spectral states that reflect the phase of the outburst in which the microquasar is. These phases are defined as follows:

- At the beginning of an outburst, the source is in a Hard State (HS) where the

X-ray spectrum exhibits a thermal component and a dominant non-thermal, power-law distribution. The luminosity increases by several orders of magnitude while the non-thermal component is still present.

- The source then undergoes a hard-to-soft State transition (ST) as the non-thermal component of the X-ray spectrum disappears. In some cases, intermediate states may be defined around the transition as the Hard Intermediate State (HIMS) and Soft Intermediate State (SIMS).
- The X-ray spectrum is then dominated by the soft, thermal component, and the source is then in a Soft State (SS). During this state, the luminosity usually decreases.
- A second ST, soft-to-hard, closes the loop in the HID as the non-thermal component reappears in the spectrum.

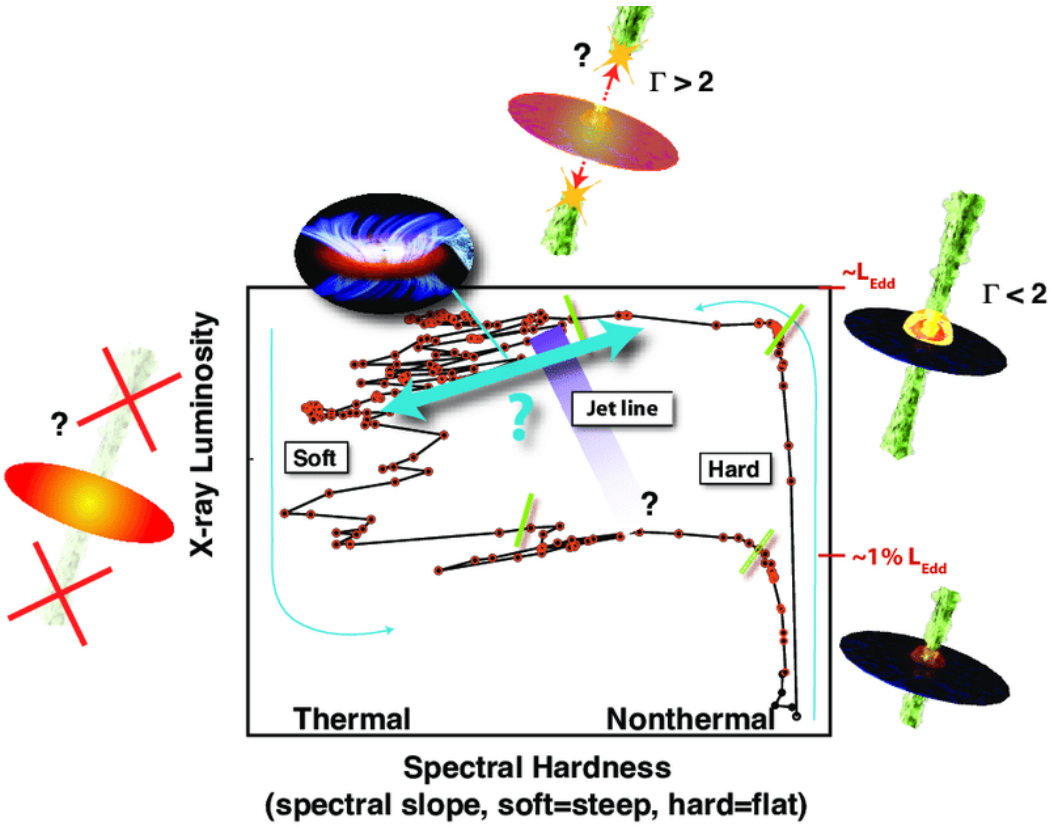

Figure 3.6.: Example of a typical HID q-shaped path of an outburst of GX339-4. Schematics of the disk-jet system configurations for different states are represented and are discussed in the following sections. L_{Edd} is the Eddington luminosity as given by Equation 3.2. Γ is the bulk Lorentz factor of the ejected jet matter. Figure from [3].

3.3.2. Radio X-Ray correlation

The radio luminosity, mostly coming from synchrotron emission from electrons in the jet, is strongly correlated with the X-ray state. It was observed that the radio and X-ray luminosities are correlated in the HS [73], and that this correlation is conserved between multiple outbursts of the same source (see [74] for GX339-4 or [75] for GRS1915+105). For example, in GX339-4 as seen in Figure 3.7 [76], where a correlation of the X-ray luminosity L_X to the radio luminosity L_R was found as $L_X \propto L_R^{0.6-0.7}$. This fact suggests a causal link between the corona and the jet.

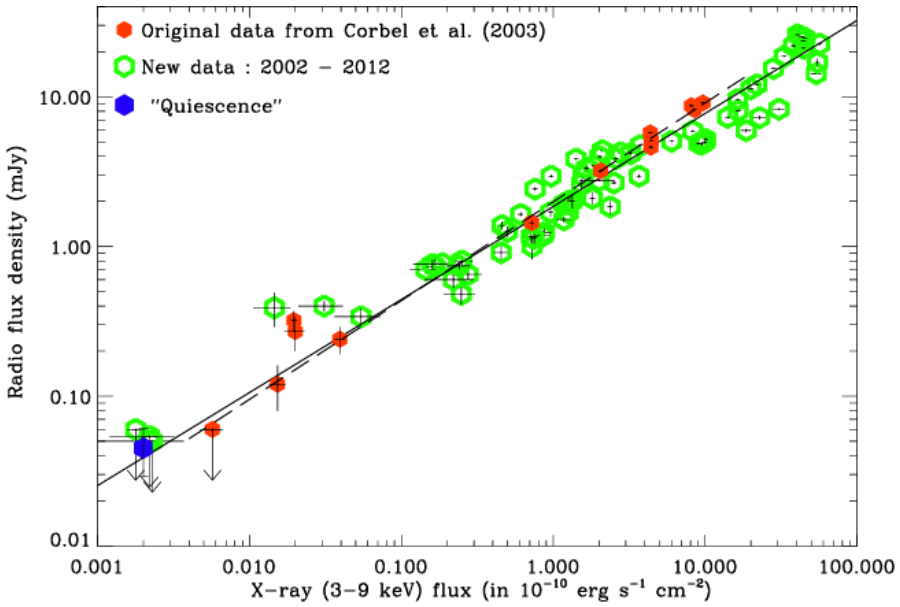

Figure 3.7.: 9 GHz radio flux density vs X-Ray flux in the HS of GX 339-4 over multiple outbursts. Fits of the correlation are shown as a dashed line for older data and as a solid line for new data from [76].

This correlation however ceases during a hard-to-soft ST where the emission from a steady compact jet becomes undetectable [77]. In the following SS, a steady jet is typically not observed. This phenomenon is known as the *jet quenching* and is mostly correlated with the X-ray hardness ratio of the source. A line, known as the jet *line*, can indeed be drawn on the HID and delimits a threshold below which the jet is quenched. Discrete ejections however are expected at the crossing of the jet line.

3.3.3. Fast X-ray variability

The luminosity of a flaring microquasar can exhibit a variability on a second-to-minute timescale which can be studied with the power density spectrum of the X-ray lightcurve. The intensity of the variability is usually quantified with the fractional Root Mean Square (RMS) of the lightcurve. This variability can also have a quasi-periodic

component, known as Quasi-Periodic Oscillation (QPO)[2]. As seen on Figure 3.8, QPOs can be classified into 3 types depending on their power spectra [78], and it was observed that the appearance of the different types of QPO depends on the spectral state of the source.

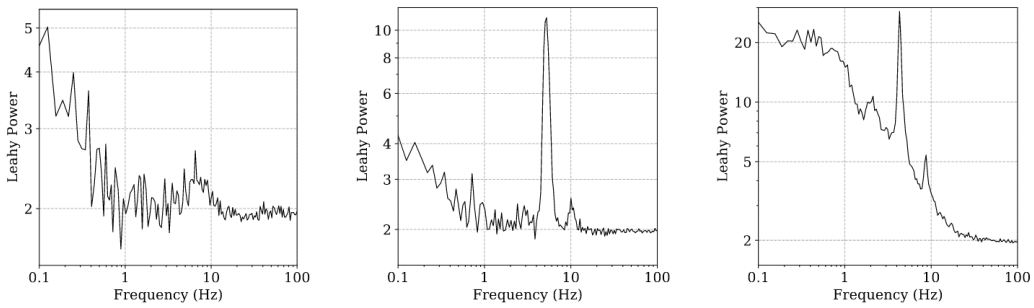

(a) *Type A.* (b) *Type B.* (c) *Type C.*

Figure 3.8.: Figure taken from [79] showing examples of power spectra of QPOs from RXTE/PCA lightcurve of GX339-4.

The classification is as follows:

- **Type A** are detected in the SS, this type is characterized by a broad, low-power, excess in the power spectrum around 6 to 8 Hz. The RMS is low (around a few percent).
- **Type B** are characterized by a sharp excess in the power spectrum, of a fundamental frequency around 6 Hz and the presence of harmonics. The low-frequency component of the power spectrum is weak, with an RMS around 5%. This type is observed during state transitions and characterizes the SIMS.
- **Type C** exhibit also a sharp excess and its harmonics, but the low-frequency component is this time higher in the power spectrum, and the RMS is higher as well and can reach 30%. This type is observed in the HS with frequencies that can be observed in a broad range, from mHz to ~ 30 Hz. As it was observed that the frequency of the QPO increases with the luminosity of the source during the HS, it is understood as originating from the inner radius of a truncated disk approaching the compact object.

A correlation between the X-ray RMS and the hardness of its spectrum can be observed, with the lightcurve exhibiting a lower variability in the SS than in the HS.

3.3.4. Discrete ejection

Observed for the first time with GRS 1915+105 in 1994 [54], microquasars can launch discrete matter ejecta with relativistic speed. The discovery of this property from a

[2] "Quasi" because they show a broadening in the power spectrum, as opposed to an actually periodic oscillation that would appear as a Dirac δ.

galactic source, which was until then only known for AGN, renewed the interest of the community around this type of object.

Let's consider the apparent velocity β' of an approaching relativistic ejecta:

$$\beta' = \frac{\beta \sin\theta}{1 - \beta\cos\theta} \tag{3.4}$$

With β the bulk velocity of the ejecta in the central object frame and θ the angle between the line of sight and the axis of motion of the ejected matter. We see that we can have $\beta' > 1$ for $\beta > 1/\sqrt{2}$ (~ 0.7). The motion is then *apparently superluminal*, and is often simply called superluminal.

As seen for example in MAXI J1820+070 (Figure 3.9 from [80]), ejections are bright in radio due to synchrotron emission from internally accelerated electrons, and can be observed following a ballistic trajectory for months after being emitted. Two, bi-polar, ejecta are resolved with radio telescopes with different luminosities due to relativistic (de-)boosting.

Discrete ejections are mostly observed during an X-Ray hard-to-soft ST and are strongly correlated with the appearance of type B QPO, as seen in Figure 3.10. In this work, the quenching of the compact jet is observed during the ST and a rapidly rising and decaying radio flare is detected during a period of type B QPO in the X-Ray band. This radio flare is identified as the launching of the discrete ejecta identified in Figure 3.9.

The radio bright ejection can in some sources be rapidly slowed down after following a ballistic trajectory, which is interpreted as a collision of the ejecta to a wall of sharply increasing density in the interstellar medium. See for example MAXI J1348-630 [82] whose ejecta was emitted during a state transition and followed a linear trajectory before being slowed down 8 months after its emission.

3.3.5. Summary of the standard picture of a low-mass microquasar outburst

Let us have a look back at Figure 3.6 and summarize the typical behavior of a microquasar LMXB during its flare with the following steps:

1. **Quiescence** The microquasar is not (or barely) detectable in all wavelengths, with the possible exception of the emission from its companion star.

2. **Roche Lobe overflow** Matter from the companion star starts transferring into the compact object with the formation of an accretion disk.

3. **Hard State**. The luminosity gradually increases. The X-ray flux has a significant high energy, non-thermal component from the corona, and a thermal component from a truncated disk. A variability with a detectable QPO frequency and a low-frequency noise is observed. The radio spectrum is flat, dominated by a compact jet.

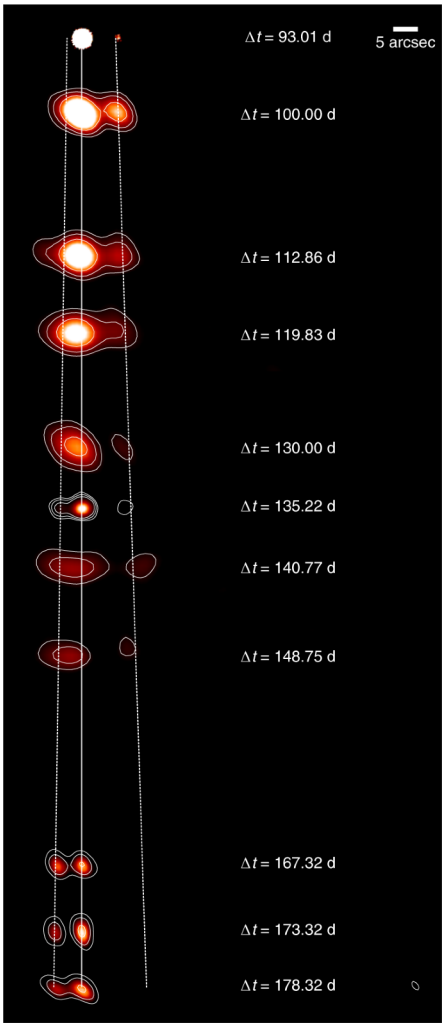

Figure 3.9.: Resolved radio images from [80] of the core and ejection of MAXI J1820+070 during its 2018 outburst. The time in days since the radio flare that occurred during the ST in noted Δt.

4. **Hard-to-Soft state transition**. With a stable luminosity, the X-ray spectrum softens as it becomes dominated by the thermal component from a disk that is being filled close to the compact object. The steady compact jet and the corona become undetectable and discrete ejecta are launched.

5. **Soft State**. X-rays are dominated by the thermal emission of the disk and the luminosity gradually decreases. The jet is quenched. The X-ray frequency spectrum shows less significant QPO.

6. **Soft-to-hard state transition**. The X-ray spectrum hardens and the compact jet reappears, at a lower luminosity.

On the other side, while HMXB microquasars are usually steady sources due to the mass transfer from the stellar wind, these objects can also exhibit a similar outburst

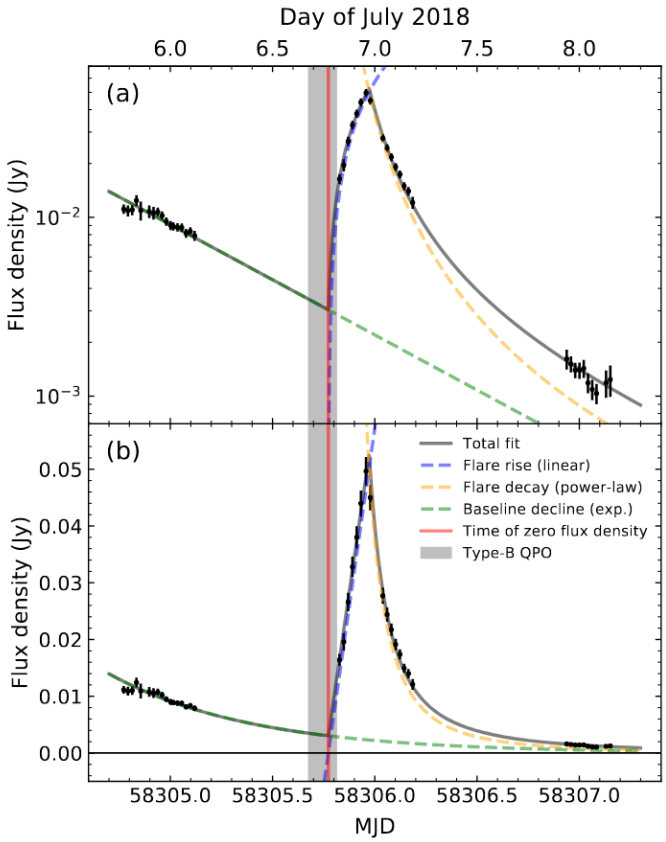

Figure 3.10.: Radio lightcurve of MAXI J1820+070 during its 2018 outburst from [81]. Data is fitted in 3 periods: exponential decay of the compact jet in green, linear rise of the flare corresponding to a discrete ejection in blue, and its power-law decay in yellow. The grey area shows the time window in which a type B QPO was observed in X-rays. The red vertical line shows the extrapolated start time of the flare from the linear fit. The flux density is represented on a log-scale in (a) and on a linear scale in (b).

pattern. For example, Cygnus X-1 is occasionally seen transitioning from a hard to a soft state [83]. Another microquasar with a high-mass companion, V4641 Sgr, was observed in outburst with clear evolution of its spectral state [84]. This behavior can be explained by occasional Roche Lobe overflow events in the system.

3.4. High energy emissions from microquasars

In this section, we present an overview of the literature regarding the high energy emissions of HMXB and LMXB microquasars.

3.4.1. γ-ray detection from microquasars

Soft γ-rays

Soft γ-rays (few hundred keV to few MeV) signals were detected in several microquasars. For example, GX 339-4 was observed in 1991 by the Compton Gamma Ray Observatory which found an extension of its X-ray spectrum to ~ 500 keV [85]. During an outburst in 2015, microquasar V404 Cygni was observed with the ISGRI telescope onboard the INTEGRAL satellite [86] which detected a component reaching into soft γ-ray, up to a few 100 keV as well.

In addition to the non-thermal X-ray emission, a higher energy component was also detected with ISGRI that reached into the soft γ range up to 2 MeV, as discussed in [87]. This component was observed in the HS of MAXI J1820+070 and MAXI J1348-630 and the ST of MAXI J1535-571. As the soft γ component becomes undetectable in the SS, the authors suggest it originates from the corona or the compact jet of the systems. The hypothesis of the soft γ-ray emission coming from the jet is reinforced in the case of MAXI J1348-630 where polarimetry measurements found a high polarization fraction of the emission, suggesting that it originates from an ordered, strong magnetic field, consistent with the base of the jet.

HE γ-rays

An analysis of Fermi/LAT data was performed in [88] and found a significant HE signal from the HMXB Cygnus X-1 that confirmed a previous 4σ detection [89]. It was shown that this HE γ component only appeared in the HS of Cygnus X-1 when a compact jet was present. Additionally, an orbital modulation of the HE signal was observed, which hinted toward an origin from Inverse Compton interaction between particles accelerated in the jet and stellar photons.

Similarly, a HE γ signal modulated by the orbital period of the HMXB Cygnus X-3 was discovered in [90]. It was later shown in [91] however that the gamma flux is transient and is mostly detected in ST, both hard-to-soft and soft-to-hard, and is strongly correlated with the radio flux coming from the jet.

Regarding V404 Cygni, a Fermi/LAT search was performed in [92] that found a 4σ signal in coincidence with the 2015 outburst. A later re-analysis [93] revealed that the excess was in fact due to contamination from a nearby blazar.

VHE γ-rays

A VHE signal was detected by the MAGIC Imaging Atmospheric Cherenkov Telescope (IACT) originating from the microquasar Cygnus X-1 [94] at around 3.2σ in coincidence of an X-Ray flare in 2006. That signal could not be confirmed with new observations in a later analysis [95] using ~ 100 hours of data taken between 2007 and 2014.

Among the 9 binary systems known to emit VHE γ-rays, two were at the time of their respective detections identified as microquasars: LS I +61 303 [96] and LS 5039 [97]. This would have made this class part of the selective γ-ray binaries. However, further studies of their radio features [98] revealed that what was thought of as a jet could be instead interpreted as a pulsar wind, "comet-like", tail. VHE emission from these sources is in this case not originating from accretion-ejection-powered particle

acceleration. This interpretation is at this day favored for LS 5039, and remains unclear for LS I +61 303[99].

The most compelling evidence of the ability of emission to the VHE comes from observations of the interaction region between the jet and the surrounding interstellar medium. The HAWC collaboration indeed reported the detection of photons above 25 TeV originating from two spatially resolved lobes consistent with the jet termination locations around the microquasar SS 433, as seen in Figure 3.11. This detection was recently confirmed with HESS [100] where the study of the energy-dependant morphology of the VHE signal hints toward an origin from an energetic electron population.

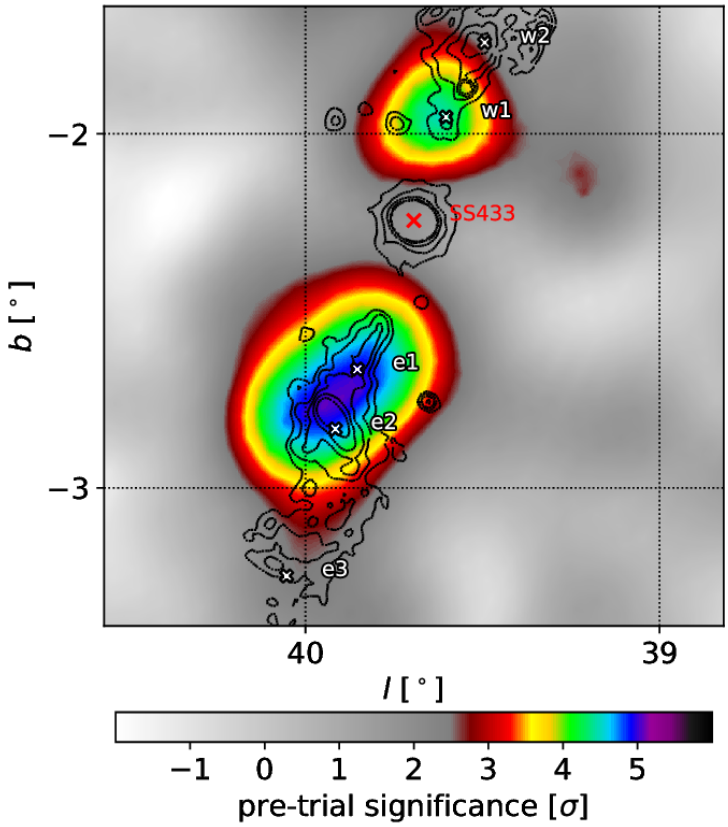

Figure 3.11.: HAWC image of SS 433 and the surrounding nebula W50. The color scale represents the statistical significance of excess in HAWC data
. Jet termination regions as observed in X-Ray data are noted e1, e2, e3, w1, and w2. Solid lines are X-ray contours given by ROSAT observations. Figure from [101].

Similarly to SS 433, the HAWC collaboration reported [102] a significant VHE photon

excess compatible with the location of microquasar V4641 Sgr. In order to study this VHE signal, HESS has scheduled new observations of this system. At the time of writing this manuscript, the data taking is still ongoing and a dedicated analysis will be performed in a later work.

3.4.2. γ-ray emission models

Different models predicting the emission of γ-ray from microquasars have been proposed. Among them, modeling of γ-rays coming from the interaction between the jet of a system and winds from the stellar companion have been developed in [103]. It is mostly applicable for HMXB, spectral types stars O and B exhibiting the most intense winds. In this model, the interaction is purely hadronic.

Concerning LMXBs, [39] proposes a model involving hadronic emission processes from proton accelerated at the base of a proton-dominated compact jet. This model however predicts a contribution due to proton synchrotron in the 100 MeV to 100 GeV range and a contribution from photo-pions above 10 TeV, making detection in the VHE range around 1 TeV difficult.

To postulate the production of VHE from microquasars, one can take into consideration their supermassive equivalent. Indeed, AGN are often detected in this energy range [104]. VHE-emitting AGN are mostly radio-loud, suggesting γ-ray production in a relativistic jet. Blazars, where the jet orientation is aligned with the line of sight, are particularly bright VHE emitters. We note that the detection of *micro-blazars*, i.e. microquasars with a jet aligned to the line of sight, can be challenging due to the difficulty of resolving the jet to measure its orientation. As an example, we can mention V4641 Sgr whose study of the proper motion of radio ejecta finds a jet axis angle below 16°, which makes it indeed consistent with such appellation [105].

The modelization used in chapter 10 of this thesis relies on simple assumptions [106] of primary particle energy distribution, which is used to fit a set of parameters of the system into a broadband SED.

3.4.3. Neutrino production models

The connection between gamma and neutrino emissions through pion productions naturally leads every hadronic model of gamma production to predict a significant high-energy neutrino flux [39].

Even though its nature as a microquasar was challenged, [107] studies the VHE gamma emissions of LS 5039 and argues an efficient photo-pion production from the interaction of protons at the base of the jet with X-ray photons emitted by the accretion disk. The gamma being emitted at the base of the jet would then trigger electron-photon cascades which would result in an absorption of the gamma flux. The authors compute from the observed gamma flux and its estimated absorption a neutrino flux that would lead to ~ 0.2 events per year with ANTARES, which would have resulted in a significant signal within the detector lifetime.

An earlier model from 2001[108] expresses the expected flux at Earth of ν_μ above 1 TeV emitted during the ejection of plasma blob with relativistic bulk speed as :

$$F_{\nu_\mu} \approx \frac{1}{2}\eta_p \Gamma^{-1}\delta^3 \frac{L_j/8}{4\pi D^2} \text{erg/cm}^2\text{/s} \tag{3.5}$$

with η_p the fraction of the jet energy injected as non-thermal protons, Γ bulk Lorentz factor of the ejecta, δ the Doppler factor $\delta = \Gamma^{-1}(1-\beta\cos\theta)^{-1}$ with θ the angle between the jet axis and the line of sight, $4\pi D^2$ the isotropic geometric factor with D distance to the source and L_j the luminosity of the jet, with a factor 1/8 due to energy lost to pion production to muon neutrinos.

This model was expanded upon in [109] with measurements from jet parameters, and gives the ν_μ flux at Earth as from microquasars with unresolved radio jet as:

$$F_{\nu_\mu} = \frac{1}{16(1-\alpha_R)} \frac{\eta_p}{\eta_e} f_\pi \eta_r^{-1} S_{\nu_{\text{high}}} \nu_{\text{high}} \tag{3.6}$$

with:

- α_R the spectral index of the jet synchrotron radio emission
- ν_{high} the highest observed frequency of synchrotron emission
- $S_{\nu_{\text{high}}}$ the flux density at this frequency
- $\eta_r \lesssim 0.1$ the electron synchrotron energy loss fraction
- $\eta_p \sim 0.1$ the fraction of the jet energy carried by non-thermal protons
- $\eta_e \sim 0.1$ the fraction of the jet energy converted to relativistic electrons and magnetic field.
- f_π the fraction of energy converted to pions and is given by (with ϕ the opening angle of the jet):

$$f_\pi \approx 0.1 \left(\frac{\eta_e}{0.1}\right)^{0.5} \Gamma^2 \left(\frac{\phi}{0.2}\right)^{-1} \left(\frac{L_j}{10^{38}\text{erg/s}}\right)^{0.5} \tag{3.7}$$

This model predicts detectable neutrino fluxes with the ANTARES telescope from several microquasars, these predictions are compared to observation in chapter 9.

Consideration of energy losses from charged particles in the intense magnetic fields in the base of the jet leads however to the significant reduction of the detectable neutrino flux from microquasars, as studied in [110]. The authors find that these losses are expected to reduce the neutrino flux by orders of magnitude above $\sim$ 10 TeV, but are not significant around neutrino energy of 1 TeV or below. Synchrotron losses however would be negligible in jet-wind interactions far from the compact object, as described in [111].

A high-energy neutrino flux is computed from VHE gamma measurements of SS 433 in [112] and is found to be too faint to be detectable with current detectors.

In [113] however, the authors build a model in which neutrinos are produced at the base of the jet. They also take into consideration the absorption of γ photon and conclude that the microquasar GX 339-4 could be detected as a steady source after a few years of observation with a next-generation neutrino telescope.

3.4.4. Neutrino searches

A search for neutrinos in correlation to X-ray flares from galactic binary systems was performed in 2017 with the ANTARES neutrino telescope [114]. No significant excess was found. The work presented in chapter 9 of this thesis expands on this search for a few microquasars.

A recent search of high energy neutrinos from XRB with the IceCube neutrino telescope[115] finds a pre-trial p-value of 1.4% for the correlation of an X-Ray flare from microquasar V404 Cygni. When accounting for the trial factor introduced by the number of sources in the study however[3], the result becomes compatible with the hypothesis of originating from background-only, with a post-trial p-value of 75%. In the same publication, the authors find a time-integrated correlation of neutrinos with the coordinates of HMXB Cygnus X-3 at a 3.6% p-value. A dedicated neutrino search from this source was performed in [116] and found a 3.3σ correlation between IceCube data and the HE γ-ray activity of the microquasar.

3.5. Implications of VHE signal from low-mass microquasars

As we have seen, the study of high-energy neutrinos and photons from microquasars has been well-documented but is still uncertain to this day.

VHE photons from microquasars, close to the compact object, would indicate efficient acceleration in a low-density medium. The detection of neutrinos would indicate a significant population of accelerated protons in the system, which would make this class of source a contributor to the observed cosmic ray spectrum [117]. Furthermore, it would allow a probe of the hadronic fraction in the jet, which would give valuable information on the jet formation models.

Finally, the transient nature of microquasars with their phases of outbursts, makes them an interesting application of time-domain, multi-messenger astronomy.

[3] $p_{\text{post}} = 1 - (1 - p_{\text{pre}})^N$ with N the number of sources.

4. Observatories

The work presented in this thesis relies on data analysis from the IACT H.E.S.S. for VHE γ-ray astronomy and from the deep-sea neutrino telescopes ANTARES and KM3NeT. This chapter provides an overview of the detection principles of the respective instruments, as well as a presentation of their usual data reduction procedures. H.E.S.S. is addressed in section 4.1 and neutrino telescopes in section 4.2. Finally, a brief description of several other telescopes used in this work can be found in section 4.3.

4.1. H.E.S.S.

4.1.1. Detection principle

Atmospheric showers
Astronomy in the VHE domain (> 100 GeV) requires the use of large instrumented surfaces, due to the lower flux at this energy, which makes the detection from ground-based instruments necessary. The detection of photons with an IACT makes use of the fact that a particle with a high enough energy will, after interacting with matter in the atmosphere, trigger a chain reaction of secondary particles known as an extensive air shower, as shown in Figure 4.1. The topology of the shower depends on the primary particle and can be classified into two types:

- **Electromagnetic showers** An incoming primary γ photon will induce the production of an electron-positron pair in the vicinity of the electric field of a nucleus in the upper atmosphere. In turn, the leptons will induce the emission of γ photons via Bremsstrahlung radiation. This process repeats in a cascade until the photon's initial energy is distributed enough that the produced photons cannot induce a pair creation or that the lepton energy loss is dominated by ionization of the surrounding medium. This happens at a critical energy of $E_c \approx 86\text{MeV}$. We can define a radiation length X_0 which corresponds to the loss of $1 - e^{-1}$ of electron energy through Bremsstrahlung radiation. The energy loss distance via pair production is of the same order of magnitude, with X_0 corresponding to 7/9 of the photon mean free path. In the atmosphere $X_0 \approx 37\text{g}\,\text{cm}^{-2}$. A shower induced by a photon of energy E_γ reaches a maximum number of particles at a radiation depth given by:
$$X = X_0 \frac{\ln(E_\gamma)}{E_{th}} \tag{4.1}$$
- **Hadronic showers** Interaction of cosmic protons and nuclei trigger a cascade of particles, including π^0, $\pi^\pm$ but also K^0 and $K^\pm$ and a small fraction of D mesons.

The topology of these showers is then more complex than in the electromagnetic case due to the multiple decay channels of the kaons and the production of neutral pions which can lead to the appearance of electromagnetic sub-showers. In addition, hadronic sub-showers induced by inelastic collisions of secondary particles with nuclei can be observed.

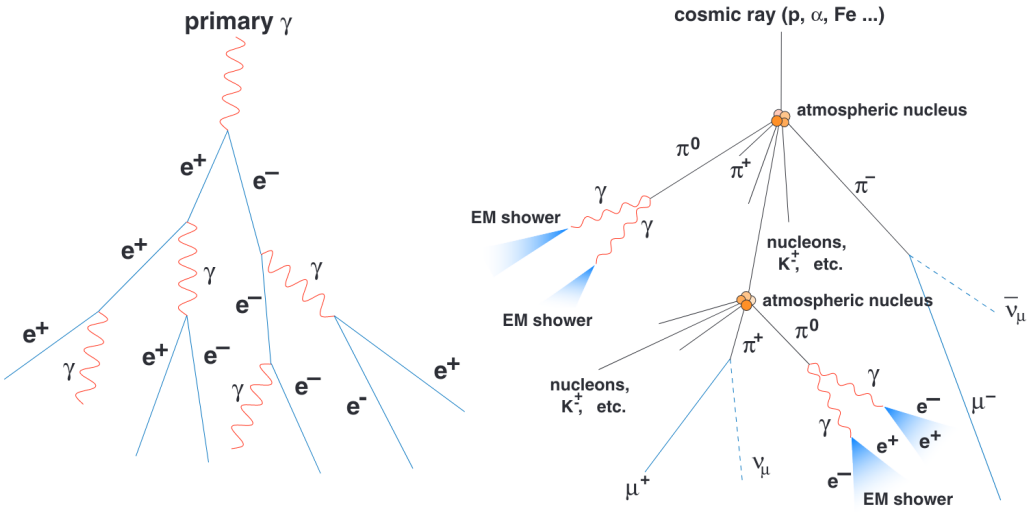

Figure 4.1.: Schematic view of an electromagnetic air shower (left) and a hadronic air shower (right). From [118].

Cherenkov light

Charged particles traveling through a medium induce a polarisation of the medium which, in turn, induces a production of light. When these particles travel at a relativistic speed, the light emitted along the particle's path interferes constructively and takes the form of a Cherenkov cone [119] of opening angle α:

$$\cos\alpha = \frac{1}{\beta n} \tag{4.2}$$

with n the refractive index of the medium and $\beta = v/c$. The emission of Cherenkov radiation thus requires that the particle travels at a greater speed than the light in the medium. This condition is met for charged particles in atmospheric showers[1], which leads to the projection of a cone of Cherenkov light from the shower to the ground, as sketched in Figure 4.2. This light reaches the ground in a flash of a few nanoseconds, and peaks at a wavelength of around 400 nm, which can be exploited considering the atmosphere is transparent to visible light. We note that the energy loss from Cherenkov radiation of an atmospheric shower is negligible with respect to the particle's initial energy.

[1] (n-1) $\approx 10^{-4}$ at a 10 km altitude.

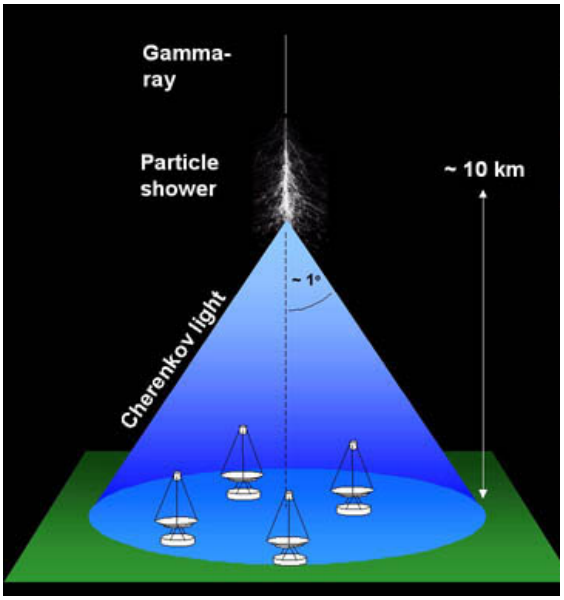

Figure 4.2.: Schematic of a light cone produced from the Cherenkov light of an electromagnetic shower. Figure from the HESS Collaboration [2].

4.1.2. Telescopes

H.E.S.S., the High Energy Stereoscopic System [120], named after Victor Hess, is an array of 5 IACT located on the Khomas Highlands in Namibia, at an altitude of 1800m. Its primary scientific mission is to detect γ photons from astrophysical sources at VHE, from around 20 GeV up to 100 TeV.

The experiment began operations end of 2002 with 4 telescopes with 12m diameter mirrors located in a 120 m square. In the following, this configuration will be referred to as **HESS-I** and the individual telescopes as CT1-4. Telescopes have a Davies-Cotton design [121] with a dish made of independent mirrors reflecting toward a Cherenkov camera built from an array of 960, 2×10^5 gain, Photo-Multiplier Tube (PMT) acting as pixels in the detector [122]. The Field of View (FoV) of a camera is close to 5°.

In 2014, a larger telescope with a parabolic mirror equivalent diameter of 28 meters, referred to as CT5, was inaugurated and this phase of HESS operations is known as **HESS-II**. The larger light collecting area allows for the sensitivity to showers with lower energy. The camera is made of 2048 pixels for a 3.2° FoV. CT1-4 cameras were upgraded in late 2016, this 4 telescope configuration is referred to as **HESS-IU**. The CT5 telescope camera was also upgraded in 2019 [123] with a prototype designed for the CTA observatory.

The trigger system [124] allows the recording of data in individual events. An image taken with a camera will then correspond to a single atmospheric shower. The trigger is done at 2 levels: at the level of the single telescope, the recording of data is

[2] www.mpi-hd.mpg.de/hfm/HESS/pages/about/telescopes

triggered if at least 3 neighboring PMT record more than 4 photo-electrons within 1.3 nanoseconds. The image is then sent to a Central Trigger of the telescope array. If at least two telescopes trigger within 80 nanoseconds, the data is recorded as images that correspond to a single event.

Data-taking is performed in observation periods, called *runs*, of usually 28 minutes. Data is then transferred to computing centers where images are calibrated (subsection 4.1.3) and from which the photon parameters are reconstructed (subsection 4.1.5). In the HESS Collaboration, two official analysis chains have been developed. It allows independent calibration, reconstructions, and high-level analyses in order to increase the reliability of the results by the use of systematic cross-checks. The main analysis of this work relies on the *ParisAnalysis* chain, the other one is named *HAP* (HESS Analysis Package).

4.1.3. Calibration

In an image of events recorded by cameras, the raw data is a digitized amplitude of the analog signal emitted by each PMT. The digitization is done with an Analog-to-Digital Converter (ADC) and is then given as a number of ADC counts. Multiple steps are performed to go from this number to the actual intensity of the atmospheric shower and are described in this section.

Camera electronics are separated into two channels [125]: the high gain and the low gain channels. The high gain channel provides a more sensitive measurement of low-intensity signals and the low gain channel is able to measure high-intensity signals without saturating the electronics. This allows a large dynamic range of signal intensities.

In a single PMT, the amplitude of the signal in photo-electrons is given from the amplitude of the ADC counts as:

$$A^{HG} = \frac{\mathrm{ADC}^{HG} - P^{HG}}{\gamma_e^{ADC}} \times FF \tag{4.3}$$

$$A^{LG} = \frac{\mathrm{ADC}^{LG} - P^{LG}}{\gamma_e^{ADC}} \times \frac{HG}{LG} \times FF \tag{4.4}$$

where :

- γ_e^{ADC} is the gain of the high gain channel in ADC per photo-electron (ADC/pe), with nominal values of 60 and 50 ADC/pe for the CT1-4 and CT5 telescopes, respectively. It is determined by calibration runs where the camera is illuminated with a pulsed light source. The distribution of ADC is measured and fitted, as seen in Figure 4.3.
- HG/LG is the amplification ratio of high gain to low gain, also determined in dedicated calibration runs. Its nominal value is 40.
- P^{HG} and P^{LG} are the pedestal positions of both channels. The pedestal is the mean ADC value in the absence of Cherenkov light and is regularly determined

during observation runs when the camera pixels do not contain Cherenkov light. It is then directly linked to the Night Sky Background (NSB), which is the light entering the detector in the absence of a Cherenkov flash: residual scattered Moon and artificial light, and star light.

- FF is the flat-field coefficient. It is determined by flashing a uniform (flat) light into the camera to assess the pixel-to-pixel efficiency discrepancies.

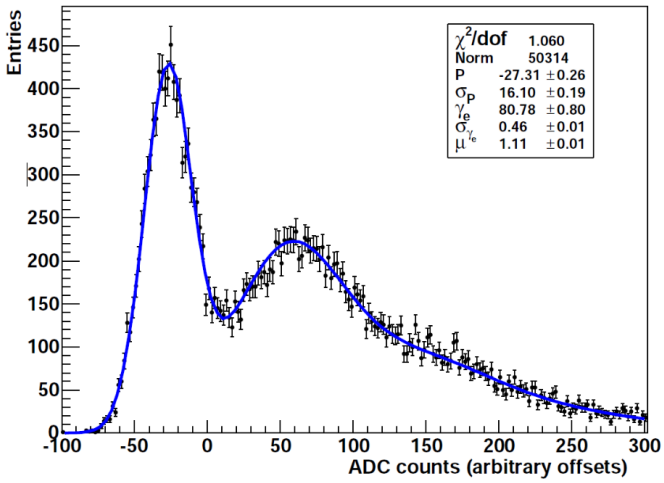

Figure 4.3.: Distribution of ADC counts for a single photo-electron in the high gain channel. In blue a function is fitted to the measurement. Figure from [126].

Once the PMT response to light is calibrated, the optical efficiency is determined by muon ring calibration [126]. The optical efficiency is defined as the fraction of photons remaining in the PMT to the total number of photons entering the detector. This variable can be calibrated for each observation run by analyzing the images of Cherenkov rings (see Figure 4.5, left) on the camera induced by muons. Indeed, the total number of photons entering the telescope can be directly computed from the measured parameters of the muon ring in the camera [127]. The atmospheric light absorption can be ignored as each image results from Cherenkov emission from a muon reaching the telescope. The computed number of photons is then compared to the measured number of photo-electrons in the camera.

Finally, the absorption of Cherenkov photons by the atmosphere can vary from night to night (or even from run to run) as the transparency of the atmosphere can be impacted by the meteorological conditions or the presence of aerosols. A Transparency Coefficient is introduced to quantify this effect. As the trigger rate of the detector is dominated by Cherenkov light reaching the detector from showers induced by cosmic protons, whose flux is constant in time and only zenith dependent, we can use the variation of the trigger rate to determine the transparency coefficient [128]:

$$T = \frac{1}{N \cdot k_N} \sum_i^N \frac{R_i^{\frac{1}{1.7-\Delta}}}{\mu_i \cdot \gamma_i} \tag{4.5}$$

where N is the number of active telescopes, k_N is a corrective factor on the number of active telescopes, and R_i is the trigger rate in telescope i. The exponent $\frac{1}{1.7-\Delta}$ comes from the estimation of the cosmic proton spectrum in the relevant energy range. Δ is an energy-dependant corrective factor on the cosmic proton spectral index introduced to take into account energy-dependant differences between proton-induced hadronic showers and electromagnetic showers. μ_i is the muon ring optical efficiency and γ_i is the average pixel gain of telescope i.

4.1.4. Simulations

Data analysis, event reconstruction, and performance evaluation rely on Monte-Carlo simulations (MC). The ParisAnalysis chain uses simulations built upon the KASKADE software [129] for air shower simulation and Cherenkov light production. The detector response simulation uses a HESS-dedicated simulation framework, SMASH [130]. On the other hand, the HAP analysis chain uses the CORSIKA software [131] for air shower simulation and *sim_telarray* for detector response [132].

While most of the simulations are performed using averaged data-taking conditions, a framework of Runwise Simulations (RWS) production taking into account actual conditions from related runs, to improve result accuracy, has been recently developed in the ParisAnalysis chain [133].

4.1.5. Event reconstruction

The γ photon parameters such as the direction or the energy are reconstructed from the calibrated images of atmospheric showers in the telescope camera. Historically, the reconstruction from shower images was done using a Hillas parametrization method [134]. This technique, as shown in Figure 4.4, relies on fitting ellipses to the images and extracting a set of relevant parameters from which the primary photon direction could be deduced either analytically, or with the use of MC.

The reconstruction methods were later improved. The one used in the analyses of this thesis, named *Model*++ (M++), relies on comparisons of camera data to a semi-analytical model of particle showers, developed in [135] and extended with the installation of CT5 [136]. This model is obtained from the parametrization of the Cherenkov light from MC events with respect to the shower zenith angles, impact distances from the telescope, primary photon energies, and interaction depths.

The actual intensity of light received in each pixel is compared to the model templates using a Probability Density Function (PDF) defined as :

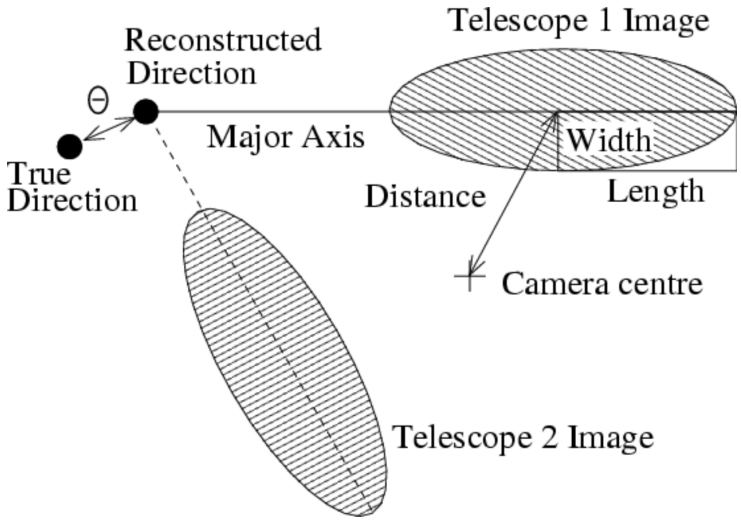

Figure 4.4.: Definition of Hillas parameters from two superimposed shower images. The reconstructed direction of the primary photon is simply the intersection of the major axes of both ellipses. From [120].

$$P(s|\mu,\sigma_p,\sigma_\gamma,\sigma_c) = \sum_{n=0}^{\infty} \frac{\mu^n e^{-\mu}}{n!\sqrt{2\pi(\sigma_p^2 + n\sigma_\gamma^2 + n^2\sigma_c^2)}} \exp\left(-\frac{(s-n)^2}{2(\sigma_p^2 + n\sigma_\gamma^2 + n^2\sigma_c^2)}\right) \tag{4.6}$$

where n is the number of photo-electrons in the PMT, s is the measured intensity in the pixel in photo-electrons, and μ is the expected mean number of photo-electrons from the model. The systematic uncertainties are represented as a Gaussian spread of the PMT resolution with parameters: σ_p the pedestal width (pure noise charge distribution), σ_γ the width of a single photo-electron peak and σ_c the calibration uncertainties.

For the fit of data measured in i pixels a log-likelihood function can be defined from the individual likelihood of each pixel as:

$$\ln\mathscr{L}_{\text{set}} = \sum_i \ln\mathscr{L}_i = \sum_i -2 \times \ln P(s|\mu,\sigma_p,\sigma_\gamma,\sigma_c) \tag{4.7}$$

The reconstruction of the primary photon parameters is done by maximizing this log-likelihood function.

Once the fit is performed, the uncertainty of the reconstructed direction can be computed from the second derivative of the log-likelihood function around its maximum:

$$\Delta Dir = \left(\frac{\partial^2 \ln\mathscr{L}}{\partial Dir^2}\right)^{-1/2} \tag{4.8}$$

In a `Combined (Stereo HESS-I + Stereo HESS-II)` analysis, events are both

reconstructed without and with CT5, providing respectively a HESS-I and HESS-II solution. For each of these events, the best reconstruction, i.e. the one that yields the lowest direction error ΔDir is chosen over the other.

The HAP analysis chain, on the other hand, uses a method described in [137]. It is similar, except that the recorded images are compared to model images directly from MC, not using a parametrization of the reconstructed parameters.

4.1.6. Event selection

Most of the events are hadronic showers originating from cosmic protons. This constitutes a background noise that needs to be reduced. The discrimination between hadronic and electromagnetic showers induced by VHE photons exploits topology differences between them. In particular, γ induced showers are more regular and do not exhibit additional Cherenkov light emitted by a hadronic component, as seen in Figure 4.5.

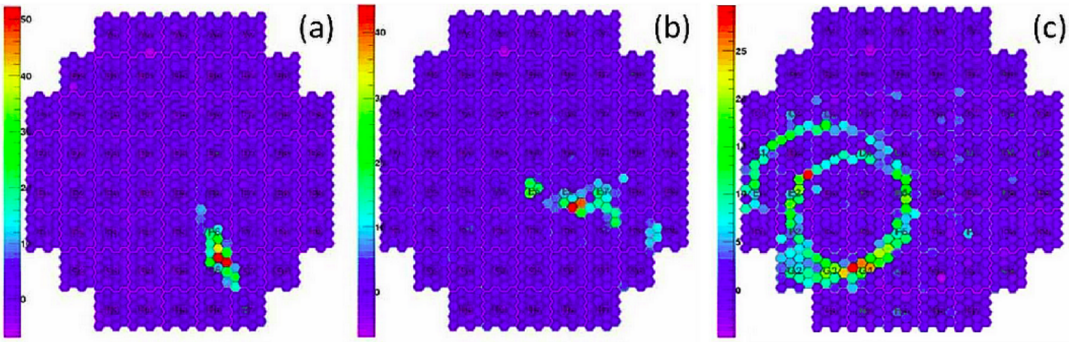

Figure 4.5.: Examples of images of Cherenkov light induced from a γ (a), a hadron (b), and a muon (c). The Cherenkov cone of muons appears ring-like in the camera.

The pixels of an image are separated into two regions:

- *Shower core* pixels, defined as those with a predicted amplitude from the fitted model above 0.01 photo-electrons and their 3 closest neighbors.
- *Background pixels*, the remaining pixels of the image.

These two regions are determined after the likelihood fit and are used to define the main variables used in the event selection. *Shower core* pixels contribute to the *Shower Goodness* defined from the comparison of the likelihood to its expected value from the model template as:

$$G_{\mathrm{SG}} = \frac{\sum_i \left(\ln \mathscr{L}(s_i|\mu_i) - \langle \ln \mathscr{L} \rangle |_{\mu_i}\right)}{\sqrt{2 \cdot \mathrm{NdF}}} \tag{4.9}$$

with NdF is the number of degrees of freedom of the fit and is equal to the number of Shower core pixels minus 6. The expected log-likelihood value can be simplified for a high μ as:

$$\langle \ln \mathscr{L} \rangle |_{\mu_i} = 1 + \ln(2\pi) + \ln\left(\sigma_p^2 + \mu(1+\sigma_\gamma^2)\right) \tag{4.10}$$

Equation 4.9 can be scaled to the number of telescopes involved in the event reconstruction to define the *Mean Scaled Shower Goodness* (MSSG). Distributions of this variable for photons and background events are shown in Figure 4.6.

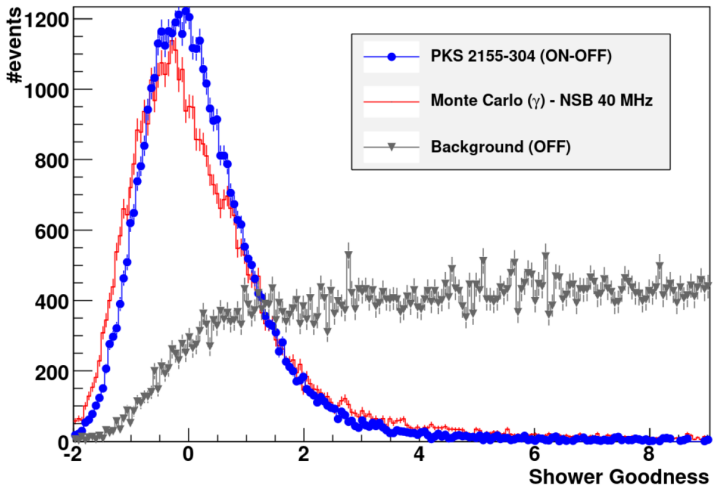

Figure 4.6.: MSSG example from [135]. Blue: photons observed from source PKS 2155-304. Red: MC generated photons. Black: Background events.

Similarly to Equation 4.9, we can define a NSB Goodness as the comparison of the likelihood for *background pixels* to its expected value in a background-only hypothesis:

$$G_{\mathrm{NSB}} = \frac{\sum_i \left(\ln \mathscr{L}(s_i|0) - \langle \ln \mathscr{L} \rangle |_0\right)}{\sqrt{2 \cdot \mathrm{NdF}}} \tag{4.11}$$

As shown in Table 4.1, 3 sets of selection parameters have been optimized for a `Stereo` analysis in order to separate photons from background:

- **Loose**. Initially optimized for observations of stronger sources, it provides a lower energy threshold at the price of a poorer background rejection.
- **Standard** (Std). Optimized for a photon index $\alpha = -2.5$
- **Faint**. Initially optimized for fainter sources. Provides a higher energy threshold and better background rejection. This set of selection parameters is more suited for the study of sources with a hard spectrum.

Additionally, the following selection is applied in all cases:

- The direction error ΔDir, as defined in Equation 4.8 less than 0.2°.

	Loose	Standard	Faint
MSSG	[-4,0.9]	[-4,0.9]	[-4,0.6]
G_{NSB}	>15	> 20	> 40
MinCharge	40	60	120
PixelAbove5PE	4	5	5

Table 4.1.: Selection cuts for 3 analysis profiles. MSSG is defined in Equation 4.9 and G_{NSB} in Equation 4.11. MinCharge is the minimum image amplitude per telescope and PixelAbove5PE is the number of pixels per telescope with intensity higher than 5 photo-electrons.

- The reconstructed depth of the first interaction, between -1.1 and 4.4, in units of the radiation length of the atmosphere X_0.
- The event is required to be reconstructed with at least 2 telescopes (*Stereo* reconstruction).
- The shower containment fraction, defined as the fraction of the best-fit shower model intensity inside the camera FoV is required to be above 0.2.

4.1.6.1. Performances

The performances of a detector are quantified with its Instrument Response Functions (IRF), such as its effective area, or the angular and energy resolution of the reconstruction.

Figure 4.7 shows the effective areas of HESS for different analysis configurations. We can note the lower energy threshold for a reconstruction using only CT5 (Mono), at the cost of a lower effective area at higher energy. A combined reconstruction allows us to take advantage of the different configurations.

The angular resolution obtained with HESS-I Stereo with Standard selection cuts is shown in Figure 4.8. The 68% containment angle defining a Point-Spread Function (PSF) is below 0.1° for most observations.

The energy resolution, when defined as the RMS of the relative error between the true energy and the reconstructed energy:

$$E_{\mathrm{err}} = \frac{|E_{\mathrm{true}} - E_{\mathrm{reco}}|}{E_{\mathrm{true}}} \tag{4.12}$$

is of the order of 10% above 1 TeV.

4.1.7. Run selection

The data-taking conditions can be dependent on several factors. External, like the atmospheric conditions or the location of the Moon, or internal, like the telescope

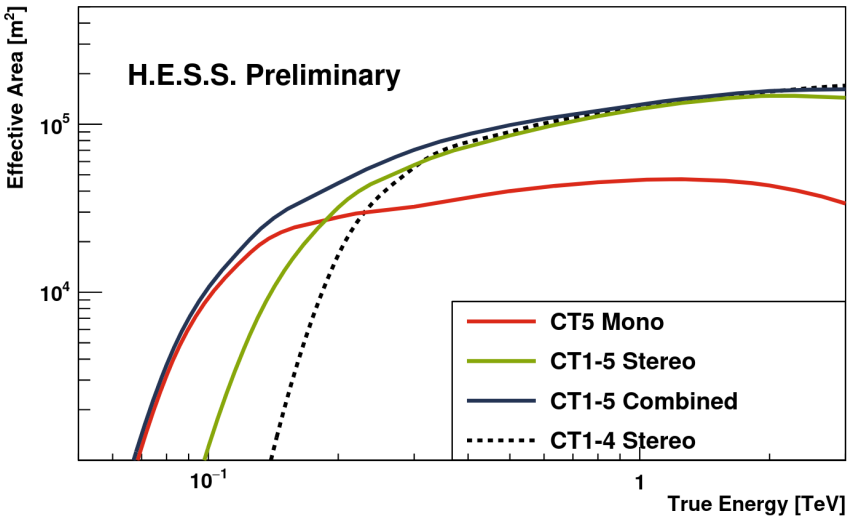

Figure 4.7.: Effective Areas of HESS for different analysis configurations. From [136]

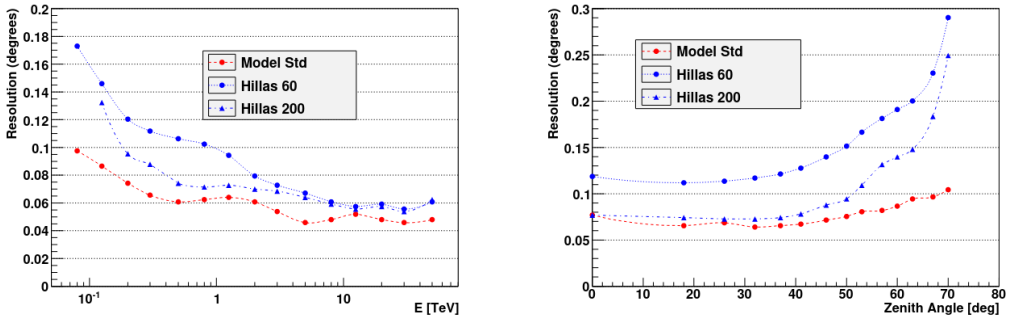

Figure 4.8.: Angular resolution (defined as the 68% containment radius obtained with the Model reconstruction procedure and Standard selection cuts). Left: as a function of Energy. Right: as a function of zenith angle, for a E^{-2} spectrum. The resolution is compared to the Hillas method. Plot from [135].

sky tracking performances or the presence of issues with the electronics. A set of criteria was then designed to ensure good data quality, which translates into a good match between the simulated IRF and the actual telescope behavior, and allows sufficient reliability of the scientific results. These criteria are usually put on parameters associated with each observation run, with the removal of runs not meeting them.

The run selection criteria for an analysis using the HESS-I configuration are:

- **Run duration**: A short run could be related to numerous data-taking issues. The threshold livetime for a run to be analyzed is 5 minutes.

- **Trigger rate**: In optimal conditions, the telescopes are triggered from the cosmic ray flux. As this flux is stable, a high trigger rate may be related to residual

Moon or background light, and a low trigger rate may be related to bad weather conditions or an issue with the detector. The Central Trigger rate is then required to be between 100Hz and 600Hz, with less than 10% variability.

- The minimum validity of a run requires that it was taken with **3 functioning telescopes** with trigger rate variability below 10%.
- **Dead time**: Issues might arise that translate into telescopes not triggering during data-taking. This dead time is required to be below 15% of the run live time.
- **Weather conditions**: A set of radiometers (one per CT1-4 telescopes) measure the temperature of the sky, with a high temperature meaning the presence of clouds or poor atmosphere quality. We require that:
  - The radiometer temperature is below -20°C.
  - The radiometer temperature stability is below 3°C.

  Additionally, we require that the relative humidity is below 90% during data-taking.
- **Broken pixels**: Issues with the electronic might cause some pixels of the camera to malfunction. We require less than 15% of broken pixels in at least 3 telescopes.
- **Pointing**: The telescopes need to track the position of the pointing for the whole duration of the run. The discrepancy between the nominal telescope pointing and its actual direction needs to be below 100 arcseconds.

When the analysis includes data from the CT5 telescope, additional conditions apply on top of the previous ones. For example in an analysis using 5 telescopes (HESS-II Stereo) analysis:

- **Central Trigger** The presence of CT5 induces an increase in the trigger rate. We then require it to be between 800Hz and 3000Hz, with less than 15% variability.
- **Dead time** Less than 5% for CT5.
- **Broken pixels** Less than 5% in CT5

We note that in the case of a run being rejected due to conditions on CT5 but not on HESS-I (CT1-4) conditions, the run is better analyzed using a HESS-I reconstruction profile, removing CT5 data entirely.

4.1.8. Background subtraction

After event selection, the observed events sample is still dominated by a population of irreducible, γ-like high-energy cosmic proton showers. However, this background is assumed to be isotropic and to appear as a flat distribution with respect to solid angle. The background subtraction uses an ON/OFF technique, where the number

of background events in an ON region is estimated from the number of events in a single, or multiple, OFF region. Although the telescope's acceptance of γ-like events is highly dependent on the distance from the event direction to the center of the camera, we can assume that it is constant in a ring centered on the middle of the camera FoV. We can make use of that fact by performing the observation with a *wobble offset*, i.e. with an offset from the FoV center to the observed target coordinates.

As shown in Figure 4.9, this offset allows us to draw multiple regions with a similar acceptance to the one containing the target of the observation. This method is known as the Multiple Off Regions Background. An excess can then be simply given as:

$$N_{\text{exc}} = N_{\text{ON}} - \alpha \times N_{\text{OFF}} \tag{4.13}$$

with $N_{\text{ON/OFF}}$ the number of events in the ON/OFF regions and α the ratio of the time-integrated acceptances in the ON and OFF regions. In the case of a Multiple Off Regions Background computation, under the assumptions that the acceptance is indeed axisymmetric, that the observation live time is the same in all regions, and that all considered regions have the same surface on the 2D FoV, α simplifies to 1/(Number of Off Regions). Given the fact that the proton flux is dependent on the zenith, a slight correction factor is applied to α with respect to the zenith of each Off region.

Thus, increasing the offset angle increases N_{OFF} and reduces the statistical error of the background estimation. This angle is usually chosen between 0.5° and 0.7° to still ensure a sufficient acceptance around the observation target.

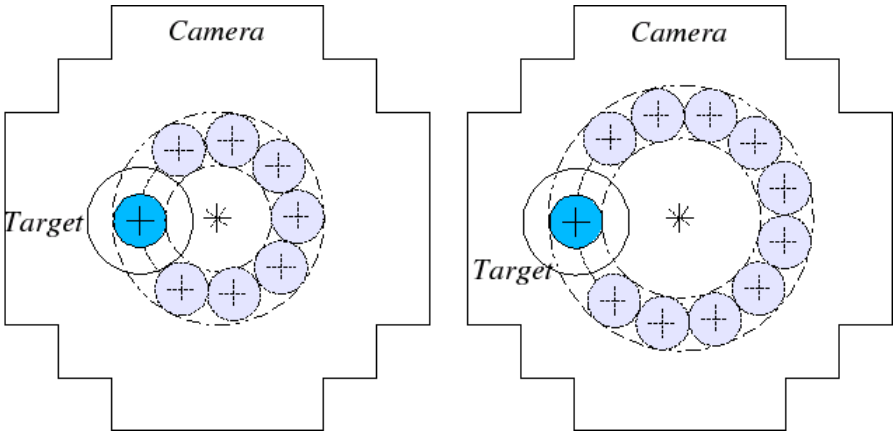

Figure 4.9.: Schematic view of the Multiple OFF technique. The target position is the blue circle. An exclusion region is represented around the target region. The grey circles are the OFF regions.

When accumulating data from multiple runs with different wobble offsets (leading to multiple α_i), the averaged α is given by:

$$\alpha = \sum_i \frac{\alpha_i \times N_{\text{OFF},i}}{N_{\text{OFF}}^{tot}} \tag{4.14}$$

to ensure that the total excess is the sum of the excesses found in each run:

$$N_{\text{exc}}^{tot} = N_{\text{ON}}^{tot} - \alpha \times N_{\text{OFF}}^{tot} = \sum_i \left(N_{\text{ON},i} - \alpha_i \times N_{\text{OFF},i} \right) \tag{4.15}$$

In order to prevent another source from interfering with the background estimation, we can draw excluded regions around known VHE γ emitters. In the Multiple Off method, that translates into not including any Off region intersecting with an excluded region in the background estimation, as schematized in Figure 4.10. We note that an exclusion region is drawn in any case around the target region, to reduce the number of photons originating from the source contaminating the background estimation.

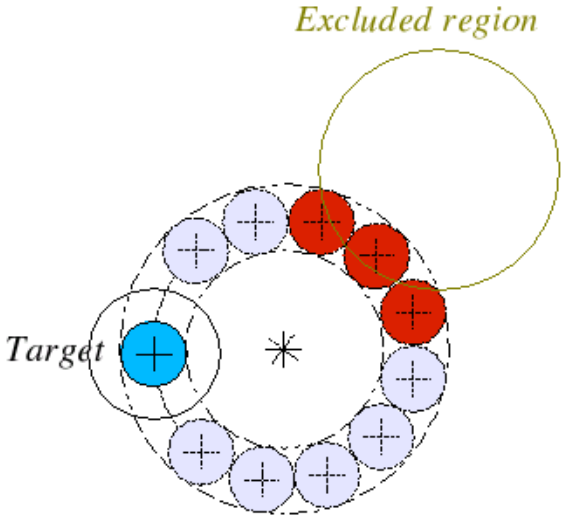

Figure 4.10.: Schematic view of the multiple OFF technique, with an exclusion region. All OFF regions intersecting with the exclusion region are not considered for the background subtraction.

To further ensure a proper background estimation, we can plot the distribution of ON and OFF events with respect to the squared angular distance θ^2 from the center of their respective regions. This allows us to plot the event density distribution around the target, as the solid angle of bin i is located at an angle $\theta : \Omega \propto \theta^2$. An example of this θ^2 distribution can be found in Figure 4.11. In this figure, we can see the distribution of ON events in green and the normalized number of OFF events $\alpha \times N_{\text{OFF}}$ as crosses, with a source clearly appearing at $\theta = 0$ and a properly estimated background, as we can see the tails of both the ON and OFF events distributions are superimposed. The number of excess events N_{exc} is then the sum of events above the background inside the target region.

4.1.9. High-level analysis

4.1.9.1. Signal significance

Li and Ma [138] derive the significance of an excess given by $N_{\text{exc}} = N_{\text{ON}} - \alpha \times N_{\text{OFF}}$ in an ON/OFF experiment with a likelihood ratio between a background-only hypothesis

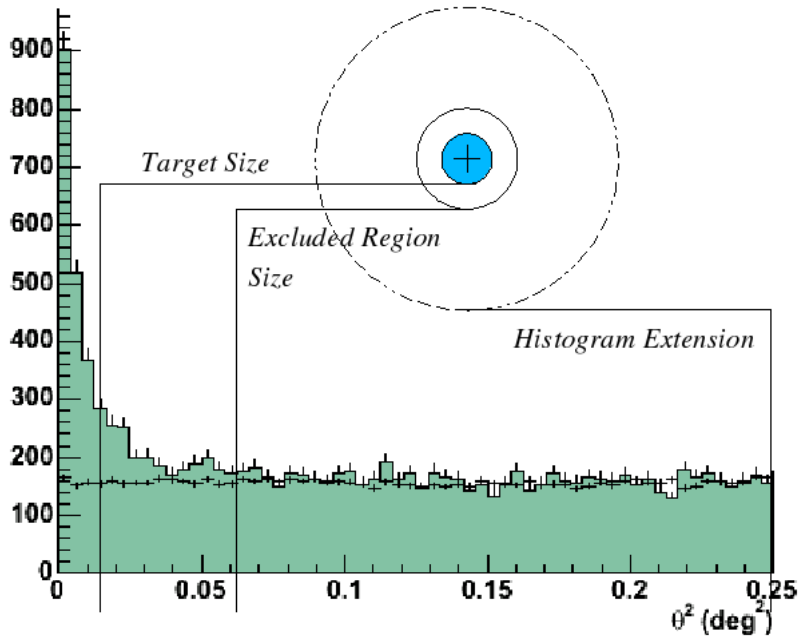

Figure 4.11.: θ^2 event distribution and the related regions.

and a hypothesis with a signal as:

$$\Lambda = \frac{L(N_{\mathrm{ON}}, N_{\mathrm{OFF}}|\mu_s = 0, \hat{\mu}_b)}{L(N_{\mathrm{ON}}, N_{\mathrm{OFF}}|\hat{\mu}_s, \hat{\mu}_b)} = \left(\frac{\alpha}{1+\alpha}\frac{N_{\mathrm{ON}}+N_{\mathrm{OFF}}}{N_{\mathrm{ON}}}\right)^{N_{\mathrm{ON}}} \times \left(\frac{1}{1+\alpha}\frac{N_{\mathrm{ON}}+N_{\mathrm{OFF}}}{N_{\mathrm{OFF}}}\right)^{N_{\mathrm{OFF}}} \tag{4.16}$$

with $\hat{\mu}_s$ and $\hat{\mu}_b$ the numbers of signal and background events maximizing the likelihood.

The significance, defined as a number of standard deviations is then given by :

$$S = \sqrt{-2\ln\Lambda} \tag{4.17}$$

As $-2\ln\Lambda$ follows asymptotically a χ^2 distribution with 1 degree of freedom in a background-only hypothesis, assuming N_{ON} and N_{OFF} follow Poisson statistics with a sufficiently high number of events (more than 10).

In case of a negative excess N_{exc}, the convention is usually taken to give the significance as a negative value.

4.1.9.2. Sky Maps

In addition to the calculation at the coordinates of the source, an excess and the significance of that excess can be computed at any point of the sky in the FoV of an analysis. Excess and significance maps can then be drawn in order to study extended sources. Figure 4.12 shows an example of such maps, borrowed from chapter 7.

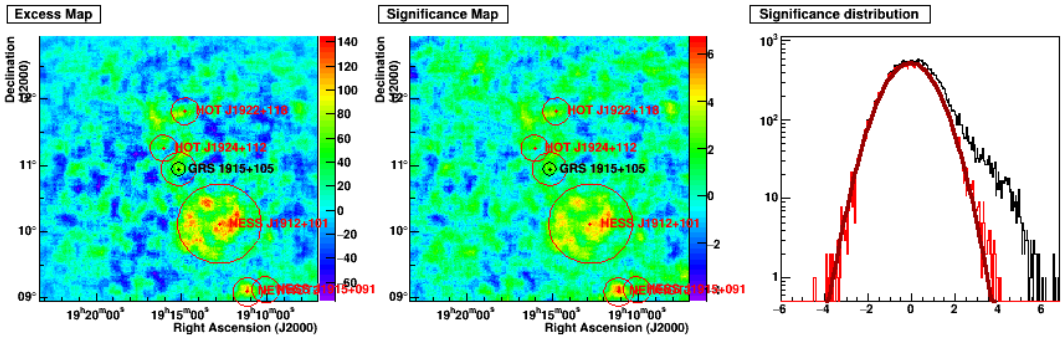

Figure 4.12.: Left: Excess map. Center: Significance map. Excluded regions are circled in red on the maps. Right: significance distributions of all pixels (black histogram) and pixels outside of excluded regions (red histogram). In the absence of a source, the significance is distributed from random fluctuations and follows a standard normal distribution.

For all positions in the map without a photon-emitting source, the excess is randomly distributed. This leads to a significance distribution of the pixels in the map that follows a standard normal distribution, as seen on the red histogram in the right panel of Figure 4.12. This distribution is then a check on the proper characterization of the background, i.e. if every source has been properly excluded from the background computation.

4.1.9.3. Flux determination

Simulations allow us to compute the effective area for a given set of selection cuts:

$$\mathscr{A}(E,\theta,\delta) = \int dS \times \epsilon(\vec{r},E,\theta,\delta) \tag{4.18}$$

with E the true energy, θ the zenith angle, and δ the distance of the event from the center of the camera. $\epsilon(\vec{r},E,\theta,\delta)$ is the detection probability and the integral is computed over the surface on the ground.

We can also determine the energy resolution, defined as the probability of reconstructing an energy E_r for a given true energy E: $P(E_r|E)$.

The expected number of events for a given flux $\Phi(E)$ between reconstructed energies E_r^1 and E_r^2 for an observation live time Δt is then:

$$n_\gamma = \Delta t \int_{E_r^1}^{E_r^2} dE_r \int dE \times \Phi(E) \times \mathscr{A}(E,\theta,\delta) \times P(E_r|E) \tag{4.19}$$

For an incoming flux assumed to be a power-law of spectral index α:

$$\Phi(E) = \Phi_0 \left(\frac{E}{E_0}\right)^\alpha \tag{4.20}$$

the flux normalization Φ_0 can then be computed from a measured number of photons

from Equation 4.19 as:

$$\Phi_0 = \frac{n_\gamma}{\Delta t \int_{E_r^1}^{E_r^2} dE_r \int dE \times \left(\frac{E}{E_0}\right)^{\alpha} \times \mathscr{A}(E,\theta,\delta) \times P(E_r|E)} \tag{4.21}$$

4.1.9.4. Upper Limits determination

As given by [139], we can draw a confidence interval of compatible values of Φ_0 with respect to the results of an ON/OFF experiment from a likelihood function given by:

$$\mathscr{L} = \frac{(\epsilon n_\gamma + b)^{N_{\mathrm{ON}}}}{N_{\mathrm{ON}}!} \times \frac{(b/\alpha)^{N_{\mathrm{OFF}}}}{N_{\mathrm{OFF}}!} \times \frac{1}{\sigma_\epsilon \sqrt{2\pi}} \exp\left[-\frac{1}{2}\left(\frac{\epsilon - \epsilon_0}{\sigma_\epsilon}\right)^2\right] \tag{4.22}$$

With b the expected background in the ON region and the detector efficiency ϵ are treated as nuisance parameters. Detector mean efficiency and its standard deviation are noted ϵ_0 and σ_ϵ.

A likelihood ratio between any n_γ to the number of photons that maximizes the likelihood $\hat{n}_\gamma$ is given as:

$$\lambda = \frac{\mathscr{L}(n_\gamma, \hat{b}(n_\gamma), \hat{\epsilon}(n_\gamma))}{\mathscr{L}(\hat{n_\gamma}, \hat{b}, \hat{\epsilon})} \tag{4.23}$$

with $\hat{n_\gamma}, \hat{b}, \hat{\epsilon}$ the values that maximises $\mathscr{L}$ and $\hat{b}(n_\gamma), \hat{\epsilon}(n_\gamma)$ are the values that maximise $\mathscr{L}$ for a given n_γ.

We can draw an interval of all n_γ that is compatible with our observation within a $n\sigma$ confidence level with $n = \sqrt{-2\ln\lambda}$. The upper limit on the number of photons is then the upper bound of that interval, and the upper limit of the flux can be computed from this number, the effective area, and the observation time.

4.2. Deep-Sea Neutrino detectors: ANTARES and KM3NeT

The deep sea offers an ideal medium for the detection of high-energy neutrinos, as the water offers a large volume for neutrino interaction while offering a transparent medium for the propagation of Cherenkov light. Moreover, a deep-sea detector benefits from the shielding of the water from most of the particles produced in cosmic ray showers, and from an environment with low background light.

This section presents the topologies of neutrino interaction in water, then presents the two detectors used in this thesis's analyses: ANTARES and KM3NeT. An overview of the data processing schemes in both detectors is finally provided.

4.2.1. Interaction Topologies

High-energy neutrinos interact with nucleons through the weak interaction via two channels:

- Charged Current (CC) interaction with the exchange of a W boson:

$$\nu_l + N \rightarrow l + X$$

- Neutral Current (NC) interaction with the exchange of a Z boson:

$$\nu_l + N \rightarrow \nu_l + X$$

with ν_l a neutrino or antineutrino of flavor associated with lepton l (ν_e/electron, ν_μ/muon or ν_τ/tau), N is a nucleon and X represents the hadronic shower induced by the interaction. The convention of naming ν_l both the neutrino and its corresponding antineutrino is used in the rest of this thesis, unless indicated otherwise.

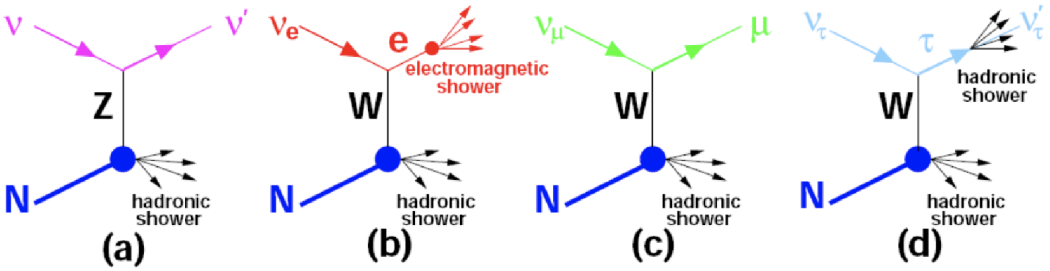

Figure 4.13.: Pseudo-Feynman diagrams of high-energy neutrino interactions. (a) NC interaction with scattered neutrino ν'. (b) CC interaction of a ν_e resulting in the emission of an electron, itself inducing an electromagnetic shower. (c) CC interaction of a ν_μ resulting in a muon μ. (d) CC interaction of a ν_τ resulting in a tau τ, that quickly decays and induces another hadronic shower and the production of another ν_τ. From [140]

As shown in Figure 4.13, different neutrinos flavors exhibit different event signatures:

- **Electron neutrino CC interaction**: Such interaction induces the production of a high-energy electron that will produce a γ photon via Bremsstrahlung and initiate an electromagnetic shower of a few meters [141]. We note the Glashow resonance of electron anti-neutrino on electrons [142]: $\bar{\nu}_e + e^- \rightarrow W^-$ peaking at $\bar{\nu}_e$ energy of 6.3 PeV.

- **NC interactions**: As the NC interaction is not flavor-changing, it results in an out-going neutrino that is not observed in the detector. Given that the out-going neutrino might carry away a significant fraction of the initial interaction, the resulting hadronic shower intensity is not well-correlated with the initial neutrino energy.

- **Tau neutrino CC interaction**: The tau lepton produced in the interaction travels some distance in the detector before quickly decaying after 2.9×10^{-13} seconds in its proper time. The traveled distance depends then mostly on the time it takes to decay in the detector frame, thus its Lorentz factor. Its path length in water is shown on Figure 4.15. The tau lepton can decay in multiple channels, inducing in most cases another (electromagnetic or hadronic) shower, or a muon.

- **Muon neutrino CC interaction**: The muon's higher mass relative to the electron and its longer lifetime relative to the tau lepton make that it travels a longer distance and that no additional particle cascade is associated with the initial hadronic shower. However, the muon might decay close to the detector in an electron inducing an electromagnetic shower.

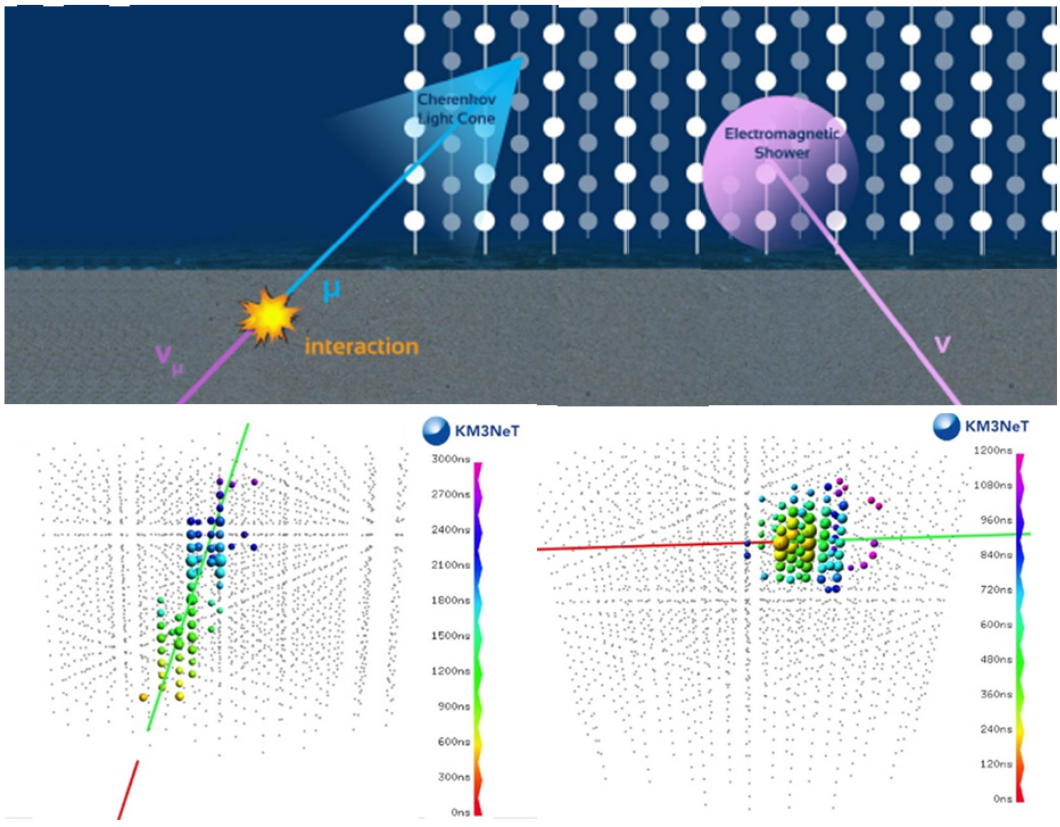

Figure 4.14.: The two main event topologies in a high-energy neutrino detector. The upper part shows a schematic of the event topologies while the bottom part shows event displays of corresponding topologies. Left: ν_μ interacting outside the detector volume, producing a muon propagating inside it and inducing the emission of a detectable Cherenkov cone. Right: ν_e interacting inside the detector volume, inducing an electromagnetic shower. From [4].

As a result of the different event signatures, distinct topologies can be distinguished in high-energy neutrino detectors:

- **Track-like**: Essentially dominated with ν_μ, with additional contribution from ν_τ with very high energy (> PeV) and ν_τ decaying in a channel producing a muon. As the muon tracks can travel multiple kilometers, as seen on Figure 4.15, the neutrino interaction can happen outside of the detector volume. Moreover, the linear trajectory allows the reconstruction of the muon direction which can be related to the initial ν_μ direction by the interaction kinematics. The average angle between an incoming neutrino of energy E_ν to the muon is given by (from [143]):

$$\langle \theta_{\nu\mu} \rangle \leq \frac{0.6^\circ}{\sqrt{E_\nu / 1\text{TeV}}} \tag{4.24}$$

  The propagation line of the muon track is then close to the direction of origin of the neutrino, which makes this event topology particularly interesting for neutrino astronomy.

- **Shower-like** (or **Cascade-like**): Other neutrino flavors appear as localized in the detector. This topology does not allow for a good localization of the neutrino direction but allows a good energy estimation in the case of CC interaction as the amount of Cherenkov light emitted is directly linked to the shower energy. On the other hand, energy estimation in the case of NC interaction is made harder by the fact that the outgoing neutrino is not detected. Plus, electromagnetic and hadronic showers are not distinguishable in deep-sea neutrino detectors due to the low instrument density not allowing for precise shower topology determination.

- **"Double bang"**: Although expected to be rarer than the others, another event topology could be determined in the case of a ν_τ interaction. A so-called *double bang event*, characterized by two distinct showers separated by a track, can happen under some circumstances. Both the shower initiated by the primary ν_τ interaction and the shower initiated by the decay of the τ lepton need to happen in the detector's volume, and the τ lepton energy needs to be high enough for it to travel some distance in the detector in order to both shower to be clearly separated.

We also note that the difference between neutrino and anti-neutrino interaction is not visible in such a detector, with the exception of the Glashow resonance. However, as it takes place at very high energy, it is mostly negligible in the overall neutrino flux.

4.2.2. Detection principle

Similarly to Cherenkov flashes in the atmosphere (section 4.1), relativistic charged particles traveling through water will induce the emission of light in a cone-like shape.

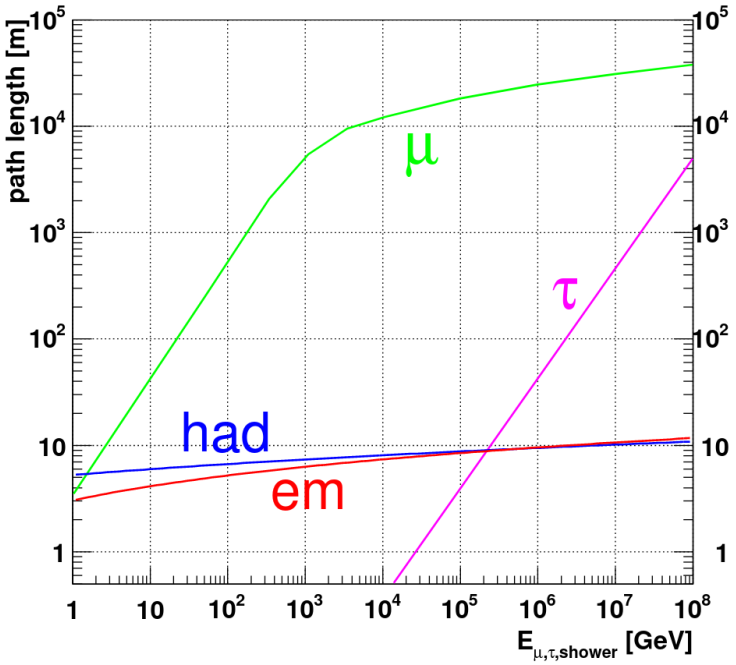

Figure 4.15.: Path length of neutrino interaction products in water. Blue: Hadronic shower. Red: Electromagnetic shower. Green: muons. Magenta: tau leptons. Figure from [141]

Water has a higher refractive index than air, $n \approx 1.35$, which means a lower energy threshold for Cherenkov emission and a higher intensity of emitted light, as the number of emitted photons N in a propagation distance dx is given by:

$$\frac{d^2N}{dxd\lambda} = \frac{2\pi\alpha}{\lambda^2}\left(1 - \frac{1}{\beta^2 n(\lambda)^2}\right) \tag{4.25}$$

with λ the wavelength of the emitted light, β the particle velocity, α the fine structure constant, n the refractive index of the medium.

Muon track events appear then as a single cone-like feature going through the detector, and shower-like events as a fairly localized light-emitting region.

4.2.3. Detectors

ANTARES (Astronomy with a Neutrino Telescope and Abyss environmental RESearch) [144] was an under-sea neutrino telescope anchored 2,500 meters deep in the Mediterranean Sea, offshore of Toulon (France). It was optimized for the detection of high-energy neutrinos with energy ranging from a few hundred GeV to a few PeV. Data taking ran from March 2006 to February 2022.

KM3NeT (Kilometer Cubed Neutrino Telescope) [145] is the successor to ANTARES operations. It is under construction on two sites, each site having its own configuration:

- **ORCA** (Oscillation Research with Cosmics in the Abyss) Located near Toulon at 2500 meters below sea level, near the ANTARES site. It is optimized for the detection of neutrino energy in the GeV to low-TeV range.

- **ARCA** (Astroparticle Research with Cosmics in the Abyss) Located 3500 meters deep offshore of Portopalo di Capo Passero in Sicily (Italy), optimized for the detection of neutrino energy in the TeV to PeV range.

It is important to note at this point that, even if the ORCA detector was initially designed for the study of neutrino oscillations, its design does not prevent its use for neutrino astronomy. In fact, its sensitivity to lower energy brings a complementary role relevant to the study of potential neutrino sources despite its lower instrumented volume.

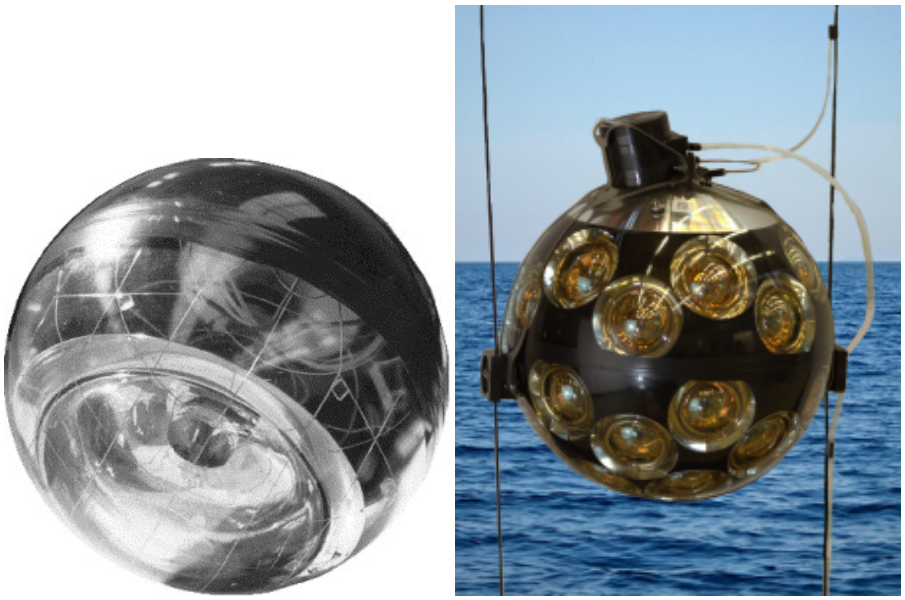

Figure 4.16.: Left: ANTARES Single-PMT optical module. Right: KM3NeT Multi-PMT optical module.

The detectors are built with vertical Detection Unit (DU), also known as lines, anchored to the sea floor, into which are fixed regularly-spaced optical modules to collect Cherenkov light into PMT.

The ANTARES detector was made of 12 lines ~70 meters apart, with 75 optical modules built into 25 storeys 14.5 meters apart. The optical modules [146] (Figure 4.16, left) were glass spheres with a single 10-inch PMT mounted to face 45° from the horizontal plane. A schematic picture of the detector is shown in Figure 4.17.

The KM3NeT optical module [147] (Figure 4.16, right) uses a multi-PMT design where each Digital Optical Module (DOM) contains 31 3-inch PMTs in a glass sphere. They are mounted on lines anchored to the sea floor. The planned number of lines is 115 for ORCA and 230, with two 115-line building blocks for ARCA.

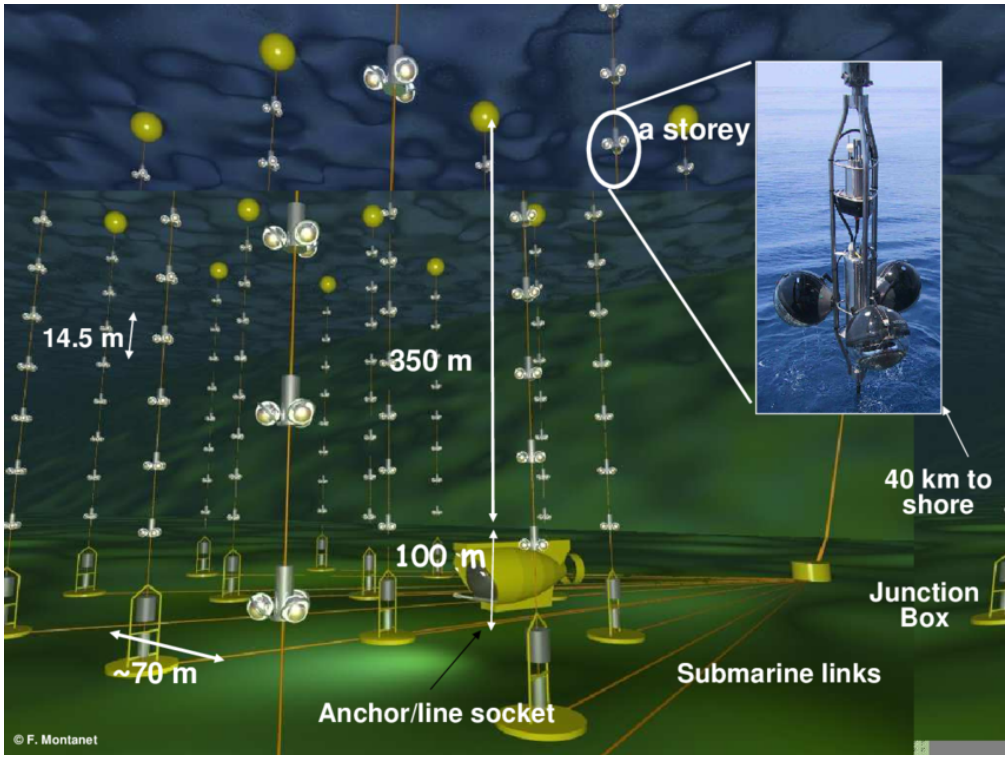

Figure 4.17.: Schematic picture of the ANTARES detector. From [143]

Both KM3NeT detectors, ORCA and ARCA, are built from the same detector core design. They only differ in their instrumented densities and instrumented volumes. Where the ORCA DOMs are 9 meters apart vertically and 20 meters horizontally, ARCA DOMs are 36 meters and 90 meters apart vertically and horizontally, respectively. The planned layouts of the lines are shown in Figure 4.18. This spacing difference results in the different energy ranges studied by either site.

4.2.4. Optical Background

In a seawater medium, a background light arises from the radioactive material, mostly from the potassium-40 as β decay [3]:

$$^{40}K \rightarrow {}^{40}Ca + e^- + \bar{\nu}_e$$

or electron capture:

$$^{40}K + e^- \rightarrow {}^{40}Ar + \nu_e + \gamma$$

both of these phenomena emit enough energy, of the order of the MeV, to induce the emission of Cherenkov light localized around an optical module. Moreover, this

[3] Other radioactive materials, such as Uranium and Thorium present in the module glass spheres, also contribute to this background.

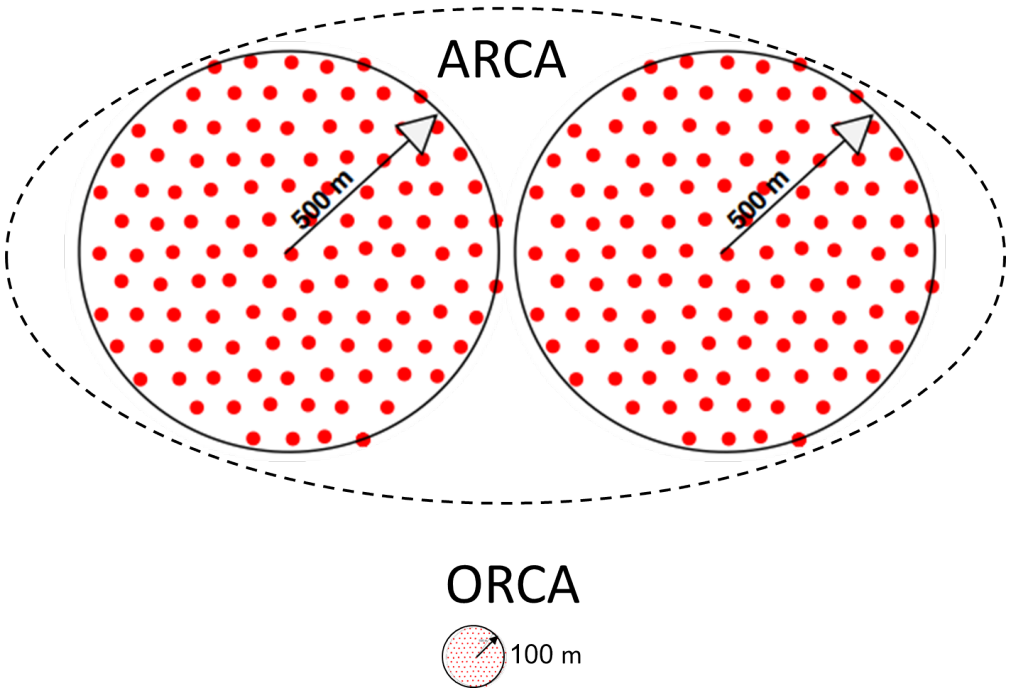

Figure 4.18.: ARCA and ORCA planned complete layouts. Red dots represent DU anchors.

radioactive background has a high enough rate to trigger the detector with coincident decays and be misreconstructed as a low-energy neutrino-induced event.

Another source of background light comes from bioluminescence, as bacteria and sea organisms emit a glowing light bright enough for it to be recorded in multiple PMT and to trigger the detector. Contrary to radioactivity, the intensity of the bioluminescence is variable and may depend on sea current, depth, and seasonal variation. To account for this optical noise that can repeatedly trigger the detector and pollute the recorded events, we introduce a High Rate Veto (HRV), a criteria that discards the data of DOMs whose trigger rates go above a threshold. A HRV fraction is subsequently defined as the fraction of time a DOM is vetoed, averaged over all DOMs in the detector.

4.2.5. Event triggering

The digitized data from PMT is sent from the detector to the shore in an *all-data-to-shore* strategy. All data however is not saved to disk, as the volume of raw data is largely dominated (>10^6 times) by background light. In order to filter out the bulk of background data, the assumption is made that photons from bioluminescence or radioactive decay are uncorrelated. The use of triggers based on correlations between photons is then applied on shore, in real-time during data taking.

In ANTARES, the trigger is done on multiple levels:

- **Level 0**: This corresponds to the raw data sent to shore. Analog signals sent by

the PMT are digitized with a TDC (Time-to-Digital Converter [148]) into a stream of binary data: when the amplitude of the PMT signal goes above a threshold of 0.3 photo-electrons, a level 0 **hit** is recorded with a Time over Threshold (ToT) corresponding to the duration until the PMT signal goes back under 0.3 photo-electrons.

- **Level 1**: When two level 0 hits are recorded from PMTs located on the same storey within 20 ns, or a PMT signal goes above a threshold of 3 photo-electrons, a level 1 hit is triggered.
- **Event triggering**: Multiple conditions are defined to trigger the recording of the data as an individual event.
  - *3N trigger*: > 5 pairs of Level 1 hits need to be recorded in a time compatible with the hypothesis that they are recorded light emitted by the same muon track.
  - *T3 trigger*: two level 1 hits needs to be recorded in 2 neighboring storeys.
  - *2T3 trigger*: within 2.2 microseconds, two T3 triggers are recorded in the same line, or four in the entire detector.

In KM3NeT, the trigger scheme follows a similar pattern:

- **Level 0**: The threshold condition of 0.3 photo-electrons is also applied.
- **Level 1**: Similarly than in ANTARES when two level 0 hits are recorded from PMT located on the same DOM within 25 ns, a level 1 hit is triggered.
- **Event triggering (Level 2)**: If multiple level 1 hits are recorded within a time window compatible with the hypothesis that they are causally related, they are bundled together and saved as a *triggered event* with every other Level 0 hit recorded in the same time window. The causality hypotheses are as follows:
  - *3DMuon*: > 3 level 1 hits on 3 different DOMs within a cylinder of 43 meters (in ORCA), > 4 level 1 hits on 4 different DOMs within a cylinder of 120 meters (in ARCA).
  - *3DShower*: > 3 level 1 hits on 3 different DOMs within a sphere of 52 meters in ORCA, 250 meters in ARCA.
  - *MXShower*: one level 1 hit and > 7 level 0 hits on 3 different DOMs within a sphere of 47 meters in ORCA, 110 in ARCA.

4.2.6. Simulations

Event simulation is performed with a chain including different steps: initial interaction, propagation of secondary particles and Cherenkov light, and response to the detector to light. Each step requires the use of dedicated algorithms, described in this section.

First, the neutrino interactions with the medium and their resulting secondary particles are generated through Monte-Carlo simulations, taking into account the cross-sections of the different processes involved. The neutrino interaction simulation is achieved using the GENHEN [149] program in ANTARES and KM3NeT. As GENHEN provides a neutrino energy threshold of around 10 GeV, another code gSeaGen [150] was developed for KM3NeT. It allows a lower energy threshold for the simulated neutrino. This is particularly useful for the ORCA detector which is sensitive to energies at the GeV level. This step allows the creation of sets of generated events that are passed down to the rest of the simulation chain.

The MUPAGE [151] code is used for the simulation of atmospheric muons propagated through multiple kilometers of seawater. This program is used both in ANTARES and KM3NeT.

Once the neutrino interactions have been simulated, the induced particle propagation, as well as the Cherenkov light emission and its propagation in water is simulated with the *KM3sim* package, based on the widely used GEANT framework [152]. Another light propagation algorithm, *JSirene* [153], was developed and is used in parallel with KM3NeT.

Finally, the detector response to Cherenkov light is simulated at the same time as the radioactivity background with dedicated routines from either detector.

The resulting events from the simulation chains are weighted to a desired flux spectrum to emulate an atmospheric spectrum or an astrophysical-like incoming flux. This allows the use of the same MC for multiple spectra hypotheses without the need to re-generate the sample. The generation weight is given for each event as:

$$w_{\text{gen}} = \frac{1}{N_{\text{Tot}}} \cdot I_E \cdot I_\theta \cdot T_{\text{gen}} \cdot A_{\text{gen}} \cdot N_\nu \cdot E^X \cdot P_{\text{scale}} \cdot P_{\text{Earth}}(E, \cos\theta) \tag{4.26}$$

where N_{Tot} is the total number of simulated incoming neutrinos, I_E is the generation spectrum E^{-X} integrated over the simulated neutrino energy range, I_θ is 1 for point or extended sources and $2\pi(\cos\theta_{\text{max}} - \cos\theta_{\text{min}})$ for a diffuse flux. T_{gen} is the simulated livetime. A_{gen} is the area of the generation surface, N_ν is the number of generated neutrino types, E^X is the inverse of the generation spectrum at neutrino energy E. P_{scale} is the GENIE interaction probability scale for events generated with gSeaGen and P_{Earth} is the neutrino transmission probability through the Earth at energy E and zenith angle θ.

MC events can then be simply weighted to a flux $f(E,\theta,\phi)$ with:

$$w_{\text{evt}} = w_{\text{gen}} \times f(E,\theta,\phi) \tag{4.27}$$

In ANTARES and KM3NeT, the simulation strategy follows a *run by run* scheme, where the calibration and conditions of each run are used as inputs for the simulating algorithms. It is in that sense similar to the RWS in HESS (section 4.1).

4.2.7. Detector calibration

In order to properly reconstruct the parameters of the primary neutrino, the time and position of the arrival of each Cherenkov photon, as well as the PMT response to Cherenkov light need to be assessed with great precision. To achieve that, calibration procedures are performed regularly and follow the same pattern in both detectors, with a few differences in the instrumental design [154].

Position calibration Sea currents induce a displacement of the detectors' modules that translates into a distortion of the array. The position of each module is measured by acoustic systems, with acoustic emitters located at the line anchors[4] and others at some distance from the detector [155, 156]. Emitters send an acoustic signal that is received by hydrophones located on the modules, whose location can be determined by triangulation of the time delay measured by the hydrophones. This allows the positioning precision of each module to be within 10 cm. Additionally, modules are equipped with compasses and tiltmeters to measure their rotations around the vertical and horizontal axes, respectively. This allows for a proper estimation of the orientation of each PMT.

Time calibration The times of PMT hits need to be estimated with relative precision on the order of the nanosecond in order to perform a reconstruction with sufficient precision. As such, the time delays between the arrival of light and the recording of a signal are calibrated before deployment in a controlled environment. However, the properties of the detector electronics can drift over time which means that the timing synchronicity needs to be regularly calibrated. Multiple calibration methods coexist in ANTARES [157] and KM3NeT [158]. First, the synchronization between multiple PMT of the same storey or DOM (respectively in ANTARES and KM3NeT) takes advantage of the background light from ^{40}K radioactive decay, as a decay product Cherenkov light can trigger multiple nearby PMT. This method allows to determine the time delay between PMT, as well as its uncertainty due to their transit time spread. The next method uses a pulsed light emitted from underwater LED beacons [159, 160] during dedicated calibration runs. This allows to determine the time delay between multiple modules and the uncertainty due to light scattering in seawater. A final method can be used after the reconstruction of tracks induced by atmospheric muons (subsection 4.2.8). The accuracy of the calibration can then be checked by comparing the arrival time of Cherenkov light on an element of the detector to the expected arrival time from the reconstructed track.

Charge calibration This calibration step is necessary in order to translate PMT signals into numbers of photoelectron [161], and to tune the PMT High-Voltage to ensure that the PMT pulse amplitudes match the pre-defined hit threshold of 0.3 photo-electron. The relation between the ToT and the number of photo-electrons is

[4] Positions of the anchored instruments are determined with GPS during deployment.

measured under the assumption that the majority of hits are single photo-electrons, after which the peak of the ToT distribution is set to correspond to 1 photo-electron. Similarly to the time calibration, measurements are performed before deployment to obtain nominal values and are then re-assessed during dedicated calibration runs. This allows to take into account the loss of performance over time of the electronic components.

4.2.8. Event reconstructions

Reducing the calibrated PMT data from an event into the parameters of the primary particle (such as its direction, the location of the interaction vertex, or its energy) is a complex computation due to the non-linearity of the problem, or to the unrelated hits recorded in the event. The event parameters reconstruction algorithms then usually follow multiple steps. These include initial rough estimations of the results (pre-fits), removal of the hits causally incompatible with the initial event estimation, and fits of increasingly complex functions each taking the results of the previous ones as starting points. Algorithms are designed assuming a given topology, track or shower, and each event can be reconstructed both as a track and shower. The real event topology is deduced by comparing the quality of each reconstruction.

4.2.8.1. Track reconstruction is ANTARES

The two main methods for reconstructing the event parameters from the data are known as AAfit [162] and BBfit [163]. The latter provides a faster execution time making it more suited for quick, real-time reconstruction. On the other hand, the AAfit algorithm yields better performances and is described in the following, as it is the one used in the analysis of this thesis.

The AAfit algorithm includes multiple steps: a linear pre-fit, an M-estimator pre-fit, and a maximum-likelihood pre-fit. The pre-fit steps are performed multiple times (9) using randomly distributed starting track directions. The last step is a final maximum-likelihood fit.

The final likelihood function $\mathscr{L}$ is defined as the product of the individual hit likelihood to be associated with a given track $P = P(t_i|t_i^{th}, a_i, b_i, A_i)$. , where the variables of the likelihood are: t_i the time of hit i, t_i^{th} the theoretical arrival time of the photon from the track, a_i the expected angle of incidence of the photon on the OM, b_i the expected photon path length, and A_i the amplitude of the hit.

The quality of the likelihood fit can then be given by the following value:

$$\lambda_{\text{AAfit}} = \frac{\log(\mathscr{L}_{\text{max}})}{N_{\text{hits}} - 5} + 0.1 \times (N_{\text{comp}} - 1) \tag{4.28}$$

with $\mathscr{L}_{\text{max}}$ the maximum value of the likelihood, N_{hits} the number of hits in the fit, subtracted by 5 to get the number of degrees of freedom, and N_{comp} the number of times the repeated initial steps of the reconstruction converged to the same result within 1°. The latter can go from 1 for events with a poor reconstruction to 9 for

well-reconstructed events. The coefficient 0.1 was chosen to maximize the separation in λ between simulated signal and misreconstructed downgoing muons [164].

The track angular error β_{AAfit} can then be estimated as:

$$\beta_{\text{AAfit}} = \sqrt{\sigma_\phi^2 \sin^2(\theta) + \sigma_\theta^2} \tag{4.29}$$

with σ_ϕ and σ_θ the errors on the azimuth and zenith angles estimated from the error covariance matrix **V** around the maximum likelihood:

$$[\mathbf{V}]_{ij} = -\frac{\partial^2 \log(\mathscr{L})}{\partial x_i \partial x_j} \tag{4.30}$$

where x is the vector of fitted track parameters.

The energy of the event can be estimated from the muon energy loss dE/dX with the energy deposited in the detector [165] as:

$$\frac{dE}{dX} \approx \frac{\sum_i Q_i}{\epsilon(\vec{x})} \frac{1}{L_\mu(\vec{x})} \tag{4.31}$$

where $\epsilon(\vec{x})$ is the light detection efficiency, Q_i is the charge recorded by the i-th hit fulfilling the causality condition that it was caused by a Cherenkov photon compatible with the reconstructed track. Finally, L_μ is the reconstructed track length within the detector instrumented volume, defined as the actual detector volume extended by 110 meters (twice the light radiation distance in seawater). Neutrino energy is then estimated from this energy loss with the use of MC.

4.2.8.2. Shower reconstruction in ANTARES

In the case of a shower event topology, the location of the interaction vertex can be reconstructed in addition to the shower direction. The ANTARES Collaboration uses 2 algorithms to determine the shower, and subsequently the primary neutrino, parameters.

The first algorithm, TANTRA [166, 167], relies on two steps: vertex position and then shower direction determination. The vertex position is estimated by filtering out the events that can not be causally related with a similar source, then fitting:

$$(\vec{r}_i - \vec{r}_{\text{shower}})^2 = (c/n)^2 \times (t_i - t_{\text{shower}})^2 \tag{4.32}$$

with $\vec{r}_i$ and t_i individual hit position and time, $\vec{r}_{\text{shower}}$ and t_{shower}, the fitted shower position and time, and c/n the speed of light in water. A final fit, taking into account the charges of the hits is performed with an M-estimator:

$$M = \sum_i \left(q_i \times \sqrt{1 + t_{\text{res,i}}^2/2} \right) \tag{4.33}$$

where q_i is the charge of the i-th hit and $t_{\text{res,i}}$ is its time residual i.e. the difference between its recorded and expected times.

The shower energy and direction are then fitted using a maximum-likelihood method.

The second algorithm, named Dusj [168], includes a χ^2 pre-fit followed by a maximum-likelihood fit. Its main difference from the previous algorithm resides in the use of an event classification with a Random Decision Forest algorithm.

4.2.8.3. Event reconstruction in KM3NeT

In KM3NeT, a different algorithms chain is employed to fit data to a Cherenkov light cone hypothesis, as described in [169]. A pre-fit (*JMuonPrefit*) is performed with a χ^2 minimizer based on the time difference between the photon arrival time and its expected arrival time from a given trajectory hypothesis. The pre-fit is performed with multiple initial guesses (around 100) on the track directions.

The results of these pre-fits are given to the main algorithm *JMuonGandalf* which performs a search around them. It is a maximum-likelihood search of hit clusters compatible with a track direction and with a likelihood function described by a set of PDF of the PMT response to a muon track hypothesis. This PDF, computed semi-analytically, is the probability of observing each measured hit at a time Δt of its expected value from the track hypothesis. It is parametrized from the minimum distance of the muon to the PMT, and their respective orientations. An example of such parametrization is given in Figure 4.19.

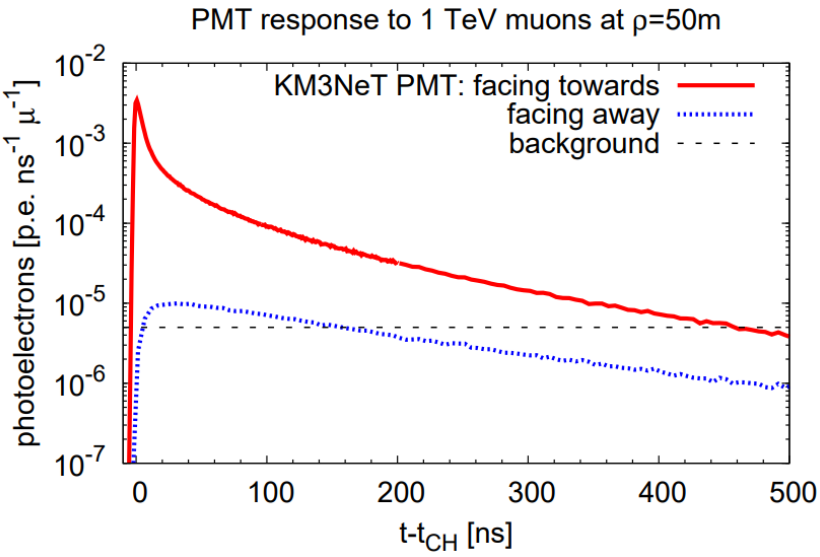

Figure 4.19.: Expected number of photons hitting a PMT per nanosecond, for a 1 TeV muon track 50 meters from the PMT facing toward it (red), and away from it (dotted) line). Hits originating from the background at a rate of 5 kHz are given as reference (dashed). From [169].

The *JMuonStart* step reconstructs the earliest photons compatible with the fitted Cherenkov cone, thus finding a starting point of the track, from which its length can

be determined. We note that this starting point might be the interaction vertex or the furthest point the track can be detected above the background.

Finally, the muon energy is estimated using the *JMuonEnergy* step with another likelihood fit on the intensity of the hits recorded in a cylindrical volume around the previously reconstructed track direction. The likelihood is then given as a function of muon energy as:

$$\ln(\mathscr{L}(E)) = \sum_{i=1}^{N} \ln\left[(1-2e^{-\mu_i(E)})\mathbf{I}_{n>0} + e^{-\mu_i(E)}\right] \tag{4.34}$$

where N is the total number of PMT in the cylinder, $\mathbf{I}_{n>0}$ is 1 for $n>0$ and 0 otherwise, $\mu_i(E)$ is the expected number of hits in the i-th PMT for muon energy E and n the number of recorded hits.

Showers are also reconstructed using dedicated algorithms. These reconstructions are however not used in this work. More details can be found in [169] for shower reconstruction with ARCA and [170] for shower reconstruction with ORCA.

4.3. Other telescopes

Among the facilities contributing to the domain of high-energy astronomy, we can mention hard X-ray/γ-ray space telescopes such as *Granat* which operated from 1989 to 1999 and was able to monitor the sky from 4 keV to 100 MeV with its variety of instruments. Similarly, *INTEGRAL*, launched in 2002 and still in operation, can study the γ-ray sky up to 10 MeV with its imager *IBIS* and its spectrometer *SPI*. In the VHE domain, other IACTs are observing the sky from the northern hemisphere: MAGIC, located in La Palma in the Canary Islands, and VERITAS, located in Arizona, United States. Additionally, operating with 1 telescope at the time of writing, the future Cherenkov Telescope Array (*CTA*)) will reach better sensitivity from ~ 20 GeV to more than 200 TeV from both hemispheres thanks to its 60 telescopes planned both in La Palma and Chile. Another technology for astronomy in the TeV range, the water Cherenkov method, is used by facilities such as HAWC, completed in 2005 in Mexico, or LHAASO, completed in 2019 in Sichuan, China. This method can reach photon detection to energy to ~ 1 PeV but offers a lower instantaneous sensitivity than IACTs due to its non-pointing observation technique.

The rest of this section briefly describes instruments whose data take a significant place in the work developed in this thesis.

4.3.1. FERMI/LAT

The Large Area Telescope (LAT) is a high-energy γ-ray telescope, sensitive from 20 MeV to 300 GeV, onboard the *Fermi Gamma-Ray Space Telescope* [171] located on low Earth orbit. With a 2.4 steradian FoV it was initially able to perform an all-sky scan every 3 hours (two Earth orbits). However, since March 2018 an issue has prevented a solar panel from rotating, which prevents a complete scan during certain periods. It is

a pair conversion detector, meaning incoming photons are converted in an electron-positron pair as seen in Figure 4.20. The telescope is built as an array of 4-by-4 modules that include a tracker of charged particle directions and a calorimeter to determine their energy. The parameters of the primary photon are determined from the electron-positron pair reconstructed parameters.

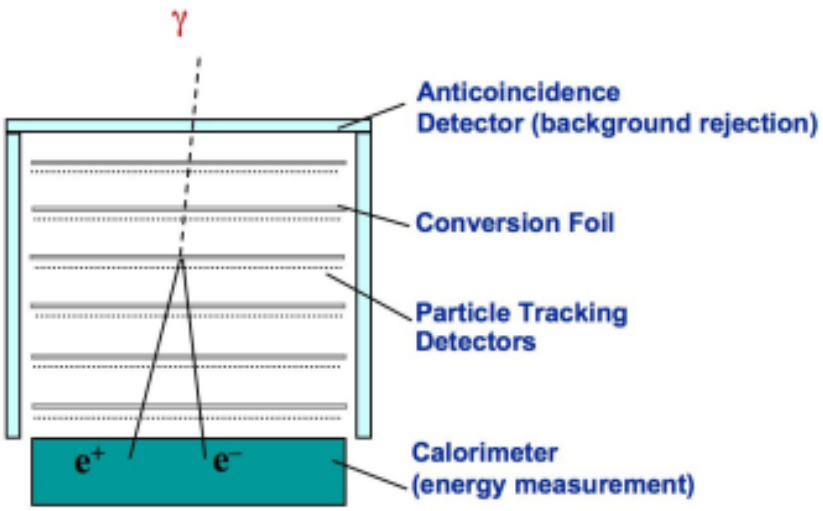

Figure 4.20.: Schematic of a LAT module. An incoming γ-ray is shown passing through the anticoincidence detector without triggering it. It is then converted into an electron-positron pair in a Tungsten sheet. Its direction is then tracked in the plate detectors. The pair's propagation is stopped in the calorimeter where its deposited energy is used to compute the energy of the photon. Credit: Fermi/LAT Collaboration[5].

Each tracker is made of 19 layered plates of semiconductor Silicon strips arranged in alternating directions to track the path of the electrons. In order to induce pair production, a process more efficient in a dense material, layers of Tungsten foil are inserted between the Silicon tracker plates. The 12 first Tungsten sheets are 0.3 mm thick, and the next 4 are 0.72 mm thick. A pair produced in the former layers is classified as *Front*, while a pair produced in the lower layers is classified as *Back*. Front events have a better angular resolution thanks to the larger number of plates measuring the electron's path. The last 3 tracker layers do not have a Tungsten converter sheet, as it was estimated that the angular resolution of such an event would be too poor. The electron energy is measured with a calorimeter made of Cesium Iodide to induce the production of an electromagnetic shower and the measurement of its topology. Additionally, the telescope is covered with a plastic scintillator to act as an anticoincidence detector to discriminate incoming γ from the dominating background flux of charged particles. Charged particles, contrary to photons, are indeed able to induce

[5] www-glast.stanford.edu/instrument.html

the emission of light in the scintillator which acts as a veto for the event in the case of a coincident signal in the Silicon trackers.

Performances of the telescope are shown in Figure 4.21. We can see that the 95% containment angle of a 100 MeV photon is 10°, and it drops to ~ 0.4° at 100 GeV. The effective area reaches ~ 1 m^2 at 1 GeV. Moreover, the higher quality of *Front* events can be seen with respect to *Back* events, as the former have a high effective area, and better angular and energy resolutions.

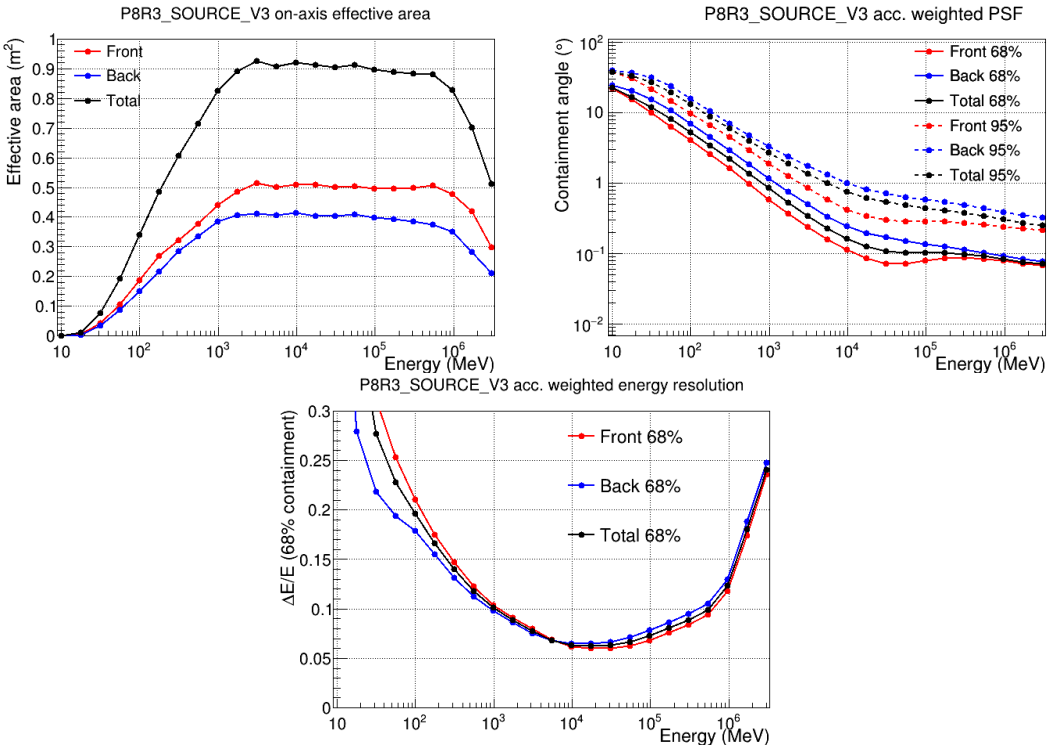

Figure 4.21.: LAT performances as a function of the photon energy, for Front events (red), Back events (blue), and all events (black). Left: Effective Area of on-axis (aligned with the tracker direction) photons. Right: Acceptance-weighted PSF, shown as the 68% and 95% containment angles of the direction error. Bottom: Acceptance-weighted energy resolution, defined as the 68% containment half width of the reconstructed photon energy. Figures from the Fermi/LAT IRFs public description[6].

4.3.2. NICER

The Neutron star Interior Composition ExploreR (NICER [172]) is a soft X-ray telescope onboard the International Space Station since 2017. It is a non-imaging pointing instrument sensitive to photons from 0.2 to 12 keV with a FoV of 5 arcmin. Its main detector is the X-ray Timing Instrument (XTI) which is an array of 56 independent

[6] slac.stanford.edu/exp/glast/groups/canda/lat_Performance.htm

modules that each concentrate photons into a silicon detector. Its principal mission is timing studies, with a time resolution below 300 ns, and the telescope is sensitive to faint sources, around 10^{-6} Crab for a 10ks exposure.

4.3.3. Swift/BAT

The *Neil Gehrels Swift Observatory* is a space observatory whose primary mission is the detection and rapid follow-up observations of GRB. It includes on board 3 instruments: the X-Ray Telescope (XRT), which is a soft X-ray pointing telescope sensitive to energies from 0.2 to 10 keV, the UltraViolet/Optical Telescope (UVOT), and the Burst Alert Telescope (BAT). The latter is briefly described in this section. In order to accomplish its primary mission, the Swift Observatory uses the BAT to determine the position of any possible GRB in its FoV with the GRB hard X-ray emission. The telescope then automatically slews toward the location of the GRB candidate and observes for a soft X-ray counterpart with XRT, which is also used to improve the localization of the GRB. UVOT is also observing, to detect the afterglow of the GRB.

Swift/BAT is a large FoV telescope [173], with sensitivity to a fourth of the sky at any time. The telescope is sensitive in the hard X-ray range (15 to 150 keV) with an average PSF of 17 arcmin and a 1.4 steradian FoV. Its sensitivity for a full-day observation reaches 5.3 mCrab and it observes around 90% of the sky each day.

Encoded images are formed on a CdZnTe detector with a coded mask composed of 50,000 lead tiles 1 meter above the detector plane. Patterns in the detector are then deconvoluted from the mask topology in order to recover the position and luminosity of the source. This method allows the formation of images with hard X-ray photons in an energy range where light focusing is difficult to achieve.

The analyses developed in this manuscript rely on the BAT Transient Monitor [174]. This monitor allows the BAT instrument to go beyond its main scientific goal of detection of GRBs and provides monitoring of close to a thousand hard X-ray sources. The hard X-ray fluxes in the 15-50 keV range of these sources are then measured and reported publicly multiple times a day to obtain long-term lightcurves.

4.3.4. MAXI/GSC

The Monitor of All-Sky X-Ray Image (MAXI)[175] is an instrument installed on the International Space Station since 2009 whose main scientific goal is the detection of transient X-Ray events. It is composed of 2 sub-detectors: the Gas Slit Camera (GSC), sensitive in an energy range of 2 to 30 keV, and the Solid-State Camera (SSC), sensitive from 0.5 to 12 keV. The detector is able to monitor the full sky with each ISS orbit of 96 minutes with a sensitivity of 20 mCrab, and a PSF angle of around 0.2°. The work in this thesis uses the X-ray flux measured by the GSC. It is made publicly available in 3 energy bands which can be used to monitor the spectral evolution of the sources: 2-4 keV, 4-10 keV, and 10-20 keV. Similarly to Swift/BAT, this monitoring is updated multiple times a day and is available in orbit and day averages.

4.3.5. RXTE

The Rossi X-Ray Timing Explorer is a space observatory that operated from 30 December 1995 to 12 January 2012 [176]. Its instruments were:

- **All-Sky Monitor (ASM)**: Large FoV telescope, with 80% of the sky scanned every 90 minute orbit. Its sensitivity was around 30 mCrab in a 1.2 to 12 keV band, with an ellipsoidal PSF of around 3 by 15 arcminutes. It was built with 3 gas (Xenon) proportional counters. Similarly to Swift/BAT and MAXI/GSC, a long-time lightcurve of several sources is publicly available and is used in this thesis, can be accessed in 3 energy ranges: 1.2-3 keV, 3-5 keV, and 5-12 keV.
- **Proportional Counter Array (PCA)** Collimator sensitive at 0.1 mCrab in a 2 to 60 keV band and a 1° FHWM PSF. Suited for source timing measurement, with a temporal resolution of the order of a microsecond.
- **High Energy X-Ray Timing Experiment (HEXTE)**: Hard X-Ray (12 to 250 keV) collimator with a 1° FoV.

Part II.

Search for a high energy emission from microquasars

Contents

Introduction

This part presents a multi-messenger, multi-wavelength search for markers of particle acceleration to very high energy in microquasars. Considering the fact that microquasars are transient sources where periods of intense outbursts occur between periods of quiescence, we assume for this search that this acceleration takes place during outbursts, where a high X-ray flux denotes an intense accretion-driven heating of matter near the compact object, and associated ejecta in the form of a compact jet or discrete launches. This environment provides suitable conditions for the appearance of shocks, as seen in the non-thermal X-ray spectral distribution. The restriction of the search in time windows where particle acceleration is more likely also allows us to reduce the background noise contribution from quiet periods in the analyses. Our search then focuses on X-ray flares detected in the continuous monitoring of sources by large field-of-view X-ray telescopes. Furthermore, subdivisions of these time periods are drawn to take into account the variability of the multi-wavelength behavior of microquasars related to the underlying physics. After a presentation of the sources in chapter 5, the determination of relevant periods from X-Ray data is defined in chapter 6. Then, a search for γ-rays is performed, in the VHE range (100 GeV to 100 TeV) from HESS observations in chapter 7, and in the HE range (100 MeV to 100 GeV) with the Fermi/LAT telescope chapter 8. The analysis is then carried out in the domain of neutrino astronomy with the ANTARES and KM3NeT/ORCA detectors in chapter 9. With the addition of MWL data, studies of SED modeling of a few states of some sources are shown in chapter 10. Finally, a system of automatized monitoring of microquasar activity in X-ray, HE γ-ray and neutrino, and its implementation in the observation strategy of HESS is shown in chapter 11.

5. Studied sources

For this study, we have selected sources presenting periods of clear X-ray flaring, with X-ray spectra and luminosities following the characteristic cycle on a HID diagram as shown in section 3.3. This behavior is generally correlated with the presence of relativistic compact jets and with discrete ejections of matter during spectral state transitions. These matter ejections could provide suitable particle acceleration sites for the emission of significant γ-ray and neutrino fluxes by the acceleration of particles in shocks.

13 microquasars, all LMXBs, were found to follow these criteria and are visible with ANTARES and HESS. They are listed in Table 5.1, with their coordinates, estimations of the masses of their compact objects and companion stars, and distances. A skymap showing our sources in galactic coordinates is given in Figure 5.1.

Source	Dec (deg)	RA (deg)	$M_{CO}/M_{\odot}$	M_*/M_{CO}	Dist. (kpc)	Refs.
IGRJ17091-3624	-36.407	257.282	8.7	-	10.4-14.6	[177]
XTEJ1550-564	-56.458	237.757	7.8 -15.6	~ 0.03	4.5 $\pm$0.5	[178]
V4641 Sgr	-25.407	274.84	6.4 ± 0.6	0.63 - 0.70	6.2 $\pm$0.7	[179]
AqlX1	0.585	287.817	1.23	-	2.74-8.77	[180]
4U1630-472	-47.394	248.502	10.0	-	4.7-11.5	[181]
GRS1915+105	10.945	288.798	11.2 $\pm$2	0.042 $\pm$0.024	9.4 $\pm$0.8	[182]
V404 Cyg	33.867	306.016	9	0.067 ± 0.005	2.39 ± 0.14	[183] [184]
H1743-322	-32.234	266.565	15	-	7.7-9.3	[185]
GX339-4	-48.789	255.706	2.3 - 9.5	0.18 ± 0.05	> 5	[186]
MAXIJ1820+070	7.1856	275.091	5.71-8.10	0.07$\pm$0.01	2.96$\pm$0.33	[187]
MAXIJ1535-571	-57.23	233.832	10.39	-	4.3-7.2	[188]
MAXIJ1348-630	-63.274	207.054	8.7	-	3.01-3.77	[189]
GRS1716-249	-25.017	259.904	4.9-8.0	-	2.4 $\pm$0.4	[190] [191]

Table 5.1.: List of studied sources. Dec and RA are Declination and Right Ascension in the J2000 epoch. M_{CO} is the mass of the compact object, given in units of solar masses $M_{\odot}$. M_*/M_{CO} is the ratio between the mass of the companion star of the binary system and the mass of the compact object.

All these sources host Black Holes or Black Hole candidates, with the exception of Aql X1. It was however decided to have this last source in the selection as it exhibits a disk-jet coupling very similar to the one observed in a Black Hole LMXB [192].

More information and references about the objects can be found in the catalogs

XRBcats[1] and BlackCAT[2].

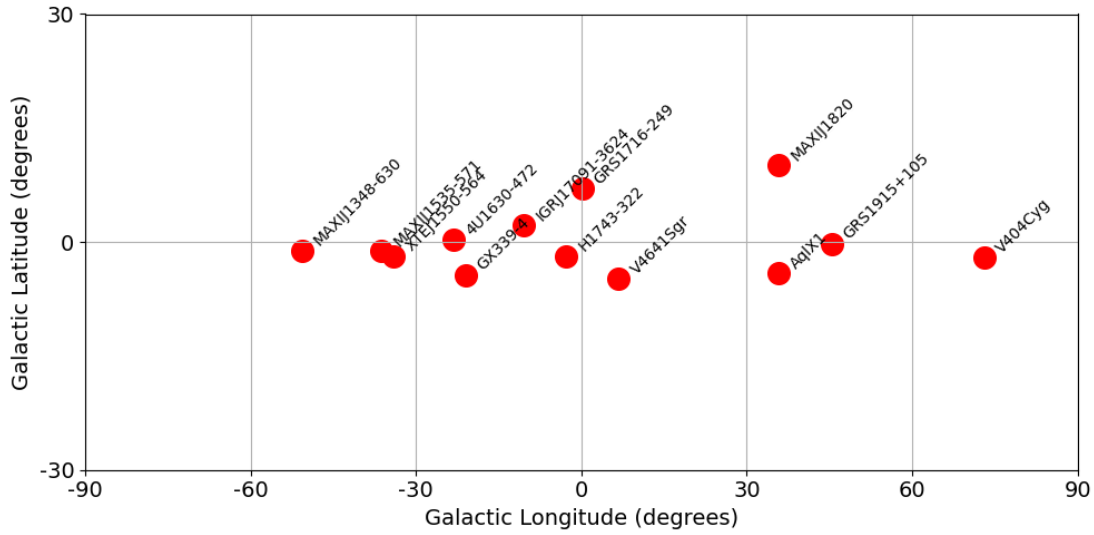

Figure 5.1.: Galactic sky map of our source list.

[1] http://astro.uni-tuebingen.de/~xrbcat
[2] https://www.astro.puc.cl/BlackCAT/

6. Time periods determination from X-Ray telescopes

The base for this study is the X-ray monitoring data from the large FoV telescopes RXTE/ASM, MAXI/GSC, and Swift/BAT. We give a description of data availability:

- **RXTE/ASM data** are retrieved from the following link: xte.mit.edu/asmlc/ASM.html. Available data range from 20/02/96 to 01/01/2012 (MJDs 50133 to 55927), with photon energy between 2 and 10 keV. Each data point is the one-day averaged flux measured from the source, with errors computed as the quadrature average of the estimated errors on the individual observation made of the source on that day (typically between 5 and 10). The data are given as counts per second fitted from the source over an expected background. We convert the flux in Crab units with the count rate given by the ASM team of 75 counts per second from the Crab nebula.

- **MAXI/GSC data** are retrieved from the following link: maxi.riken.jp/top/slist.html. Available data starts at 08/08/2009 (MJD 55051) and are updated multiple times a day at the time of writing this thesis. The data are available as a flux in photons/s/cm2 in an energy band between 2 and 20 keV, split into 3 bands: 2-4 keV, 4-10 keV, and 10-20 keV. The reference flux for the Crab Nebula is given at 3.8 photons/s/cm2 in the 2-20 keV band. The data points are given with the background subtracted, which can lead to negative values and, more notably, flare-like profiles in periods where the background rate is mischaracterized, which can happen near Sun occultation or during movement of the ISS solar panels. The used data are daily lightcurves, which is the average measurement of the source over 24h, one measurement being approximately 60 seconds, every 92 minutes. We can define the hardness ratio of a source as the ratio between the fluxes in the 4-10 keV band and the 2-4 keV band.

- **Swift/BAT data** are retrieved from the BAT Transient Monitor [174] on the following link: swift.gsfc.nasa.gov/results/transients. Data are available from 12/02/2005 to today, in an energy range between 15 and 50 keV. Data are available in count/s/cm2, and we convert it to a Crab flux from the given reference flux of 0.22 count/s/cm2 for the Crab Nebula. The Swift/BAT team gives error bars computed from the systematic study of the Crab Nebula and from error estimation of the background rate from blank positions in the sky i.e. positions without any reported X-ray source in a 10 arcminutes radius. We select the

lightcurves as daily data points, which are averages of observations made during a UTC calendar day.

This section describes the time window determinations from the daily lightcurves that are used in the following sections. We first determine flaring periods as time windows where the source exhibitedhigh level of X-ray activity. Then, we select additional time windows, with the goal to select periods where a source is in a definite X-Ray spectral state, in order to build SED with consistent measurements. A particular consideration is given to periods in which observations were made with HESS.

6.1. Flaring periods

Flaring periods are determined as time windows where the flux is measured significantly above the usual source baseline[1]. An estimation of the average baseline rate and its standard deviations for each source and telescope is performed with a Gaussian fit of the daily averaged rates of the lightcurves. An example of this fit of the distribution of the daily flux of GX339-4, as measured by RXTE/ASM is shown Figure 6.1. A Gaussian is fitted to the first bump, around 0, in the distribution and its mean value characterizes the baseline of the GX339-4 ASM lightcurve. The second bump, around 0.3 Crab units, arises from the daily rates data points when the source is flaring in the ASM band.

The selection of the flaring periods is done in two steps: first, we select a set of high-significance data points, and then we run down from these points to lower-significance points that mark the boundaries of the flaring time periods.

To obtain our set of high-significance data points, daily flux averages are retained from the lightcurves that verify:

$$F - \Delta F > \mu_{\mathrm{BL}} + 8\,\sigma_{\mathrm{BL}} \tag{6.1}$$

with F the flux given by the daily data-point and ΔF its corresponding error, μ_{BL} and σ_{BL} the mean and standard deviation of the Gaussian fitted baseline. The value of 8σ above baseline was chosen empirically in order to filter out any potential minor flare or flare-like periods coming from background mischaracterization. Furthermore, to account for possible instrumental effects, data points verifying this criterion are removed if they are not accompanied by another selected point in a $\pm$ 5-day time window. This allows us to remove any singled-out high-significance point that might be most likely coming from an instrumental error that was not accounted for. We note that while this filter might remove any short, burst-like flare, it is more relevant to focus our study on longer flares that are usually observed in microquasars. However, as the data processing is fully automated for the X-ray lightcurves, systematic effects may still be present.

[1] The baseline value is compatible with 0 in the case of a source in complete quiescence if the contribution from the background is properly removed from the measurement by the automatic processing of the respective telescopes.

The resulting high-significance data points are used as seeds to search for flaring time windows: starting from each point, the flaring period is defined by the time window in which the flux verifies

$$F - \Delta F > \mu_{\mathrm{BL}} + 2\sigma_{\mathrm{BL}} \tag{6.2}$$

in at least 1 point in a 5-day sliding time window starting from each high-significance data point. The 5-day length of the window is chosen to take into consideration any missing daily data points. Moreover, the loose 2σ above the baseline threshold was chosen in order to select time windows that completely frame the X-ray outbursts.

The final flaring periods considered in the analyses for a given source are then simply the time windows where at least one of the lightcurve of the source fulfills the criteria.

An example of the flaring periods can be found in Figure 6.2 for GX339-4 with the ANTARES, ORCA6, and HESS observations highlighted. Similar figures for all studied sources can be found in Appendix section A.

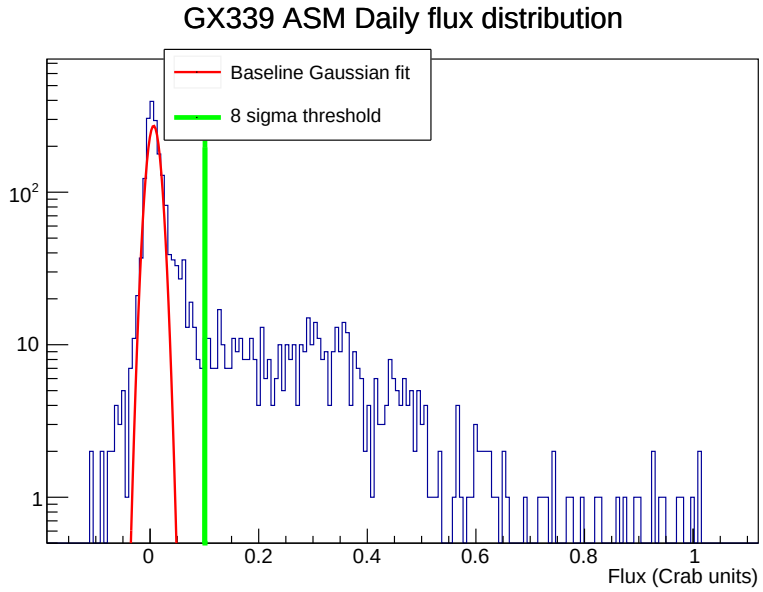

Figure 6.1.: Distribution of daily flux of GX339-4 measured with RXTE/ASM, in Crab units. A Gaussian fit of the baseline is shown in red. And the 8σ threshold for high-significance data points is given in green.

6.2. Additional time windows

Microquasar spectra exhibit high variability during a flare. In order to correlate our results to MWL data and draw SED that can meaningfully be interpreted as representing a given phenomenological state of the system, we define more restricted time

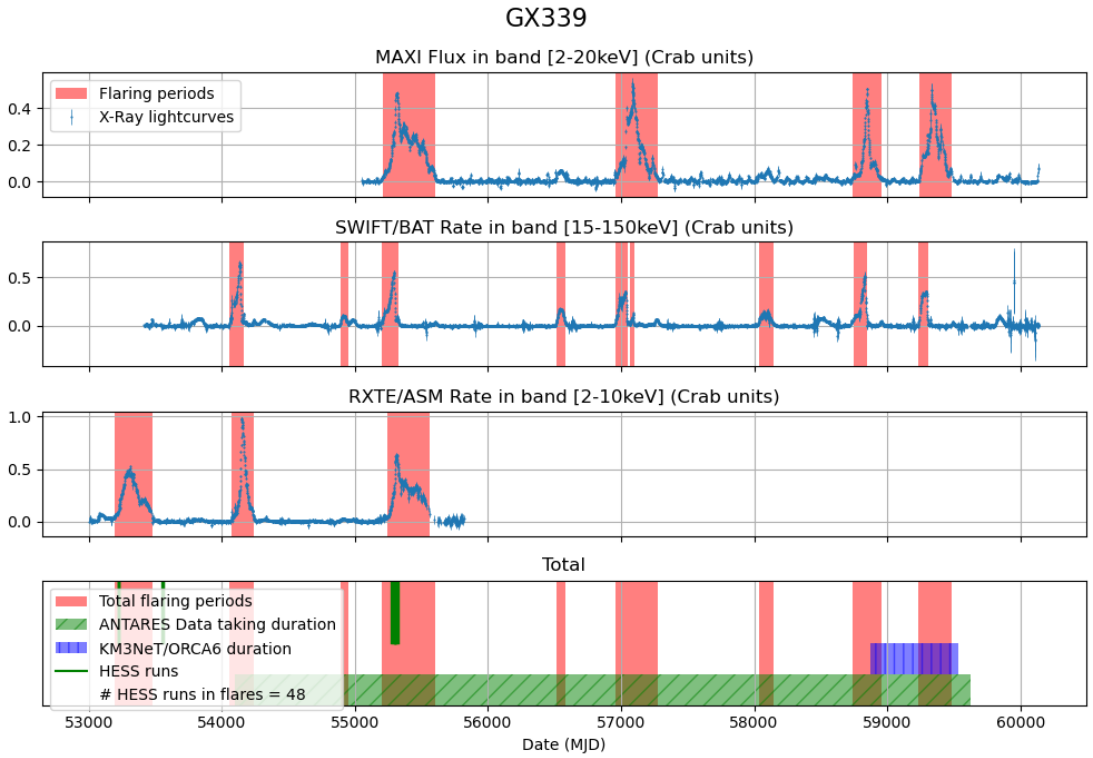

Figure 6.2.: X-Ray lightcurves from GX339-4, recorded by MAXI/GSC, Swift/BAT, and RXTE/ASM. Flaring periods are highlighted in red. The ANTARES data-taking duration is represented as a green horizontal band and the KM3NeT/ORCA6 data-taking duration is represented as a blue band. HESS observation times are given as green vertical lines. The total flaring periods are a stacking of the flaring periods in each telescope.

windows representing well-defined X-Ray spectral states, state transitions, and/or in an X-Ray state compatible with a one in which observations were taken with HESS.

For sources MAXIJ1820+070 and GX339-4, we define 3 subdivisions of the flaring periods, each corresponding to a given X-Ray spectral state: the HS, Hard-to-Soft ST, and SS. This is motivated by the fact that these sources exhibit different phenomenologies and multi-wavelength properties in each state, and high-energy γ and neutrino fluxes are expected to also differ, as described in section 3.2.

For MAXIJ1820+070, which went through a single major period or outburst, the definition of periods is taken from [193], as seen in Table 6.1 from [1], rounded to the floor/ceiling Modified Julian Day (MJD) for the beginning/end of the period. They are as follows, given in MJD: Hard State from 58189 to 58304, State Transition from 58304 to 58311, and Soft State from 58311 to 58380.

GX339-4 exhibits regular flares and state transitions. The spectral states were divided using X-ray hardness ratios from RXTE/ASM and MAXI/GSC, with total livetimes of 248, 30, and 634 days for the HS, ST, and SS respectively. These periods are shown in

Source state	Start [MJD]	End [MJD]	Start [Gregorian]	End [Gregorian]
Hard State I	58189.0	58303.5	12 Mar. 2018	4 Jul. 2018
HS → SS	58303.5	58310.7	4 Jul. 2018	11 Jul. 2018
Soft State	58310.7	58380.0	11 Jul. 2018	19 Sep. 2018
SS → HS	58380.0	58393.0	19 Sep. 2018	2 Oct. 2018
Hard State II	58393.0	58420.0	2 Oct. 2018	29 Oct. 2018

Table 6.1.: Starting and ending times used for each X-ray state of MAXI J1820+070, based on the results of [193] Hard State I and II refer, respectively, to the initial and final states of the source, during its 2018 outburst. Table extracted from [1].

Appendix B as lightcurves and hardness ratios.

Time periods coinciding with HESS observations

- **GRS1915+105**

As this source was in a high activity and high variability state for most of ANTARES and HESS operations, we chose to focus our search around HESS observations that took place in a plateau state in the Swift/BAT range after a re-brightening. The selected time window ranges from MJD 54569 to MJD 54737, as shown in Figure 6.3.

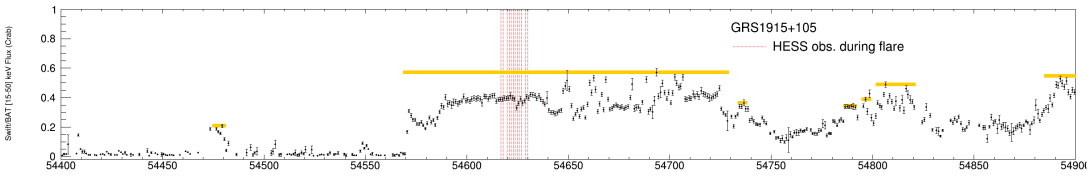

Figure 6.3.: GRS1915+105 Swift/BAT lightcurve, zoomed around HESS observations. Nights of HESS observations are represented by vertical red dashed lines. The flaring time windows are represented by horizontal yellow lines. For this study, the selected time window is the flaring period containing the HESS observations.

- **MAXI J1535-571** and **MAXI J1348-630**

These two sources were observed while in state transition with HESS. For this study, we focus our search on time windows framing HESS observations, as shown in Figure 6.4 and Figure 6.5:

- MAXIJ1535-571: MJD 58006 to MJD 58018
- MAXIJ1348-630: MJD 58518 to MJD 58521

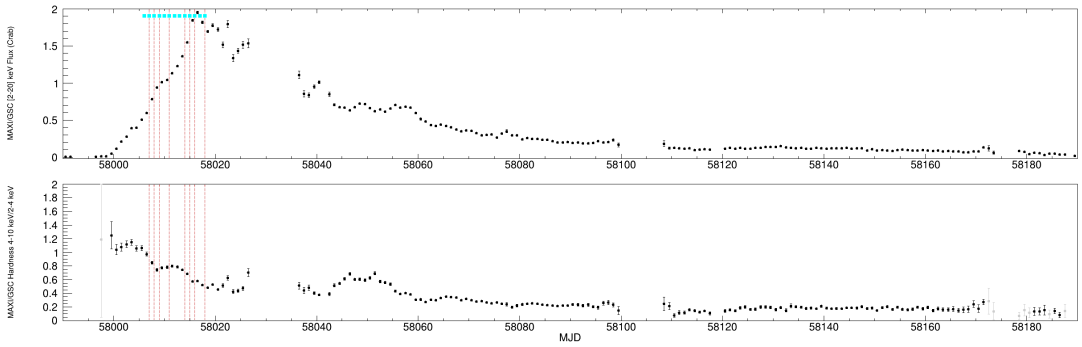

Figure 6.4.: MAXI/GSC lightcurve and hardness ratio for MAXIJ1535-571 focused around HESS observations. Nights of HESS observations are represented by vertical red dashed lines. Studied time windows are highlighted by blue horizontal lines.

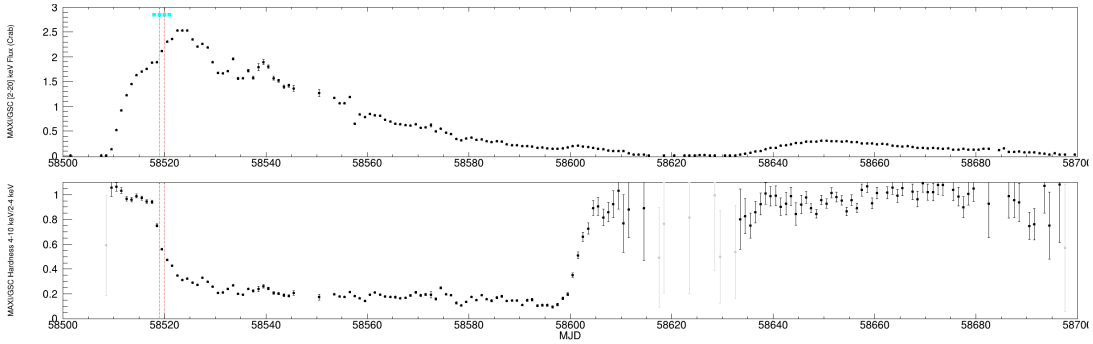

Figure 6.5.: MAXI/GSC lightcurve and hardness ratio MAXIJ1348-630 focused around HESS observations.

- **GRS1716-249**

GRS1716-249 was observed with HESS during a major flare in 2017, but not in a clear state transition (see Figure 6.6). To keep a consistent SED, we define a time window with the following criteria on the flux intensities and hardness ratio. First, we find the range of X-ray hardness ratio and the flux exhibited by the source during HESS observation days. Then, we select a time period in which the hardness ratio is within that range and above 80% of that flux. The selected MJD range is 57755 to 57873.

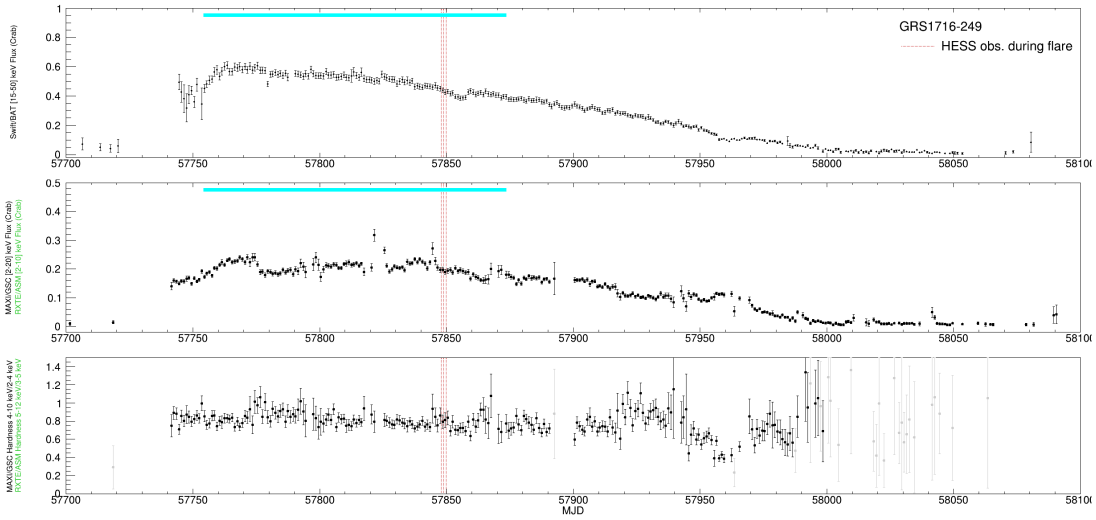

Figure 6.6.: Swift/BAT, MAXI/GSC lightcurves, and MAXI/GSC hardness ratio for GRS1716-249 focused around HESS observations. Nights of HESS observations are represented by vertical red dashed lines. The studied time window is highlighted in blue.

7. Very High Energy γ-rays with H.E.S.S.

This chapter focuses on the study of potential VHE γ-ray emission from microquasars with the H.E.S.S. telescope array. First, we will present a common analysis of data taken with IACTs HESS, MAGIC, and VERITAS during the 2018 flare of microquasar MAXI J1820+070. We will then show the results of a search based on all available HESS data of other microquasar sources, regardless of whether the object was observed in a flaring state or not. Finally, we will develop the analyses of observations made during outburst episodes of sources GRS 1716-249, MAXI J1535-571, MAXI J1348-630, GRS 1915+105, and GX 339-4.

7.1. Gamma observations of MAXI J1820+070

Microquasar MAXI J1820+070 was discovered on March 11, 2018, by MAXI. It underwent a particularly high outburst following its discovery, peaking around 4 Crab units in the Swift/BAT band, and stayed in a HS until July 2018 when it went through a ST to a SS that lasted until late September 2018 before transitioning back to the HS and going back to quiescence, as seen in Figure 7.1. This particularly long period of activity, in addition to its location away from the galactic plane (Galactic Latitude = 10.15°), gave this source a wide MWL coverage.

Among them, IACTs performed their observations in search of a VHE counterpart. A MWL study was performed in [1] using data from the Fermi/LAT telescope, and a combination of data from HESS, MAGIC, and VERITAS. The total good-quality data taking live time over the 3 instruments is 59.5 hours with HESS contributing for 26.3 hours.

The data-taking periods were separated according to the X-Ray states, as defined by [193]. Similar periods are chosen for the neutrino search in chapter 9.

The combination of the data from different IACTs into a single result was done using a joint likelihood function:

$$\mathscr{L}_{\text{tot}} = \prod_i \mathscr{L}_i(N_{\text{ON,i}}, N_{\text{OFF,i}}, \alpha_i, \Delta t_i, \mathscr{A}_{\text{eff,i}}) \tag{7.1}$$

with $\mathscr{L}_i$ the likelihood computed for individual telescope according to Equation 4.22. Δt_i and $\mathscr{A}_{\text{eff,i}}$ their individual live times and effective areas used in the computation of the number of photons n_γ. Similarly to the likelihood ratio defined in Equation 4.23, we build the likelihood ratio λ_{tot} from the joint likelihood as the sum from likelihood

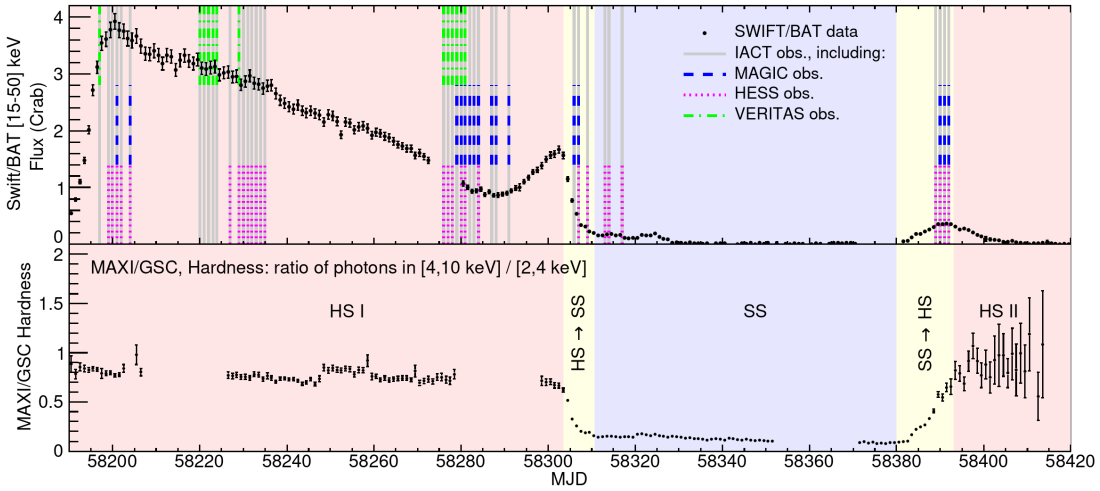

Figure 7.1.: Top: X-Ray flux in the Swift/BAT band (15-50 keV), with the good-quality VHE observation dates superimposed as vertical lines with different styles for each collaboration. Bottom: Evolution of the MAXI/GSC hardness ratio (4-10 to 2-4 keV). The source states are superimposed as light red (HS), light blue (SS), and light yellow (ST) background colors. Figure from [1].

ratios computed individually in each experiment λ_i:

$$-2\ln\lambda_{\text{tot}} = \sum_i -2\ln\lambda_i \tag{7.2}$$

The upper limit can then be computed with a $n\sigma$ confidence level as the maximum value of the flux normalization that gives a λ_{tot} compatible with $n = \sqrt{-2\ln\lambda_{\text{tot}}}$, in a similar manner than the one for a single detector.

The γ spectrum is assumed to follow a power law of spectral index -2.5 as it was the measured value for γ-ray binaries [194], under the assumption that this microquasar hosts similar particle acceleration and gamma emission mechanisms. This assumption will be taken for the analyses of other sources in the following sections as well. We note however that this assumption has a limited impact on the results when they are given as differential upper limits, and is only significant when considering a large (~ order of magnitude scale) energy range.

No significant excess was detected in the Fermi/LAT band nor in the VHE band, either in an individual or in the joint analysis. Individual and combined VHE differential upper limits are shown in Figure 7.2 for each source state, and for the complete data set. The energy threshold was taken at 200 GeV for events from each experiment, in order to harmonize the data set. During the second transition (SS-HS), a 300 GeV threshold was chosen instead due to the high zenith angle of the observations. We can see that combining the data leads to more restrictive ULs in almost all cases, except where large differences between individual ULs are obtained.

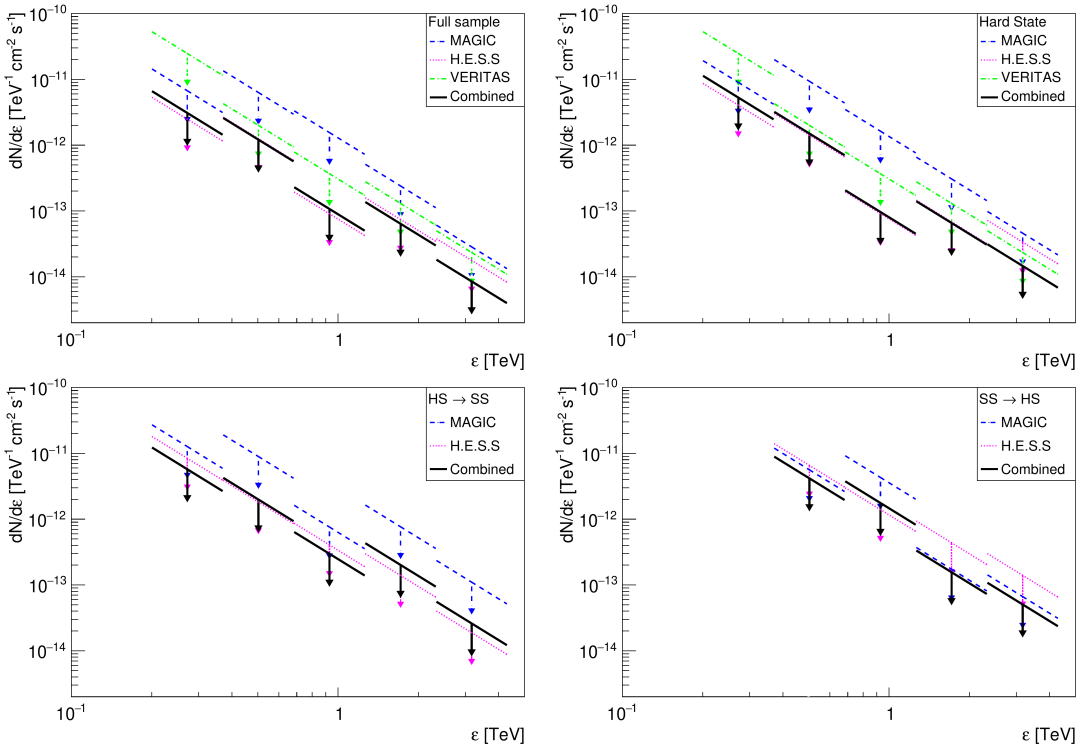

Figure 7.2.: Differential flux upper limits of MAXI J1820+070 for different energy bins and source states. Colored markers represent the results for the individual experiments, while black lines show the combined upper limits. Figure from [1].

In order to contextualize the HE and VHE results with respect to the X-ray state, a dedicated data analysis of NICER observations was performed. The telescope observed for 109 h, 21.8 h, and 4.56 h during the HS, hard-to-soft ST, and soft-to-hard ST, respectively. Pre-processed event files were retrieved through the HEASARC database. Re-processing and filtering were done using standard criteria with the `nicerl2` task from the NICERDAS software available in the HEAsoft distribution[1] (v6.26). Spectra were extracted using the extractor function from the *ftools* package. Energy and gain calibrations were performed using the HEASARC Calibration Database version XTI(20200722). To avoid telemetry saturation, the fraction of active modules had to be adjusted. This was taken into account considering that each module contributes equally to the effective area. The fluxes were corrected for interstellar extinction using a hydrogen column density of $N_H = 1.4 \times 10^{21} \mathrm{cm}^{-2}$ [195].

Results are shown in a broadband SED in Figure 7.3, averaged over the HS and the two ST. It includes measurements in radio from [80]. The radio flux originates dominantly from the compact jet close to the Black Hole in the HS and from the launching of discrete ejecta in the Hard-to-Soft ST. During the second transition, the compact jet reappears which leads to a re-brightening of the radio flux. The softening

[1] https://heasarc.gsfc.nasa.gov/docs/software/lheasoft

of the X-ray spectrum can clearly be observed in the NICER energy range.

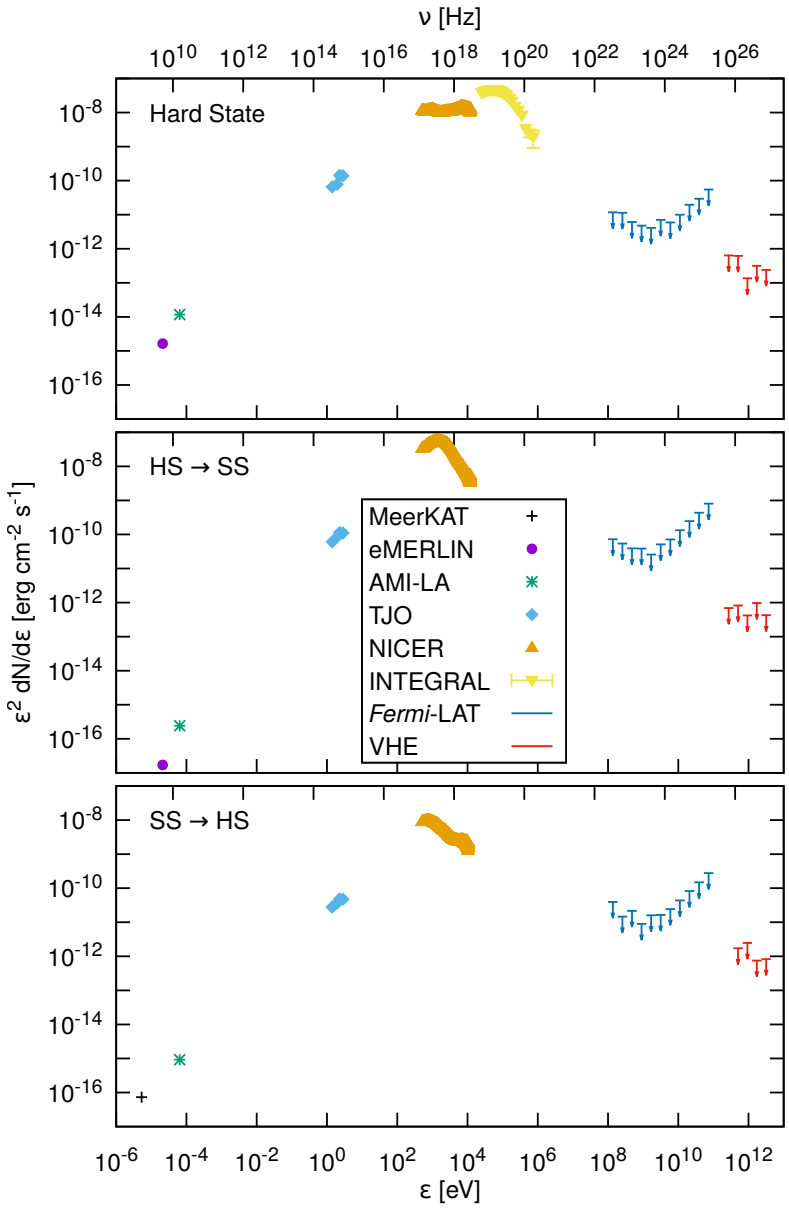

Figure 7.3.: SED of MAXI J1820+070 averaged over the HS, hard-to-soft ST and soft-to-hard ST. Fermi/LAT and HESS upper limits are given with a 95% confidence level. Figure from [1].

7.2. Available data of microquasars observations in HESS.

The rest of this section is dedicated to the analysis of HESS data from the observation of other microquasars, with the list of studied sources in Table 7.1. These data can be categorized in multiple cases. First, the case in which the microquasar was directly observed, i.e. the source is the target of the observation run. These observations have been taken from regular scheduling or triggered from the Target of Opportunity (ToO) program, in which data taking is performed if a source exhibits a MWL behavior that could translate to favorable conditions for VHE emission: a state transition or a particularly bright flux. The microquasar is then necessarily observed in a flaring state. The second case is a so-called fortuitous observation, where a microquasar was not the primary target of an observation run but was nonetheless in the camera FoV. It should be noted that in this case the performances of the observations are expected to decrease the further away the source is from the center of the FoV, as the acceptance is reduced away from the center of the camera of the telescopes. For this analysis, data are selected from good-quality runs if the corresponding microquasar is located at less than 1.5° from the center of the camera.

Name	On target runs	Analysis runs
XTEJ1550-564	0	42
GRO J1655-40	0	23
GRS 1915+105	49	96
GX339-4	59	59
H1743-322	0	87
IGRJ17091-3624	0	19
V404 Cyg	0	21
MAXI J1535-571	12	129
MAXI J1348-630	10	63
GRS1716-249	4	4

Table 7.1.: Number of on-target runs and of runs used in the analysis

Table 7.1 shows the number of runs taken on-target and the total number of runs used in the analysis.

The analysis is performed in multiple steps. First using all available analysis runs, then with runs coinciding with X-Ray flares as described section 6.1. Finally, we study the case of GX339-4 where observations were performed in multiple well-defined X-Ray states. We note that in this first analysis, the source significance is the main result. Indeed, any indication of the flux or its upper limit while mixing observations where a source is flaring and in quiescence is averaged on these states and can hardly be correlated with MWL behaviors.

Analyses are performed using Model++ with ParisAnalysis (PA). The analysis uses

a `Combined Stereo` reconstruction for runs taken with the CT5 telescope, meaning each event was reconstructed both with and without the CT5 telescope, and the best reconstruction according to Equation 4.8 is kept over the other. The event selection in all analyses uses a `Standard` cut configuration described in subsection 4.1.6, which is the cut configuration that has been optimized for sources with a spectral index -2.5. In order to verify the validity of the results, an independent cross-check analysis was performed with the HAP analysis chain[2]. In this section, results from this cross-check are shown alongside the results from the main analysis.

7.3. Results with all available data

The significance is computed with the method developed by [138], as shown in Equation 4.16 and upper limits are evaluated from the confidence intervals computation method developed in [196], as given in Equation 4.22, assuming an efficiency with a Gaussian uncertainty of 30% to account for systematic effects, and given with a 95% confidence level. The upper limits computations assume the sources follow a power law with a spectral index of -2.5.

Source	LiveTime (h)	Significance	Energy thresh. (TeV)	U.L.
XTEJ1550-564	17.6	-1.2	0.34	0.56
GRO J1655-40	9.1	-0.8	0.26	0.71
GRS 1915+105	39.5	2.6	0.31	1.5
GX339-4	23.6	-0.1	0.28	1.7
H1743-322	38.4	0.9	0.17	2.0
IGRJ17091-3624	7.8	1.1	0.26	3.1
V404 Cyg	9.7	0.5	1.36	1.0
MAXI J1535-571	52.9	1.9	0.31	1.9
MAXI J1348-630	26.3	-1.0	0.283	1.9
GRS1716-249	1.3	0.0	0.19	2.4

Table 7.2.: Analysis results for all available runs. Integral upper limits (U.L.) are given in 10^{-8}ph/m^2/s and are computed above the energy thresholds.

Table 7.2 gives the observation livetimes for each source, the significances and the integral upper limits of their flux computed above the energy threshold[3]. No significant signal was found. However, two sources show marginal excess: GRS1915+105 (2.6σ excess significance) and MAXIJ1535-571 (1.9σ excess significance). Figure 7.4 shows the excess and significance maps, with significance distributions of the analyses of all runs around GRS1915+105 and MAXI J1535-571. We can see that the excess at the coordinates of MAXI J1535-571 can be attributed to the source HESS J1534-571, which

[2] All cross-check HAP results presented in this section were performed by Laura Olivera-Nieto.
[3] Defined as the energy at which the effective area is evaluated at 15% of its maximum value.

is a shell SNR appearing as an extended source that completely encloses the microquasar [197]. The marginal excess resulting from the analysis of this location in the sky therefore cannot be attributed to the microquasar. On the other hand, GRS1915+105 is located in a crowded region, close to hotspot HOT J1924+112 and source HESS J1912+101, a shell SNR candidate (also described in [197]). The marginal excess should then be interpreted with caution at this time, more observations followed by a morphological study of the crowded region are needed to extract a hypothetical contribution of the microquasar to the gamma flux.

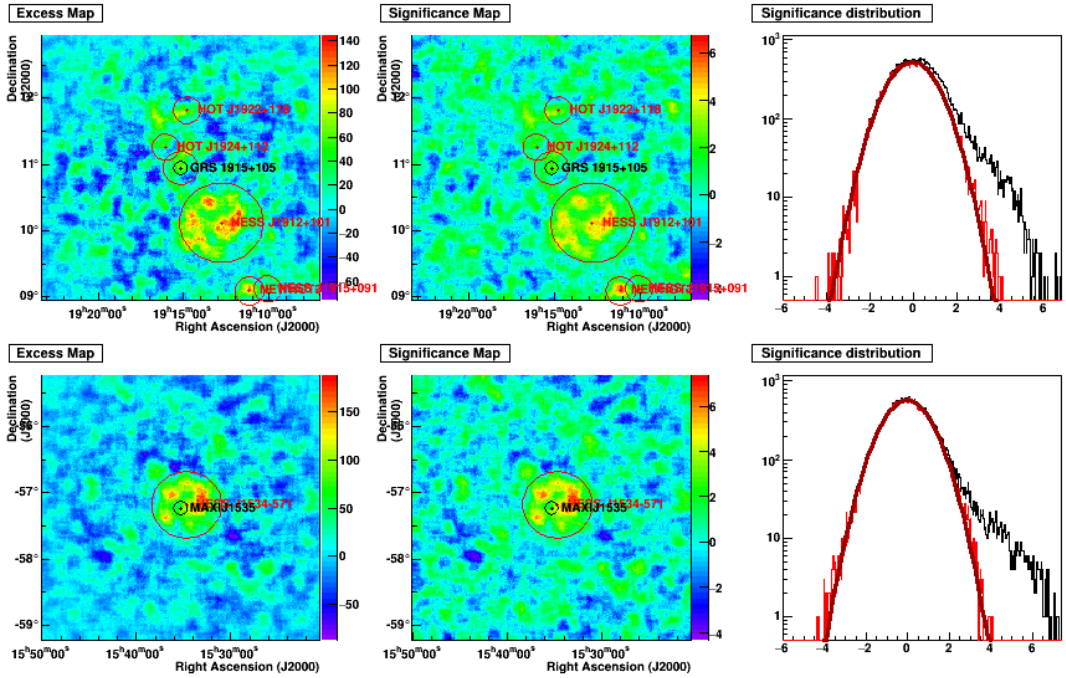

Figure 7.4.: Event excess maps, significance maps and significance distributions for GRS1915+105 (top) and MAXI J1535-571 (bottom). The red circles show regions excluded from the background estimation as described in subsection 12.3.4. Plots on the right show significance distributions of all pixels (black histogram) and pixels outside of excluded regions (red histogram).

7.4. Results for flares

From the initial source list, 5 sources were observed in flaring state, 3 of them being ToO observations: GRS 1716-249, MAXI J1535-571 and MAXI J1348-630. The 2 others are GRS 1915+105 and GX339-4. A summary of results and integral upper limits are given in Table 7.3. Details and differential upper limits are given in the following sections.

Source	LiveTime (h)	Significance	Energy thresh. (TeV)	U.L.
GRS 1915+105	10.9	1.9	0.38	1.4
MAXI J1535-571	5.3	-0.5	0.62	1.4
MAXI J1348-630	4.2	-1.2	0.28	0.82
GRS1716-249	1.3	0.0	0.19	2.4
GX339-4 (All flare)	19.1	-0.6	0.31	1.5
GX339-4 (HS)	2.0	-0.2	0.31	5.2
GX339-4 (ST)	8.2	-0.3	0.31	2.1
GX339-4 (SS)	8.9	-0.6	0.31	1.1

Table 7.3.: Analysis results for runs in flares. Integral upper limits (U.L.) are given in 10^{-8}ph/m^2/s and are computed above the energy thresholds.

Evaluation of the impact of the random Poissonian fluctuation of the number of events in the ON region on the results. As seen in section 4.1, the upper limits are computed using the number of events measured in the ON region, $N_{\rm ON}$. In a background-only hypothesis, this number is estimated from the number of events in the OFF regions with $N_{\rm bkg} = \alpha \times N_{\rm OFF}$. The upper limit is then computed to find the maximum signal compatible with the measurement, at a given confidence level. If we assume that the ON region contains indeed only background events, we can estimate the effect of their Poissonian fluctuation on the final upper limit. Let us consider the probability of measuring k events in the ON region, given an expected value of $N_{\rm bkg}$:

$$P(N_{\rm ON} = k) = e^{-N_{\rm bkg}} \frac{(N_{\rm bkg})^k}{k!} \tag{7.3}$$

We can then calculate the probability of $N_{\rm ON}$ to be measured in an interval $[a,b]$ containing $N_{\rm bkg}$, and evaluate the upper limits on the source flux at the boundaries of that interval. This probability can be expressed in terms of $n\sigma$. We note that due to the discrete Poisson distribution, the computed values for $n\sigma$ cannot be made for an arbitrary n. Thus, in the following plots, these intervals are given as color gradients.

Additionally, we give in each case the average expected upper limit in the background-only hypothesis by weighting all possible upper limits by their Poisson probability:

$$< UL >= \sum_{n=0}^{\infty} UL(n, N_{\rm OFF}, \alpha) \times e^{-N_{\rm bkg}} \frac{(N_{\rm bkg})^n}{n!} \tag{7.4}$$

where $UL(n, N_{\rm OFF}, \alpha)$ is the Rolke [139] upper limit when $N_{\rm ON} = n$.

7.4.1. GRS 1716-249

GRS 1716-249 was detected in outburst by MAXI/GSC on December 19th 2016 (MJD 57741, ATel#9876), peaking at around 250 mCrab in the MAXI/GSC band and around 600 mCrab in the Swift/BAT band around MJD 57770. It underwent a slow hard-to-soft

transition, with multiple failed transitions characterized by a temporary re-hardening of the X-ray spectrum, as reported in [198]. The spectra first began softening at MJD 57830 and reached a soft state at MJD 57960. ToO observations were triggered and data was taken on April 5th, 6th and 7th, 2017 (MJD 57848 to 57850). Five observation runs were performed, for a total of 1.51 hours. For two of these runs, the telescope CT5 was taking data. However, the fraction of broken pixels in CT5 was too high in these runs, around 9% (in comparison to the 5% criterion). The analysis is then performed only with a **HESS-I** configuration, with the CT1-4 telescopes. The analysis livetime after run quality selection is 1.3 hours, as a run was removed due to insufficient quality of the sky tracking. We note that these observations are the only ones taken at GRS1716-249 coordinates and are then the same analysis as section 7.3.

Analysis results can be found in Figure 7.5. The analysis cross-check shows a good agreement with the main analysis. This analysis results indicate a low energy threshold of 190 GeV, even without the use of CT5. This is due to the fact that the source was observed at a low zenith angle, around 5°, where the airmass traversed by the Cherenkov photons from an atmospheric shower of this energy is low enough to be detected by the CT1-4 telescopes. Figure 7.6 gives the energy thresholds as a function of the zenith angle for HESSI and Combined reconstructions.

7.4.2. MAXI J1535-571

This source was discovered by MAXI/GSC during its 2017 outburst as reported by the MAXI Collaboration in ATel#10699 on September 03, 2017 (MJD 57999). It quickly peaked at a flux of 2 Crab in the MAXI/GSC band and 400 mCrab in the Swift/BAT band [199] on MJD 58017 and was announced to be transitioning to a soft state on MJD 58006 (ATel#10729). ToO observations were triggered on that day. A total of 18 observation runs were taken, for an 8.1 hour livetime. 8 of these runs were taken with the full 5 telescope array. However, due to problems with the CT5 telescope resulting in a below-threshold central trigger rate, none of these runs pass the data quality selection for an analysis involving the CT5 telescope and should therefore be analyzed only with CT1-4. Additionally, 6 more runs do not pass the quality selection for any analysis configuration due to bad weather conditions. The total livetime after run quality selection is 5.3 hours with 12 runs.

Analysis results can be found in Figure 7.7. For this analysis, we observe some discrepancies in the computed upper limits between the main analysis and the cross-check. A tentative explanation for these discrepancies is given by exploring data-taking conditions. Figure 7.8 gives distributions of variables related to these conditions for the 12 runs of this analysis. We can see that the transparency coefficient during the runs taken in the ToO was poor and the source zenith angle is high, around 50°. This leads to uncertainties in the energy estimation of events as well as a mismatch between the simulated detector and the real one leading to an uncorrect estimation of the effective areas in either analysis chain.

Upper limits using dedicated simulations

The IRFs used in the computation of upper limits usually come from simulations

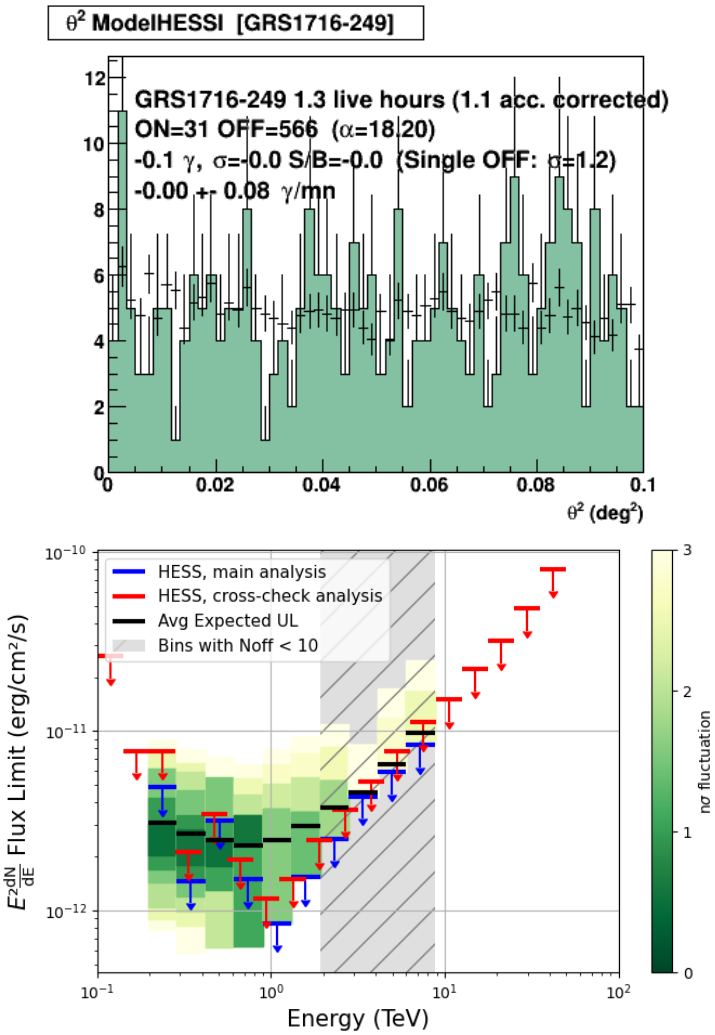

Figure 7.5.: HESS analysis results for GRS 1716-249 ToO observations. Top: θ^2 plot. Bottom: differential upper limits from the main analysis (PA, blue) and the cross-check (HAP, red). For each bin, intervals are given that represent ranges of fluctuation of N_{ON} around the expected value. The confidence level of these fluctuations is given as $n\sigma$ indicated by the color gradient. The average expected upper limit (black) was computed using Equation 7.4. A grey hatched area is drawn over bins where $N_{\mathrm{OFF}} < 10$ in the main analysis, which is a limit of validity for the upper limit computation.

considering the detector in average data-taking conditions. As seen in Figure 7.8, these conditions were quite poor during the ToO observations. This may introduce a systematic uncertainty that is not taken into account in the generic simulations. Dedicated simulations taking into account the conditions of each run, RWS, were performed and the upper limit was computed using the resulting effective area.

Without RWS, the energy threshold is 0.62 TeV with an integral upper limit of 1.4 ×

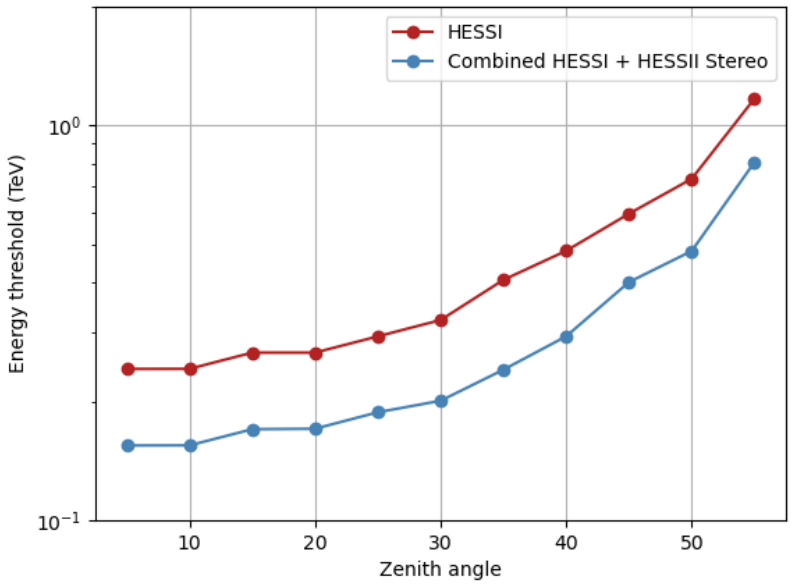

Figure 7.6.: Energy thresholds (defined at 15% of maximum effective area) as a function of zenith angle, for a Stereo HESSI and Combined (Stereo HESSI + Stereo HESSII) reconstructions. The off-axis (*wobble*) angle is 0.7° and the optical efficiency is 0.54.

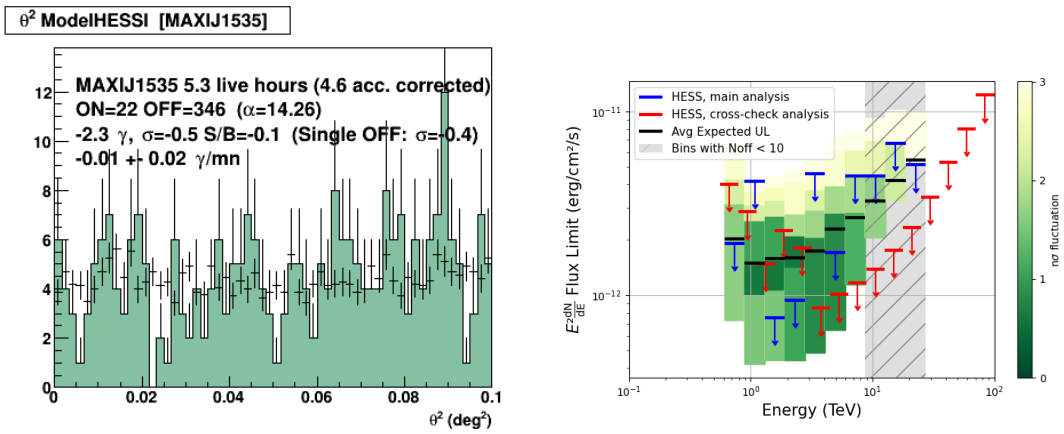

Figure 7.7.: HESS analysis results for MAXI J1535-571 ToO observations. Left: θ^2 plot. Right: differential upper limits from the main analysis (PA) and the cross-check (HAP).

10^{-8}ph/m^2/s while with RWS the energy threshold is 1.01 TeV and the upper limit is 0.49×10^{-8}ph/m^2/s. The main impact of dedicated simulation is therefore an increase in the energy threshold of the analysis. This is due to the fact that a lower transparency coefficient of the atmosphere means that less light from the atmospheric showers reaches the detector. As the events with lower energy and lower number of emitted

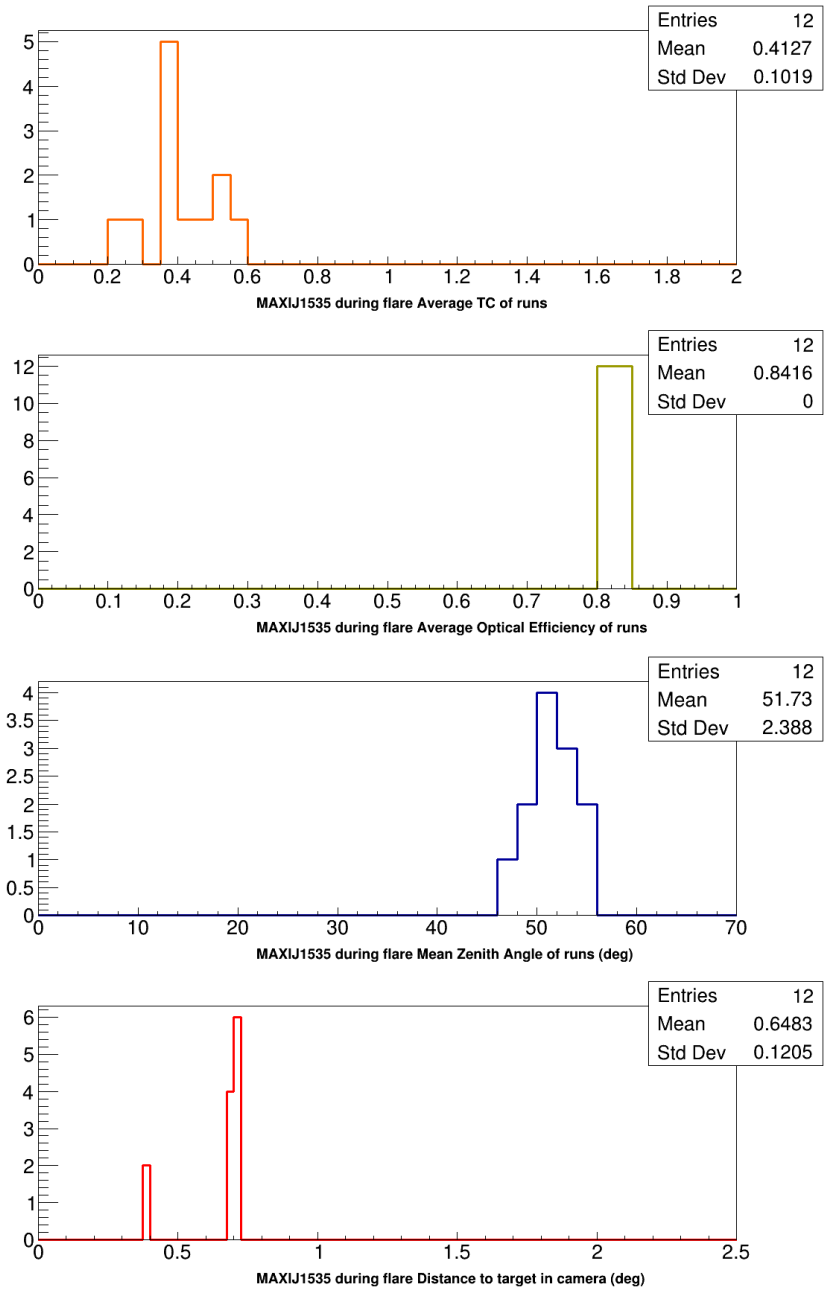

Figure 7.8.: Distributions of data-taking condition variables for runs in the MAXI J1535-571 ToO analysis. Orange: Average transparency coefficient. Green: Average Optical efficiency. Blue: Mean Zenith angle. Red: Distance of the source from the center of the camera.

Cherenkov photons are more impacted, the effective area is significantly lower at this energy.

Figure 7.9 shows a comparison between the differential upper limits with and without RWS. We can see the impact on the energy threshold increase, and at higher energy,

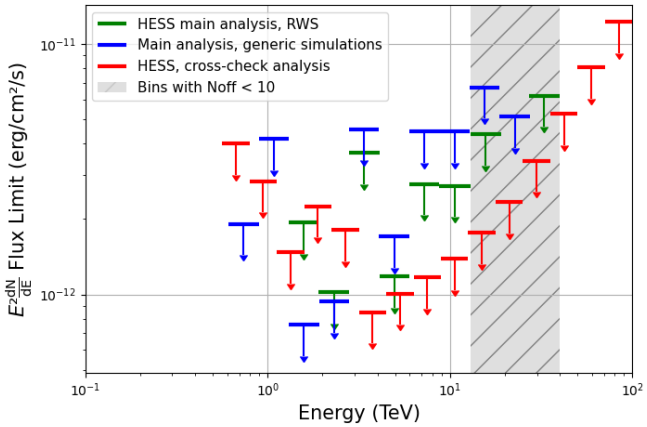

Figure 7.9.: Differential upper limits with ParisAnalysis and generic simulations (blue), ParisAnalysis with RWS (green) and HAP (red) for the MAXIJ1535-571 ToO analysis.

the impact of RWS on the results is marginal and mostly due to statistical fluctuations.

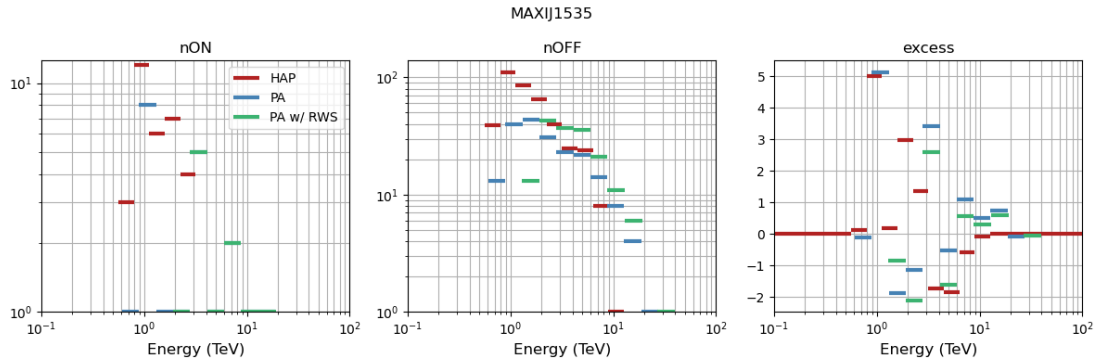

Figure 7.10.: N_{ON} (left), N_{OFF} (middle) and excess (right), with ParisAnalysis and generic simulations (blue), ParisAnalysis with RWS (green) and HAP (red) for the MAXIJ1535-571 ToO analysis.

Comparisons of low-level variables between the main analysis with and without RWS and the cross-check analysis can be found in Figure 7.10. As we can see, while there is evidently no event in energy bins below the threshold, the first energy bin is significantly less populated with the use of RWS. This is due to the fact that as the transparency coefficient varies from run to run, so does the energy threshold, which leads to only a few runs contributing to the first bin. This can be seen in Figure 7.11 which compares the effective areas from the average IRFs and from the RWS.

Contribution of the background source

As mentioned in the previous section, MAXI J1535-571 is located at coordinates close to extended source HESS J1534-571. Figure 7.12 shows excess and significance maps and significance distribution, and we can see that the extended source does not

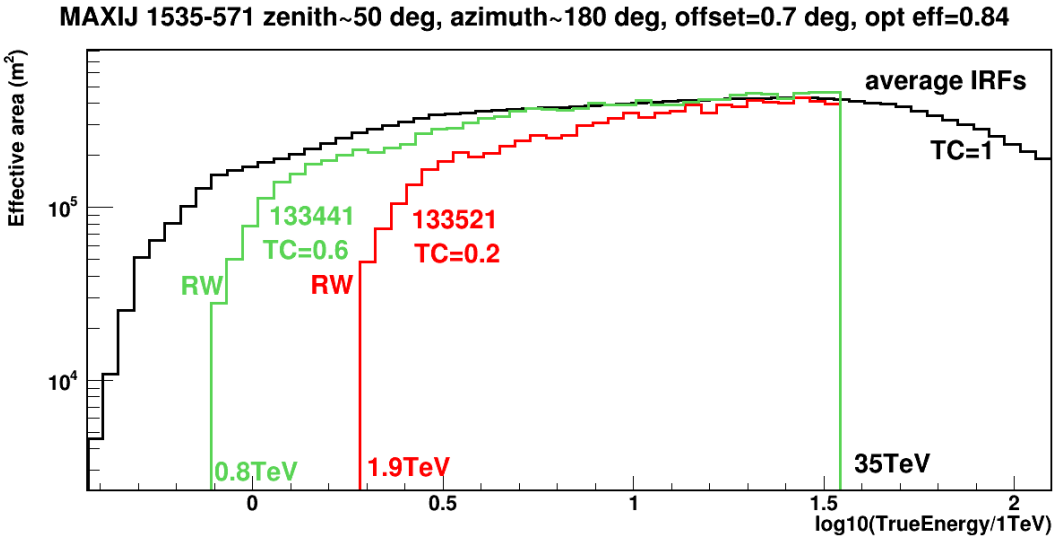

Figure 7.11.: Effective area comparison between the average IRF (in black) and RWS from two runs in the MAXIJ1535-571 run list. The effective areas in green and red are for the runs with the, respectively, highest and lowest transparency coefficients. A decrease of the transparency coefficient leads to an increase of the energy threshold. This value is quoted for their corresponding runs.

appear significantly with the shorter observation livetime used in this analysis.

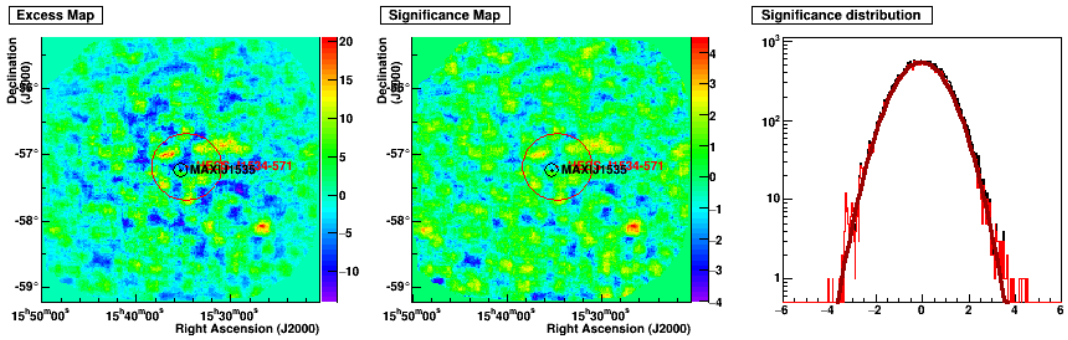

Figure 7.12.: Event excess maps, significance maps, and significance distributions of all pixels (black) and pixels outside of excluded regions (red) for MAXI J1535-571 in the ToO periods.

In the following, we estimate the contribution of this extended source to the upper limits on the flux from MAXI J1535-571 during its flare. To do that we compute the excess in each energy bin from the full 52.9h data set. We consider that this excess is entirely attributed to the extended source. We then compute the number of ON events expected in the 5.3h livetime in the i-th energy bin N^i_{exp} with the following formula:

$$N^i_{exp} = \frac{t_{\text{flare}}}{t_{\text{total}}} \cdot \frac{A^i_{\text{flare}}}{A^i_{\text{total}}} \cdot \text{exc}^i_{\text{total}} \tag{7.5}$$

where $t_{\text{flare/total}}$ are the observation livetimes during the flare and in total; $A^i_{\text{flare/total}}$ are the corresponding effective areas in the i-th energy bin and $\text{exc}^i_{\text{total}}$ is the excess computed in the i-th energy bin from the analysis of the total data.

N^i_{exp} is then subtracted from the obtained number of ON events in the ToO analysis, and the differential upper limits are recomputed. This is equivalent to assuming the gamma events from the SNR are contributing to the background of our analysis. The result of this study can be found in Figure 7.13 with RWS for the main analysis. We can see that the effect of the extended source on the upper limits presented in this section is minor. The correction to ON events in fact does not exceed 1 per bin.

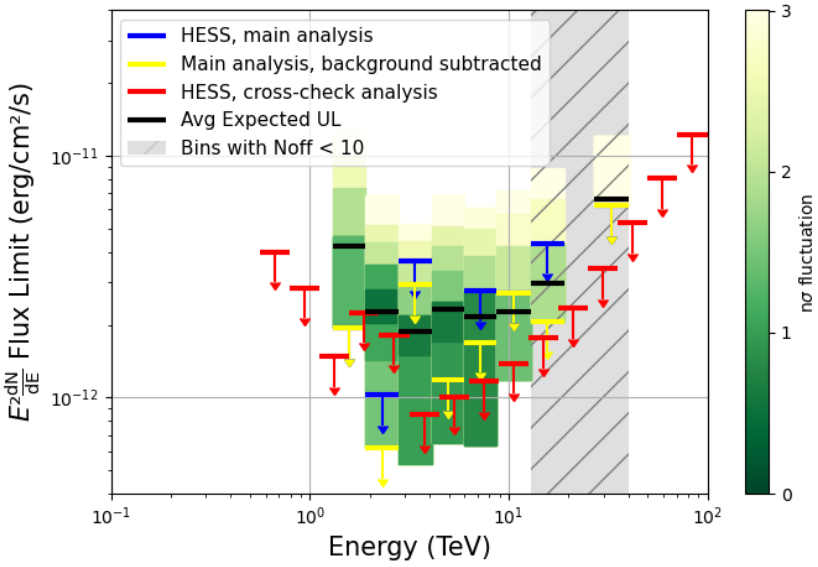

Figure 7.13.: Comparison of upper limits from the main PA analysis (blue), from the main PA analysis after subtraction of excess flux expected from HESS J1534-571 (yellow) and cross-check analysis (red).

7.4.3. MAXI J1348-630

This source was discovered in outburst on January 26th, 2019 (MJD 58509) ATel#12425). Its flux peaked at 2.5 Crab on the MAXI/GSC band and at more than 4 Crab in the Swift/BAT band [200]. It underwent a fast state transition on February 3rd (MJD 58517), and ToO observations were triggered on February 4th and 5th for a total of 13 observation runs, 8 of them with the full telescope array, 2 with only the CT5 telescope and 3 with the CT1-4 telescopes. The data taken with only the CT5 telescope is not analyzed in this work, and an additional run was dropped due to poor weather

conditions. The final live time after selection is 4.2 hours with 10 runs. Runs taken with the 5 telescopes are analyzed with a Combined Stereo event reconstruction. However, as seen in Figure 7.14, the observations were taken at a high zenith angle (> 40°), which leads to the high energy threshold of 280 GeV despite the presence of CT5 in the reconstruction.

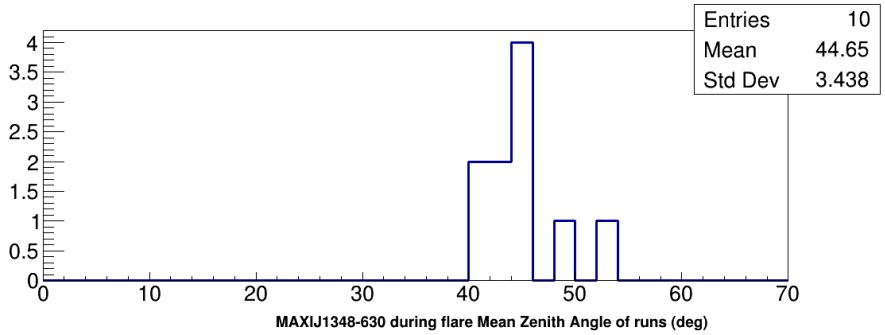

Figure 7.14.: Distribution of the zenith angle of observations of MAXI J1348-630 during its flaring period.

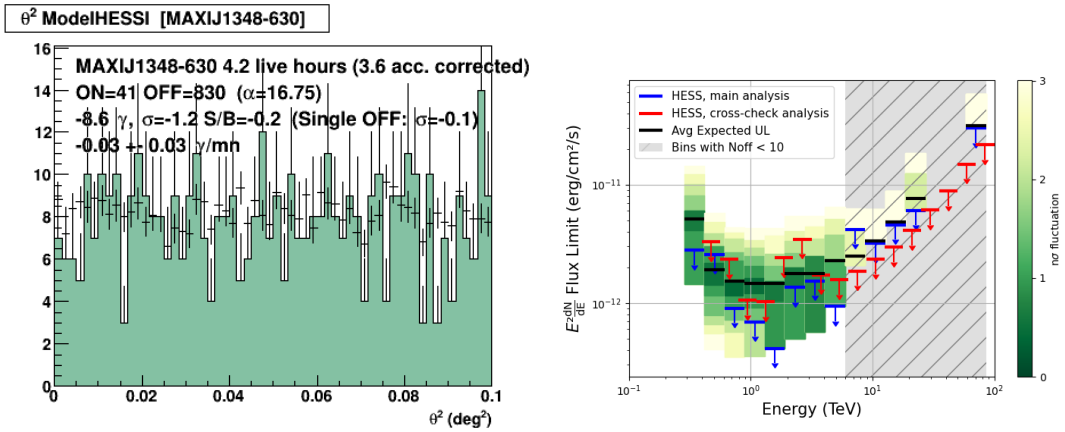

Figure 7.15.: HESS analysis results for MAXI J1348-630 ToO observations. Left: θ^2 plot. Right: differential upper limits from the main analysis (PA) and the cross-check (HAP).

As shown in Figure 7.15, no significant excess was found. The analysis cross-check yields comparable results. Numbers of ON, OFF events and excess per energy bin can be found in Figure 7.16 where we can see that the number of events used in each analysis for limit computations can vary due to their different efficiencies and event selections while the resulting upper limits are indeed comparable.

7.4.4. GRS 1915+105

As this source was in a flaring state during most of HESS operations, a stricter selection of runs was performed. The analysis is performed on 25 runs taken between MJD

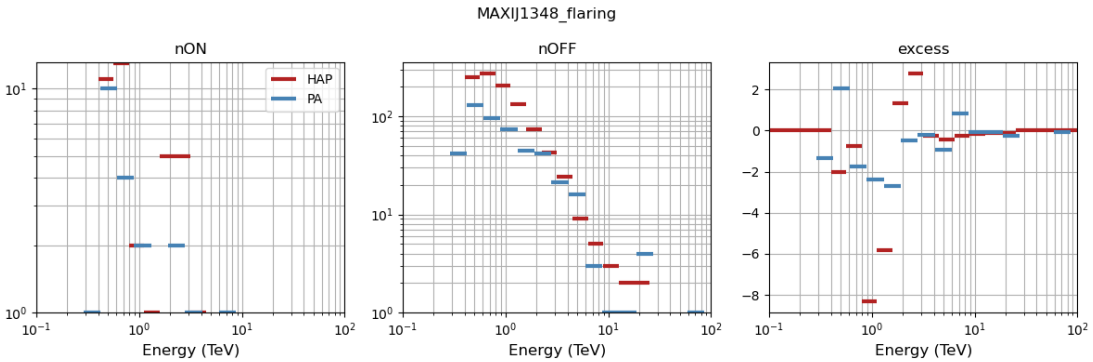

Figure 7.16.: N_{ON} (left), N_{OFF} (middle) and excess (right), with ParisAnalysis and HAP (red) for the MAXIJ1348-630 ToO analysis.

54615 and MJD 54630 when the source was in a re-brightening period after a year of relative quiescence, as seen in Figure 7.17.

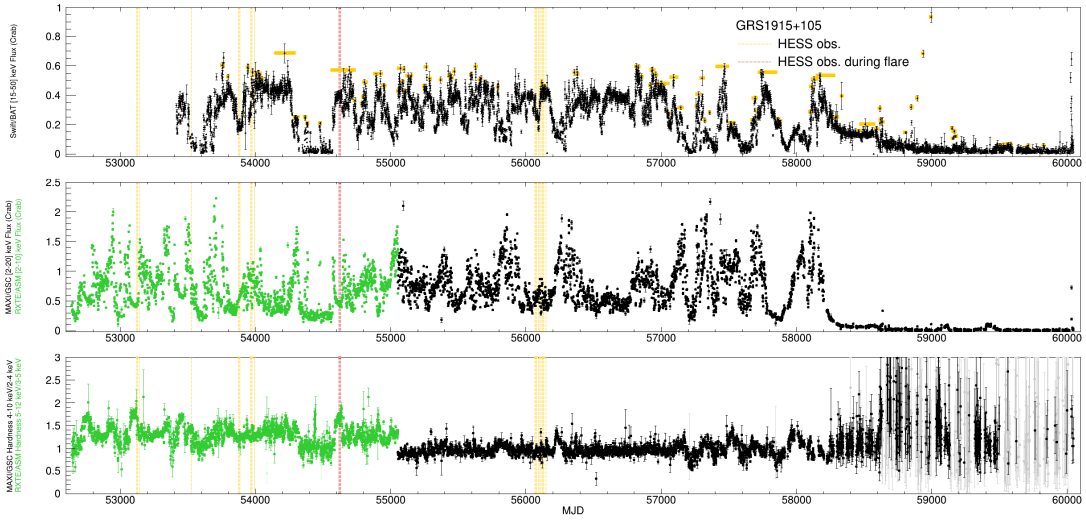

Figure 7.17.: X-Ray lightcurve of GRS1915+105. Top: Swift/BAT lightcurve. Middle: RXTE/ASM (green) and MAXI (black) lightcurves. Bottom: RXTE/ASM (green) and MAXI (black) hardness ratio. Flaring periods are highlighted as yellow horizontal bars. HESS observation MJDs are represented as dashed vertical bars, red if they are analyzed in this section, yellow otherwise.

Figure 7.18 shows analysis results. A marginal excess of 1.9σ significance can be observed, and a similar comment than for the total period can be made relative to the crowded region, as seen in Figure 7.19.

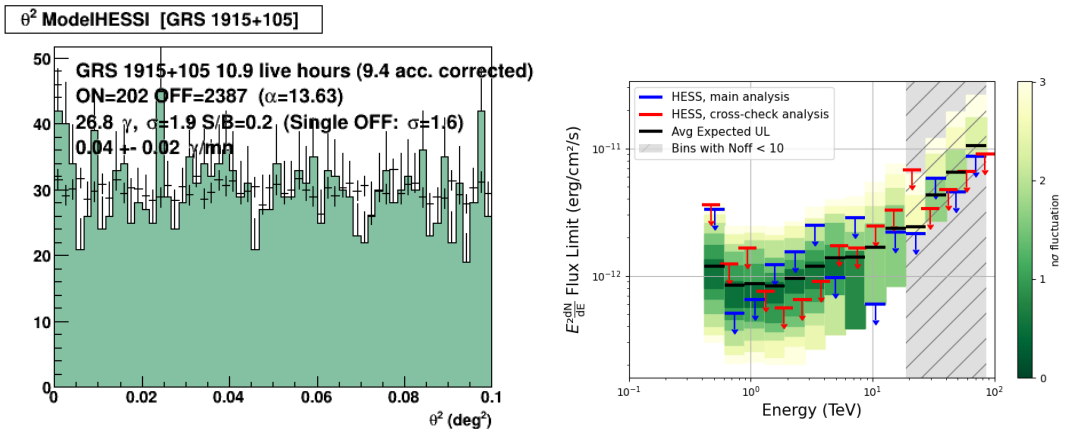

Figure 7.18.: HESS analysis results for GRS1915+105 observations in a flaring state. Left: θ^2 plot. Right: differential upper limits from the main analysis (PA) and the cross-check (HAP).

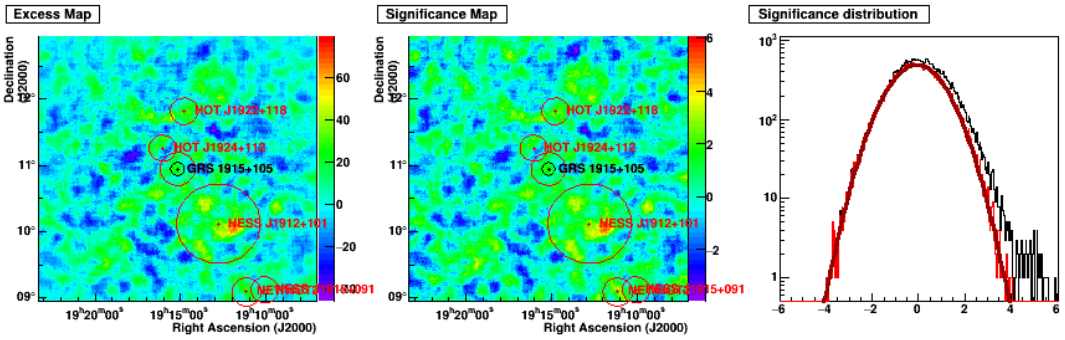

Figure 7.19.: Excess map, significance map, and significance distribution of all pixels (black) and pixels outside of excluded regions (red) of GRS1915+105 analysis in the re-brightening subset of runs.

7.4.5. GX339-4

As this source undergoes regular periods of outbursts, observations were performed during two separate flares, and the two sets of runs taken were then analyzed together. For this analysis, we consider the MWL behavior of the source to follow a similar pattern in each flare, as seen in Figure 7.20.

The first set of observations was taken early in the detector lifetime following ATel#318, as the source was observed in a hard-to-soft transition on August 10th, 2004. After run quality selection, 14 runs come from these observations. The second set of 34 runs was taken around another transition following ATel#2573 in April 2010. As this source presents clear spectral states and sharp transitions between them, we can further sub-divide the observations into 5 runs (livetime = 2.0H) during the HS, 22 runs (livetime = 8.2H) during ST and 21 runs (livetime = 8.9H) during the SS. These subdivisions are reported in Figure 7.21 and Figure 7.22, where we can see X-ray lightcurves with flaring periods highlighted. The highlighting color shows the

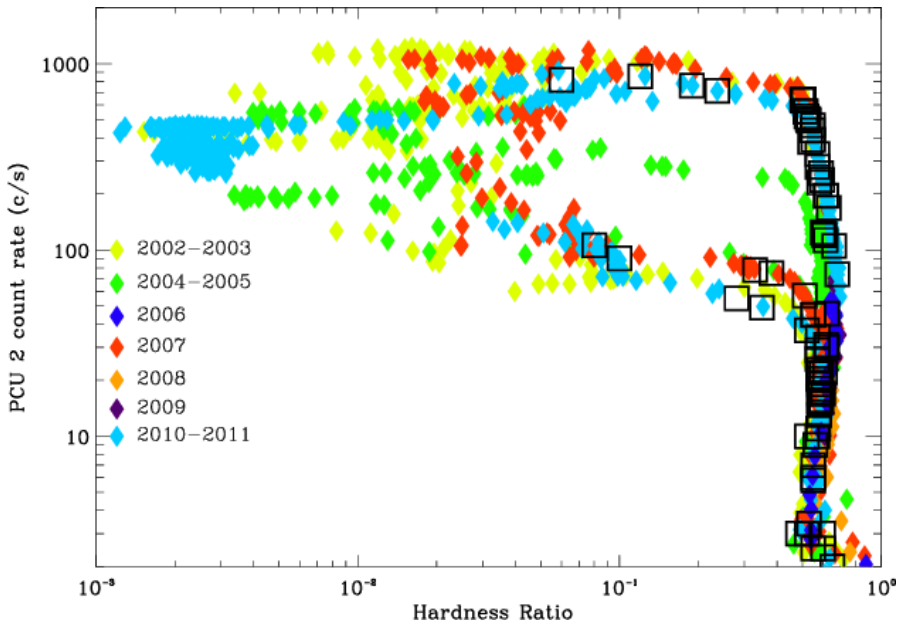

Figure 7.20.: HID from RXTE/PCA data of GX339-4. Different flaring periods are covered, noted by different colors. Figure taken from [74]. Squares are radio observation epochs from the mentioned paper.

spectral states of the source, red being the HS, yellow the ST, and blue the SS. This figure also shows HESS observation dates during these periods as vertical lines, with red/green/blue runs taken during the HS/ST/SS respectively.

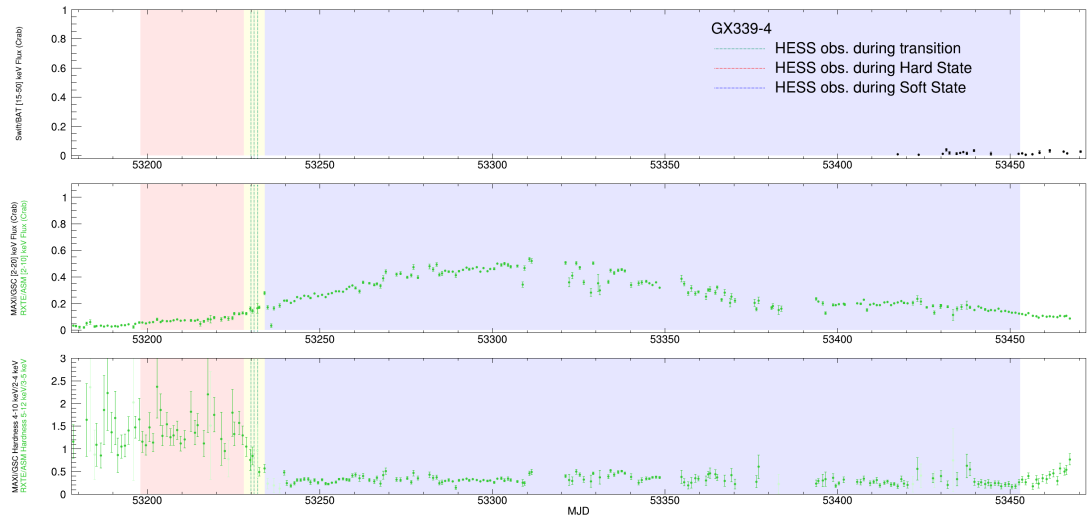

Figure 7.21.: X-ray lightcurves of GX339-4 during the first flaring period coinciding with a HESS observations. Top: Swift/BAT lightcurve. Middle: RXTE/ASM lightcurve. Bottom: RXTE/ASM hardness ratio.

The analysis is first performed with all runs, with a livetime of 19.1 hours. Results

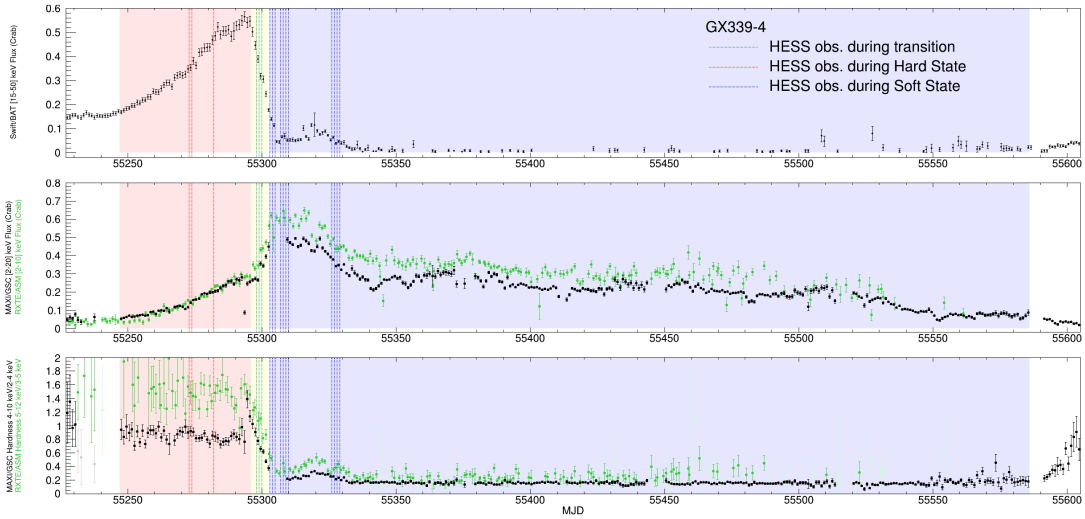

Figure 7.22.: Same as Figure 7.21, for the second flaring period coinciding with HESS observations. For the middle and bottom plots, RXTE/ASM data is shown in green while MAXI/GSC data is shown in black.

are shown in Figure 7.23.

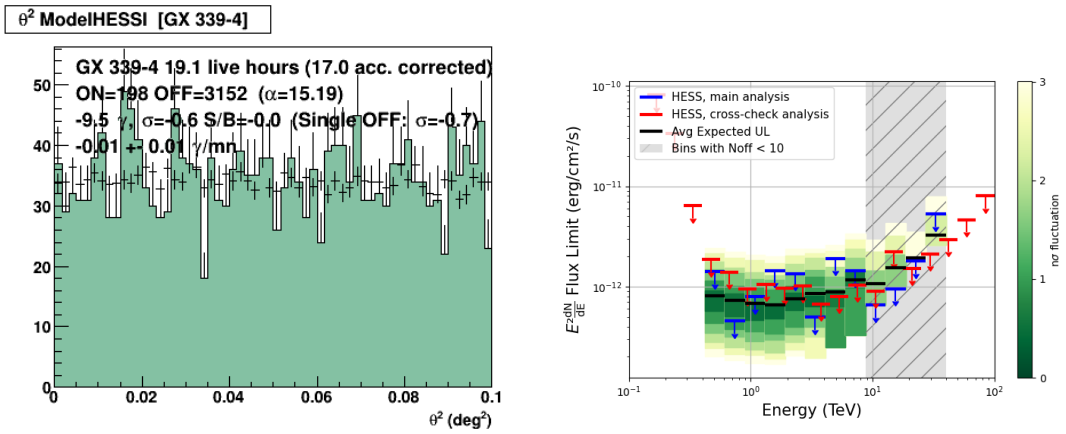

Figure 7.23.: Analysis results for all runs coinciding with GX339-4 in flaring period.

The analysis is then performed in each individual spectral state. No significant excess was obtained and differential upper limits are found in Figure 7.24.

The discrepancy between the two analysis chains can be observed in the HS. In Figure 7.25 the comparisons of low-level variables in this analysis can be found. We note that the number of OFF events is comparable, the discrepancy only arising due to the short livetime introducing statistical variations on the number of ON events.

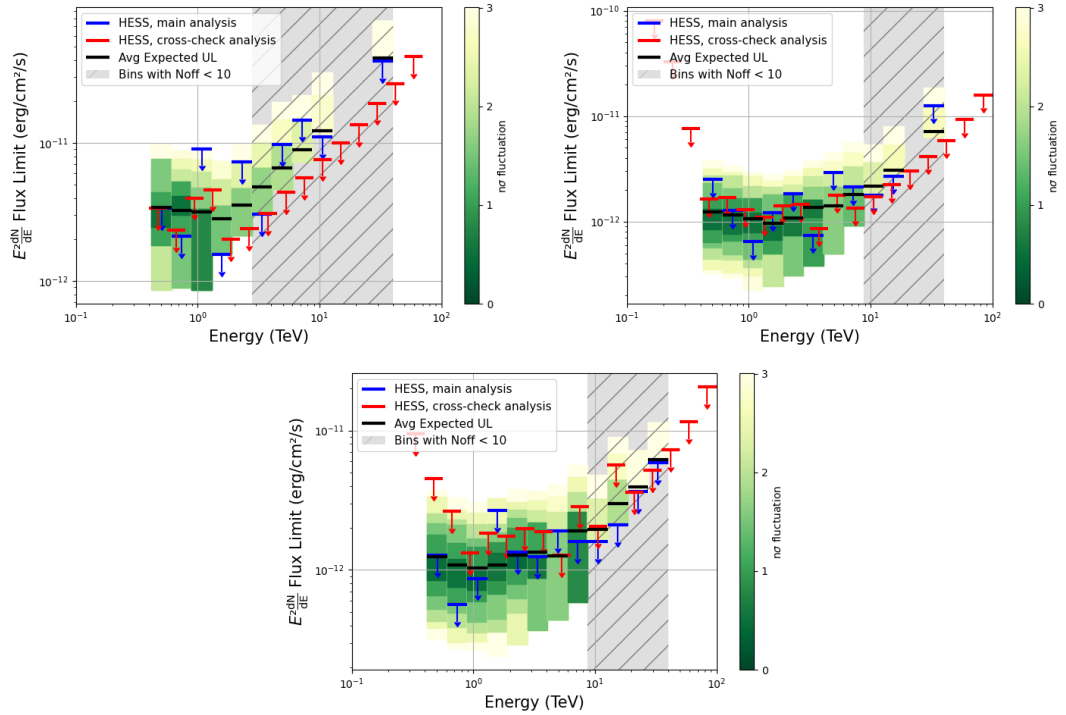

Figure 7.24.: Differential upper limits for the HS, ST, SS of GX339-4.

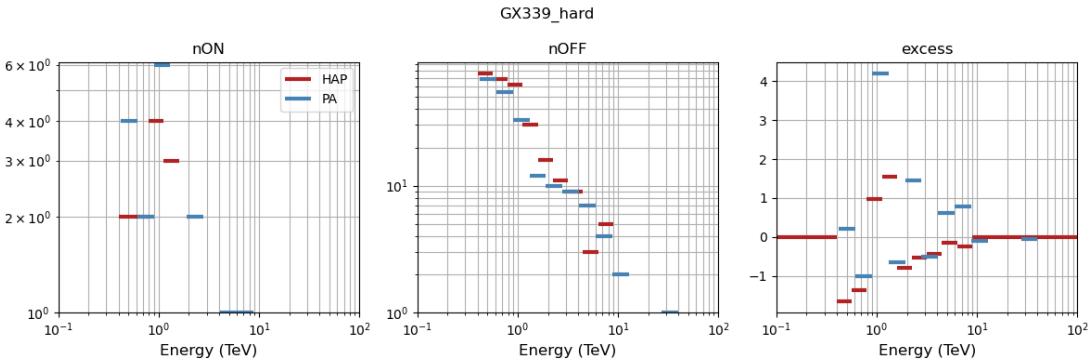

Figure 7.25.: Low-level variable comparison for the analysis in the hard state of GX339-4.

8. High Energy γ-rays with the Fermi/LAT

This section describes the analysis using Fermi/LAT data of a HE signal coming from microquasars in the periods previously determined. We first go over the generalities of the standard data analysis method before describing the configuration chosen for this analysis and going over the results.

8.1. Analysis Method

The analysis uses publicly available data and software by the Fermi/LAT Collaboration, known as *fermitools* [1], in its version 2.2.0, and using its python wrapper. A summary flowchart of the available tools is shown in Figure 8.1. For this analysis a likelihood optimization technique [201] is used. The data is binned with respect to events direction and energy, and the likelihood of the data assuming a given model is then:

$$\mathscr{L} = e^{-N_{exp}} \prod_i \frac{m_i^{n_i}}{n_i!} \tag{8.1}$$

With N_{exp} the total number of events predicted by the model, m_i the expected number of counts by the model in the i-th bin, and n_i the measured number of events in the bin.

The base model, which constitutes the null hypothesis in this search, is based on the LAT 10-year Source Catalog (4FGL-DR2 [9]), with a diffuse galactic interstellar emission template (version *gll_iem_v07*) and an isotropic emission model named (version *iso_P8R3_SOURCE_V3_v1*). An uncatalogued source search is performed by computing a likelihood ratio Test Statistic (TS), given by:

$$TS = -2\ln\left(\frac{\mathscr{L}_{max,0}}{\mathscr{L}_{max,1}}\right) \tag{8.2}$$

where $\mathscr{L}_{max,0}$ is the maximum likelihood value for the model without the additional source (null hypothesis), and $\mathscr{L}_{max,1}$ is the maximum likelihood of the model given by the model with an additional source that is the object of the search. This TS, as stated by the Wilks' Theorem [202], can be asymptotically approximated by a χ^2 distribution, and the detection significance of the source is $\sigma \simeq \sqrt{TS}$

[1] https://github.com/fermi-lat/Fermitools-conda/wiki
[2] fermi.gsfc.nasa.gov/ssc/data/analysis/scitools/overview.html

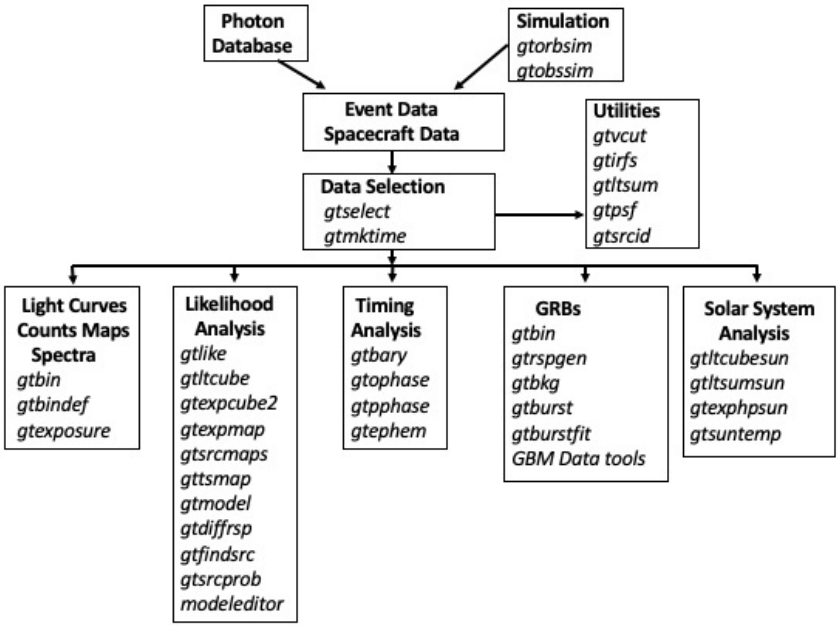

Figure 8.1.: Fermi/LAT analysis flow summary. From the LAT data analysis tools public documentation[2]

.

8.2. Pipeline configuration

This analysis uses the latest Fermi/LAT IRF, version *P8R3_SOURCE_V3*.

Data is selected using *gtselect* in a 10° Region of Interest (RoI) around the source with reconstructed photons energy between 100 MeV and 100 GeV. Events are chosen with the SOURCE photon class which is the recommended choice for Pass 8 Fermi/LAT data version [203]. Moreover, events tagged as both *Front* and *Back* are used in this analysis. In order to clean the event sample from photons of terrestrial or solar origin, events are selected at a maximum zenith angle of 90° and at an angle from the Sun superior to 15°.

Good Time intervals (GTI), represent time intervals in which the satellite was working in standard data-taking conditions and the data-taking quality was good according to the Fermi/LAT Collaboration. This information is extracted from the public *spacecraft* files and is used to further filter the events with the *gtmktime* tool.

Filtered events are then binned using *gtbin*, with a spatial binning of 0.1° and a logarithmic energy binning of 10 bins per decade. The expected binned count map from the model is computed using *gtsrcmap* from the spectral parameters of the cataloged sources fixed to their cataloged values.

The likelihood fit, implemented in the *gtlike* tool and using the NewMinuit algorithm, is performed in the ROI with binned data and the model count map, keeping as free parameters the flux normalizations of cataloged sources within 5° of the searched source.

The likelihood is performed in multiple steps. A first fit is done without the searched

source, to take into account possible flux variability in nearby sources. It should be noted that as the spectral parameters are not free parameters, the spectral variability of these nearby sources is not taken into account. If this fit does not result in a satisfactory convergence, an additional step is done by freezing all parameters of the sources in the ROI with TS < 5. The searched source is then added to the model, which is built as a Power Law :

$$\frac{dN}{dE} = N_0 \left(\frac{E}{E_0} \right)^{\gamma} \tag{8.3}$$

with a fixed spectral index $\gamma = -2.5$. The final fit is performed with all other source parameters frozen, except the normalizations of the galactic and isotropic diffuse background fluxes.

In these fits, all sources are considered point-like, except in the lowest energy range (100 MeV to 1 GeV), where source extensions are considered, to take into account the broadening of the detector PSF at lower energy. It should be noted that in the case of non-continuous time windows, the search is performed only once, with a stacking of the multiple periods.

8.3. Results

The analysis is performed on the time periods as determined section 6.1. Results of the search in the total flaring periods can be found in Figure 8.2, Figure 8.3, and Figure 8.4. A marginal excess $\sim 3\sigma$ can be found for GRS1915+105 in the 1 to 10 GeV energy range. However, as stated in chapter 7, the presence of nearby, unrelated sources might contaminate the estimation of the source significance. Results of GX339-4 in time windows corresponding to its spectral states are shown in Figure 8.5 and results of GRS1716, MAXI J1535, and MAXI J1348 in time periods coinciding with HESS observations are shown in Figure 8.6. Overall, no significant excess could be detected in all studied cases.

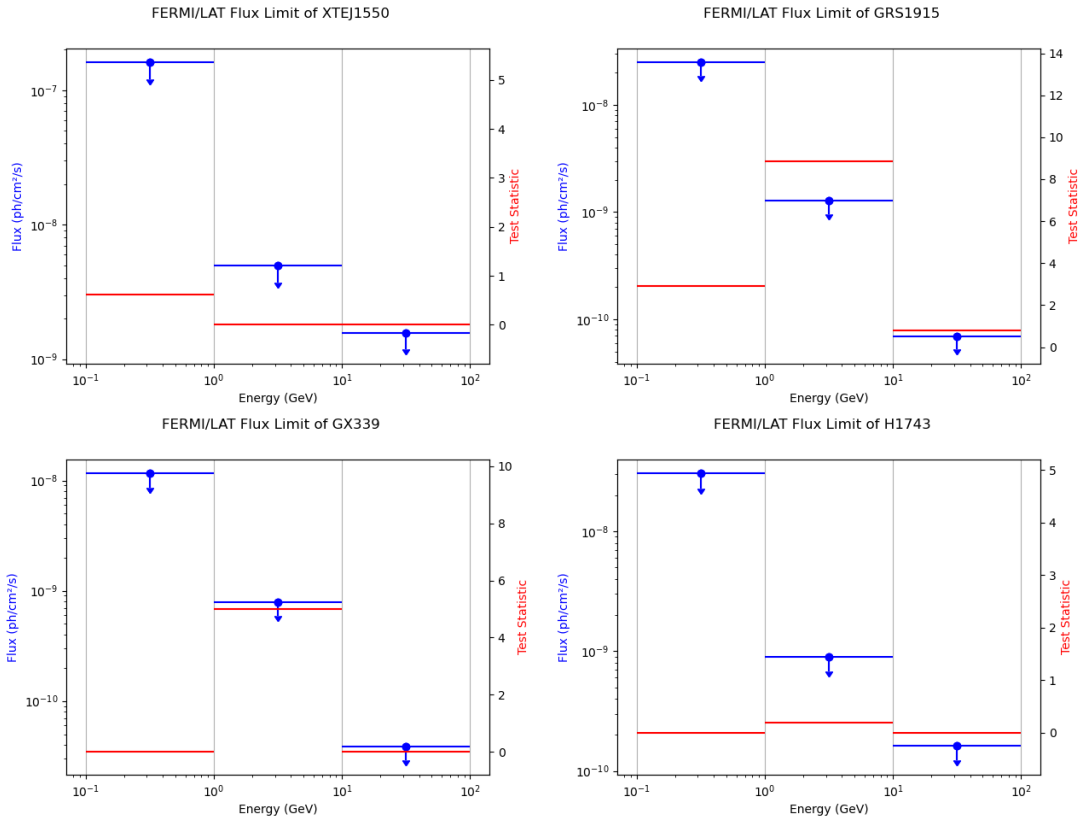

Figure 8.2.: Fermi/LAT results of total flaring periods. Flux upper limits (blue) and Test Statistics (red) results are shown for XTEJ1550 (top left), GRS1915 (top right), GX339 (bottom left), and H1743 (bottom right).

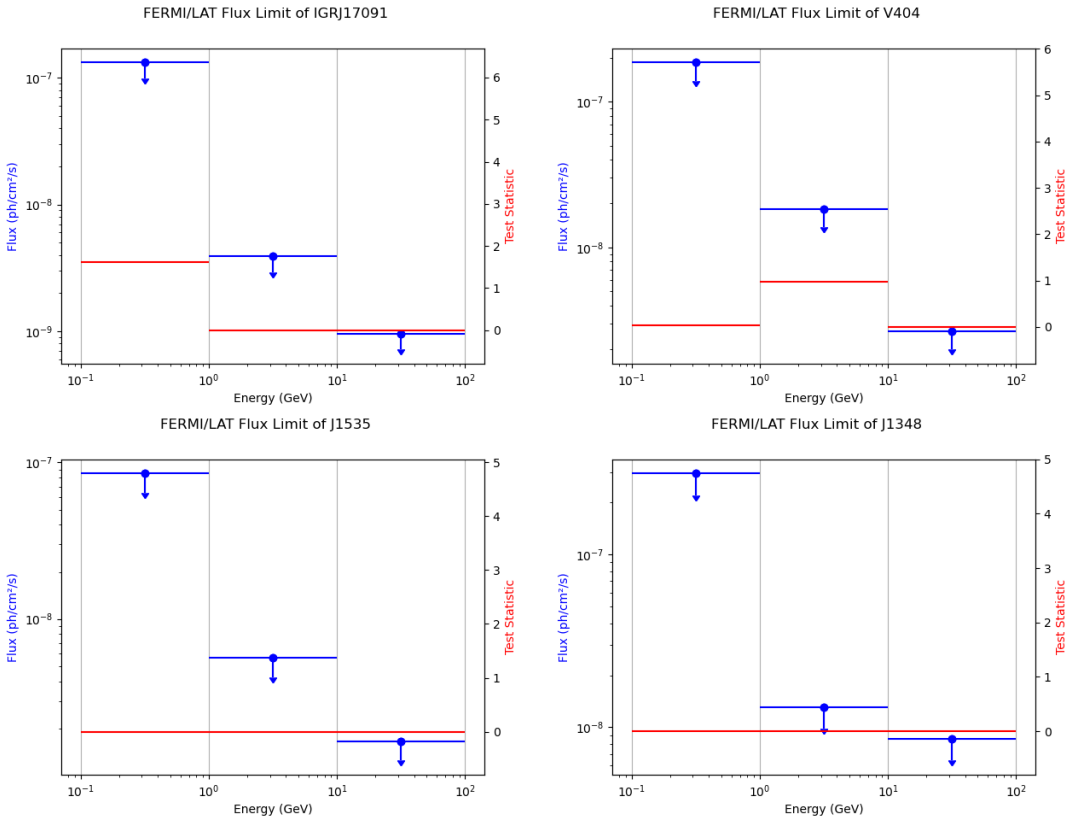

Figure 8.3.: Fermi/LAT results of total flaring periods. Flux upper limits (blue) and Test Statistics (red) results are shown for IGR J17091 (top left), V404 Cyg (top right), MAXI J1535 (bottom left), and MAXI J1348 (bottom right).

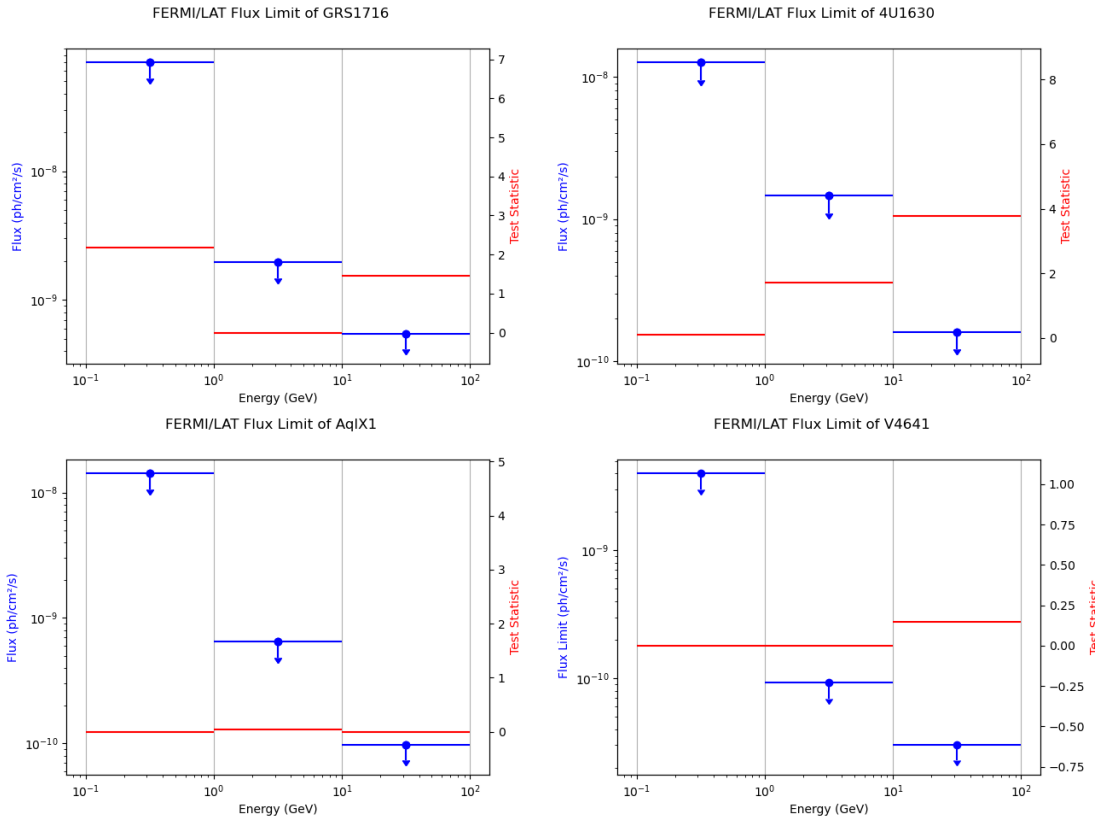

Figure 8.4.: Fermi/LAT results of total flaring periods. Flux upper limits (blue) and Test Statistics (red) results are shown for GRS1716 (top left), 4U1630 (top right), AqlX1 (bottom left), and V4641 Sgr (bottom right).

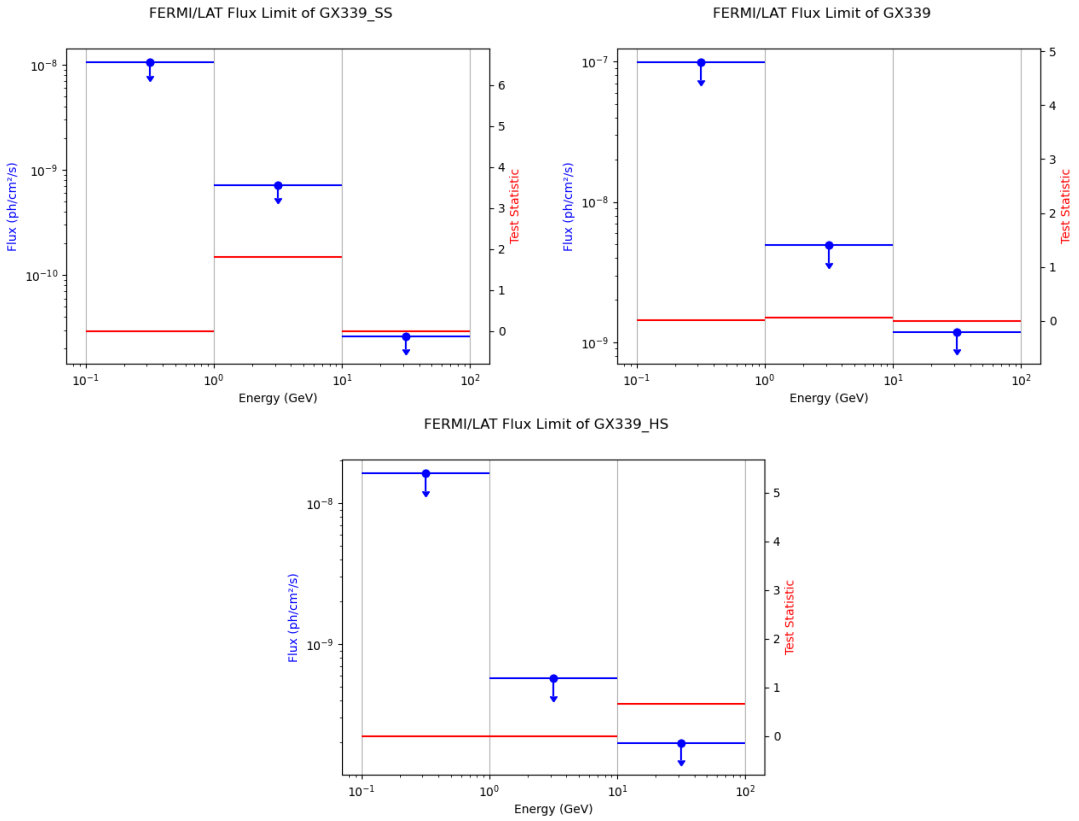

Figure 8.5.: Fermi/LAT results for GX339-4 in different spectral states. Flux upper limits (blue) and Test Statistics (red) results are shown for the SS (top left), ST (top right), and HS (bottom).

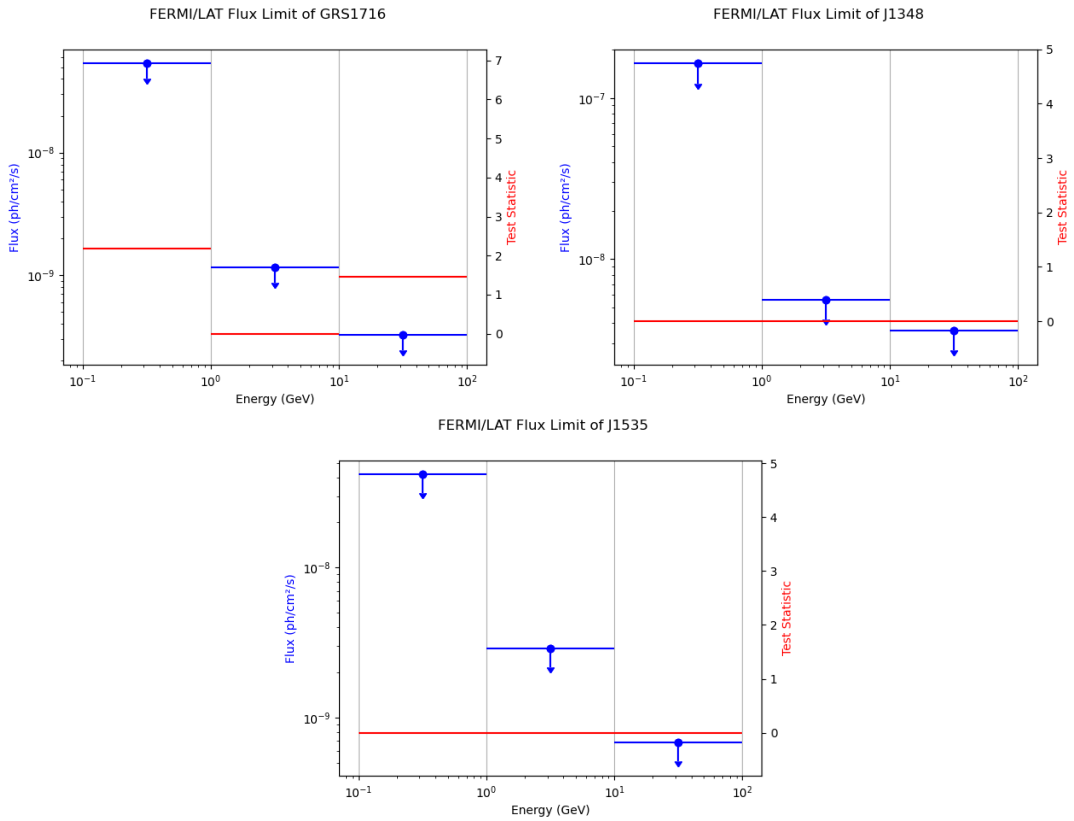

Figure 8.6.: Fermi/LAT results of during periods coinciding with HESS observations for GRS1716, MAXIJ1348, and MAXIJ1535.

9. High energy neutrinos with deep-sea neutrino telescopes

9.1. ANTARES

The ANTARES analysis is an unbinned standard likelihood analysis using spatial, time, and energy ingredients to build its PDF, taking into account event rate fluctuations over the detector livetime. This method was built upon previous point-source analyses like the ones described in [114] with a search of neutrinos from galactic binaries or [204] with a search of neutrino correlations with events from IceCube. Pseudo-experiments are performed to obtain the distribution of Test Statistic used to compute flux sensitivities for each source. The search is performed in time windows obtained in chapter 6.

Data used ranges from 01/01/2007 to 13/02/2022. The analysis is done taking into account both shower-like and track-like event topologies. For the latter, the cut from the AAfit reconstruction quality parameter λ defined in Equation 4.28 can be optimized.

9.1.1. Analysis Method: Time dependant unbinned likelihood fit

9.1.1.1. Event selection

As deep-sea detectors are largely dominated by the atmospheric muon flux, we need to perform an event selection to discriminate between the muons and neutrinos. In the following, we chose as the main criterion to only consider events that are reconstructed as *upgoing*, meaning that the trajectory of the event is not compatible with an atmospheric muon that would go downward in the detector. However, after this selection, muons with a misreconstructed trajectory are still present in the sample. An additional selection is chosen in order to remove this contribution to the event sample. Indeed, as these events have a poorly reconstructed trajectory, we can choose a set of selection cuts based on the quality of the reconstruction in order to remove them.

Besides muons, our other source of background is of course atmospheric neutrinos. A neutrino going through the detector is not able to trace its origin, we have to infer it from its direction, time of arrival, or energy, under the hypothesis that the signal we are searching for has a spectral distribution that is different from the atmospheric neutrino flux. We can then generate from MC probability distributions with respect to

the direction or the energy of the event in order to distinguish neutrinos coming from the source or the atmosphere. The discrimination between signal and background is however not trivial and the selection needs to be optimized to increase the sensitivity of the analysis.

The selection parameter that will be optimized here is the quality of the track reconstruction λ_{AAfit}, as defined in Equation 4.28. No optimization is performed on the shower events, as too few of them remain in the sample after the removal of misreconstructed muons.

In order to reduce the contribution from misreconstructed atmospheric muons, a first event selection is performed with the following parameters.

For events reconstructed as tracks:

- $\cos(\theta_{\text{AAfit}}) > -0.1$, with θ_{AAfit} the zenith angle reconstructed by the AAfit algorithm. We only keep events reconstructed as upgoing or horizontal.
- $\beta_{\text{AAfit}} < 1\,\text{deg}$, the estimated angular error from the AAfit algorithm, defined in Equation 4.29.
- $L_\mu > 380\text{m}$, the reconstructed muon track length
- $\frac{dE}{dX} > 10^{1.6}$, from the energy estimator
- λ_{AAfit}, to be optimised. This variable will be taken in the interval [-5.1,-5.4], λ_{AAfit} > -5.4 being considered a loose selection.

For events reconstructed as showers the following selection criteria are applied:

- Not being selected as a track. This is necessary in order to not have twice the same event in the studied sample.
- $\cos(\theta_{\text{Tantra}}) > -0.1$, events reconstructed as upgoing or horizontal by the Tantra algorithm.
- Shower contained inside the detector: distance from the reconstructed vertex location by the Tantra algorithm:
  - to the detector center: < 300m horizontally
  - to the closest storey of the detector < 250m vertically
- $t_M < 1000$, the value of the M-estimator from the Tantra algorithm
- $\beta_{\text{Tantra}} < 10\,\text{deg}$, estimated angular error from the Tantra algorithm
- $\mathscr{L}_\mu > 50$, Likelihood of the event under the hypothesis that it is a muon
- $L_{\text{Dusj}} > 0.3$, Random Forest Decision score from the Dusj algorithm

This selection is applied to ANTARES data ranging from 01/01/2007 to 13/02/2022. With a cut $\lambda_{\text{AAfit}} > -5.2$, the event sample is then:

- 11031 Tracks
- 234 Showers

9.1.1.2. Likelihood function

The contribution of signal events to the overall sample is done with a fit of a likelihood function under the hypothesis that the signal is emitted from the microquasar coordinates, in its flaring time window.

The number of signal events μ_{sig} is fitted from data or simulations by maximizing the following likelihood function:

$$\log \mathscr{L} = \sum_{j}^{N_{\text{sam}}} \sum_{i}^{N_j} \log \left[\frac{\mu_{sig}^{j}}{N_j} \mathscr{S}_i^j \times P_{Sig}^{j}(t_i) + \left(1 - \frac{\mu_{sig}^{j}}{N_j} \right) \mathscr{B}_j^i \times P_{Bkg}^{j}(t_i) \right] \tag{9.1}$$

with N_{sam} the event sample (track or shower), N_j the number of events in the sample, the total number of signal events is then given as the sum of signal events in the track and shower samples $\mu_{sig} = \mu_{sig}^{\text{tracks}} + \mu_{sig}^{\text{shower}}$.

The signal and background PDFs depend on the angular error estimator β, and are given respectively by:

$$\mathscr{S} = P_{Sig}(\alpha, \beta) P_{Sig}(E, \beta) \tag{9.2}$$

and

$$\mathscr{B} = P(\delta) P_{Bkg}(E, \beta) \tag{9.3}$$

- $P_{Sig}(\alpha, \beta)$ corresponds to the PSF and is the probability for a signal event to be reconstructed at an angle α from the source coordinates. An example is given in Figure 9.1.
- $P_{Sig}(E, \beta)$ and $P_{Bkg}(E, \beta)$ are the energy probability distributions for signal and background events, as seen on Figure 9.2 for tracks and Figure 9.3 for showers.
- $P(\delta)$ is the atmospheric background distribution for declination δ, as seen in Figure 9.4.
- $P_{Sig}(t)$ and $P_{Bkg}(t)$ are time PDF and are constant in the flaring time windows determined in chapter 6 and 0 outside.

In each pseudo-experiment, the maximum value of the likelihood function is found with respect to the number of signal events. To compute the significance of the signal, a likelihood ratio Test Statistic can be defined as the difference between the fitted likelihood and the likelihood of the background-only hypothesis:

$$TS = \log \mathscr{L}(\mu_{sig} = \mu_{max}) - \log \mathscr{L}(\mu_{sig} = 0) \tag{9.4}$$

with $\mathscr{L}(\mu_{sig} = \mu_{max})$ the maximum likelihood given with μ_{max} signal events and $\mathscr{L}(\mu_{sig} = 0)$ the likelihood of the background-only hypothesis.

As Wilks Theorem here does not apply ($-2TS$ does not follow a χ^2 distribution of degree 1), a significance cannot be trivially computed from the values of TS obtained in the experiment. Background-only pseudo-experiments are then performed to obtain

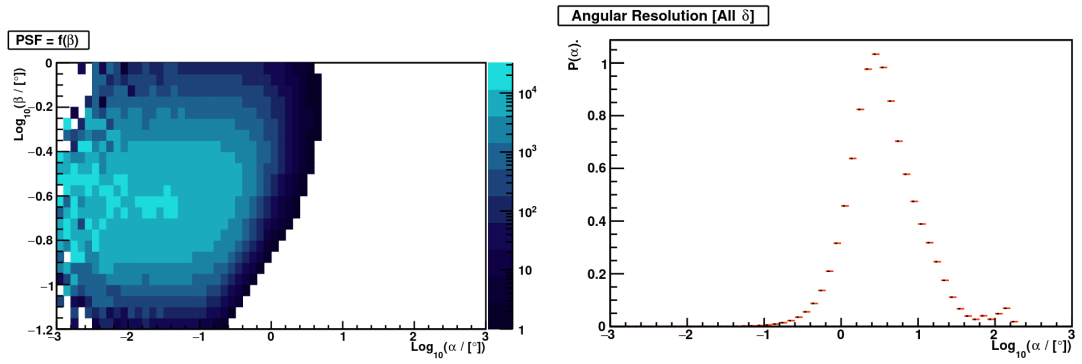

Figure 9.1.: Left: Probability of a track event to be reconstructed at an angle α from the source, given an estimated error of β and a cut at $\lambda_{\text{AAfit}} > -5.2$. Right: Probability distribution of shower event to be reconstructed at an angle α from the source. Given the low number of events, the PDF for showers is kept one-dimensional.

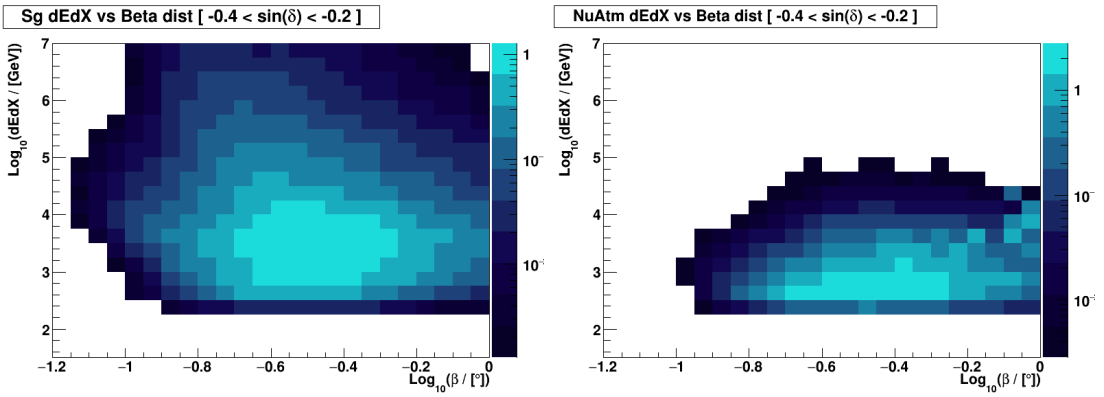

Figure 9.2.: Probability density to the reconstructed energy loss dE/dX and estimated angular error of β, for signal modeled as a power law $\phi \propto E^{-2}$ (left) and atmospheric (right) track-like events with reconstructed declination δ and $\lambda_{\text{AAfit}} > -5.2$.

the TS distribution, which allows us to compute a probability of obtaining a given TS without a signal, and to link it to the usual significance of a Gaussian distribution. Given that the number of pseudo-experiments might not be reliable due to the low number of high TS, the tail of the TS distribution is fitted by an exponential function for the extrapolation. An example of this distribution is given in Figure 9.5.

Each microquasar is treated as a separate experiment, and 1×10^8 pseudo-experiments are performed in each case.

From background-only TS distribution, the sensitivity can be obtained by computing the number of signal events n_s that verify:

$$Sen = \sum_{i=0}^{\infty} P(TS^i > TS^{n=0}_{\text{median}})\text{Poisson}(i|n_s) \tag{9.5}$$

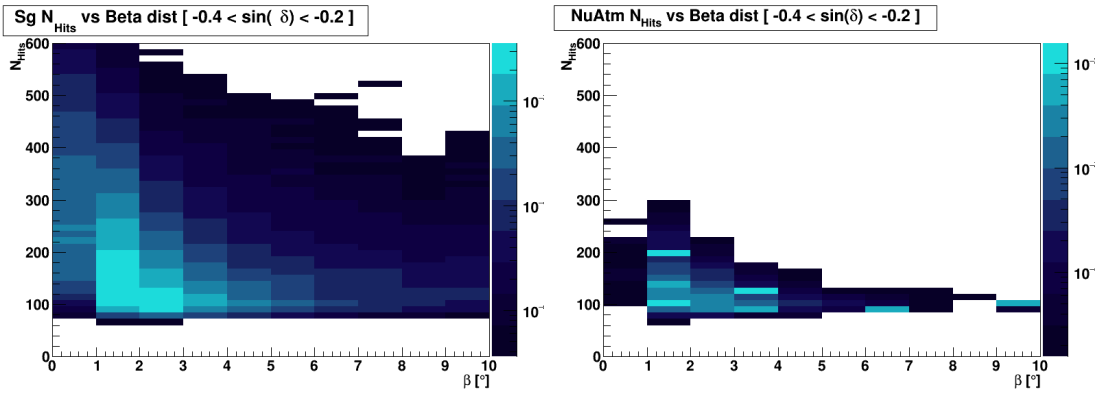

Figure 9.3.: Probability density to the number of hits and estimated angular error of β, for signal (left) and atmospheric (right) shower-like events with reconstructed declination δ.

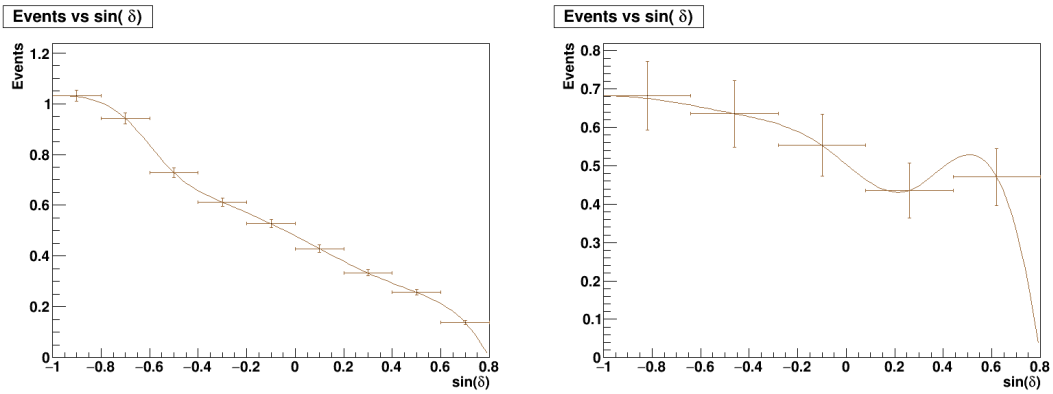

Figure 9.4.: Probability distributions of atmospheric background events w.r.t. the declination, for tracks (left, λ_{AAfit} > -5.2), and showers (right). Distributions are interpolated with a spline fitting.

with Sen the median sensitivity, usually taken at a 90% confidence level, TS^i the TS value obtained for i events, $TS^{n=0}_{\text{median}}$ the median TS value in the background-only hypothesis and Poisson$(i|n_s)$ the Poisson probability of having i with an expected n_s.

Similarly, we can compute a 5σ Discovery Potential:

$$DP^{5\sigma} = \sum_{i=0}^{\infty} P(TS^i > TS^{n=0}_{5\sigma})\text{Poisson}(i|n_s) \tag{9.6}$$

with $DP^{5\sigma}$ the probability of making a 5σ discovery, given an expected number of signal events n_s [1] and $TS^{n=0}_{5\sigma}$ the value on the TS that yields a 5σ discovery. This last value is computed from Figure 9.5.

An example of distributions of sensitivities and discovery potentials is given in Figure 9.6, where we can see the median sensitivity, 3σ and 5σ discovery potentials

[1] usually taken at 50%, i.e. a signal with n_s expected events has 50% probability to lead to a 5σ discovery

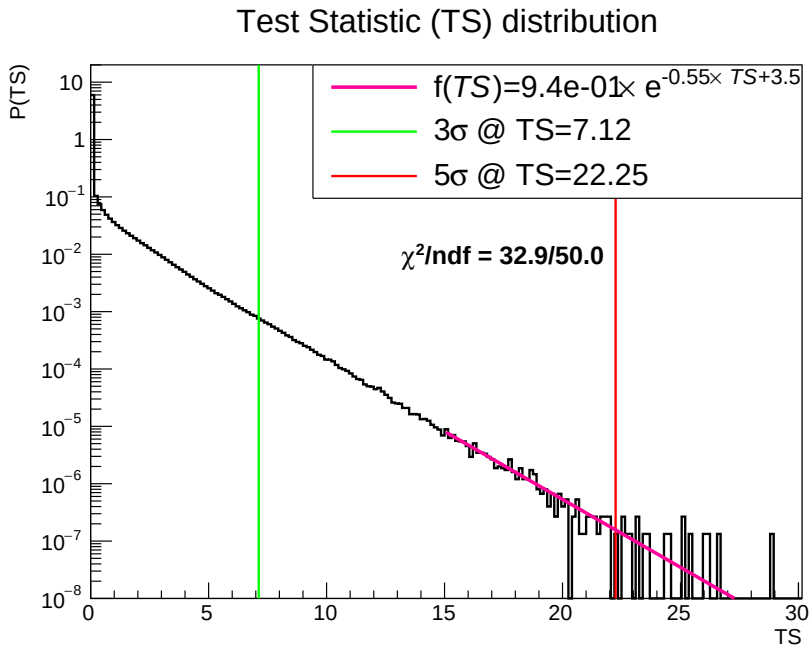

Figure 9.5.: Background-only Test Statistic distribution obtained from pseudo-experiments. The green and red lines give the TS at the 3σ and 5σ levels. An exponential fit of the distribution for extrapolation to 5σ is shown in magenta.

as a function of the number of expected signal events n_s. The number of signal events corresponding to 90% CL sensitivity, 3σ, and 5σ significance at a 50% discovery potential are given.

Finally, the Model Discovery Potential (MDP), which is the probability of a 5σ discovery assuming a given model can be computed as:

$$MDP = \sum_i \text{Poisson}(i|n_{model}) DP_i \tag{9.7}$$

with:

$$n_{model} = \phi_0 \times \text{Acc}^{\delta_s}_{period} \tag{9.8}$$

The number of events predicted by the model with flux normalization ϕ_0 and the acceptance of the period δ_s computed from the total acceptance of the detector livetime :

$$\text{Acc}^{\delta_s}_{period} = \frac{\text{Acc}(\delta_s)}{\sum_\delta \text{Acc}(\delta)} \tag{9.9}$$

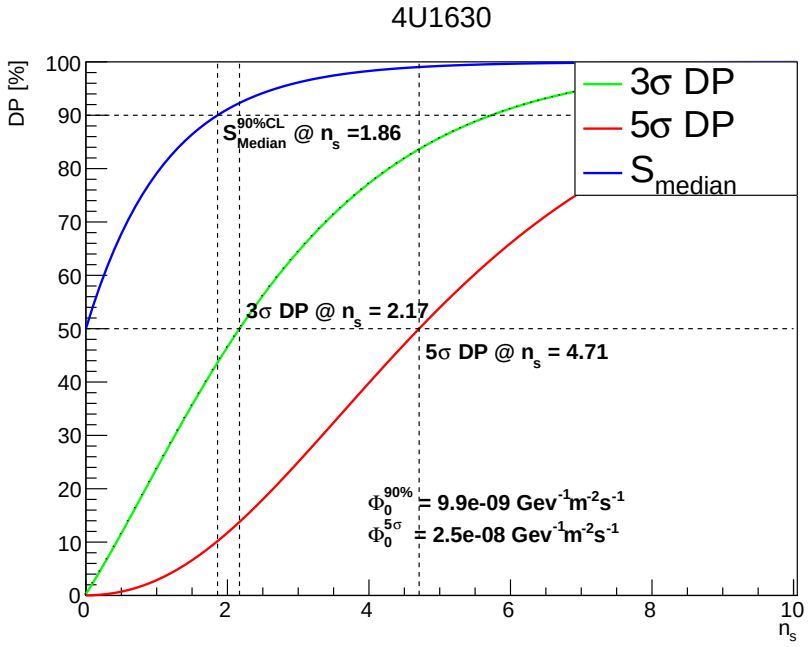

Figure 9.6.: Median sensitivity (blue), 3σ (green), and 5 σ (red) discovery potentials, as a function of the number of signal events. The number of signal events yielding a 90% CL sensitivity, 50% DP are given. Fluxes normalisations for a neutrino flux $\Phi(E) = \Phi_0 \times E^{-2}$ at 90% CL sensitivity and 5σ, 50% DP are quoted.

9.1.1.3. Systematics

In order to take into account systematic uncertainties that can not be easily reproduced from the event simulation, the following is applied:

- Detector acceptance uncertainty: a Gaussian convolution is applied to the TS distribution for n_s signal events, with a relative deviation of $\sigma = 15\%$. This is a conservative value, usually applied in point-sources analyses [205], and computed by considering a threshold detector efficiency degradation where the observed atmospheric neutrino flux is incompatible with the MC. The convolution is:

$$D(TS|\hat{n}_s) = \sum_{n_s=0}^{\infty} D(TS|n_s) \int \text{Poisson}(n_s|\bar{n}_s)\text{Gauss}(\bar{n}_s|\hat{n}_s,\sigma_{\hat{n}_s})d\bar{n}_s \qquad (9.10)$$

- Event reconstructed direction: the PSF is convoluted with a Gaussian with a relative deviation of 15% in order to smear the event generation. This value was estimated by applying a variation of the time resolution of the PMTs in the MC, which translates into a degradation of the angular resolution [205].

- A final uncertainty comes from the error of the absolute pointing of the detector.

It was found [155] to be precise within 0.13° and 0.06° in the horizontal and vertical directions, respectively. To account for this, another Gaussian smearing is applied with these values.

Finally, a correction is applied to the energy given by the track event reconstruction algorithm. This is done by comparing the estimated energy loss dE/dX to the real event energy from simulated events and applying a polynomial fit whose parameters are a function of time, β, and λ cuts, event zenith angle, and signal index.

9.1.1.4. Performances

Figure 9.7 shows the number of events expected from a hypothetical source with respect to the declination, over the whole detector live time of 4541 days, after the applied selection cuts.

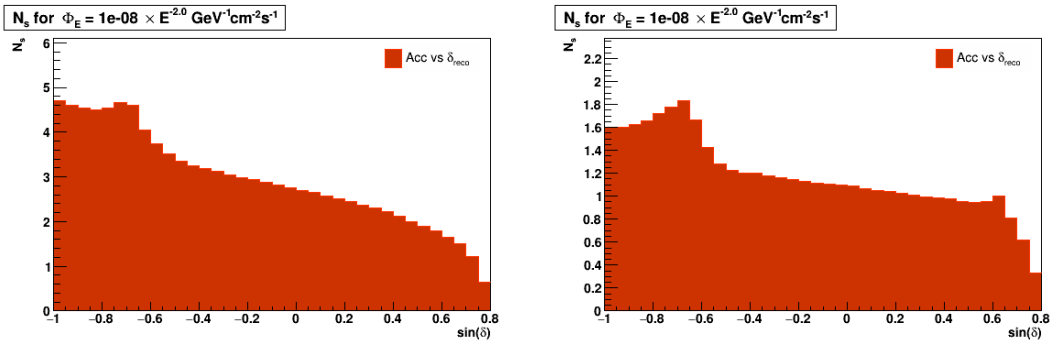

Figure 9.7.: Performance of the detector after selection cuts, given as the number of tracks (left) and shower (right) events N_s expected from a source with flux $\phi = 1 \times 10^{-8} \times E^{-2}\text{GeV}^{-1}\,\text{cm}^{-1}\,\text{s}^{-2}$, located at declination δ.

9.1.2. Cut optimisation

As mentioned above, the λ parameter from the track reconstruction algorithm is optimized by computing the MDP for each case with $\lambda > \lambda_{min} \in [-5.1, -5.2, -5.3, -5.4]$.

Table 9.1 shows sensitivity results for multiple λ cuts in the time windows previously determined. The upper section shows results from flaring periods determined section 6.1 and the lower 3 sections from time windows determined in section 6.2, with spectral states written as follows: Hard State (HS), Transition State (TS) and Soft State (SS). The analyses coinciding with HESS observations are noted as (HESS). Table 9.1 gives the 5σ MDPs (in %, given for a reference flux of $\phi(E) = 10^{-7} \times \text{E}^{-2}\,\text{GeV}^{-1}\,\text{cm}^{-2}\,\text{s}^{-1}$) , 90% flux sensitivities ($F_{90\%}$), 5σ discovery fluxes $F_{5\sigma}$ and fluences $\mathscr{F}$ upper limits for multiple λ cuts. Note: for the total flaring periods of GRS1915+105, GX339-4, and 4U1630-472 the reference flux normalization is taken at 10^{-8} instead; the MDP being too close to 100% otherwise.

The λ cuts yielding the highest MDP are then used in the final analysis.

The fluence is defined as :

$$\mathscr{F} = \Delta T \int_{E_{5\%}}^{E_{95\%}} E \frac{\mathrm{d}N}{\mathrm{d}E} \mathrm{d}E \tag{9.11}$$

With $E_{5\%}$ and $E_{95\%}$ the 5th and 95th energy percentiles of the signal events energy distribution, assuming the following spectral distribution:

$$\frac{\mathrm{d}N}{\mathrm{d}E} = F_{90\%} E^{-2} \tag{9.12}$$

This defines the energy range where the detector is most sensitive, with this selection we have for all sources: $E_{5\%} \approx 3$TeV and $E_{95\%} \approx 3$PeV.

9.1.3. Results

The likelihood fit yielded no signal event for each source and time period. The final results are then fixed to the 90% sensitivity as the upper limit.

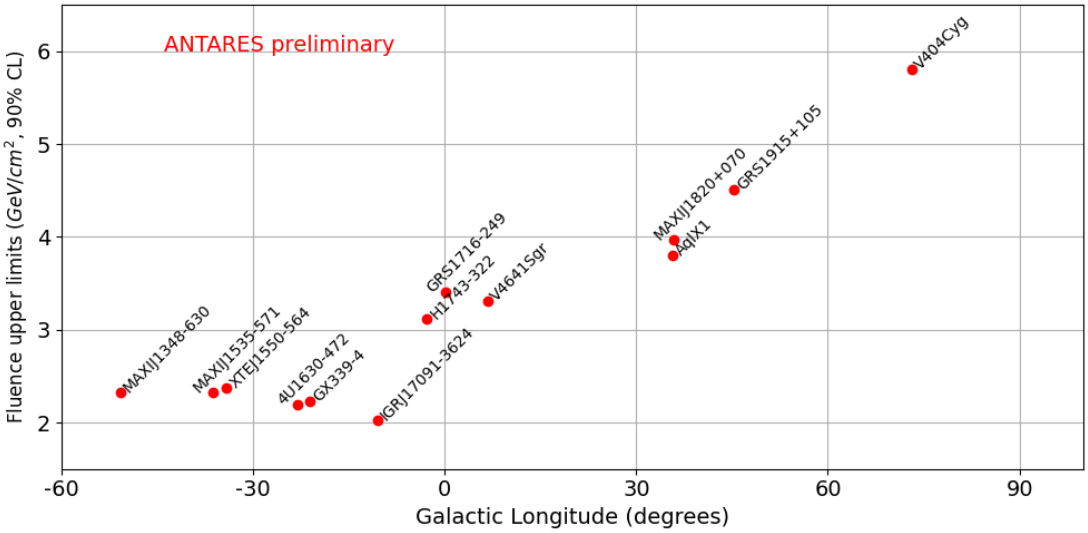

Figure 9.8.: Neutrino fluence upper limits with ANTARES against the galactic longitudes of the studied sources.

The upper limits on the fluence for the flaring periods are shown as a function of the source galactic longitude Figure 9.8. The relationship between the source location and the constraints on the fluence appears clearly, due to the better detector sensitivity to lower declination. The fluence limits as a function of the search livetimes are shown in Figure 9.9. It appears that these limits remain relatively similar with respect to the window into which the search is performed. In other terms, the constraint on the neutrino flux normalization is inversely proportional to the studied time window. For the different spectral states of MAXIJ1820+070 and GX339-4, the upper limits on the fluence and flux normalization are given in Figure 9.10. Due to the smaller observation

			$\lambda > -5.1$				$\lambda > -5.2$				$\lambda > -5.3$				$\lambda > -5.4$			
Source	Time flares (d)	Livetime (d)	MDP	$F_{90\%}$	$F_{5\sigma}$	$\mathscr{F}$	MDP	$F_{90\%}$	$F_{5\sigma}$	$\mathscr{F}$	MDP	$F_{90\%}$	$F_{5\sigma}$	$\mathscr{F}$	MDP	$F_{90\%}$	$F_{5\sigma}$	$\mathscr{F}$
IGRJ17091-3624	45	33	4.07	3.6	5.6	2.12	**4.31**	3.4	5.3	2.02	4.29	3.2	5.2	1.90	3.84	3.1	5.3	1.83
XTEJ1550-564	18	18	-	-	-	-	**0.97**	7.3	11.1	2.37	0.96	7.0	10.9	2.27	0.84	6.7	11.0	2.17
V4641 Sgr	96	96	8.26	2.1	3.3	3.58	**9.75**	1.9	3.0	3.31	9.72	1.8	3.0	3.11	7.40	1.7	3.2	3.0
AqlX1	664	629	68.9	0.36	0.75	4.03	**72.1**	0.33	0.71	3.8	68.2	0.32	0.77	3.6	-	-	-	-
4U1630-472	1437	1241	9.39	0.11	0.26	2.37	**10.2**	0.099	0.25	2.19	9.17	0.099	0.26	2.21	-	-	-	-
GRS1915+105	3873	3418	**20.0**	0.074	0.18	4.51	18.2	0.071	0.18	4.33	18.1	0.069	0.18	4.20	15.0	0.071	0.19	4.35
V404 Cyg	13	13	**0.68**	25.0	27.5	5.80	0.49	22.7	26.2	5.28	0.40	21.4	26.2	4.98	0.35	19.7	25.9	4.58
H1743-322	737	708	82.1	0.27	0.60	3.38	**85.6**	0.25	0.56	3.12	84.1	0.24	0.60	3.07	81.9	0.24	0.64	3.09
GX339-4	1277	1132	8.24	0.12	0.29	2.41	7.85	0.11	0.28	2.32	**8.44**	0.11	0.27	2.23	-	-	-	-
MAXIJ1820+070	226	221	23.4	1.08	1.77	4.28	**24.8**	1.00	1.70	3.97	24.8	0.95	1.67	3.74	21.1	0.91	1.80	3.60
MAXIJ1535-571	206	206	32.1	0.71	1.37	2.61	33.1	0.66	1.35	2.44	**35.5**	0.63	1.29	2.33	32.7	0.61	1.35	2.27
MAXIJ1348-630	171	171	28.9	0.84	1.50	2.58	28.9	0.80	1.48	2.43	**29.0**	0.76	1.47	2.32	28.4	0.74	1.48	2.27
GRS1716-249	297	296	37.5	0.68	1.25	3.62	**37.8**	0.64	1.23	3.40	37.1	0.61	1.25	3.26	32.0	0.61	1.35	3.23
GX339-4(HS)	248	204	46.5	0.57	1.06	2.08	46.7	0.53	1.06	1.95	**47.4**	0.51	1.05	1.85	45.5	0.50	1.07	1.81
GX339-4(TS)	30	27	-	-	-	-	2.78	4.27	6.40	2.07	**3.14**	4.02	6.04	1.94	2.64	3.85	6.21	1.86
GX339-4(SS)	634	576	-	-	-	-	91.8	0.21	0.50	2.13	92.3	0.20	0.50	2.05	**93**	0.20	0.49	2.03
MAXIJ1820+070(HS)	115	111	10.93	2.10	3.03	4.19	**10.94**	1.95	2.92	3.87	10.8	1.83	2.89	3.63	9.3	1.75	3.00	3.48
MAXIJ1820+070(TS)	8	8	**1.28**	30.0	28.2	4.29	0.91	27.6	28.2	3.94	0.80	25.6	27.4	3.67	0.70	24.0	27.1	3.44
MAXIJ1820+070(SS)	69	69	3.93	3.51	5.33	4.34	4.02	3.25	5.05	4.01	**4.13**	3.05	4.89	3.77	3.13	2.92	5.17	3.61
GRS1915+105(HESS)	168	91	**14.5**	1.49	2.46	2.42	13.5	1.39	2.45	2.26	14.1	1.31	2.37	2.13	11.6	1.27	2.53	2.06
MAXIJ1535-571(HESS)	12	12	**1.32**	11.8	14.1	2.53	0.81	10.9	14.7	2.35	0.89	10.3	14.0	2.22	0.78	9.85	14.1	2.11
MAXIJ1348-630(HESS)	4	4	**0.56**	35.1	37.2	2.51	0.45	32.4	36.5	2.32	0.45	30.4	35.0	2.17	0.36	28.9	35.3	2.07
GRS1716-249(HESS)	118	117	16.3	1.65	2.38	3.46	**16.3**	1.55	2.34	3.24	15.8	1.47	2.33	3.11	15.1	1.45	2.37	3.07

Table 9.1.: ANTARES sensitivities for multiple λ cuts. The Model Discovery Potential (MDP, in %) is given for a flux $\phi(E) = \phi_0 \times \mathrm{E}^{-2}\,\mathrm{GeV}^{-1}\,\mathrm{c}m^{-2}\,\mathrm{s}^{-1}$. With $\phi_0 = 10^{-8}$ for GX339-4, 4U1630-472 and GRS1915+105; and $\phi_0 = 10^{-7}$ for the rest. The optimal ones are highlighted. $F_{90\%}$ and $F_{5\sigma}$ and are the 90% flux sensitivity and the 5σ discovery flux, in $10^{-7}\mathrm{GeV}^{-1}\,\mathrm{c}m^{-2}\,\mathrm{s}^{-1}$. Fluences $\mathscr{F}$ are given in $\mathrm{GeV\,cm}^{-2}$. Some values are missing due to low-quality fit in the TS distribution from pseudo-experiments.

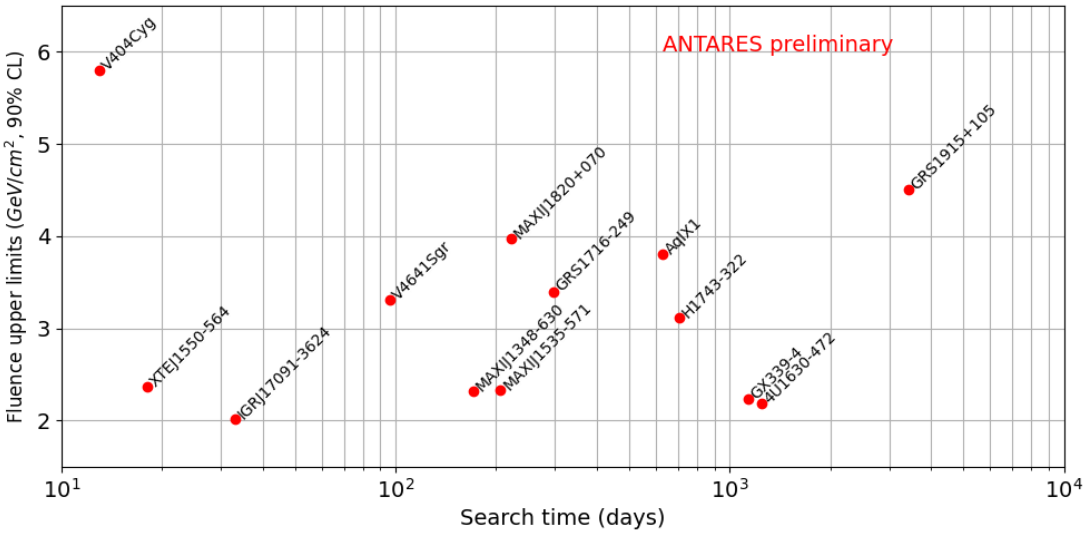

Figure 9.9.: Neutrino fluence upper limits with ANTARES against the search time. This duration corresponds to the flaring time of each source under good data-taking conditions.

time windows, the flux is less constrained during the state transition periods, but it should be highlighted that these periods are the most favorable for neutrino emission in the case of luminous ejecta with high bulk Lorentz factor [206].

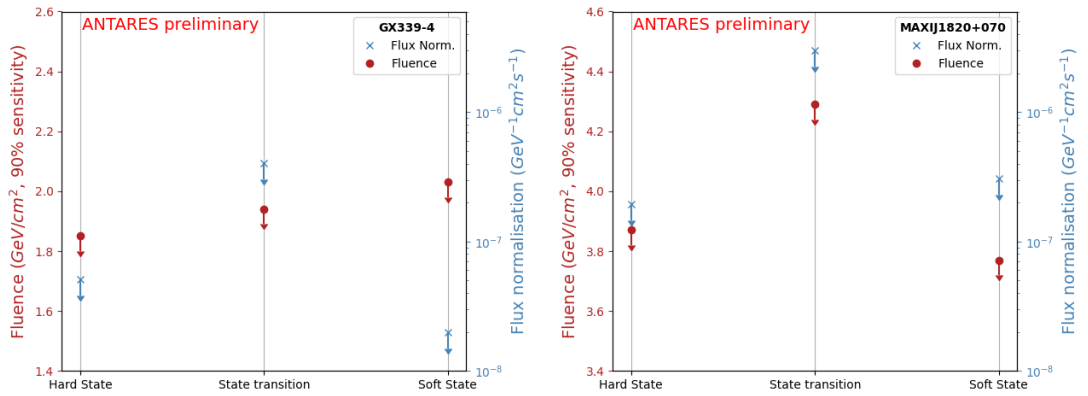

Figure 9.10.: Upper limits with ANTARES on neutrino fluence (in GeVcm^{-2}) and flux normalizations (in $\mathrm{GeV}^{-1}\mathrm{cm}^{-2}\mathrm{s}^{-1}$), assuming an incoming neutrino flux with an energy spectrum $\phi(\mathrm{E}) \propto \mathrm{E}^{-2}$. Limits are given in 3 X-ray spectral states: Hard State, State Transition, and Soft State for GX339-4 (left) and MAXIJ1820+070 (right).

Early work from 2004 during the preparatory phase of ANTARES [207] estimated the number of events detected from microquasars using the results from [108] and [109]. Among them, 3 sources have been studied in this work and a comparison

of estimations and upper limits is shown in Table 9.2. As we can see, for sources GRS1915+105 and GX339-4 the fluence upper limits greatly constrain the expected ones, as a significant neutrino signal was expected (more than 20 in the case of GX339-4) that was not observed during the operations of the detector.

Source	N_{exp}	$\mathscr{F}_{\text{exp}}$	$\mathscr{F}_{UL}$
XTEJ1550-564	5.3×10^{-3}	0.02	2.37
GRS1915+105	5.4	43.8	4.51
GX339-4	22.7	127	2.33

Table 9.2.: Comparison of expected number of events N_{exp} from [207], fluence expected $\mathscr{F}_{\text{exp}}$ from the model developed in [109] and fluence upper limits $\mathscr{F}_{UL}$ derived in this work. The expected values are re-computed from event rates and fluxes obtained in the references with observation livetimes from this work. Fluences are given in GeV cm^{-2}.

A previous ANTARES analysis of galactic X-ray binaries with transient activity was performed in [114] on data taken from 2008 to 2012. This analysis uses a comparable strategy to the one presented in this work, with the notable differences that the search is performed only on track-like event topology and that the intensity of the X-Ray flux enters into consideration in the PDF, whereas here the time component is box-shaped around the flare duration. A comparison of results obtained in this previous work with respect to this work for overlapping sources is given in Table 9.3. We can give a direct comparison between the 2 analyses from results obtained with IGR J17091-3624. The studied flare is indeed the same one, with similar time windows obtained with the respective analyses. We see an improvement with a reduction by ~ 2 in the flux upper limit, due to the inclusion of the shower-like events in the analysis and incremental refinements in the analysis methods in ANTARES. Other sources show a reduction in the resulting flux upper limits as well, due to the longer observation time windows.

Source	Previous work		This work	
	LT	$F_{90\%}$	LT	$F_{90\%}$
Aql X-1	131	1.1	629	0.33
IGRJ17091-3624	34	6.1	33	3.4
GX339-4	184	0.45	1132	0.11
GX339-4 (ST)	3	100	27	4.0
4U1630-472	144	1.0	1241	0.099

Table 9.3.: Comparison of results from [114] and this work. LT is the livetimes of the analyses in days. $F_{90\%}$ is the upper limit on the normalisation of an E^{-2} spectrum flux, given in 1×10^{-7}GeV^{-1} cm^{-2} s^{-1}. GX339-4 (ST) is the source in state transition periods.

9.2. ORCA

A similar search is performed with the ORCA detector. We analyze data from its 6-line configuration (ORCA6), taken from January 2020 to November 2021. In this period, 3 sources are found to be in a flaring state: GX339-4, Aql X1, and 4U1630-472 with the following time windows (in MJD):

- 4U1630-472: from 58922 to 59013 and from 59469 to 59631.
- GX339-4: from 58737 to 58961 and from 59237 to 59487.
- AqlX1: from 58929 to 58959, from 59092 to 59141, and from 59527 to 59575.

9.2.1. Run selection

A selection of ORCA runs is performed to remove periods with conditions not allowing good data-taking quality or good calibration. The initial livetime of the 6-line detector configuration is 633 days. The following criteria are applied on each run:

- The run livetime needs to be above 1h.
- The difference between the run computed livetime and its actual wall-clock duration can not exceed 100s. This ensures the detector did not suffer significant dead time during the duration of the run.
- HRV fraction below 20%
- Mean PMT trigger rate between 4.5 and 15 kHz. The higher boundary ensures the run was not taken during a period with high bioluminescence and the lower one that there was no issue with the electronics.
- The RMS of the trigger rate below 5 kHz, to remove runs with high variability of the bioluminescence.
- Good Data acquisition and electronic status.
- Successful detector calibration.

The final livetime for this analysis after these quality selections is 555 days (88% of the initial time).

9.2.2. Analysis Method: ON/OFF binned

The analysis is a binned ON/OFF region search, in which we use the rate of events in an OFF (control) region to estimate the number of background events in an ON (signal) region, which is our search region[2]. This choice of method was made as it

[2] Similar to the method used in HESS for background subtraction.

allows results to be purely derived from data, contrary to a likelihood fit as used with ANTARES which requires the use of PDF built from simulations. Indeed, this method is the first applied for astronomy with ORCA and more refined unbinned analysis methods will be performed once a sufficient understanding of the detector is attained, in order to guarantee robust results. The ON/OFF search method is valid under the assumption that the rate of event from the background is similar in both regions. If the studied time window is long enough (more than 24 hours), the regions can be defined in equatorial coordinates as we assume that the detector efficiency is averaged with the Earth's rotation.

The ON/OFF regions are defined as follows:

- ON region = circle with a radius to be optimised (RoI) centered to the coordinates of the source
- OFF region = band in equatorial coordinates, +/- 10° around the source declination, excluding the RoI defining the ON region.

The number of events recorded in the ON/OFF regions are written as N_{ON}/N_{OFF}. Here the OFF events are recorded at the same time as the ON events, to obtain a reasonable estimate of background event rate in the search region. The expected N_{ON} coming from background is then:

$$\text{Exp. Bkg} = N_{OFF} \times \Omega_{\text{ON}}/\Omega_{\text{OFF}} \tag{9.13}$$

with Ω the solid angles of the corresponding regions. In this search, only events reconstructed as upgoing or horizontal are taken into account, with events selected with a reconstructed zenith angle θ such as $\cos(\theta) > -0.1$. This allows for a significant reduction in the number of background events coming from atmospheric muons, with the remaining background being misreconstructed muons and atmospheric neutrinos. Moreover, the analysis only uses events reconstructed as a muon track-like, typically associated with ν_μ.

9.2.3. Event selection

A first selection is made in order to reduce most of the background noise:

- **Anti-noise cuts** Sea water radioactivity or bioluminescence can trigger the detector as pure noise events. These events are not reproduced in the simulation but can trivially be removed as they appear very localized and dim in the detector. To remove events from this noise, we require that the number of triggered hits is above 20 and the reconstructed energy is above 4 GeV.
- **Anti-sparking and afterpulse cut** PMTs occasionally "spark" due to electronic noise, which will appear as hits in the detector with particularly high ToT which can be wrongly interpreted by the algorithms as a very luminous event. Furthermore, an afterpulse can appear in the electronics which artificially increases the ToT. We then require that the maximum ToT from hits in events is below 175 ns.

- **Upgoing and horizontal** As the background coming from atmospheric muons is purely downgoing, we select for this analysis only events with direction reconstructed as upgoing or horizontal, with cos(zenith) > -0.1. In the following this cut is simply referred to as "upgoing". The events from the background are then limited to muons whose direction was misreconstructed and atmospheric neutrinos.

After this first selection, the sample of events is still dominated by muons, constituting more than 99% of the data set. However, as these events are by definition misreconstructed, we can filter them out by studying parameters related to the quality of the fit from the track reconstruction algorithms or other parameters correlated with accurate direction reconstruction.

9.2.3.1. BDT classifier

Event discrimination between muons and neutrinos is done using a machine learning classification [208]. The classifier is a Boosted Decision Tree (BDT) based on gradient boosting. MC all flavor ν events are used as signals in the training and MC atmospheric muons as background. Signal efficiency (defined as the fraction of signal events remaining above a BDT cut) for all-sky atmospheric neutrinos against muon background contamination fraction is shown in Figure 9.11 after the BDT training and classification. Additionally, Figure 9.12 show these variables, plus signal and background rates as a function of the BDT score.

Note: The BDT classifier gives a score based on estimated neutrino probability, this score is then between 0 and 1. As the selection is often close to 1, the following transformation is performed for ease of use, and in the rest of this document "Score" refers to:

$$\text{new\_score} = -\log_{10}(1 - \text{BDT\_score}) \tag{9.14}$$

The classifier training is done using variables from different algorithms from the reconstruction chain which can be sorted into the following:

- **Track direction**
  - `bestmuon_dz`, the best fit track direction in z, i.e. -cos(zenith)
  - `simplex_dz`, direction z of the JMuonSimplex fit
  - `linefit_dz`, direction z of the OnlineLineFit algorithm
- **Track reconstructed quality**
  - `Q/ndf`, the ratio of the best-fit track's likelihood and number of degrees of freedom of the fit
  - `bestmuon_quality` (Q), best-fit track's likelihood
  - `n_within_1deg`, number of track candidates reconstructed within 1° of the best reconstructed track

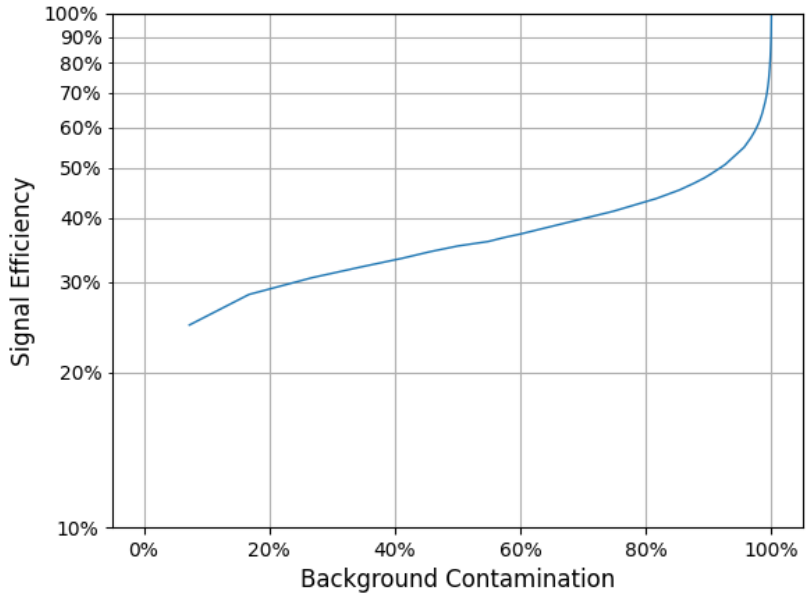

Figure 9.11.: Signal Efficiency for all-sky atmospheric ν vs μ background contamination fraction after BDT training.

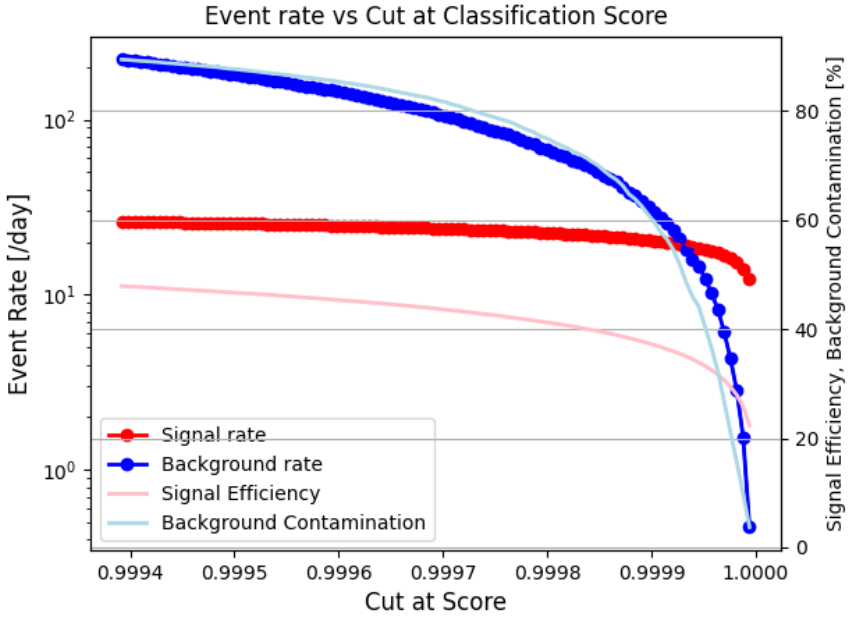

Figure 9.12.: Signal Efficiency, Background contamination fraction, signal and background rates above BDT score as a function of BDT score.

- **Track vertex position relative to the detector**

  - bestmuon_z, the reconstructed neutrino interaction vertex's z position
  - muon_start_r, horizontal distance detector center of the reconstructed vertex as given give the JMuonStart algorithm.
  - muon_start_x, x coordinate of the reconstructed vertex
  - muon_start_y, y coordinate of the reconstructed vertex

- **Track brightness**
  - tot, sum of Time Over Threshold of all triggered hits; this is a proxy for the charge observed by the triggered DOMs
  - n_trig_hits, number of triggered hits
  - muonstart_len, reconstructed track length by the JMuonStart algorithm
  - muonstart_npe_mip, number of photo-electron along the track
  - muonenergy_e, reconstructed energy

- **Track topology**
  - delta_pos_z, difference of the time-weighted z position of the earliest 20% of triggered hits and the latest 20%;
  - last_part_z, average z position of the latest 20% triggered hits;
  - first_part_z, average z position of the earliest 20% triggered hits;
  - coc, center of charge, charge-weighted triggered hits' DOM z position;
  - charge_above, charge (sum of ToT) observed by hits above the earliest hit PMT's z position
  - charge_below, charge (sum of ToT) observed by hits above the latest hit PMT's z position
  - charge_ratio, ratio of charge_above to the total charge (charge_above/tot).
  - delta_qup_qdown, charge-weighted distance of the earliest 20% of triggered hits and the latest 20%
  - delta_q_weighted_posz, difference of the charge weighted z position of the earliest 20% of triggered hits and the latest 20%
  - delta_nup_ndown_pmts, difference of hits in up-facing PMTs and down-facing PMTs
  - deltaR, distance between the earliest 20% of triggered hits and the latest 20%

9.2.3.2. Selection optimisation

The event selection is optimized using an Model Rejection Factor (MRF) minimization [209]. The MRF is defined as: MRF = $\bar{\mu}_{90}/n_s$, with n_s the expected number of signal events for a given model and $\bar{\mu}_{90}(n_b)$ the average upper limit with a confidence level of 90% for an expected number of background events n_b given by the average Feldman-Cousins upper limits weighted by their Poisson probability:

$$\bar{\mu}_{90}(n_b) = \sum_{n_{obs}=0}^{\infty} \mu_{90}(n_{obs}, n_b) \frac{(n_b)^{n_{obs}}}{(n_{obs})!} \exp(-n_b) \tag{9.15}$$

In neutrino telescopes the data is usually *blinded*, meaning that any analysis, including the event selection or the implementation of statistical methods, is elaborated without revealing the actual result until the analysis is proven to be reliable. Following this principle, minimizing the MRF is then a way to optimize the event selection by minimizing the expected upper limit from the measurement without biasing the results with unblinded data.

The two free parameters for this minimization are the classification score and the radius of the ON region (RoI). The optimization is performed using data from the OFF region defined above to estimate the background level. The number of signal events is computed with an all-flavor neutrino MC weighted to a standard flux of $F(E) = 10^{-4} E^{-2}$ GeV^{-1} cm^{-2} s^{-1}.

We note that this model can be rejected if the obtained MRF is below 1, as in that case the expected upper limit of signal events is lower than the number of signal events predicted by the model.

Table 9.4 gives optimisation results. As expected, the MRF is smaller with the larger observation time windows as the sensitivity gets better. We also note that the MRF is higher in the case of AqlX1, which is related to the higher declination of the source where the detector efficiency is lower. Figure 9.13 show 2D plots with the MRF as a function of the ROI angle and the minimum BDT score for each source, with the minimum MRF shown in each case. We note that the minimum MRF in the 2D plots slightly differs from the one in the optimization due to the binning of the plots (binning during optimizations can be considered infinitely small).

Source	4U1630	GX339-4	AqlX1
Exp. Bkg	1.15	1.35	0.60
Exp. Sig	1.0×10^{-2}	3.5×10^{-2}	3.3×10^{-3}
ROI angle	1.93	1.77	2.17
BDT score	3.39	3.60	3.30
MRF	330	100	880

Table 9.4.: Cuts optimization results.

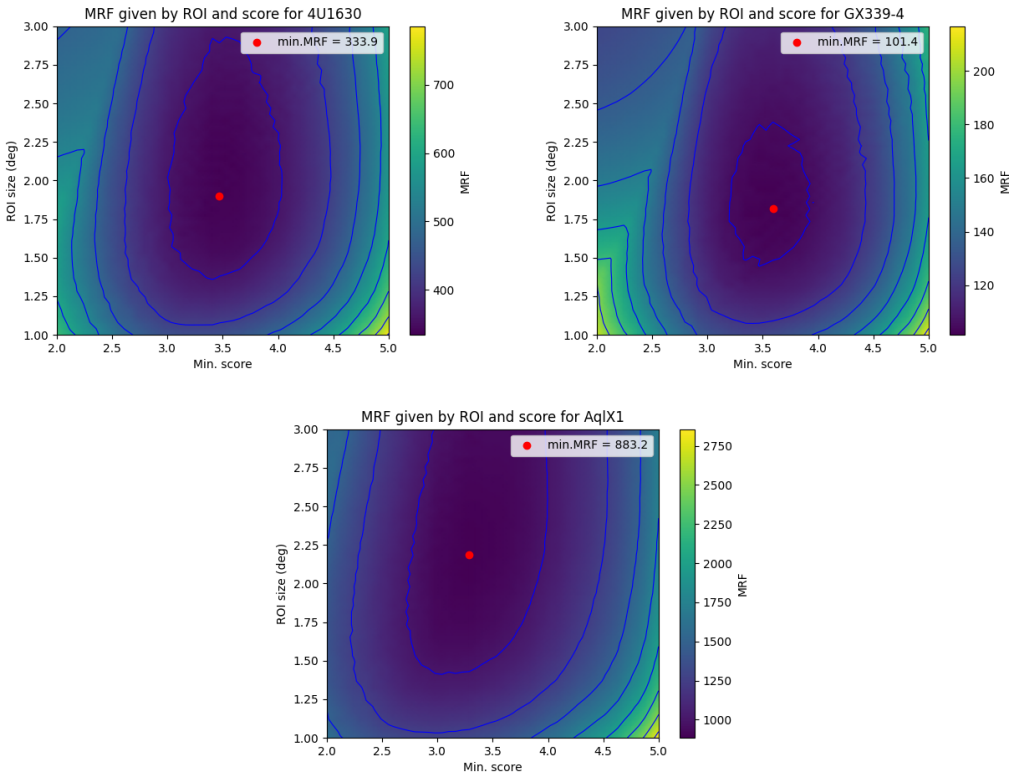

Figure 9.13.: MRF as a function of ROI angle and minimum score. For each source, the minimum MRF is shown. Contours are given with arbitrary levels.

9.2.4. Data/MC comparisons

This analysis relies on MC for optimization, event classification, and flux evaluations. Regarding the fact that the ORCA detector is still under construction, and the associated simulation algorithms can exhibit discrepancies, comparisons are made to evaluate the potential error introduced by these discrepancies.

Table 9.5 shows the event rates in data and MC (weighted to an atmospheric flux) after the selections for 3 sets of cuts: pre-cuts (anti-noise and anti-afterpulse), pre-cuts + upgoing and pre-cuts + upgoing + BDT score > 3.5. This last cut is close to the optimized cuts for the three sources and represents our selection cut. While in all-sky we obtain an overall event rate with no significant discrepancy between data and MC, we find a 23% excess in MC for the upgoing events. After the BDT selection cut however we recover a better agreement, with a 14% excess. Figure 9.14 show Data/MC distribution of the BDT score for events at the pre-cut level in all-sky and upgoing. We can see that there is an excess of MC events in the upgoing region, but we find a better agreement once the selection yields a neutrino-dominated sample. Figure 9.15 show upgoing event rate against MJD. We see two periods of disagreement around MJD 58900 and around MJD 59400. Only GX339-4 exhibits a flare in these periods that only last a few weeks. When taking into account the 250 days of livetime for this

source the effect of the disagreement should not significantly impact the final results. Finally, Figure 9.16 shows the cos(zenith) distribution at our selection level, after a score cut > 3.5, and highlights the fact that the data/MC agreement is acceptable for any event direction.

Cuts	Pre-cuts	Pre-cuts+Upgoing	Pre-cuts+Upgoing +Score > 3.5
Data event rate	4.6×10^5	9.7×10^3	14.7
MC Atm ν event rate	25.7	15.9	10.1
MC Atm μ event rate	4.6×10^5	12×10^3	6.7

Table 9.5.: Rates of event (per day) at 3 selections.

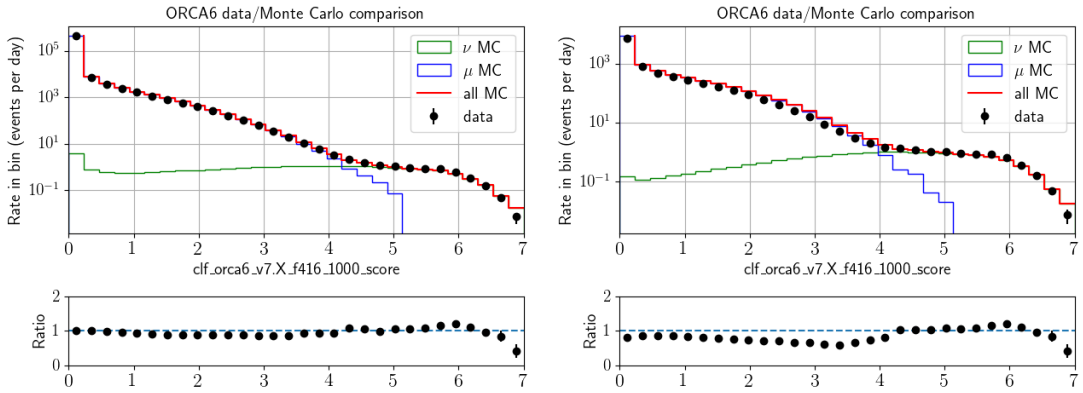

Figure 9.14.: Data/MC comparisons of the BDT score distribution for all events passing the pre-cuts (left) and upgoing events passing the pre-cuts (right)

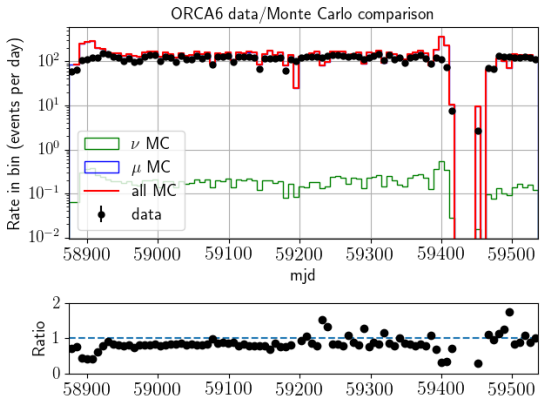

Figure 9.15.: Data/MC comparison of the event rate against MJD for upgoing events passing pre-cuts.

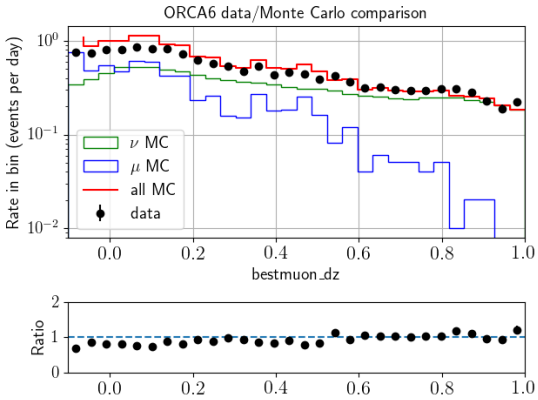

Figure 9.16.: Data/MC comparison of the cos(zenith) for upgoing events passing pre-cuts and with a BDT score > 3.5, corresponding to a selection close to the optimized one used in the analysis.

9.2.5. Selection performances

Figure 9.17, Figure 9.18 and Figure 9.19 show effective areas and signal energy differential distributions after selection for the 3 analyses. The associated energy ranges are given in Table 9.6. In each case, the results are shown after their respective optimized score selections and averaged over their respective OFF region coordinates. Figure 9.20, Figure 9.21 and Figure 9.22 show the angular resolutions after a similar selection. These resolutions are given as the Point-Spread Function, weighted by the solid angle, for an all-flavor E^{-2} spectrum; and as the median containment angle vs. Energy. The median angular error for a E^{-2} all-flavors signal is 1.53°, 1.47° and 1.45° for 4U1630, GX339-4 and AqlX1, respectively.

The energy ranges for the expected signal from the three sources can be found Table 9.6 as the 5th and 95th percentiles of the distribution from a E^{-2} weighted flux.

	5th percentile energy	95th percentile energy
4U1630	100 GeV	8.8 TeV
GX339-4	96 GeV	8.8 TeV
AqlX1	105 GeV	8.9 TeV

Table 9.6.: Energy ranges for the 3 analyses.

9.2.6. Analysis results

Results can be found in Table 9.7. No significant excess was found, with the lowest p-value being 32% for 4U1630-472 assuming that the background follows Poisson statistics. Upper limits are computed using Rolke confidence intervals [196] (using the TRolke function from ROOT), with a 90% confidence level. In this computation, the background is assumed to follow a Poisson statistic and the efficiency is modeled as

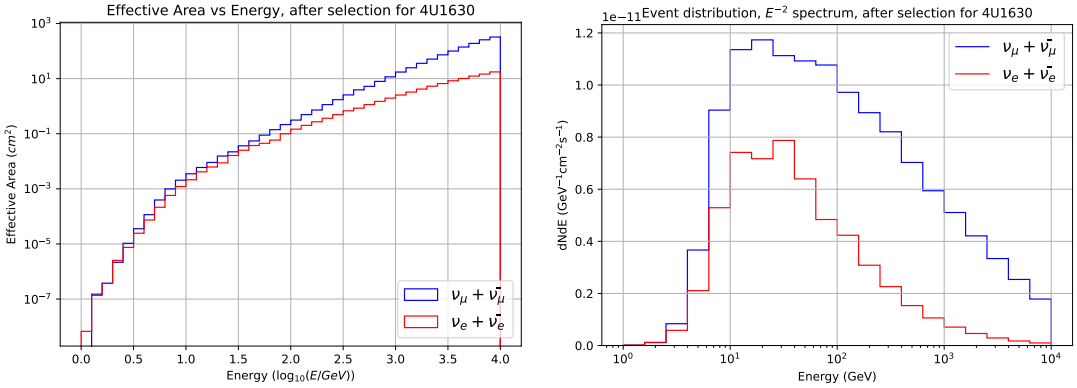

Figure 9.17.: Left: Effective Area after score selection (> 3.39) defined for the OFF band for 4U1630. Right: Signal energy differential distribution assuming an incoming neutrino flux $\Phi(E) = 10^{-4} \times E^{-2}\mathrm{GeV}^{-1}\,\mathrm{cm}^{-2}\,\mathrm{s}^{-1}$, after score selection the OFF band for 4U1630.

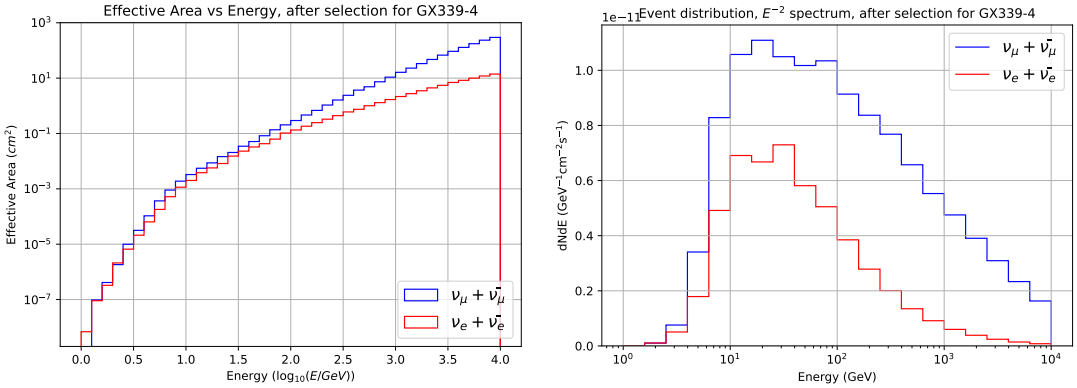

Figure 9.18.: Left: Effective Area after score selection (> 3.6) defined for the OFF band for GX339-4. Right: Signal energy differential distribution assuming an incoming neutrino flux $\Phi(E) = 10^{-4} \times E^{-2}\mathrm{GeV}^{-1}\,\mathrm{cm}^{-2}\,\mathrm{s}^{-1}$, after score selection the OFF band for GX339-4.

a Gaussian with a relative standard deviation of 30% to take into account systematic effects. This value is a conservative estimation with respect to the 15% discrepancy between data and MC.

Φ_0 is the upper limit on the normalisation of a E^{-2} signal flux, and the fluence is given by:

$$F = \Delta\mathrm{T} \int_{E_{min}}^{E_{max}} E\Phi_0 \left(\frac{E}{E_0}^{-2}\right) \mathrm{dE} \tag{9.16}$$

With E_{min} and E_{max} the 5th and 95th percentile as given in Table 9.6, $E_0 = 1$ GeV and ΔT the observation livetime.

Upper limits on the flux as a function of energy from ORCA and ANTARES can be

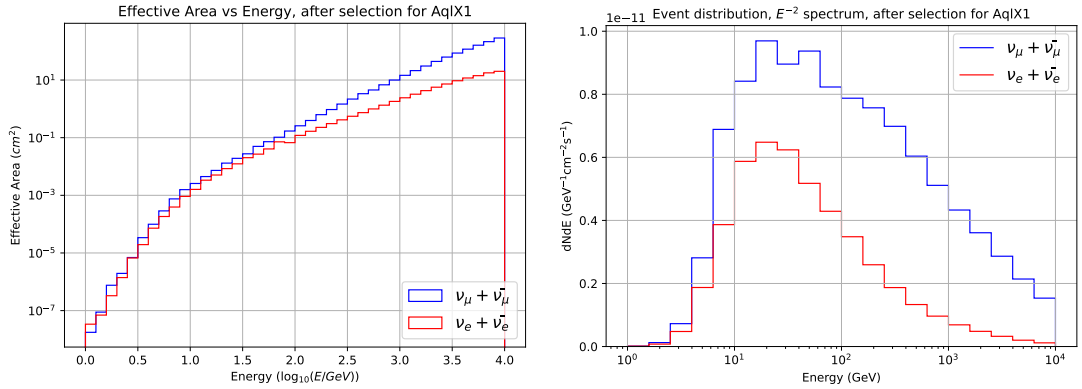

Figure 9.19.: Left: Effective Area after score selection (> 3.3) defined for the OFF band for AqlX1. Right: Signal energy differential distribution assuming an incoming neutrino flux $\Phi(E) = 10^{-4} \times E^{-2}\text{GeV}^{-1}\,\text{cm}^{-2}\,\text{s}^{-1}$, after score selection the OFF band for AqlX1.

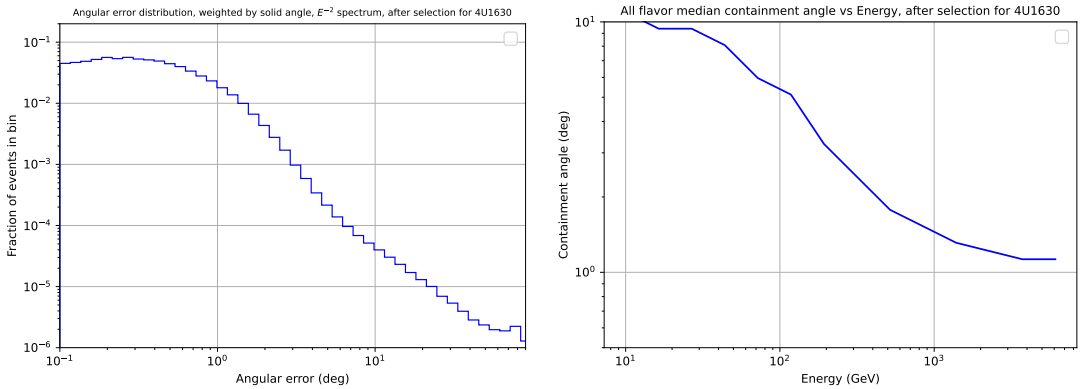

Figure 9.20.: Left: Angular error distribution, weighted by solid angle, after selection for 4U1630 in its OFF bands. Right: Median angular resolution (defined as the 50% containment angle) vs. energy.

found in Figure 9.23. The ORCA upper limit is less constraining due to the smaller detector and the shorter observation times but provides complementary coverage in a lower energy range with respect to ANTARES.

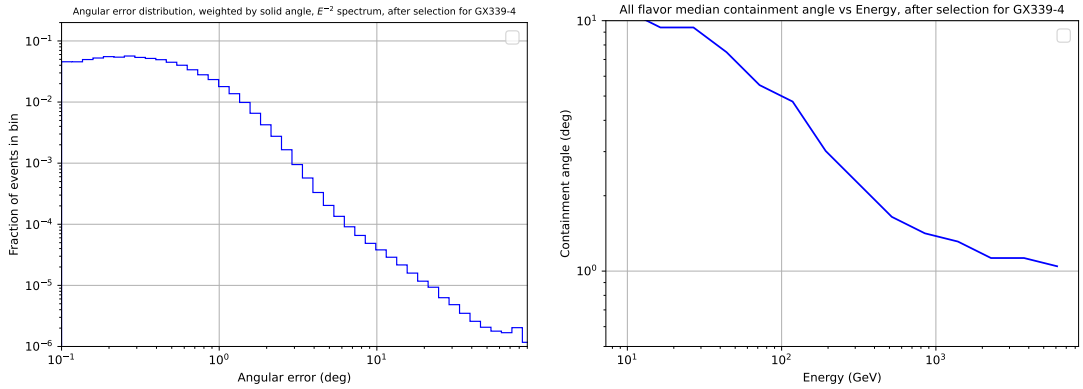

Figure 9.21.: Left: Angular error distribution, weighted by solid angle, after selection for GX339-4 in its OFF bands. Right: Median angular resolution (defined as the 50% containment angle) vs. energy.

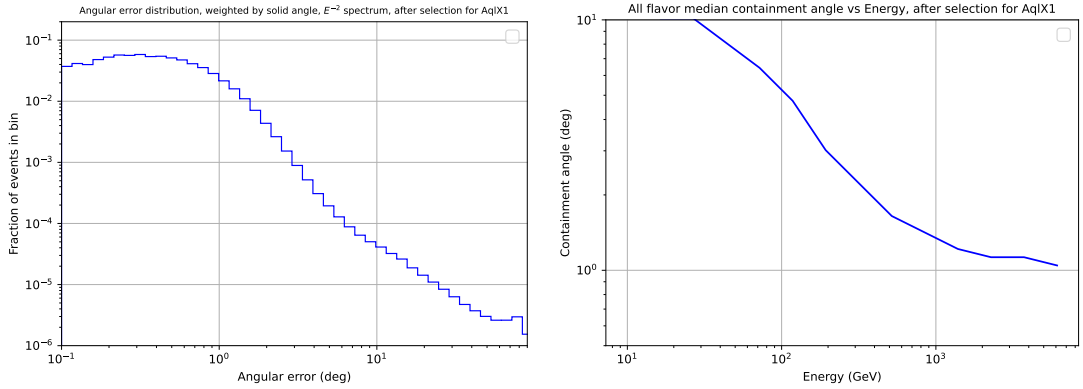

Figure 9.22.: Left: Angular error distribution, weighted by solid angle, after selection for AqlX1 in its OFF bands. Right: Median angular resolution (defined as the 50% containment angle) vs. energy.

Source		4U1630-472		GX339-4		Aql X-1	
N_{ON}	Time (MJD) Dist. from source	**2**	59495.887, 59526.473 1.77°, 1.80°	**1**	58956.383 1.35°	**1**	59128.48 1.52°
N_{OFF}		474		648		291	
Exp.Bkg		1.15		1.35		0.60	
p-value (pre-trial)		0.32		0.74		0.45	
Φ_0^{UL} (GeV^{-1}cm^{-2}s^{-1})		6.7×10^{-6}		2.2×10^{-6}		8.8×10^{-6}	
$\mathscr{F}^{UL}$ (GeVcm^{-2})		3.3×10^{2}		1.9×10^{2}		2.5×10^{2}	

Table 9.7.: KM3NeT/ORCA6 search results. N_{ON} and N_{OFF} are respectively the number of events in the ON and OFF regions after selection. The times and distances from the source are given for events in the ON region. Exp.Bkg. is the expected number of background events in the search region. The p-value is computed assuming a Poisson-distributed background. Φ_0^{UL} and $\mathscr{F}^{UL}$ are respectively the upper limits of the flux normalization and the fluence, assuming an incoming neutrino flux with an energy spectrum $\phi(E) \propto \Phi_0 E^{-2}$. Upper limits are given with a 90% confidence level.

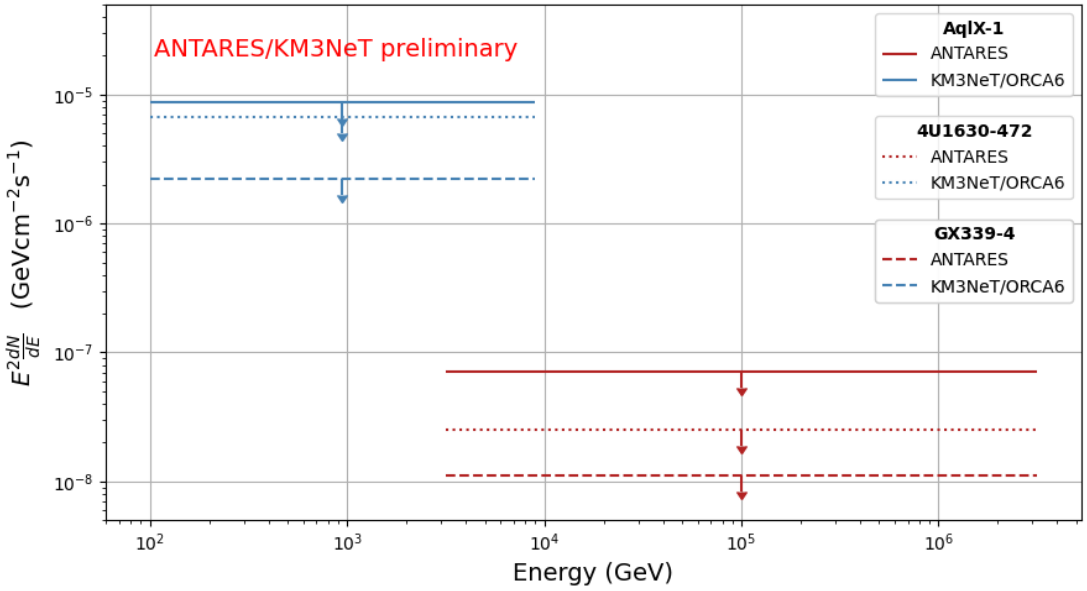

Figure 9.23.: Neutrino flux upper limits for AqlX-1 (solid), 4U1630-472 (dotted) and GX339-4 (dashed) in KM3NeT/ORCA (blue) and ANTARES (red) energy ranges. Limits are given as $E^2 \frac{dN}{dE}$, (in GeVcm^{-2}s^{-1}), assuming an incoming neutrino flux with an energy spectrum $\phi(E) \propto E^{-2}$.

10. Discussion

10.1. Comparisons between HESS and ANTARES upper limits

By using the parametrization developed by Villante and Vissani [36], we can compute a neutrino flux expected from a γ-ray flux through the production of pions.

Comparisons between this extrapolation from HESS results and ANTARES results are given on Figure 10.1. In this example, we compute the 90% CL integral upper limits from HESS observations which are then converted into an upper limit on the all-flavor neutrino fluxes assuming full mixing.

One might assume that the measurement from HESS would predict an upper limit on the neutrino flux orders of magnitude lower than the ANTARES results. However, the parametrization relies on a few assumptions that are critical in our case. The most important is that the source is assumed to be transparent to γ-rays, which is not straightforward in the case of an emission located in a microquasar jet where the photon density is expected to be high. The second important assumption is that the putative γ-ray flux is entirely generated by hadronic processes. Regarding these assumptions, we can conclude that both neutrino flux upper limits are not exactly comparable in most real cases in astrophysics. Furthermore, 10.1 illustrates the fact that neutrino telescopes, which are non-pointing, can show better results by passively accumulating livetime for observations of long-lived events.

10.2. Modeling with JetSeT

In the previous sections, we have calculated upper limits for the photon flux from several microquasars, in the HE (Fermi) and VHE (HESS) domains. It is then possible to use these upper limits within Spectral Energy Distributions gathering all the MWL data available at the epochs contemporaneous to HESS observations. We will focus on MAXIJ1820+070, Hard state, and hard-to-soft state transition, and on the transition of MAXIJ1535-571. For these targets and epochs, numerous data are available to build the SEDs and published studies provide estimations of the parameters required to define properly the systems: distance to Earth, BH mass, companion type, estimation of accretion disk parameters, and jet parameters. These inputs are essential to build the model and to have correct starting values for fitting it. We use the JetSeT framework[1] [210, 106, 211, 212]. This choice is driven by the fact that the Hard State

[1] Jets SED modeler and fitting Tool

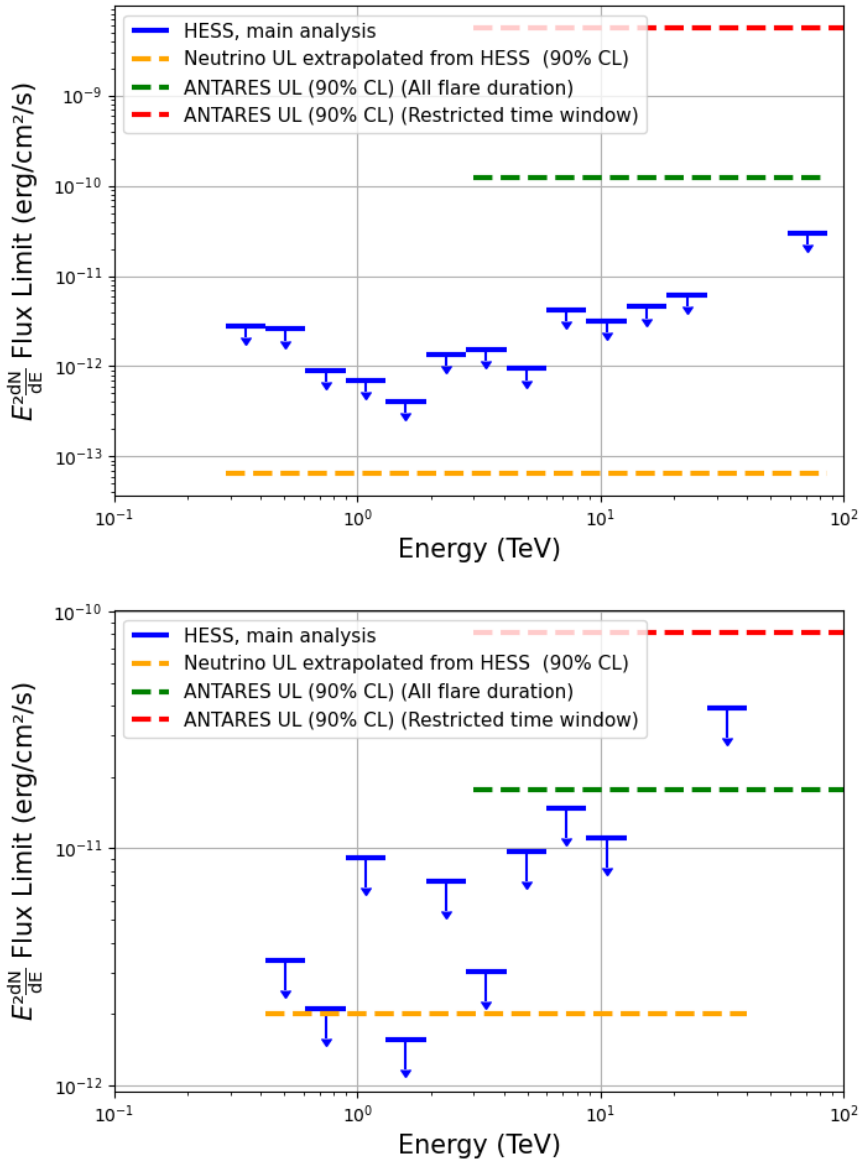

Figure 10.1.: Comparisons of neutrino flux upper limits measured from ANTARES and extrapolated from HESS upper limits (yellow). In blue are HESS differential upper limits, in green are ANTARES upper limits measured in the entirety of the flaring period, and in red are ANTARES upper limits measured in the time window framing HESS observations. **Top**: MAXI J1348-630 during its ST; Livetimes of HESS, ANTARES in the entire flaring period, and ANTARES in the restricted time window are 4.2 hours, 4 days, and 171 days, respectively. **Bottom**: GX 339-4 during its HS; Livetimes of HESS, ANTARES in the entire flaring period, and ANTARES in the restricted time window are 2.0 hours, 204 days, and 1132 days, respectively.

of MAXIJ1820+070 has been well studied with this framework in [213], modeling a compact radio-jet and an accretion disk irradiated by a corona[2]. These elements allow us to start from a good base: we study the new constraints that HE and VHE upper limits bring on the model, which has been developed without this information. We apply the same modeling to the transition of MAXIJ1535-571, for which HESS observations were essentially performed during a Hard Intermediate State. Finally, we use a simpler modeling, based on an ejected blob, to interpret the hard-to-soft state transition of MAXI J1820+070.

The question we would like to address is: in the studied cases, are the HE and VHE observations constraining? In other words, can the studied systems lead to observable HE and VHE photon fluxes?

Regarding neutrinos, the JetSeT framework implements $p-p$ hadronic interactions in jets, after Kelner et al [34]. However the modeling is more difficult than for leptonic processes because i) in addition to the proton population -and related secondary electrons-, we need to define an electron population, increasing the number of degrees of freedom, ii) possible VHE gamma-ray absorption within the jet is not implemented, with, as a consequence, a flux of photon systematically higher than the flux of neutrino. This is not suitable in cases where a strong VHE-photon absorption occurs by interaction with a strong magnetic field, such as at the base of a compact jet.

In the following, we will focus on leptonic scenarios.

10.2.1. JetSeT and modeling

JetSeT provides tools to import SEDs and to fit them with built-in models. The simplest case, that we use for MAXIJ1820+070 hard-to-soft state transition, is summarised in Figure 10.2: it consists of an accretion disk associated with a jet, itself represented by a single zone ("blob") in which we assume that accelerated electrons follow a given energy distribution. In our case, it will be a power law with exponential cut-off, governed by 3 parameters: PL index (p), cut-off (γ^e_{cut} in terms of Lorentz factor of electrons), and normalization (N_e, density of electrons in the blob). The other parameters of the system are the size of the blob (R), its distance to the black hole (R_H), its bulk Lorentz factor (γ_{jet}), the magnetic field in it (B), the ratio of cold protons to relativistic electrons, the angle of the jet with respect to the line of sight (θ_{jet}), the disk inner and outer radii, the disk luminosity, the accretion rate, the black hole mass and the distance to Earth. The disk is modeled with a multi-color black-body emission. A companion star (characterized by its temperature T_{Star} and radius R_{Star}) can be associated. The jet electromagnetic emission includes synchrotron radiation and inverse Compton: Self Synchrotron Compton (SSC), and External Compton (EC) on photon fields of the star and disk calculated at the level of the blob.

JetSeT offers the possibility to add analytical models, to reproduce visible-to-X-ray range in cases more sophisticated than the one of a simple multi-color BB disk.

[2]Parts of this work relies on unreleased code kindly provided by Andrea Tramacere, main JetSet developer.

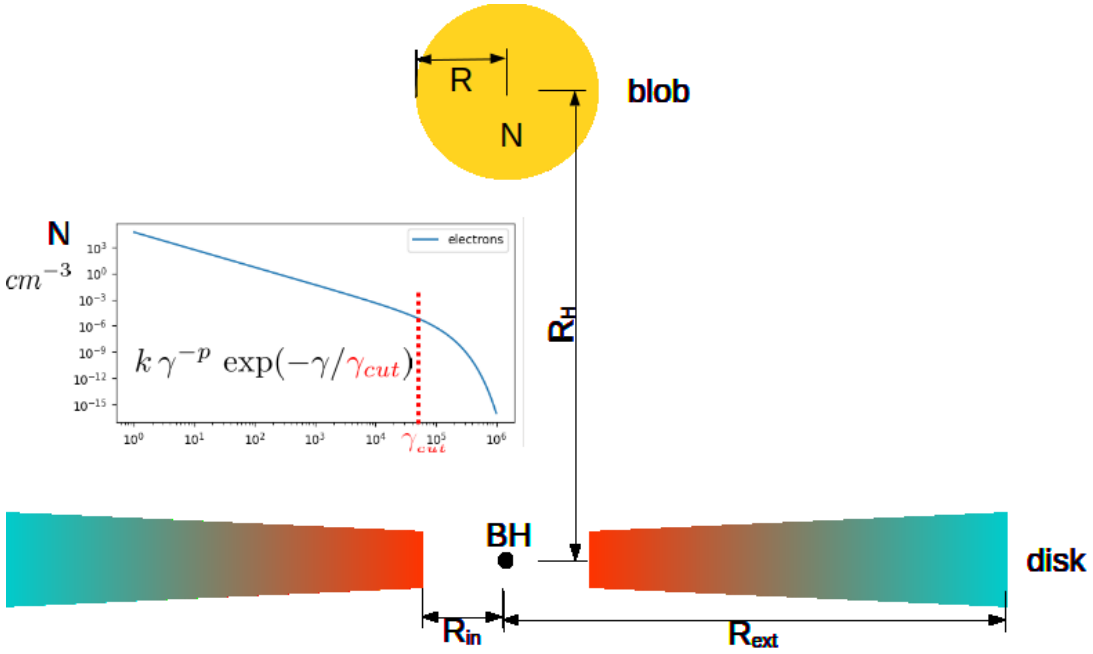

Figure 10.2.: Sketch of the simplest model used in JetSeT ([213]). In this work, the distribution of electrons in the ejected blob is always chosen as a power-law with exponential cut-off. Expressed in terms of the Lorentz factor, the energy cut-off is γ_{cut}.

Especially, in hard states, the modeling of the disk emission is complex and we have to use analytical models. In the current version of JetSeT, the calculation of the photon field from the disk modeled in this way to the jet is not implemented, for EC calculation. We then have only SSC, and we will be cautious about the consequences of our study. The two following sections describe briefly specific developments made in [213] for the study of the Hard State of MAXIJ1820+070. We will indeed use this modeling in our study of the same state of MAXI J1820+070, and also the Hard Intermediate State of MAXI J1535-571.

Irradiated Disk model In the Hard State, a commonly accepted model called the truncated disk model is composed of an optically thin and geometrically thick corona surrounding the black hole event horizon, and of an accretion disk with an inner edge at a larger distance from the black hole than in the other states ("truncated" disk). In addition to the direct light emitted by the accretion disk, several other contributions are assumed in the model: The comptonization of disk photons by a hot corona brings $\mathcal{O}$(100 keV) X-rays, a fraction of it irradiating the disk. The comptonization model is taken from [214]. The irradiation model is taken from [215] and [216]: it consists in the reflection and in the reprocessing of the Comptonized component on the disk, increasing and broadening the disk luminosity w.r.t. its intrinsic luminosity, and making consistent a larger inner radius (truncated disk). The Comptonized

component is modeled with ([214]):

$$E^2\frac{dN}{dE} = k\frac{E_{b,Comp}^{2-\Gamma_{Comp}}\exp(-E/E_{c,Comp})}{(E/E_{b,Comp})^{-3}+(E/E_{b,Comp})^{\Gamma-2}} \tag{10.1}$$

which becomes $kE^{2-\Gamma_{Comp}}\exp(-E/E_{c,Comp})$ for $E \gg E_{b,Comp}$. The normalization L_{Comp} is parameterized as a fraction of the disk intrinsic luminosity, L_{Disk}: $L_{Comp}^{ratio} = L_{Comp}/L_{Disk}$. This gives the bolometric flux $L_{bol} = L_{Disk} + L_{Comp} + L_{rep}$, where $L_{rep} = f_{in} \times L_{Comp}$ is the thermalized fraction of L_{Comp}, assumed to occur in the inner part of the disk, where corona and disk overlap: between R_{in} and a radius R_{irr}. We write $f_{in} = \frac{\Omega}{2\pi}(1-a)$, where $\frac{\Omega}{2\pi}$ is the solid angle, and a is the reflection albedo integrated over energy and angle. An additional contribution has to be taken into account in the model: the self-irradiation of the disk, because a fraction f_{out} of the bolometric luminosity irradiates the outer part of the disk. Finally, a Compton hump is also modelled in [213], with the shape $K_{hump}E^{-\Gamma_{hump}}\exp(-E/E_{c,hump})$.

In the modelling, the radii r_{in}, r_{out}, r_{irr} are written in terms of R_{in}: *i.e.* $r_{irr} = R_{irr}/R_{in}$, $r_{out} = R_{out}/R_{in}$, $r_{in} = 1$, with $R_{in} = \sqrt{\frac{L_{Disk}}{4\pi\sigma_{SB}T_{Disk}^4}}$, σ_{SB} being the Stefan-Boltzmann constant.

Radio jet model In [213], to reproduce correctly the radio behavior, a model of a compact radio jet is developed. Figure 10.3, extracted from [213], presents a sketch of this modeling. The parameters that we will fit, especially the magnetic field B, region size R, electron distribution (density N_e^{acc}, spectral index p, cut-off γ_{cut}^e) are in the acceleration region. In the first radio slice, the density of electrons is taken identically to the one in the acceleration region, which is set by the parameter $N_{frac} = 1$ (ratio between both). The evolution of magnetic field, electron density, and region size along the jet is then driven by equations of the form $X(z) \propto X_{ref}(z/z_{ref})^m$. Evolution of electron energy cut-off along the jet is calculated by taking into account the synchrotron and adiabatic losses according to [217], assuming that the power-law index is unaffected: the decrease of electron energy is carried only via the decrease of the energy cut-off.

10.2.2. Spectral Energy Distributions of the studied sources

The construction of the SEDs has been performed using i) Radio to X-ray data available in published works, ii) X-ray data provided by public web portals of Swift/XRT[3] and MAXI[4]. Low energy X-ray data (< 4 keV) have been corrected from interstellar extinction using hydrogen column density. The value of $0.14\,10^{22}\,\mathrm{cm}^{-2}$ has been taken from [195] for MAXIJ1820+070. Regarding MAXIJ1535-571, published values vary from $3.3\,10^{22}\,\mathrm{cm}^{-2}$ ([87]) to $5.5\,10^{22}\,\mathrm{cm}^{-2}$ ([218]), we fixed it to the value found in [219]:

[3] UK Swift Science Data Centre
[4] MAXI on-demand process

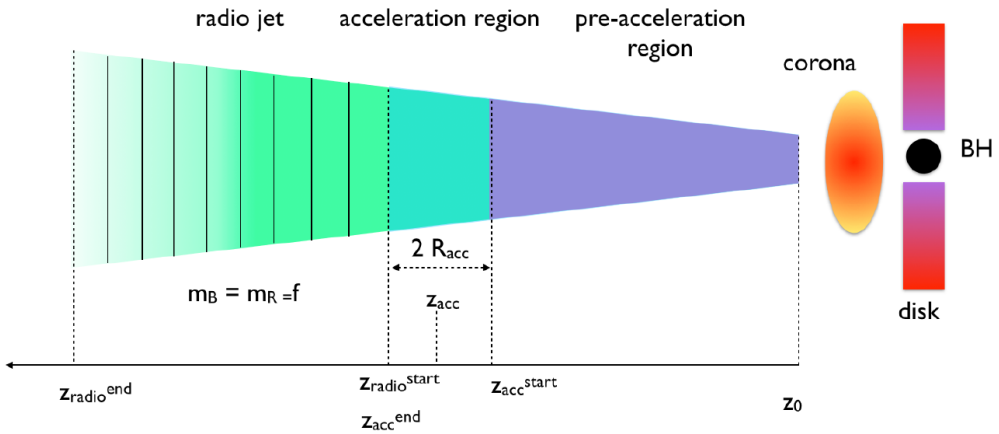

Figure 10.3.: Sketch of the model of radio jet extracted from [213]. A steady jet is split into 3 parts: pre-acceleration region, acceleration region, and radio jet, made of 20 slices of logarithmically equal thicknesses. Along the slices, the magnetic field, electron density, region size, and electron energy cut-off, are scaled. The electrons are supposed to be at their maximal energy in the acceleration region which starts at $z_{acc}^{start} \equiv z_{inj}$, and has a size of $2R_{acc}$, and ends at $z_{acc}^{end} = z_{radio}^{start}$, where the slices mostly responsible for radio emission start. The distribution of electrons is a power-law with exponential cut-off, decreasing along the jet. At z_0, the base of the jet, we note the magnetic field B_0. In the modeling, the start and end of the radio jet are expressed in multiples of z_{radio}^{start}, namely $R_{H-start-frac}$ fixed to 1 and $R_{H-stop-frac}$, fixed to 30000.

$4.05\,10^{22}\,\mathrm{cm}^{-2}$.

The MWL data used in the SEDs come from various publications:

Data used for MAXIJ1820+070 Hard Sate (in MJD [58189 – 58304]) have been collected by [213] authors, and are taken from this publication: VLITE and JVLA for radio, ALMA for millimeter WL, VLT X-shooter for IR/Vis/UVB, XMM Newton and INTEGRAL for X-rays. To this, we add the upper limits from our publication [1].

Data used for MAXIJ1820+070 hard-to-soft transition (in MJD [58304 – 58311]) are the ones collected for our publication [1]. To this, an ALMA measurement [220] is added, as well as a REM measurement from [221].

Data used for MAXIJ1535-571 hard intermediate state (in MJD [58006 – 58018]) are taken from [222] for ATCA, ALMA, REM, LCO, and VISIR. Swift/XRT and MAXI/GSC X-ray data are taken from the public web interfaces allowing for data collection and processing, and then have been treated with XSPEC[5]. Integral X-ray data are taken from [87]. We use XRT data up to 4 keV, then MAXI/GSC data, and INTEGRAL data. We use the upper limits calculated in this work for HE and VHE ranges.

A systematic error of 5% is added to all data which are not upper limits.

[5] Xspec: an X-Ray Spectral Fitting Package

	MAXIJ1820+070		MAXIJ1535-571	
distance (kpc)	2.96	[224]	5.4	[225]
M_{BH} ($M_\odot$)	8	[187, 224, 213]	10.4	[225]
γ_{jet}	2.2	[224, 213, 1]	3	
θ_{jet} (°)	64	[226, 224]	40	

Table 10.1.: Parameters of the microquasars used in the modeling. Lorentz factor and jet inclination angle being not given as values, but as limits by [223] ($\theta_{jet} \leq 45°$ and $\gamma_{jet} \geq 1.4$), we set values compatibles with these limits.

10.2.3. Leptonic model for MAXIJ1820+070 Hard State and MAXIJ1535+071 transition

To get a good starting point for the modeling, which involves up to 26 parameters, with up to 14 free ones, and needs reasonable values for fixed ones, we collected information from published studies. For MAXIJ1820+070 hard state, authors of [213] have implemented the irradiated disk model and a model of compact jet emitting in radio, and have used it for fitting the SED. This is our starting point for this state. For the transition of MAXIJ1820+070, we start from analytical estimates made in our publication [1], and we use a simple model of an ejected blob, with a standard multi-color black body accretion disk emission, and an additional contribution (hump). For MAXIJ1535-571, for which we consider the time interval [MJD 58006 - MJD 58018] framing HESS observations, we first note that the work in [87], using INTEGRAL data in addition to MAXI/GSC data, splits this time period into 2 states: Hard Intermediate State (HIMS), until MJD 58012, and Soft Intermediate State (SIMS), from MJD 58016, as shown in Figure 10.4. Among the 12 HESS runs used, 1 only falls in this SIMS. Five are in the period between HIMS and SIMS as defined by [87]. In addition, [223], from radio data measuring the position of the moving ejected knot, and extrapolating it back in time, estimate a time of launching ranging from MJD 58003 to MJD 58024, depending on the model of deceleration they consider. Finally, [222], in radio data, identify a change in the frequency of the jet spectral break at MJD 58013, included in our period. We have then clearly observed a transition, however, we will see in the SED, by comparing it with the one of the Hard State of MAXIJ1820+070, that there is a strong similarity, suggesting the presence of the same contributions to X-rays during our observation: a disk irradiated by a corona.

We use JetSeT to fit the SEDs, and we find the results as shown in Figure 10.5 and Table 10.2 for MAXIJ1820+070 Hard State, and in Figure 10.6 and Table 10.3, for MAXIJ1535-571 transition. The irradiated disk model combined with the radio-emitting jet model described in subsection 10.2.1 are used. The χ^2/ndf are 1.14 and 1.13 respectively, arguing for a correct fit. The errors on fitted parameters are given by the MINUIT MIGRAD module and are under-estimated. They should be taken with caution, and not used for comparing values, but are not determinant in the question we want to address: what is the behavior of HE and VHE components, and

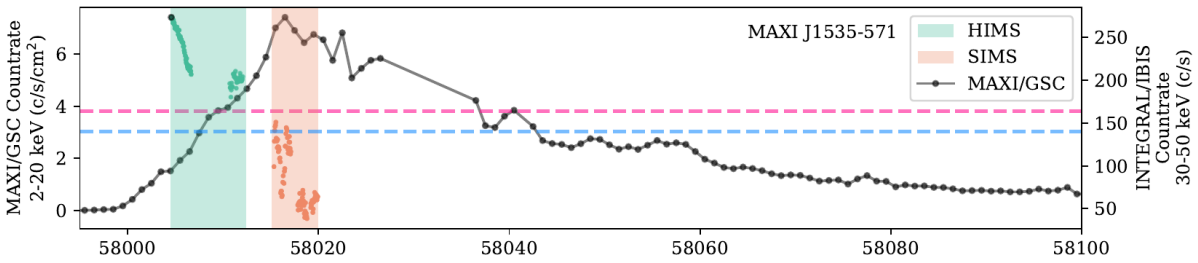

Figure 10.4.: MAXIJ1535-571 Light Curve in the 2-20 keV range of MAXI/GSC detector, and INTEGRAL/IBIS count rate in 30-50 keV. Figure extracted from [87]. It allows us to conclude that most of the VHE data, taken from MJD 58006 to MJD 58018, with only one run at the beginning of the SIMS, cover the HIMS+transition, which impacts the elements of the modeling.

how the upper limits we calculated are constraining. It has to be noted that the fitting procedure, with up to 14 free parameters in this work, is not always robust and we can't let too many parameters free. Some parameters have to be frozen. In the radio jet, the frozen parameters, except γ_{jet} and p, are established phenomenologically in [213] for MAXIJ1820+070, and we use the same assumptions and calculations (provided by the framework) for MAXIJ1535-571. The values γ_{jet} are the ones in Table 10.1, and the value of $p = 2.05$, close to the value in [213] (2.08), has been chosen after tests in range $2.0 - 2.1$, to provide the best fit χ^2/ndf of the final fit. Frozen values in the irradiated disk model result from pre-fit procedures in the X-ray range only (specifically for the hump in the case of MAXIJ1535-571), or are taken from [213] for MAXIJ1820+070 (values of f_{in}, r_{irr}, T_{Disk}). The assumed more generic value $E_{b,Comp} = 0.15$ keV is taken from [213] for both targets. The value of $T_{Disk} = 7\,10^6$ K in the case of MAXIJ1535-571 is chosen compatible with [218], who find, from NuStar and HXMT spectra, values from $4\,10^6$ K (HIMS, in which we mainly observed) to $14\,10^6$ K (SIMS). The value of T_{Disk} is not independent, as related to $r_{irr} = R_{irr}/R_{in}$ and L_{Disk} via $R_{in} = \sqrt{\frac{L_{Disk}}{4\pi\sigma_{SB}T_{Disk}^4}}$, σ_{SB} being the Stefan-Boltzmann constant. In our case, r_{irr} and L_{Disk} are free parameters.

For MAXIJ1820+070, we find results very close to [213], which is expected as we work on the same data with the same tool. The difference is the use of upper limits from HE and VHE domains, but it doesn't impact significantly the results, the predicted flux being far from this domain, as shown in Figure 10.5.

The modeling for MAXIJ1535-571 doesn't reach the HE and VHE domains either, as shown Figure 10.6. Table 10.3 shows that the fit results are rather different from MAXIJ1820+070 for the irradiated disk, especially the reprocessed fraction of the Compton tail is larger ($f_{in} = 0.3$ instead of 0.1), as well as the self-irradiation ($f_{out} = 0.036$ instead of 0.07). This can be explained by a different geometry of disk and corona, as MAXIJI535-571 is not in a pure hard state, contrarily to MAXIJ1820+070. The inner radius resulting from the fit, $R_{in} = 1.9\,R_g$ ($R_g = GM/c^2$), is not far from [218] who find it $\lesssim 1.55\,R_g$, regardless the state. We find a magnetic field in the accelerating

region of the jet of $5.4\,10^3$ G, compatible with findings of [222] during the HIMS: within $4\,10^3 - 4\,10^4$ G. Similarly, the radius of the acceleration region, which we find to be $1.6\,10^3\,R_g$, is compatible with the value calculated in [222] along the HIMS: within $10^3 - 10^4\,R_g$. These results support the validity of our modeling.

We perform then a test, consisting of fitting the SEDs while imposing a higher range for the cut-off of the electron energy distribution γ^e_{cut}. The result is shown in Figure 10.7 and Figure 10.8, with values in the right columns of Table 10.2 and Table 10.3. Interestingly, the χ^2/ndf doesn't degrade significantly: from 1.14 to 1.62 for MAXIJ1820+070 and from 1.13 to 1.17 for MAXIJ1535-571. The best-fit values of the model stay similar (except γ^e_{cut}, which is forced to be in a higher interval). In fact, only the violation of the HE upper limit allows to reject firmly a too-large increase of γ^e_{cut}. The upper limit, in terms of electron energy exponential cut-off, is 0.5 GeV, and 1 GeV for MAXIJ1820+070 and MAXIJ1535-571, respectively. We note that the fit degrades slightly in the IR region for both sources, but it is not as sharp as the HE upper limit violation.

An important caveat has, however, to be made: in the current version of JetSeT, the photon field from analytical *ad-hoc* components in the SED is not propagated at the level of the jet. This means that these photons are not considered as Inverse Compton targets for accelerated electrons. Thus, only the Self-Synchrotron Compton component is calculated in the HE and VHE regions. The addition of this External Compton would increase the flux predicted at HE, and we would violate HE upper limits for lower electron Lorentz factors. This means that the upper limit on the energy cut-off would be better (lower) than the one we currently estimate.

Finally, we do a last test, to figure out what could be observed in HE and VHE regions in case of a more favorable jet angle w.r.t. the line of sight: we take the best-fit values for the jet acceleration region of MAXIJ1820+070 (γ^e_{cut} not forced to high values), and we build a simple model with a standard jet (for the acceleration region only) and a standard accretion disk with a luminosity set to the total luminosity of the irradiated disk model. This aspect, in the X-ray range, serves to provide a reasonable photon field at the level of the jet (for non-analytical elements such as the ones used here, JetSeT fully handles photons from disk, star, etc, to the jet). We set the angle to 5°. The idea is to consider the same electron population, with a better Doppler boosting factor. The result is shown Figure 10.9. Predicted flux is closer to HE upper limits, but still doesn't reach them.

model name	name	value	error	free	value	error
Disk irr.	T_{Disk}	$1.55\,10^{+06}$	-		$1.55\,10^{+06}$	–
Disk irr.	L_{Disk}	$1.034\,10^{+37}$	$3\,10^{+34}$	✓	$9.759\,10^{+36}$	$2.4\,10^{+31}$
Disk irr.	r_{out}	3720	90	✓	3274	41
Disk irr.	r_{irr}	1.1	-		1.1	–
Disk irr.	L_{Comp}/L_{Disk}	4.369	0.043	✓	4.475	0.023
Disk irr.	$E_{b,Comp}$	0.15	-		0.150	–
Disk irr.	$E_{c,Comp}$	139.7	7.2	✓	154.1	4.3
Disk irr.	Γ_{Comp}	1.605	0.012	✓	1.641	0.006
Disk irr.	$E_{c,hump}$	20.29	0.72	✓	22.34	0.31
Disk irr.	Γ_{hump}	−1.075	0.032	✓	−0.818	0.011
Disk irr.	K_{hump}	$1.31\,10^{-04}$	$0.17\,10^{-04}$	✓	$3.12\,10^{-04}$	$0.15\,10^{-04}$
Disk irr.	f_{in}	0.1	-		0.1	–
Disk irr.	f_{out}	0.007	$3.3\,10^{-04}$	✓	0.008	$2\,10^{-04}$
Radio Jet	B_0	$6.92\,10^{+06}$	-		$6.81\,10^{+06}$	–
Radio Jet	z_0	$1.15\,10^{+08}$	-		$1.18\,10^{+08}$	–
Radio Jet	z_{inj}	$2.42\,10^{+10}$	-		$2.44\,10^{+10}$	–
Radio Jet	γ_{jet}	2.19	-		2.19	–
Radio Jet	N_{frac}	1	-		1	–
Radio Jet	$R_{H-start-frac}$	1	-		1	–
Radio Jet	$R_{H-stop-frac}$	30000	-		30000	–
Radio Jet	m index	1.206	$1.3\,10^{-05}$	✓	1.179	0.007
Radio Jet	γ^e_{cut}	56.13	0.019	✓	1009	0.005
Radio Jet	p	2.05	-		2.05	–
Radio Jet	N^{acc}_e	$1.001\,10^{+12}$	$7.3\,10^{+07}$	✓	$9.689\,10^{+11}$	$5.8\,10^{+07}$
Radio Jet	B	17481	0.018	✓	11820	270
Radio Jet	R	$2.726\,10^{+09}$	$2.9\,10^{+07}$	✓	$1.812\,10^{+09}$	$1.1\,10^{+04}$

Table 10.2.: Parameters of the fit of MAXIJ1820+070 Hard State SED with Irradiated Disk + Radio Jet models. All parameters are defined in subsection 10.2.1, units are cgs units, except for cut-off energies which are in keV. The corresponding figures are Figure 10.5 and Figure 10.7. Errors are from the MINUIT MIGRAD module. The left table is for the nominal fit, letting the energy cut-off of electrons run freely, the right one is a fit by imposing an interval around the value in red.

model name	name	value	error	free	value	error
Disk irr.	T_{Disk}	$7.000\,10^{+06}$	-		$7.000\,10^{+06}$	–
Disk irr.	L_{Disk}	$1.496\,10^{+37}$	$4.4\,10^{+34}$	✓	$2.024\,10^{+37}$	$5.7\,10^{+30}$
Disk irr.	r_{out}	70000	-		70000	–
Disk irr.	r_{irr}	1.179	$1.7\,10^{-08}$	✓	1.377	$2.8\,10^{-08}$
Disk irr.	L_{Comp}/L_{Disk}	4.651	0.009	✓	4.585	0.005
Disk irr.	$E_{b,Comp}$	0.15	-		0.150	–
Disk irr.	$E_{c,Comp}$	80.1	1.5	✓	72.72	0.77
Disk irr.	Γ_{Comp}	2.202	0.003	✓	2.120	0.002
Disk irr.	$E_{c,hump}$	60	-		60	–
Disk irr.	Γ_{hump}	−3.5	-		−3.5	–
Disk irr.	K_{hump}	$1.3\,10^{-13}$	-		$1.300\,10^{-13}$	–
Disk irr.	f_{in}	0.325	0.002	✓	0.348	$9.5\,10^{-04}$
Disk irr.	f_{out}	0.036	$2.3\,10^{-04}$	✓	0.012	$8.9\,10^{-05}$
Radio Jet	B_0	$4.354\,10^{+06}$	-		$4.354\,10^{+06}$	–
Radio Jet	z_0	$1.534\,10^{+08}$	-		$1.534\,10^{+08}$	–
Radio Jet	z_{inj}	$3.469\,10^{+10}$	-		$3.469\,10^{+10}$	–
Radio Jet	γ_{jet}	3	-		3	–
Radio Jet	N_{frac}	1	-		1	–
Radio Jet	$R_{H-start-frac}$	1	-		1	–
Radio Jet	$R_{H-stop-frac}$	30000	-		30000	–
Radio Jet	m index	1.077	$2.0\,10^{-06}$	✓	1.067	$3.8\,10^{-06}$
Radio Jet	γ^e_{cut}	89.25	0.003	✓	1950	0.004
Radio Jet	p	2.050	-		2.050	–
Radio Jet	N^{acc}_e	$9.552\,10^{+11}$	$2.2\,10^{+07}$	✓	$9.714\,10^{+11}$	$6.4\,10^{+07}$
Radio Jet	B	5394	0.055	✓	4991	0.004
Radio Jet	R	$2.486\,10^{+09}$	$3.8\,10^{+04}$	✓	$1.967\,10^{+09}$	$2.0\,10^{+04}$

Table 10.3.: Parameters of the fit of MAXIJ1535-571+070 HIMS SED with Irradiated Disk + Radio Jet models. All parameters are defined in section subsection 10.2.1, units are cgs units, except for cut-off energies which are in keV. The corresponding figures are Figure 10.6 and Figure 10.8. Errors are from the MINUIT MIGRAD module. The left table is for the nominal fit, letting the energy cut-off of electrons run freely, the right one is a fit by imposing an interval around the value in red.

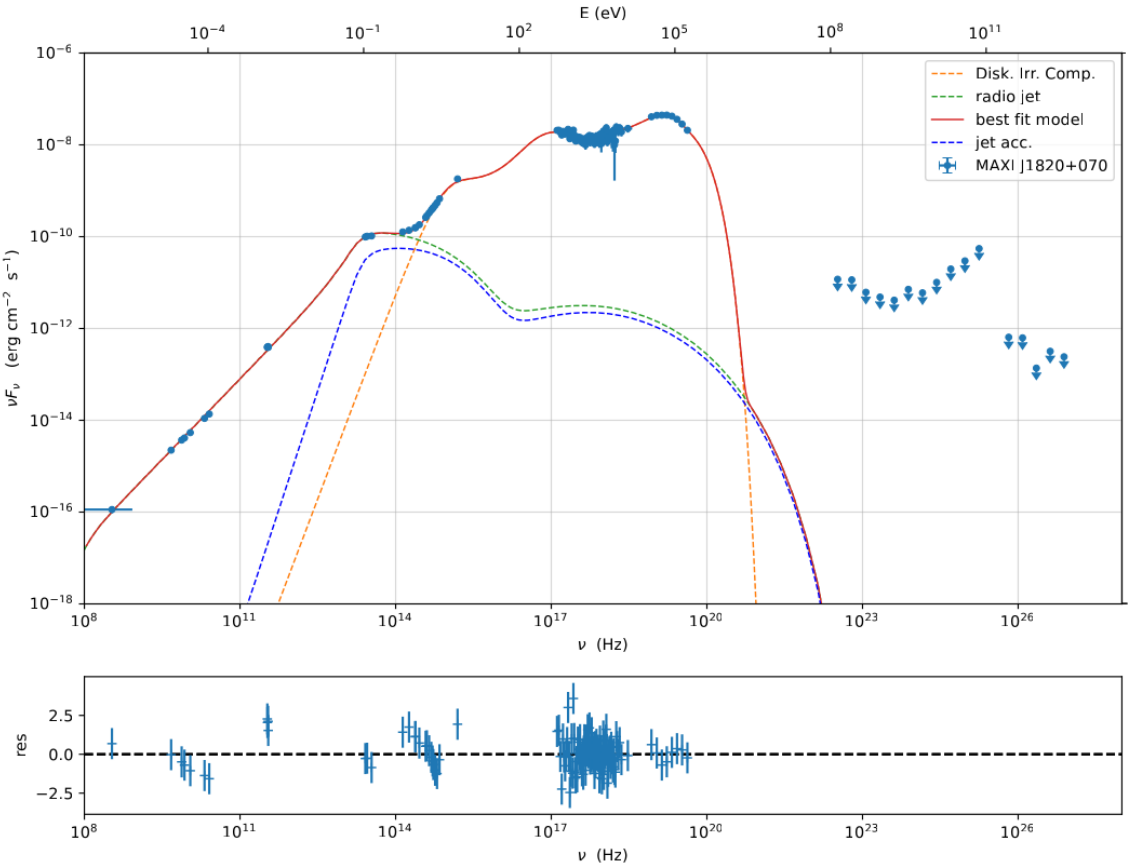

Figure 10.5.: MAXIJ1820+070 Hard State SED fit with Irradiated Disk + Radio Jet models. It has to be noted that only SSC contributes to the Inverse Compton energy range. The blue dashed curve is the contribution of the accelerating region of the jet. Parameters of this fit are gathered in Table 10.2, left columns. The residuals in the bottom panel are $(data - model)/error$. We have χ^2/ndf=1.14.

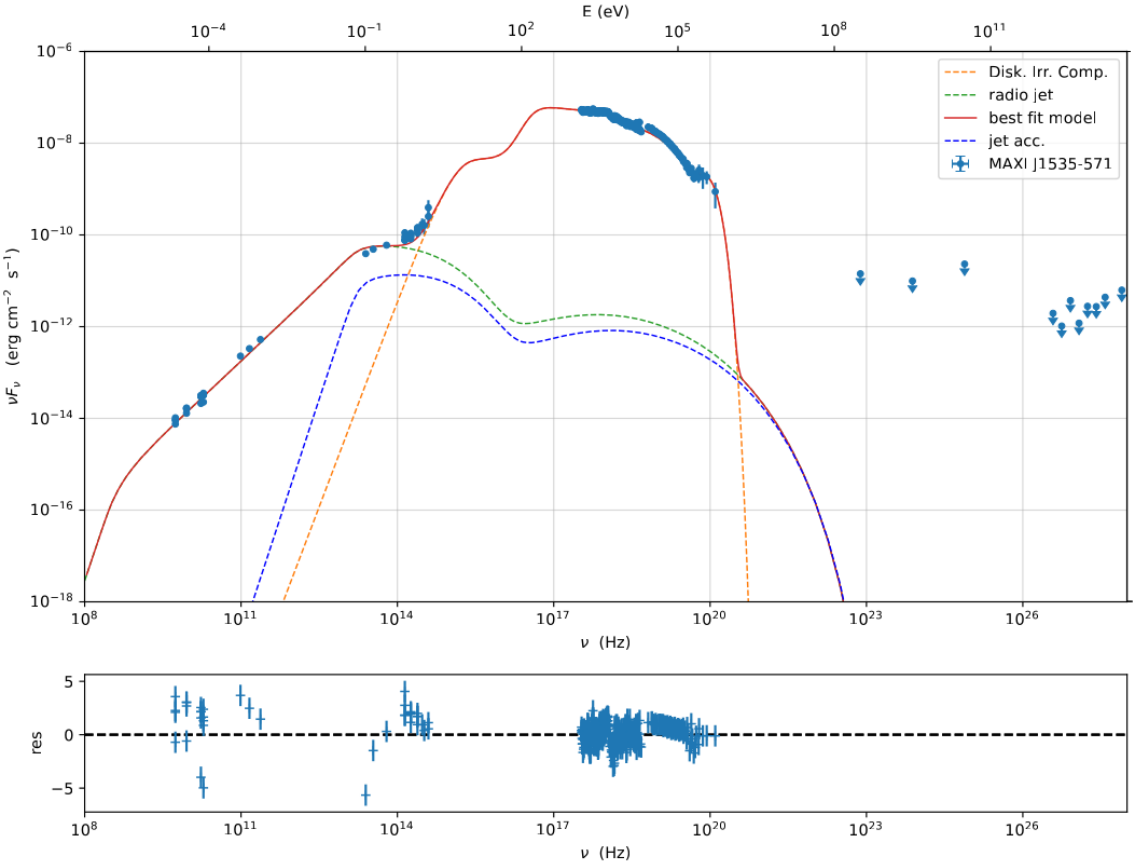

Figure 10.6.: MAXIJ1535-571 HIMS SED fit with Irradiated Disk + Radio Jet models. It has to be noted that only SSC contributes to the Inverse Compton energy range. The blue dashed curve is the contribution of the accelerating region of the jet. Parameters of this fit are gathered in Table 10.3, left columns. The residuals in the bottom panel are $(data - model)/error$. We have χ^2/ndf=1.13.

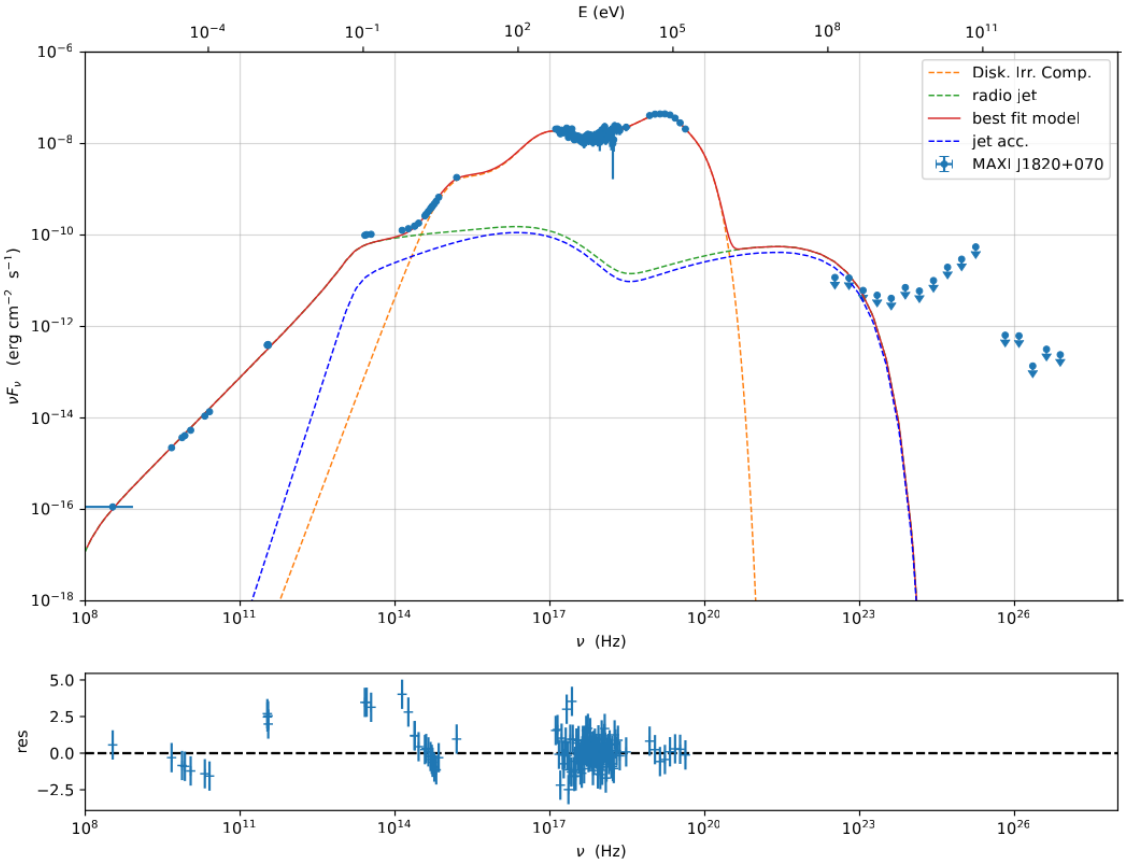

Figure 10.7.: MAXIJ1820+070 Hard State SED fit with Irradiated Disk + Radio Jet models, by constraining the electron energy cut-off to a high value. It has to be noted that only SSC contributes to the Inverse Compton energy range. The blue dashed curve is the contribution of the accelerating region of the jet. Parameters of this fit are gathered in Table 10.2, right columns. The residuals in the bottom panel are $(data - model)/error$. We have χ^2/ndf=1.62.

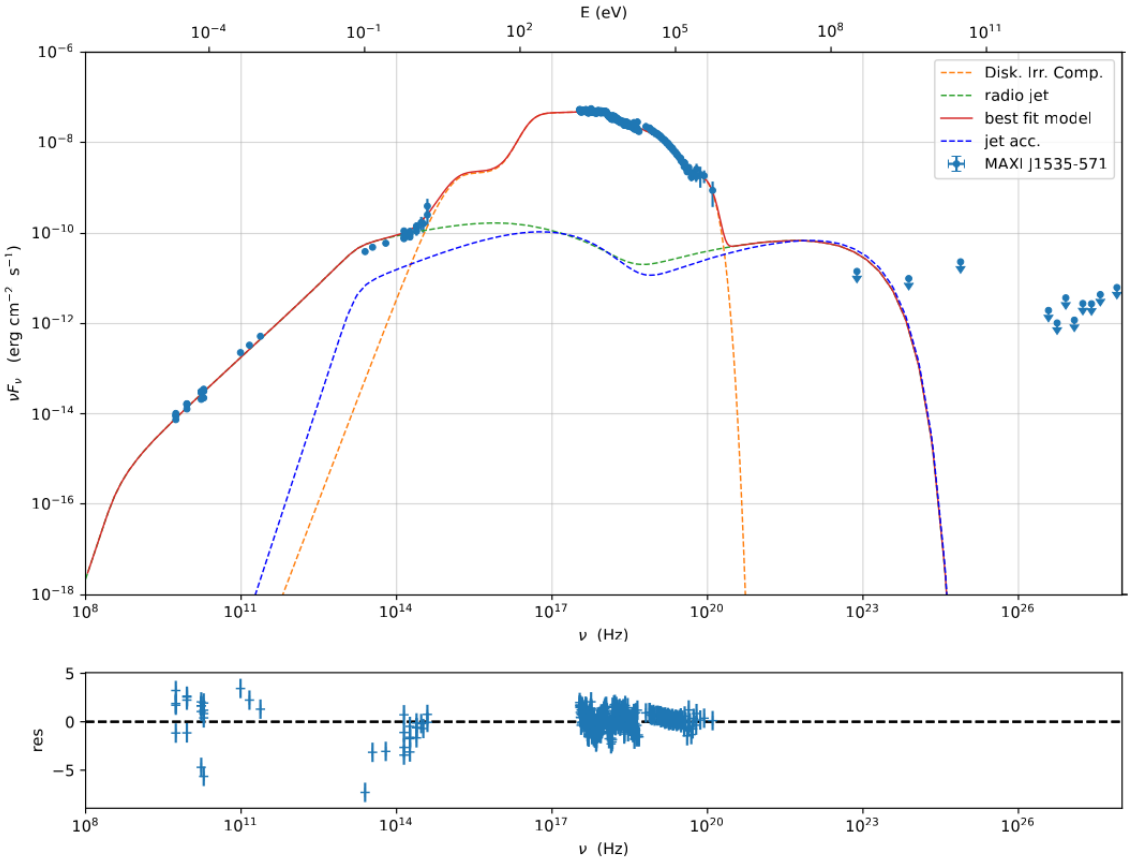

Figure 10.8.: MAXIJ1535-571 HIMS SED fit with Irradiated Disk + Radio Jet models, by constraining the electron energy cut-off to a high value. It has to be noted that only SSC contributes to the Inverse Compton energy range. The blue dashed curve is the contribution of the accelerating region of the jet. Parameters of this fit are gathered in Table 10.3, right columns. The residuals in the bottom panel are $(data - model)/error$. We have χ^2/ndf=1.17.

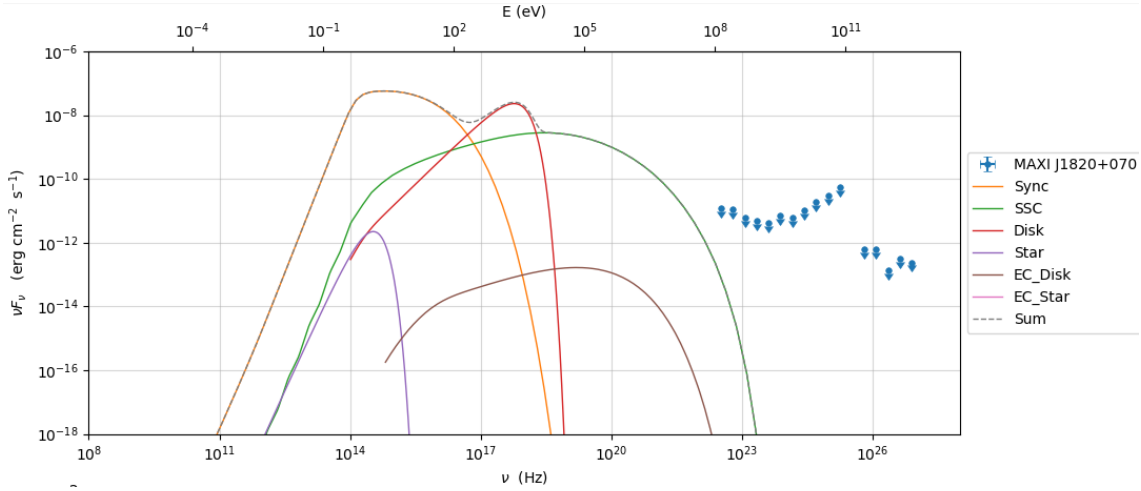

Figure 10.9.: MAXIJ1820+070 SED for a simple model of jet+ multi-color BB disk, in which the parameters of the accelerating jet of Figure 10.5 have been set, except the jet angle w.r.t. the line of sight, set at 5°, in order to estimate the observed flux for a hypothetical similar system which would be in a more favorable inclination w.r.t. the observer. The upper limits for HE and VHE are kept as a proxy of effective sensitivities for similar observation conditions. The disk luminosity set is the total bolometric luminosity found in the case of Figure 10.5.

10.2.4. Leptonic model for MAXIJ1820+070 hard-to-soft state transition

The case of the hard-to-soft transition is modeled with built-in components in JetSeT: a jet, a multi-color black-body emitting accretion disk, and the companion star, identified as a K5 spectral type star, with temperature $T \sim 4200\,\mathrm{K}$, and radius $R \sim 1.2\,R_{\odot}$ ([227]). The jet is modeled with an ejected blob. Its distance to the black hole is set to $R_H = 2\,10^{12}$ cm, according to the analytical results that we obtained in [1]. From the same publication, we take the estimated magnetic field $B = 47\,\mathrm{G}$, and the power law index $p = 2$ for the electron energy distribution, that we choose as a power-law with an exponential cut-off. This cut-off, γ^e_{cut} in terms of Lorentz factor, is fully free in a first fit (Figure 10.10 and left columns of Table 10.4), and then constrained to lie in higher bounds (Figure 10.11 and right columns of Table 10.4). Accretion efficiency is set at a value of 0.1, following [228]. The free parameters are the blob size R, the density of electrons N_e, the cut-off γ^e_{cut}, the accretion disk luminosity L_{Disk}, and the temperature of the star T_{Star}, as well as the inner and outer disk radii, R^{Sw}_{inner} and R^{Sw}_{outer}, expressed in terms of Schwarzschild radius, which is $2.36\,10^6$ cm for a Black Hole of mass=$8\,M_{\odot}$. In the fitting process, the starting value for the region size ($R = 2\,10^{11}$ cm) is taken from the analytical estimates in [1]. A hump is necessary at $\mathcal{O}(10\,keV)$, to ensure a correct fit, though its origin is unclear.

The result of the fit with a fully free γ^e_{cut} is presented in Figure 10.10 and left columns of Table 10.4. The energy cut-off best-fit value is 0.4 GeV. The fit quality is poor, with a $\chi^2/ndf = 5$, which comes from the difficulty of the simple disk model to reproduce the X-rays, even with the addition of an ad-hoc hump. Some of the results can be compared with values estimated elsewhere: [193], from MAXI/GSC data fit at the hard-to-soft transition, find a disk inner radius of 67^{+17}_{-12} km, and a disk luminosity of $\sim 1.1\,10^{38}$ erg/s, while we find 53 km, and a disk luminosity of $1.9\,10^{38}$ erg/s, respectively. The former is compatible, whereas the latter presents a discreapancy. The poor quality of the fit is also visible at the level of the star, for which a rather high temperature is required: 10000K instead of 4200K. As underlined in [1], during the outburst, the stellar surface could be heated by X-rays. However, the amplitude of the heating is unlikely. All these difficulties likely come from a lack of a more sophisticated disk model. The irradiated disk model, suitable for hard states (and HIMS as seen in the case of MAXIJ1535-571) would not suit. Further studies would be required to better model the visible to X-ray range. Nevertheless, the jet physics should remain essentially immune from our weak modeling of the accretion disk.

The conclusion that we draw is that the HE and VHE upper limits are far above the predicted Inverse Compton contribution of the flux. This kind of system, if we rely on our modeling, appears hard to detect in HE and VHE wavelengths.

Following the same reasoning as in the previous section, we do two tests: first, we constrain γ^e_{cut} to lie in higher bounds. The result is given in Figure 10.11 and right columns of Table 10.4. We have still $\chi^2/ndf = 5$. The value of γ^e_{cut} is 10^6, meaning a cut-off in the electron energy distribution of 500 GeV. This value of 500 GeV has also been assumed as a maximum acceleration energy in our paper on MAXIJ1820+070

([1]). In our modeling, Figure 10.11, we see that a major issue is the synchrotron emission which peaks in the MeV domain, which is unlikely given the strong cooling that would result from this energy. The predicted flux is closer to the HE and VHE limits, but this hypothesis presents weak points.

The second test consists of keeping all the parameters of the fit at low cut-off, except the jet angle w.r.t. the line of sight, to check if the same system in "MicroBlazar" configuration, would be more promising at high energy. We change the angle from 64° to 5°, and obtain the fluxes on Figure 10.12. In this case, a system similar to MAXIJ1820+070, but better oriented, would have fluxes closer to the Fermi upper limits.

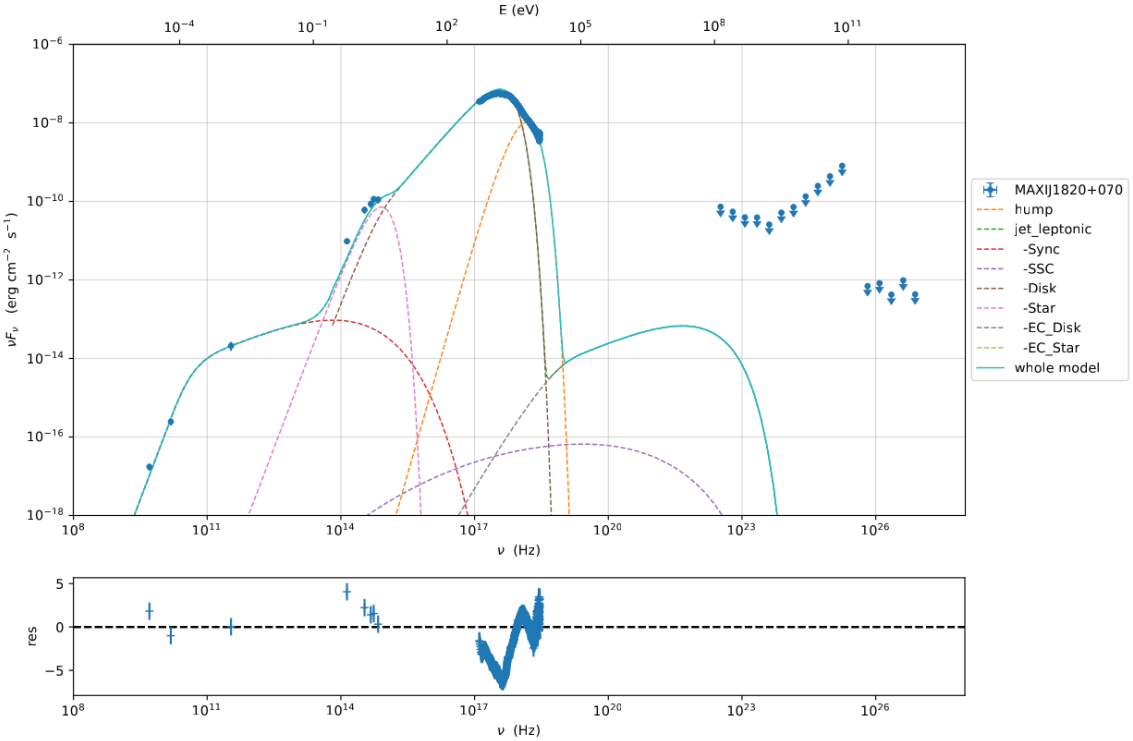

Figure 10.10.: MAXIJ1820+070 hard-to-soft state transition SED fit with Jet+Disk+Star+Hump models. It has to be noted that the star temperature required is higher than the expected one (10000K for 4200K). Parameters of this fit are gathered in Table 10.4, left columns. The residuals in the bottom panel are $(data - model)/error$. We have χ^2/ndf=5.

model name	name	value	error	free	value	error
Hump	E_c	1.535	0.003	✓	1.531	0.005
Hump	Γ	-2	0.015	✓	-2	0.013
Hump	K	0.246	0.003	✓	0.248	0.004
Jet	R	$3.441\,10^{+11}$	$2.9\,10^{+10}$	✓	$3.38\,10^{+11}$	$2.8\,10^{+10}$
Jet	R_H	$2\,10^{+12}$	-		$2\,10^{+12}$	–
Jet	B	47	-		47	–
Jet	$\frac{NH\,cold}{rel\,e}$	0.1	-		0.1	–
Jet	θ_{jet}	64	-		64	–
Jet	γ_{jet}	2.2	-		2.2	–
Jet	N_e	$2.7\,10^{+05}$	$1.0\,10^{+05}$	✓	$3.0\,10^{+05}$	$1.1\,10^{+05}$
Jet	γ^e_{cut}	823.2	8.8	✓	10^{+06}	$6.7\,10^{+05}$
Jet	p	2	-		2	–
Jet	R^{Sw}_{inner}	2.273	0.002	✓	2.277	0.009
Jet	R^{Sw}_{ext}	30000	2300	✓	30000	2400
Jet	Accr. Effi.	0.1	-		0.1	–
Jet	M_{BH}	8.000	-		8.000	–
Jet	R_{Star}	$1.200\,10^{+11}$	-		$1.200\,10^{+11}$	–
Jet	T_{Star}	10000	110	✓	10000	120
Jet	L_{Disk}	$1.850\,10^{+38}$	$3.9\,10^{+33}$	✓	$1.850\,10^{+38}$	$3.9\,10^{+33}$

Table 10.4.: Parameters of the fit of MAXIJ1820+070 hard-to-soft state transition SED with Jet+Disk+Star+Hump models. All parameters are defined in subsection 10.2.1, units are cgs units, except for cut-off energies which are in keV. The corresponding figures are Figure 10.10 and Figure 10.11. Errors are from the MINUIT MIGRAD module. The left table is for the nominal fit, letting the energy cut-off of electrons run freely, the right one is a fit by imposing an interval around the value in red.

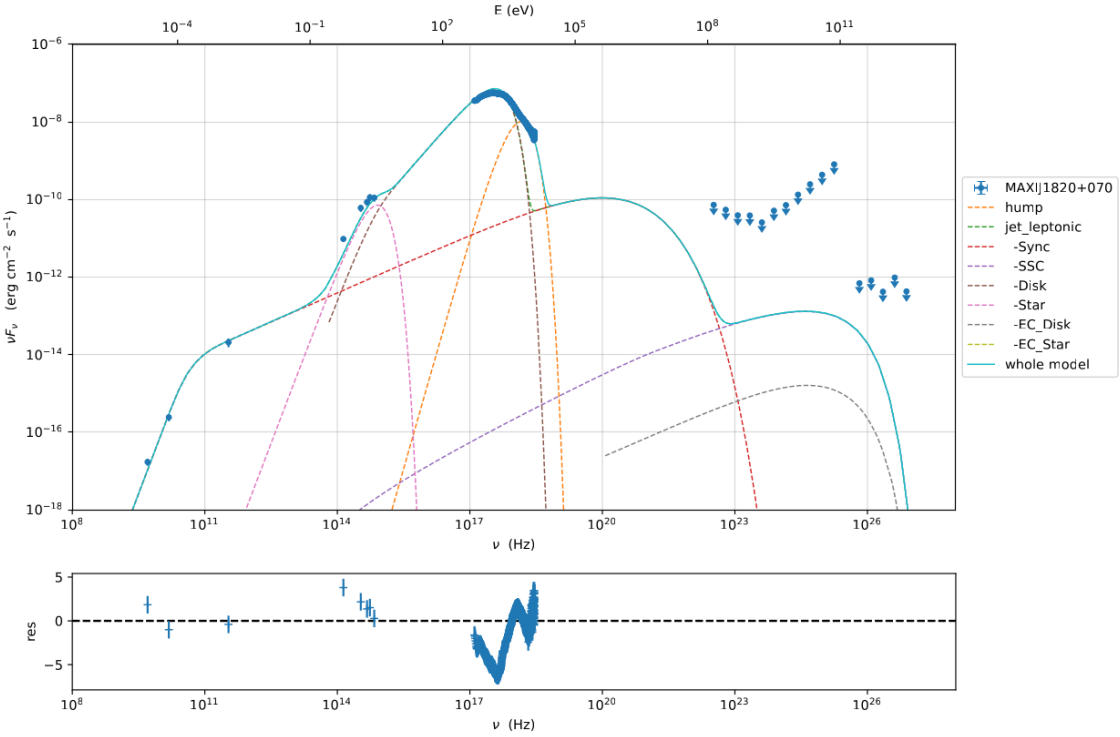

Figure 10.11.: MAXIJ1820+070 hard-to-soft state transition SED fit with Jet+Disk+Star+Hump models, by constraining the electron energy cut-off to a high value. Parameters of this fit are gathered in Table 10.4, right columns. The residuals in the bottom panel are $(data - model)/error$. We have χ^2/ndf=5.

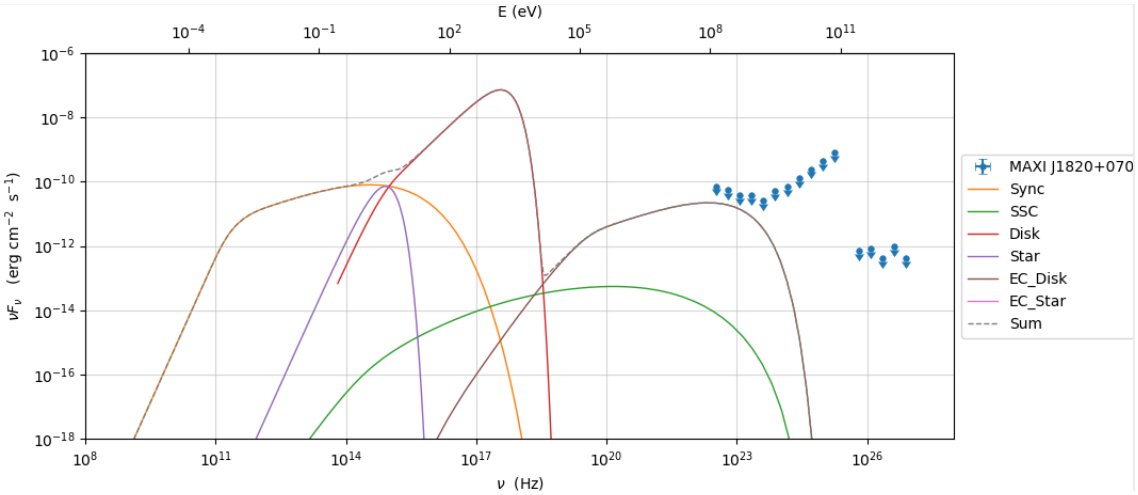

Figure 10.12.: MAXIJ1820+070 SED for the same simple model as in Figure 10.10, but with the jet angle w.r.t. the line of sight set at 5°, in order to estimate the observed flux for a hypothetical similar system which would be in a more favorable inclination w.r.t. the observer. The upper limits for HE and VHE are kept as a proxy of effective sensitivities for similar observation conditions.

11. Multi-Messenger Microquasar broker

To increase the odds of a neutrino or VHE signal discovery from microquasars in future observations, a multi-messenger, multi-wavelength continuous monitoring was developed. It is built from a regular monitoring of X-ray data from MAXI/GSC and Swift/BAT to provide an early detection of X-ray flares. A significant detection of a variation in X-ray flux automatically triggers an analysis of Fermi/LAT data. An analysis of KM3NeT real-time data, as will be described in chapter 13 of Part III is also automatically triggered. All these are incorporated in the HESS observation strategy, as a significant signal would trigger ToO observations with HESS. A summary flowchart is shown in Figure 11.1.

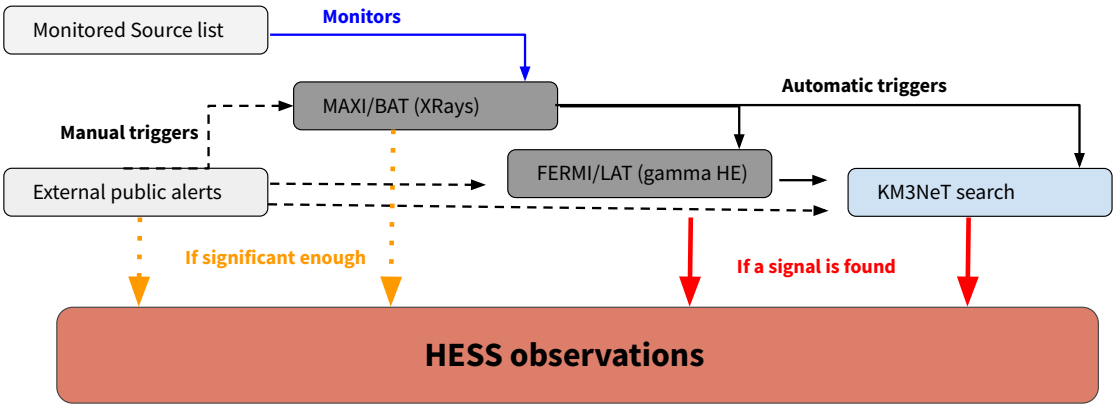

Figure 11.1.: Summary of the multi-messenger microquasar broker flowchart

It should be noted that while this tool was initially designed for microquasars, any source with publicly available X-ray data can be integrated into its monitoring.

The monitor was able to detect and perform regular Fermi/LAT searches on an outburst of GX 339-4 in August 2022, as reported for example in ATel#15578[1]. The corresponding lightcurve at the time of the initial alert from the broker is shown in

[1] ATel#15578

Figure 11.2. Similarly, the system followed recent flaring activities of sources such as 4U 1630-47[2], Aql X1[3], and the recently detected, exceptionally bright Swift J1727.8-1613[4] in August 2023.

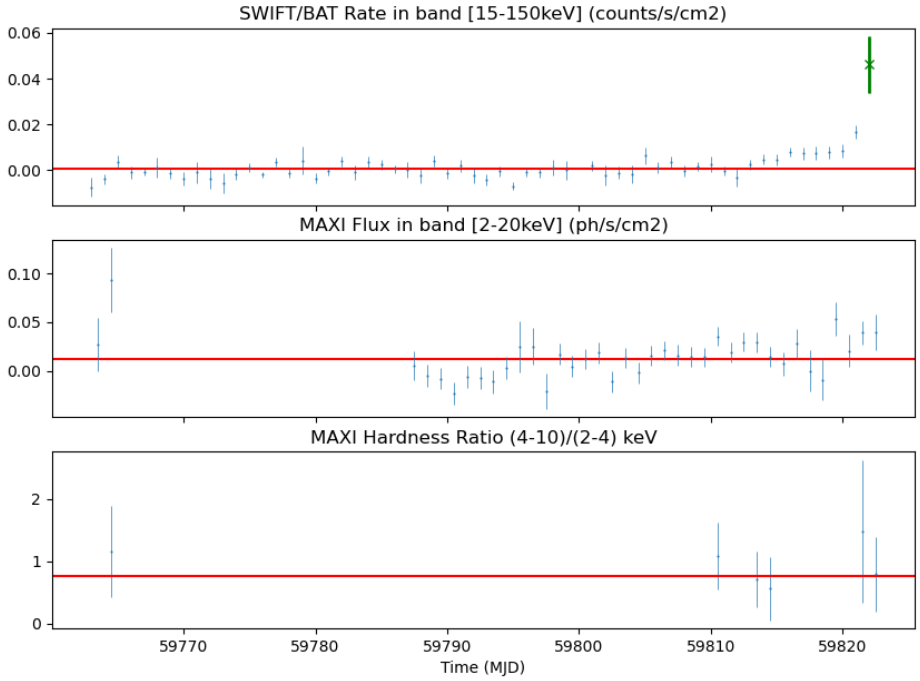

Figure 11.2.: Alert sent from a flare from GX339-4 in the Swift/BAT band. The red lines are the computed baselines. The green point highlights a data point that triggered an alert sending and a Fermi/LAT follow-up search.

11.1. X-rays

The X-ray analysis is scheduled multiple times a day of the MAXI/GSC and Swift/BAT daily lightcurve data (Note: Daily data point for a single source can be updated multiple times a day). The search for flaring differs from the one described in section 6.1 as the goal is not just to find a significant flaring, but a sudden increase of the flux marking a variation of the source state. The monitoring is also performed on the hardness ratio of the source as given by the MAXI/GSC detector. The procedure is as follows:

1. The average flux and the standard deviation from the last 3 months are evaluated.

[2] ATel#15924
[3] ATel#16187
[4] ATel#16205

2. Similarly, the hardness ratio of the 4-10 keV to 2-4 keV bands from MAXI is computed and its average flux and standard deviations are evaluated.

3. An alert is sent if the most recent flux data point verifies in either telescope:

$$F - \Delta F > \mu_{\mathrm{BL}} + N\sigma_{\mathrm{BL}} \tag{11.1}$$

with F the flux and ΔF its error. μ_{BL} and σ_{BL} are the baseline average and its standard deviation. N is a number of standard deviations that constitute a significant signal and is to be determined with respect to the desired False Alarm Rate (FAR).

4. To detect a possible hard-to-soft state transition an alert is sent if the hardness ratio verifies:

$$H + \Delta H < \mu_{\mathrm{BL}} - N\sigma_{\mathrm{BL}} \tag{11.2}$$

The alerts are circulated using VOEvent messages on a Comet server broker [229] that is configured to launch follow-up alerts.

The $N\sigma$ threshold level is computed to ensure the sending of around 40 alarms per year for the entire source list and is computed from the historical activity of the sources, as seen in Figure 11.3.

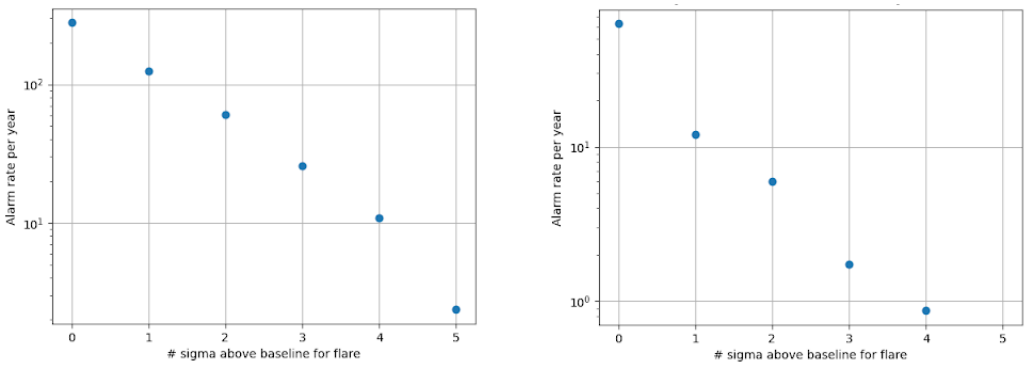

Figure 11.3.: Alarm rate with respect to $N\sigma$ flare threshold for GX339-4 (left) and IGRJ17091-3624 (right).

11.2. FERMI/LAT

Upon receiving alerts from the monitoring of X-ray lightcurves, a follow-up search for HE gamma with Fermi/LAT is automatically launched using a similar pipeline that the one described in chapter 8. This search is performed in a time window of 24 hours before the date corresponding to the data point that was significantly above baseline to the last available data from the Fermi/LAT telescope.

11.3. KM3NeT

The X-Ray monitoring acts as a broker to the KM3NeT Online pipeline as described in chapter 13. A significant rise of flux launches a follow-up analysis as a point-source search in a time window 24 hours before the date corresponding to the data point that was significantly above baseline to the latest data. An additional search is performed at the 24-hour mark after the alert which corresponds then to a ±1 day time window analysis.

11.4. In the HESS observation strategy

The HESS ToO program requires the elaboration of proposals with *a priori* criteria for the potential triggering of observations that should take over the regular observation scheduling. The triggers are separated into two classes with respect to the relevance of the criteria and the likelihood of VHE signal detection or new discovery. These classes are

- **Class A** When the criteria are met, ToO observations can be triggered directly by contacting the HESS local crew to allow for rapid response.
- **Class B** Trigger needs to be approved by the HESS Observing Committee which can cause delays in the data taking. This class is reserved for more conservative criteria or lower-priority targets.

The monitoring of microquasars enters this observation strategy with, as a criterion for a Class A trigger is the significant detection of a transient HE gamma signal following an X-ray flare. Additionally, triggers of class B might be issued if the KM3NeT online analysis results in the detection of a neutrino candidate with a significant spatial and temporal correlation with X-ray activity. Despite the scientific relevance of such detection, it was chosen to keep the trigger to a class B with regards to the fact that the KM3NeT detector is still under construction and, as such, some time must be kept to answer any possible concern from the HESS Collaboration on the relevance of the neutrino signal.

Another criterion is chosen directly from the X-ray monitoring and is based on the detection of a State Transition in a highly significant flare. The number of standard deviations above baseline to constitute a flare is then chosen to yield around 3 alarms per year in historical data over the entire source list and can be seen in Table 11.1. On top of this criterion, the detection of a hard-to-soft transition at a level of 3 σ above baseline is required to trigger a class B ToO. In historical data, approximately 20% of flares exhibit such a transition, which brings the final alarm rate to about 0.6 per year.

It should be noted that the automated monitoring is not the only criterion on the proposal for the ToO of microquasars. Indeed, a class A trigger is to be issued in the case of discovery of a γ-ray signal reported from anywhere, for example as an ATel from the Fermi/LAT collaboration or from another VHE observatory. Class B

Sources	Nσ for flares
V4641 Sgr	6.5
XTEJ1550-564	4.8
GRO J1655-40	5.4
GRS 1915+105	5.2
GX339-4	4.6
H1743-322	6.6
IGRJ17091-3624	4.0
V404 Cyg	7.4
MAXI J1535-571	4.2
MAXI J1348-630	3.9
MAXI J1820+070	4.5
GRS1716-249	8.0

Table 11.1.: $N\sigma$ for each source to be considered a significant flare as a criterion for the triggering of HESS observations.

triggers might be issued in the case of internal or external reports of a hard-to-soft transition or evidence for relativistic ejection. ToO analyses discussed in chapter 7 were triggered according to these criteria. However, ToO from external alerts requires human intervention and are not automated for non-parsable alerts such as ATels and GCN circulars.

Conclusion of Part II

In this part, we have searched for markers of particle acceleration to high energy in microquasars, in the form of γ-ray emission in the HE and VHE ranges, and neutrino emission in the energy ranges of ORCA (GeV-TeV) and ANTARES (TeV-PeV). This search was focused on time periods of X-ray flaring, denoting an environment favorable to this acceleration. No significant excess could be detected either in γ-ray or neutrino, and upper limits were derived in each case. Comparisons of expected neutrino upper limits extrapolated from the VHE γ-ray upper limits, to upper limits derived from neutrino telescope measurements would suggest that the latter ones are less constraining than the former ones. This is due to the fact that neutrino telescopes have very low statistics and must rely on extended periods of observation time to attain their sensitivity. However, constraints on the neutrino flux from the γ-ray flux assume no γ-ray absorption, and the recent discovery of neutrinos from the γ-quiet NGC 1068 by IceCube proves that this effect can be significant.

A modeling of SED was performed and suggests that emission of a detectable γ-ray flux would only be possible under the circumstances that the microquasar jet is aligned with the line of sight, in a "microblazar" configuration. This alignment is often not trivial to determine in the case of a new source discovery during an outburst, which supports the planning of observations at high energy.

As discussed in chapter 3, microquasars are indeed able to produce a detectable VHE flux at the interaction region between their jet and the ISM. This detected emission however is not transient and can benefit from the fact that observations can be made during much longer periods than the study of transient phenomena taking place during days or weeks. Construction of improved facilities like the future Cherenkov Telescope Array (CTA) and the expansion of the KM3NeT detectors ORCA and ARCA will provide a better sensitivity to these phenomena.

Part III.

Online and offline neutrino follow-up of multi-messenger alerts

Contents

Introduction

Time-domain astronomy is characterized by the communication of alerts to the community in the event of a detection, and the follow-up of these alerts with observations and data analyses in a short time delay from other facilities. As the initial detections are easier to observe with large field-of-view observatories, GW and neutrino telescopes play a significant role in the study of transient astrophysical phenomena. This part details studies and tools developed for follow-ups with the KM3NeT/ORCA detector in the context of this multi-messenger, real-time astronomy. This detector, sensitive to a lower energy threshold than its associate ARCA, provides a good complementarity for the detection of transient events. Both detectors combined are then sensitive to an extended energy range from a few GeV to a few PeV, and while the GeV range is dominated by the atmospheric neutrino flux, space and time correlations of neutrinos with transient events reported from other facilities could reveal the existence of neutrino flux counterpart in this energy range. The strategies of the automated online searches were elaborated upon follow-up analyses performed offline. These analyses are presented in chapter 12, where searches with the ORCA detector are performed for different alerts, namely neutrinos from the IceCube telescope that were correlated with blazars, GW events from the O3 run of the LIGO/Virgo collaborations and search for a neutrino signal from the exceptionally luminous GRB GRB221009A. Finally, the implementation of a real-time system of alert follow-up with KM3NeT is presented in chapter 13.

12. Offline alerts follow-up with ORCA

12.1. Follow-up searches of IceCube alerts

The IceCube Realtime Alert System [230] regularly notices the community about the detection of high-energy neutrinos with significant probabilities to be of astrophysical origin. Some of these detections are in spatial correlation with blazars, which are promising neutrino emitter candidates since the discovery of a significant neutrino flux from blazar TXS 0506+056 correlated with the IceCube alert IC-170922A [22]. This section presents follow-up analyses of 4 of these IceCube alerts correlated with blazars with the ORCA detector. The search method is an ON/OFF binned analysis similar to the one described in section 9.2, where the background event rate is estimated directly from data.

12.1.1. Follow-up of the association IC211208A-PKS0735+17

An alert was sent following high-energy track-like event IceCube-211208A on December 8th, 2021 (GCN#31191). Its estimated energy is 172 TeV, with an estimated probability of being an astrophysical neutrino of 50.2%. Gamma-ray blazar PKS0735+17 is located just outside of the 90% error region (2.2°) of the IceCube event, and that source had been observed in a MWL flaring state, with a particularly strong gamma-ray flare observed by the Fermi/LAT telescope around the time of the event, as seen in Figure 12.1. Additionally, Baikal-GVD reported a 43 TeV cascade-like event 4 hours after the IceCube event 4.68° from the blazar, with a pre-trial significance of 2.8σ. A broadband SED was fitted to a lepto-hadronic model (i.e. model including both leptonic and hadronic components) in [231], shown in Figure 12.2. The authors predict from that model a neutrino rate in Icecube of 1.5 neutrinos per year.

This follow-up analysis was performed close to the installation of new DU going from the ORCA6 to the ORCA10 configuration. Additionally, 2 DU were inactive during part of the search window, corresponding to the ORCA8 configuration. Therefore, it uses data and MC from the ORCA6 configuration for cut optimizations and the ORCA8/10 data was processed with preliminary calibration and data quality selection. Moreover, ORCA8/10 data event classification was done using a BDT classifier model trained with ORCA6 MC. To account for differing event rates after selection caused by detector performances and discrepancies between classified data and classifier training (as seen in Figure 12.3), a scaling factor is introduced on ORCA6 data during

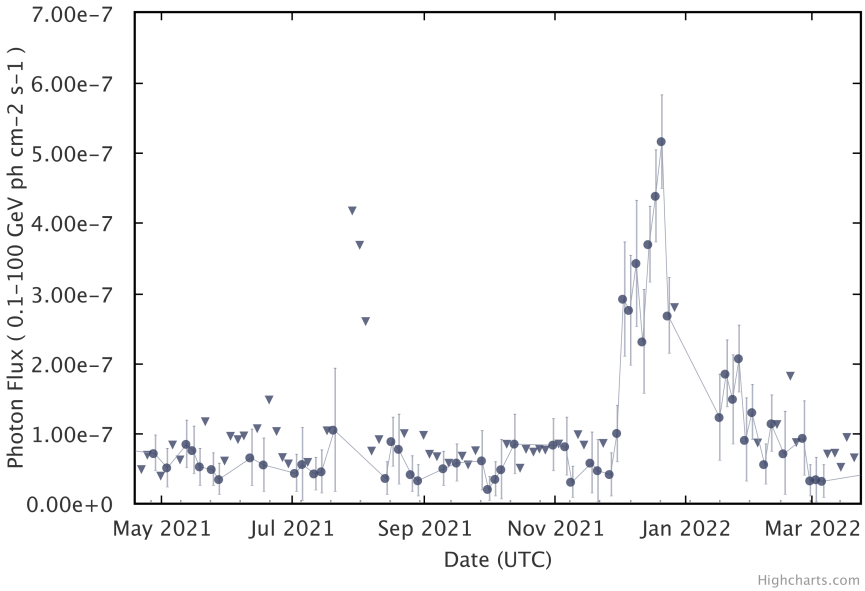

Figure 12.1.: Fermi/LAT lightcurve of PKS0735+17 from the Fermi LAT Light Curve Repository [232].Flux measurements are given as circles and upper limits as downward arrows. Upper limits are computed if the source significance is below 2σ. Data are given as 3-day averages.

cut optimization to better reproduce the expected background rate in the ORCA8/10 search region. As the optimal score cut is empirically found to be between 2 and 3, this scaling factor is chosen to be 2, as the event rate in ORCA8/10 is twice the event rate in ORCA6 at that selection level.

The ON region is defined as a circle centered to the coordinates of the blazar (RA = 114.53º, Dec = +17.71º); the OFF region is a declination band between +7 and +27 deg. The search is performed independently in two time windows. The first is ± 1 day around the IceCube event in order to search for coincident KM3NeT events. The second window is the month of December 2021, which covers most of the γ-ray flare.

The RoI radius and the BDT score cuts are optimized by minimizing a Model Discovery Factor (MDF) as developed in [233] which is an analogous method to the MRF, but the average upper limit (Equation 9.15) is replaced with a *least detectable signal*, here taken as the smallest number of events that would yield a 3σ discovery with a 50% statistical power, assuming both background and signal follow a Poisson distribution. The signal was computed with MC generated for the ORCA6 detector configuration, as no simulation of the ORCA8/10 configuration was available at the time. The signal is weighted to a standard $F(E) \propto E^{-2}$ corresponding to the spectral distribution of particle accelerated with an ideal first-order Fermi mechanism.

The optimization results can be found in Table 12.1. We can see that for the larger time window, the selection is stricter both on the ON region size and the BDT score selection.

Analysis results are shown in Table 12.2. No ON event was detected in either search.

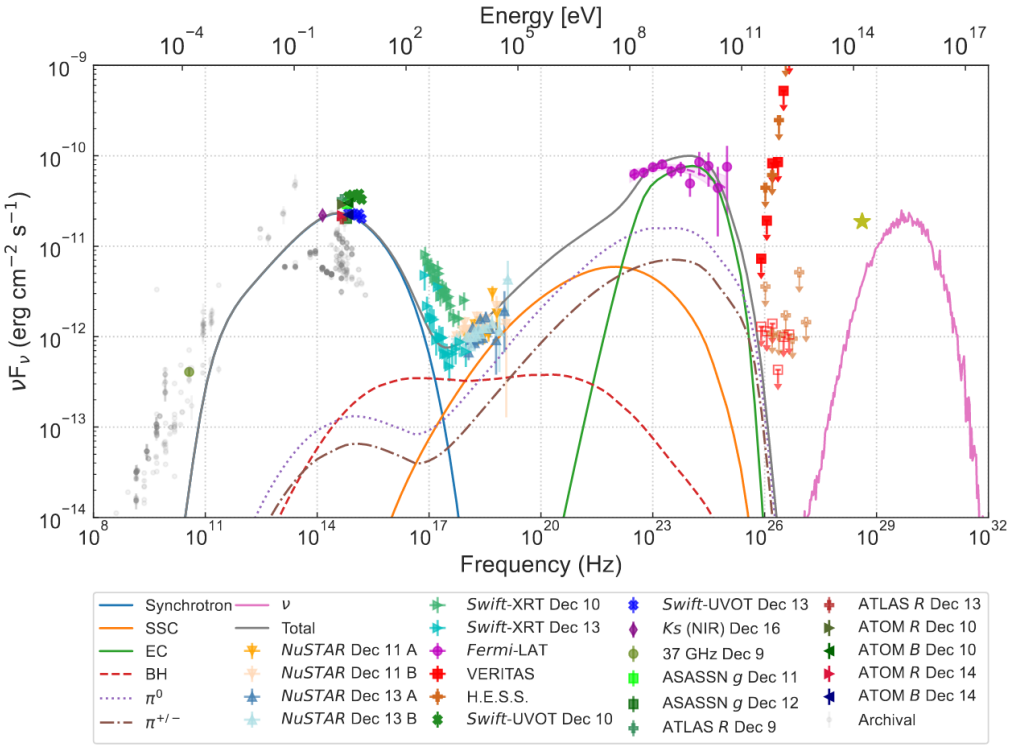

Figure 12.2.: Broadband SED from [231] of PKS 0735+17 in December 2021 at the time of IceCube-211208A. A lepto-hadronic model is fitted to the data. The pink solid line is the neutrino emission and the star marks a nominal flux of 1.5 170-TeV per year.

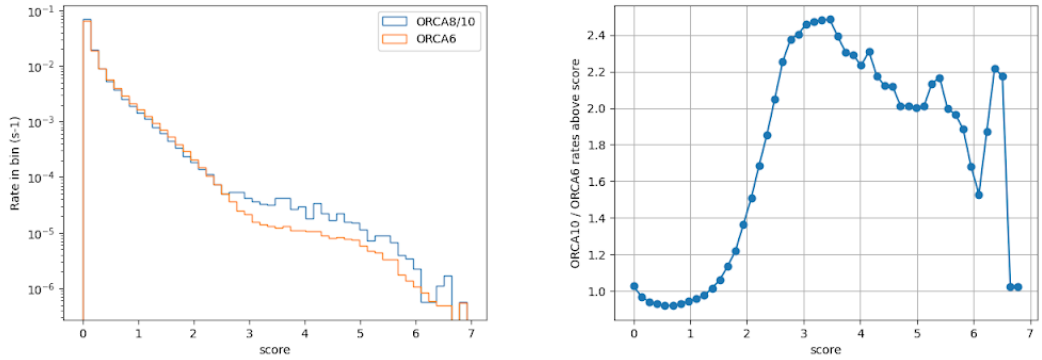

Figure 12.3.: Left: Score distribution comparison between ORCA6 data used for classifier training and ORCA8/10 data used in this analysis. Right: ORCA10 to ORCA6 event rate ratio cut above score as a function of score.

In Figure 12.4 and Figure 12.5 can be found event skymaps of the search in the 1-month time window, within ORCA and ARCA, respectively. A similar search was performed with the ARCA detector that was taking data with 8 DUs, in which 1 upgoing muon

Time window	± 1 day	1 month
RoI (deg)	3.9	2.2
Score Min.	2.3	2.6
Exp. bkg	0.08	0.28
Exp. signal	8.6×10^{-4}	1.0×10^{-2}
MDF	1853	236

Table 12.1.: Optimisation results for the two time window of the PKS0735+17 search.

neutrino candidate was observed. The p-value of this event over a Poisson-distributed background is 0.14. The search results of both ARCA and ORCA searches were reported in ATel#15290, which was the first one issued by the KM3NeT Collaboration [234].

Time window	± 1 day	1 month
N_{ON}	0	0
N_{OFF}	11	90
Exp. Bkg	0.09 ± 0.02	0.23 ± 0.02

Table 12.2.: Analysis results for the two time windows of the PKS0735+17 search. The errors are given by 1σ Poisson statistics on the N_{OFF}.

12.1.2. PKS1741-03, PKS0215+015 and TXS0310+022

In early 2022 3 alerts were issued by IceCube for high-energy neutrino events that could be correlated with blazars. On 2022-02-05, IC220205B with an estimated energy of 215.9 TeV was located within 1° of 3 sources in the 4FGL Fermi/LAT catalog. Among them is PKS1741-03 which is one of the 30 brightest radio blazars and was one of the 4 most-probable neutrino emitting blazars in [235]. IC220225A was issued on 2022-02-25 and the flat-spectrum radio quasar PKS0215+015, which was undergoing a giant radio and gamma-ray flare at the time of the alert [236] is located within the 90% containment region of the event. Finally, IC220304A was issued on 2022-03-04 with an associated false alarm rate of 0.58 events per year due to atmospheric background. Blazar TXS0310+022 is located within the 90% containment region of this event and was flaring in radio [237].

ORCA was taking data with 10 DUs during the time the 3 alerts were issued and a dedicated data production was processed, with a livetime of 11.85 days. The analysis procedure is similar to the one described in subsection 12.1.1, with the exception that only ±1 days search windows around each event are considered, and that the background estimation is done using the full processed livetime (11.85 days). The expected number of background events in each individual search is then given by:

$$\text{Exp. Bkg} = N_{OFF} \times \Omega_{\mathrm{ON}}/\Omega_{\mathrm{OFF}} \times 2/11.85 \tag{12.1}$$

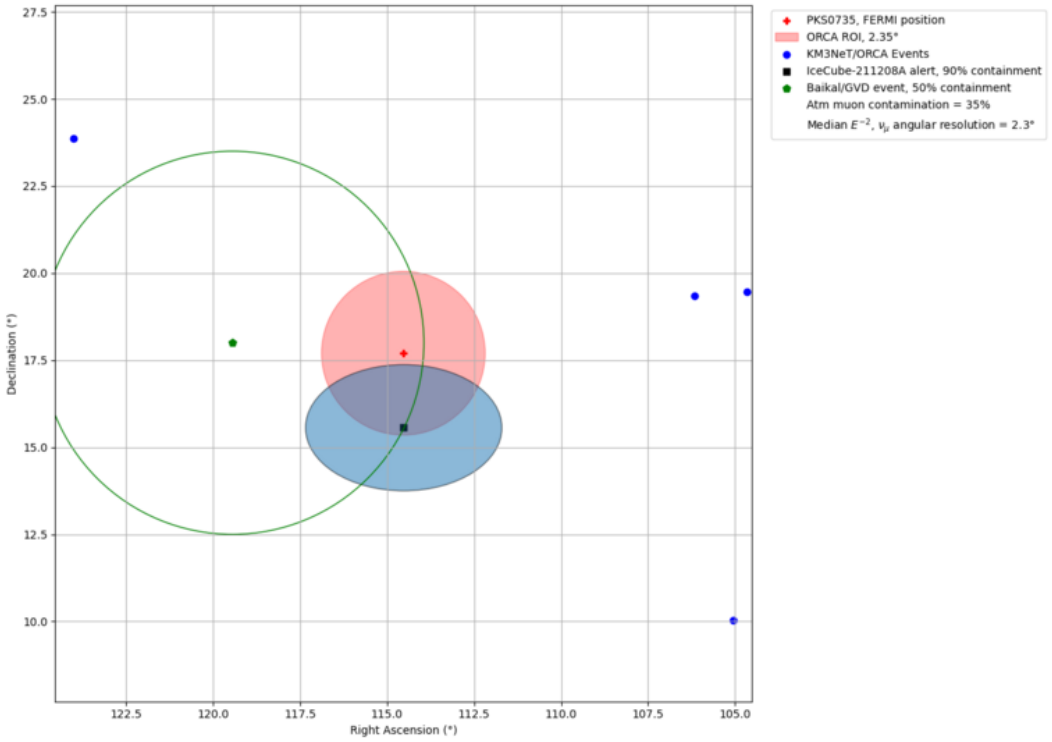

Figure 12.4.: Event Skymap in ORCA in the 1-month time window search of PKS0735+17.

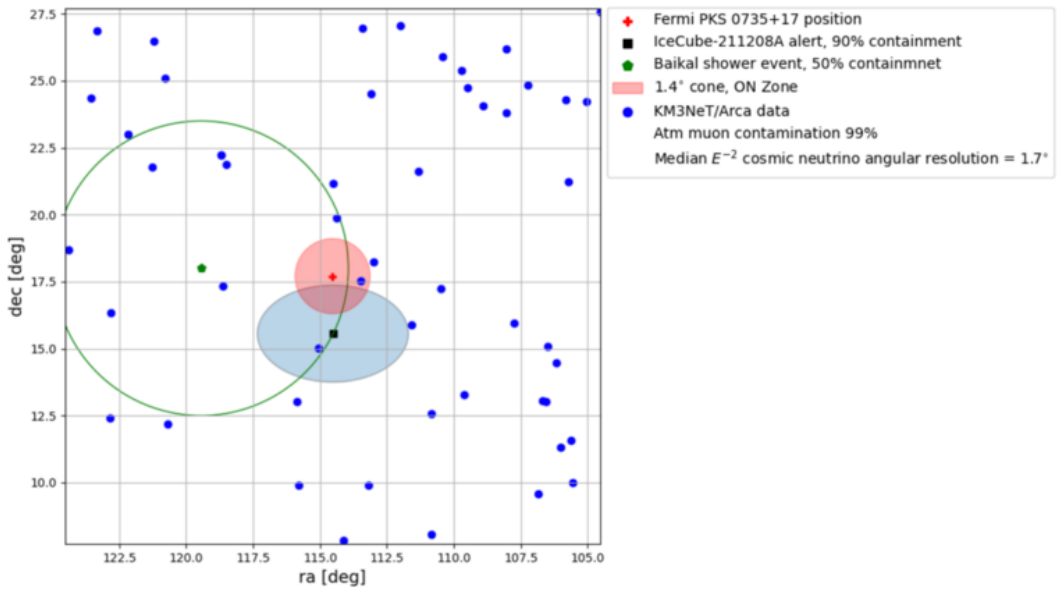

Figure 12.5.: Event Skymap in ORCA in the 1-month time window search of PKS0735+17.

Objects	PKS1741		PKS0215		TXS0310	
γ	2	2.5	2	2.5	2	2.5
ROI (deg)	3.6	4.7	4.0	4.9	4.0	4.6
Score min.	2.3	2.7	2.4	2.8	2.4	2.6
Exp. Background	0.08	0.08	0.08	0.08	0.08	0.08
Exp. Signal	6.7×10^{-4}	2.1×10^{-5}	6.5×10^{-4}	2.0×10^{-5}	6.3×10^{-4}	2.0×10^{-5}
MDF	2.4×10^{3}	7.6×10^{4}	2.4×10^{3}	7.8×10^{4}	2.5×10^{3}	8.0×10^{4}

Table 12.3.: Cuts optimization results.

Table 12.3 shows the optimization results for each object and for signal spectral indices γ = -2 and -2.5. The softer spectrum is considered to assess the effect of the spectral shape on the selection. The optimal RoI angles and minimum scores are relatively similar, which is expected since the 3 blazars have close declinations. A softer spectrum increases the optimal RoI, which comes from the average PSF being less contained at lower energy. The optimal BDT score increases to compensate for the RoI size enlargement. The values of the expected background are found to be the same in each case, as expected from the definition of the MDF, where an expected background of 0.08 corresponds to a level where 2 ON events would yield a 3σ signal significance.

	PKS1741		PKS0215		TXS0310	
	MC	Data	MC	Data	MC	Data
N_{ON}	-	0	-	0	-	0
N_{OFF}	-	98	-	81	-	77
Exp. Background	0.08	0.10 ± 0.01	0.08	0.10 ± 0.01	0.08	0.10 ± 0.01

Table 12.4.: Analysis results with the cuts obtained with γ = 2, using the 11.85 days time window for background estimation

Analysis results can be found in Table 12.4. No ON event was detected after selection. Corresponding event skymaps are shown in Figure 12.6. We can see that for the TXS0310+222 analysis, a neutrino candidate falls just outside the search region. However, the event is excluded in our binned ON/OFF search.

The analysis was also performed with ARCA with no significant excess, and both results are reported in [238].

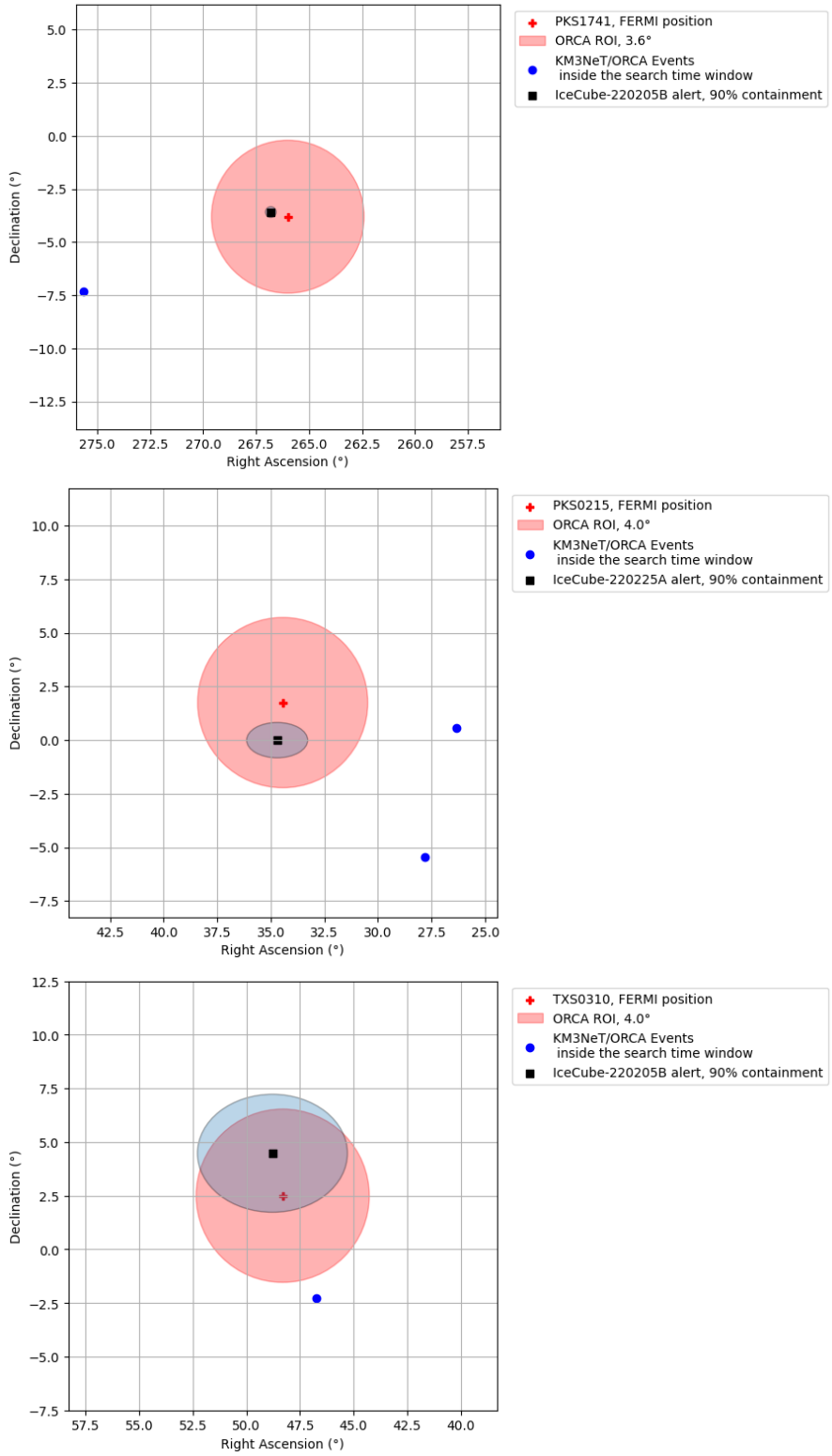

Figure 12.6.: Neutrino event skymaps for the 3 alerts around their respective sources. Blue dots are neutrino candidates that were detected inside the ±1 days search window around each alert. The red circle includes the ORCA search RoI, centered around the blazars. Positions of IceCube events are given in black, with their respective error ellipses.

12.2. GRB221009A

GRB221009A, the brightest GRB ever observed, was detected by Fermi/GBM on October 9th, 2022, at 13:16:59.0 UTC. In the following, this time is referred to as the T_0 of the event. Its coordinates were determined by follow-up by Swift at RA=288.263 and Dec=+19.803. At this time ORCA was taking data with an 11-line configuration (ORCA11), and the event was above the horizon in the detector local coordinates frame, with an elevation of 40° at T_0. A large number of follow-up observations were undertaken by the community, with notably the Fermi/LAT detecting γ-rays close to 100 GeV, which were the highest photons detected by this telescope from a GRB, or the detection in the VHE range by the LHAASO observatory that reported photons up to the TeV range [239]. Unfortunately, observations of IACT at T_0 were impossible due to Moon constraints, and observations a few days later did not detect any signal.

A first quick analysis has been performed using online data and results were reported in GCN#32741. This section describes a refined analysis, based on a more precise calibration and dedicated data and MC productions. The total processed data livetime is 40.9 days.

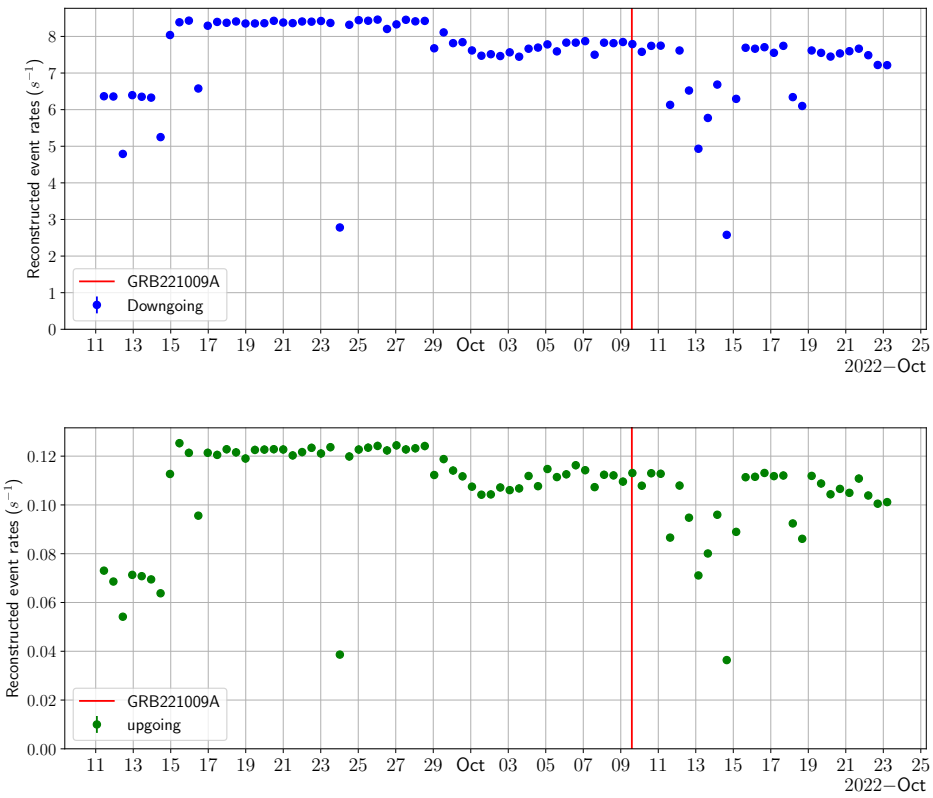

Figure 12.7.: Rate of downgoing (top) and upgoing (bottom) events at precut level

Event rates are shown in Figure 12.7, after anti-noise pre-cuts. Runs with a rate of downgoing events below 7 events per second are considered outliers and are removed

from the data set. We can see that the rates of upgoing and downgoing events are well correlated. The resulting livetime after the removal of outlier runs is 36.55 days.

The analysis method is similar to the one described in section 9.2 with the exception that the search is done in 3 independent analysis strategies:

1. **T0-50s to T0+5000s**. For this analysis, the OFF region is in local coordinates and is a band in zenith angle covering the range of the source during the time window, extended by 4°, i.e. a band of cos(zenith angle) in [-0.77,-0.46]. The GRB being above the horizon during this time window, only downgoing events will be considered. This time window, similar to the one used in the online follow-up reported in GCN#32741 was chosen to include in the search any neutrino signal prior to the γ-ray T0, and a candidate association of a 250 TeV photon reported by the Carpet-2 experiment[1].

2. **T90**. The so-called T_{90} is the time window within which was measured 90% of the GRB flux and ranges from T0 to T0+327s. The OFF region in this case is a band of cos(zenith angle) in [-0.59, -0.46].

3. ± 1 **day, downgoing events**. The search time window considered here is $\pm$ 1 day around the GRB. The OFF region is a declination band of $\pm$ 10° around the source, i.e. in [9.8°,29.8°].

4. ± 1 **day, upgoing events**. The search time window and OFF region coordinates are similar to the previous one.

A new BDT model is trained with the dedicated MC production for the ORCA11 configuration. Signal efficiency for all-sky atmospheric neutrinos against muon background contamination fraction is shown in Figure 12.8 after the BDT training and classification.

For this analysis, the RoI size and BDT score are optimized by maximizing the expected signal from a neutrino flux:

$$F(E) = 10^{-4}\,\mathrm{E}^{-2}\mathrm{GeV}^{-1}\mathrm{cm}^{-2}\mathrm{s}^{-1} \tag{12.2}$$

The expected background is kept to a value of 2.7×10^{-3} events. This background is chosen to ensure that 1 event detected in the ON region yields a 3σ significance from a Poisson distributed background. The optimization is performed using all available data as background.

The event reconstruction performed in the data production used in this analysis relies on static detector calibration, meaning that random displacements of optical modules due to sea currents are not taken into account. This effect induces an error in the reconstructed track direction that is not reproduced in the simulated events. To take into account this uncertainty, a smearing of the simulated events is applied. The smearing is done by randomly offsetting that direction and recomputing the angular

[1] ATel#15669

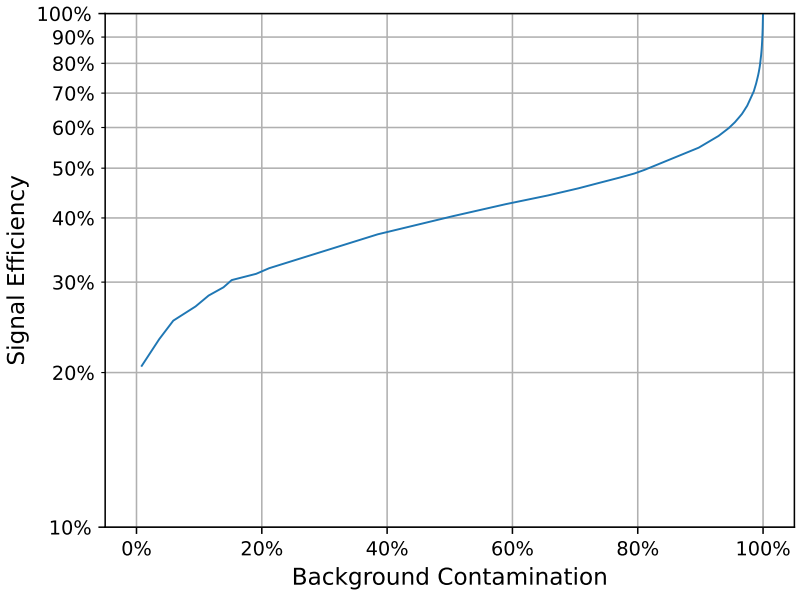

Figure 12.8.: Signal Efficiency for all-sky atmospheric ν vs μ background contamination fraction after BDT training for the ORCA11 model.

error with respect to the true track direction. The random generation is taken with a 2D Gaussian PDF with a variance of 0.5°, which is a conservative value relative to the calibration uncertainty that was observed in previous detector configurations.

	[T0-50, T0+5000]	Long downgoing	Long upgoing	T_{90}
RoI (deg)	5.4	1	1.24	2.0
Min. Score	3.28	3.12	3.45	1.84
Exp. Signal	6.9×10^{-8}	1.7×10^{-5}	3.5×10^{-4}	4.7×10^{-9}
Data evt rate	11.8	21.6	11.44	1050
MC μ evt rate	5.24	10.3	0.53	700
MC ν evt rate	1.94	2.5	11.0	7.4
5% Energy	54 GeV	68 GeV	133 GeV	147 GeV
95% Energy	8.7 TeV	8.8 TeV	8.9 TeV	9120 GeV
Median error (deg)	1.63	1.51	1.15	1.73
nOFF	115	105	70	5539
Φ_0 ($\mathrm{GeV}^{-1}\mathrm{cm}^{-2}\mathrm{s}^{-1}$)	3.8	1.6×10^{-2}	7.4×10^{-4}	5.8×10^{1}
Fluence (GeVcm^{-2})	9.8×10^{4}	1.3×10^{4}	5.4×10^{2}	7.8×10^{4}

Table 12.5.: GRB221009A ORCA analysis summary.

Table 12.5 summarises the analysis. We note that while in the upgoing region, the

agreement between data and MC is good (< 1 %), we observe a disagreement in the downgoing region, with a simulated event rate 40% lower than the observed event rate in the data, as seen on Figure 12.9. An argument can be made that this discrepancy does not result in incorrect results on the upper limits. Indeed, if the disagreement is found to originate from the simulations of muons[2], this would cause no impact on the final results, as the background is computed from data directly. On the other hand, if the disagreement originates from neutrino simulations, the measured neutrino flux is underestimated, which would result in an underestimation of the detector acceptance and an overestimation of the flux upper limits. In conclusion, we choose to not compensate for the data/MC discrepancy as it results in more conservative upper limits.

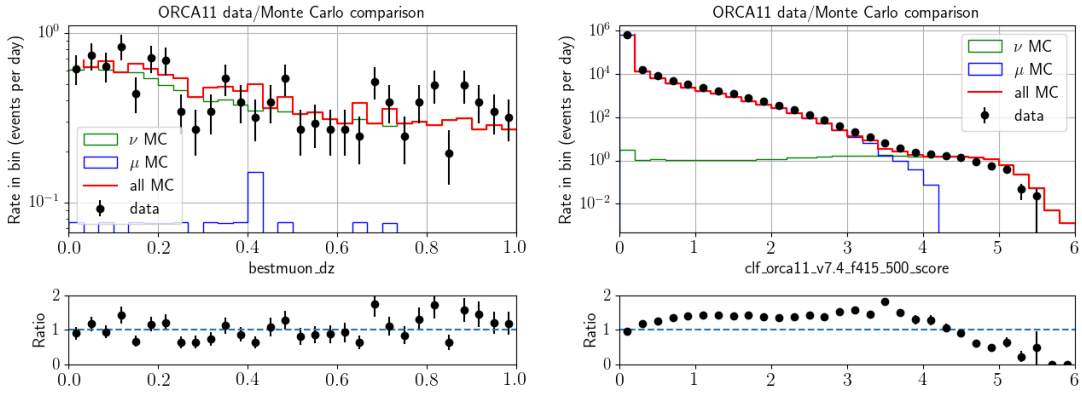

Figure 12.9.: Data/MC comparison for the GRB221009A analysis. Left: distribution of zenith angle, after a score selection of > 3.45. Right: distribution of BDT score for all-sky events.

Figure 12.10 and Figure 12.11 show performances after selection. In each case, the results are shown after their respective optimized score selections and averaged over their respective OFF regions coordinates i.e. cos(zenith) in [-0.77,-0.46] for the short time window and Declination in [9.8°,29.8°] for the long time window. It should be noted that for the long-time window selections, the upgoing signal flux dominates the signal downgoing flux, and the latter expects a higher background rate from atmospheric muons. Figure 12.11 shows the angular resolutions after a selection similar than Figure 12.10. These resolutions are given as the Point-Spread Function, weighted by the solid angle, for a E^{-2} spectrum; and as the median containment angle vs Energy.

Data unblinding yielded no event in the ON region in any case. A similar analysis was performed with the ARCA detector, which was operating with 21 lines at the time of the GRB. Results of analyses in both KM3NeT detectors, as well as with the IceCube neutrino telescope and MWL facilities (taken from [241]) can be found in

[2]This hypothesis is the most likely, as several studies, for example, the one described in [240], find discrepancies in the simulated muon flux.

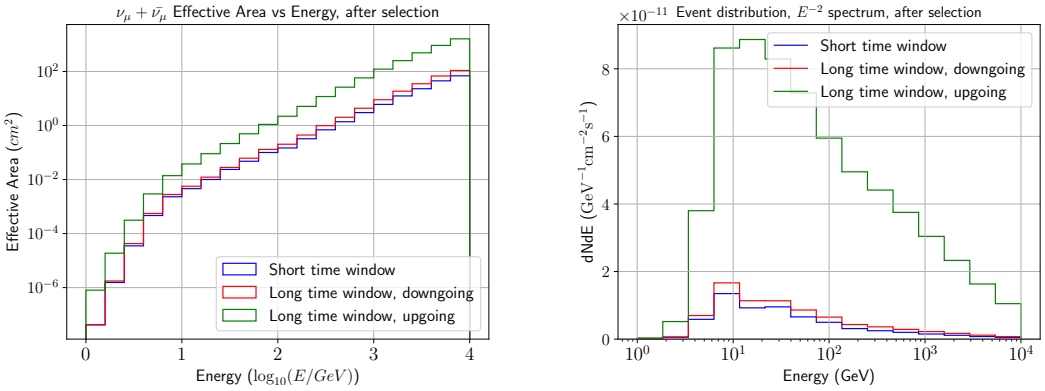

Figure 12.10.: Left: Effective Areas after score selections in their respective OFF bands for the 3 analyses. Right: Signal energy distributions assuming an incoming neutrino flux $\Phi(E) = 10^{-4} \times E^{-2} \text{GeV}^{-1}\,\text{cm}^{-2}\,\text{s}^{-1}$, after score selection in their respective OFF bands.

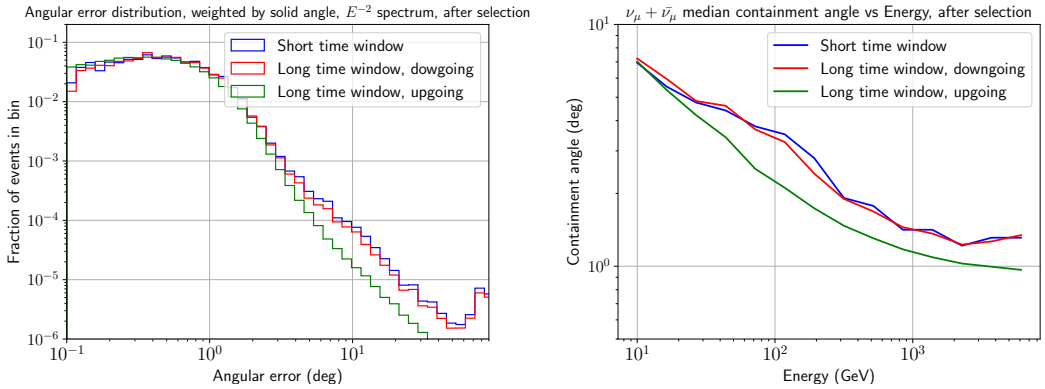

Figure 12.11.: Left: Angular error distribution, weighted by solid angle, after selection for the 3 analyses in their respective OFF bands. Right: Median angular resolution (defined as the 50% containment angle).

Figure 12.12 from [5]. We can note from this figure that the upper limits obtained from the downgoing event samples are relatively higher with ORCA than ARCA, with respect to the upper limits obtained with the upgoing event samples. This is due to the fact that the atmospheric muon rate is higher in ORCA, and its sensitivity to lower energy, which is reflected in an overall higher background rate.

12.3. Gravitational wave events

This section presents a search for neutrino tracks correlated with compact binary mergers detected during the third observing run (O3) of the LIGO and Virgo interferometers. Neutrino emission is expected to happen during these mergers in the

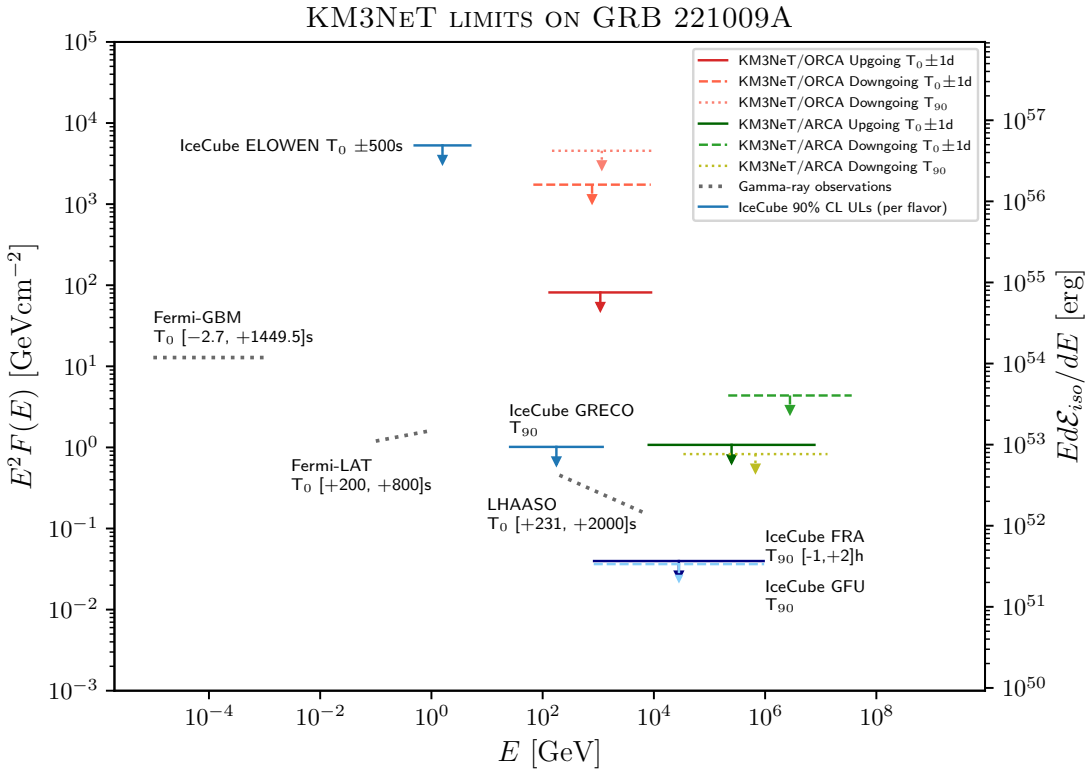

Figure 12.12.: Comparison of the upper limits derived with IceCube and KM3NeT on the fluence neutrino emission from GRB221009A (left y-axis), together with several gamma-ray observatories. The right y-axis shows the differential isotropic equivalent energy. All the neutrino ULs shown are derived for spectral index $\gamma = -2$. [5]

relativistic jets ejected during the coalescence. The neutrino flux is expected to be higher for mergers involving a neutron star such as binary neutron star mergers (BNS) [242] or neutron star-black hole mergers (NSBH) [243], but some models also predict neutrino emissions from binary black hole mergers (BBH) [244].

The mergers were reported in three catalogs:

- GWTC-2 [245]: from April to September 2019, 39 mergers.
- GWTC-2.1 [246]: update of GWTC-2 with 8 additional events not reported in GWTC-2.
- GWTC-3 [247]: from November 2019 to March 2020, 36 mergers with 7 additional candidates with marginal significance.

The search is performed in ORCA data in its 4-line and 6-line configurations, using events reconstructed as upgoing and horizontal tracks, with cos(zenith) > -0.1, in order to reduce the contribution from atmospheric muons.

The ORCA4 data-taking period overlaps with 19, 6, and 17 events in the GWTC-2, GWTC-2.1, and GWTC-3 catalogs respectively, while ORCA6 overlaps with 19 GW events reported in the GWTC-3 catalog, for a total of 61 GW events. The remaining 20 (2) events in the GWTC-2 (GWTC-2.1) catalogs occurred before ORCA4 started.

The analysis method is an ON/OFF region search. In this section we present the region definition and the event selection optimization, then we will obtain an estimation of the background rate and the acceptance for each GW event. Finally, we show how the ON/OFF counting results are used to compute limits on the neutrino fluxes emitted by the mergers.

12.3.1. Region definitions

Each merger is associated with a sky map where each pixel is associated with a probability. On this map contours can be drawn. See for example the probability map for the event GW200219 on Figure 12.13. We choose for this analysis the 90% contour containing 90% of the location probability of the GW event. Our RoI is then defined at this region in local coordinates at the time of the event, extended by an angle $\theta = 30°$ as seen as the orange contour on Figure 12.13. This extension covers the detector resolution and corresponds approximately to the 90% containment angle of ν_μ.

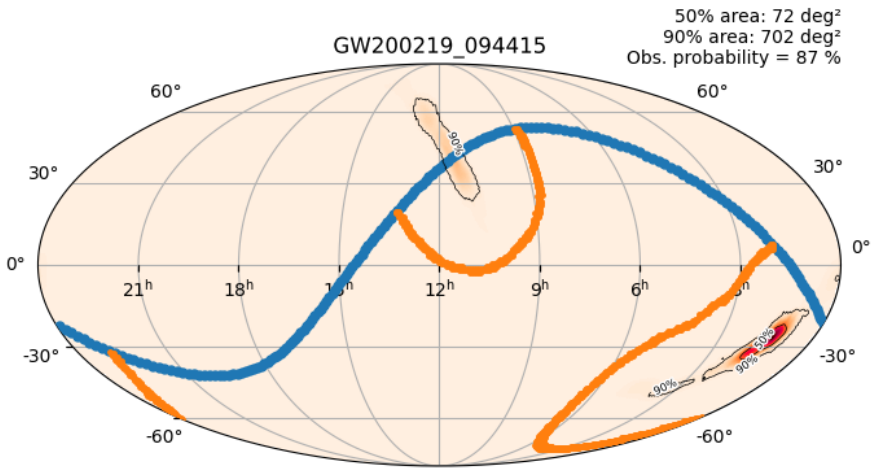

Figure 12.13.: Sky map of event GW200219. The blue line is the horizon seen by ORCA at the time of the event. The orange line shows the border of the RoI.

Contrary to the previous ORCA analyses, the short time window requires the analysis to be performed in local detector coordinates.

From the RoI we can define the ON/OFF periods as follows :

- ON: ±500 seconds time window around the GW event, which is a conservative estimate between the neutrino and the GW emission [248].
- OFF: Similar local coordinates as the ROI, in a set of runs that will be considered similar to the one in which the GW event occurred.

We then evaluate the expected background rate in the ON region as $N_{\mathrm{BKG}} = \alpha_{\mathrm{ON/OFF}} \times N_{\mathrm{OFF}}$, with $\alpha_{\mathrm{ON/OFF}}$ the ratio of the ON time window duration to the OFF region duration, and N_{OFF} the number of events observed in the OFF region.

12.3.2. Run selection

A selection of runs is performed in order to ensure sufficient data quality and stability around each GW event. This selection excludes nine GW candidates for which a follow-up is not possible due to the low quality of the data taken at the time of these mergers. In addition, two additional GWs (GW200224_222234 and GW200311_115853) are excluded as they have been constrained by GW observations as being fully above the KM3NeT horizon. A total of 50 GW sources remain, including 44 BBHs and 6 NSBHs.

Figure 12.14 shows the average rate of neutrino candidate events in the upgoing and horizontal region ($\cos(\theta) > -0.1$), in 2-day intervals, for the two detector configurations (4 lines and 6 lines) superimposed on the time periods covered by the GW catalogs. The main cause of fluctuations in the rate of reconstructed events is the variability of the bioluminescence intensity around the detector. This effect leads to fluctuations in the number of active PMTs and, in turn, fluctuations in the number of triggered events.

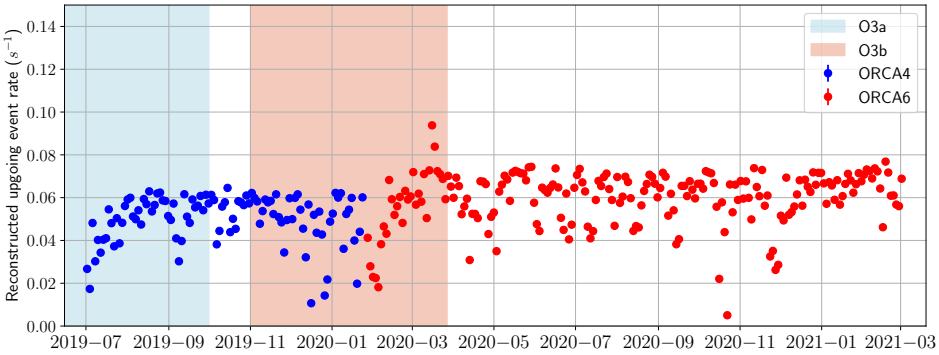

Figure 12.14.: Rate of reconstructed upgoing events averaged over intervals of two days, for the two detector configurations ORCA4 (blue line) and ORCA6 (red line) in the data set. The shaded regions indicate the O3a and O3b periods.

12.3.3. Cuts optimisation

The event selection is optimized on the BDT score for each GW with a MRF(Equation 9.15) minimization, using for the signal an all-flavor neutrino MC weighted to a standard flux of $F(E) = 10^{-4} E^{-2}$ GeV^{-1} cm^{-2} s^{-1}. We compute the expected number of signal events n_s by taking in MC events reconstructed inside the RoI, among those whose

true origin is located inside the 90% CL region. For the background, we use the total available data runs, with livetimes of 154.82 days and 343.2 days for ORCA4 and ORCA6, respectively. The event coordinates are scrambled in azimuth as the blinding strategy. Table 12.6 and Table 12.7 shows optimisation results for GW events recorded with ORCA4 and ORCA6, respectively.

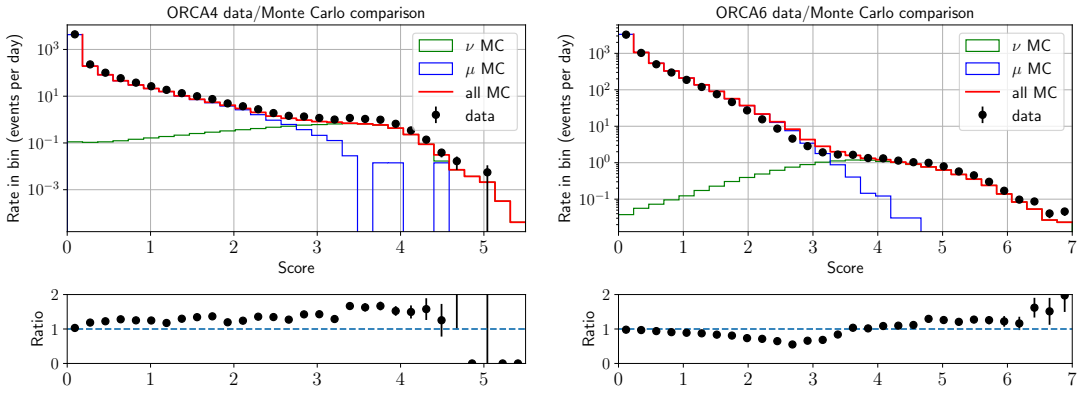

Figure 12.15.: Comparisons of the upgoing events score between data and Monte-Carlo simulation used in the BDT training and selection optimization, for the ORCA4 (left) and ORCA6 (right) detector configurations.

Figure 12.15 shows the distribution of the final BDT scores for real data and for Monte-Carlo simulations. We can see a slight underestimation of the event rate in ORCA4 data, especially with a high BDT score corresponding to a neutrino-dominated sample.

Figure 12.16 shows averages in effective area, event distributions, median angular resolution (defined as the 50% containment angle), and angular error after score selection optimizations for a $\nu_\mu + \bar{\nu}_\mu$ flux of $\Phi(E) = 10^{-4} E^{-2} \mathrm{GeV}^{-1}\,\mathrm{cm}^{-2}\,\mathrm{s}^{-1}$. It should be noted that in terms of angular resolution, ORCA4 seems to outperform ORCA6 at energies below 100 GeV as the optimized selection is stricter in this energy range for the 4-line configuration so that only higher-quality events remain. This is reflected in the event distributions, as the rate of selected low-energy events is lower. When averaged over an E^{-2} spectrum, the median angular resolution for ORCA4 and ORCA6 are 1.85° and 1.63°, respectively. This corresponds roughly to containment angles in the energy region above 100 GeV on the bottom left plot of Figure 12.16, as the events at these energies are those contributing the most to the overall expected flux.

12.3.4. Background estimation

Once we have optimized the event selection parameters, we can more precisely evaluate the expected background rates. This is done by looking for a set of runs that will be assumed to be similar to the one in which the GW event occurred. The goal is to find a set of runs that is sufficiently similar while having enough OFF events to keep a reasonable statistical error. This number is chosen to be around 100.

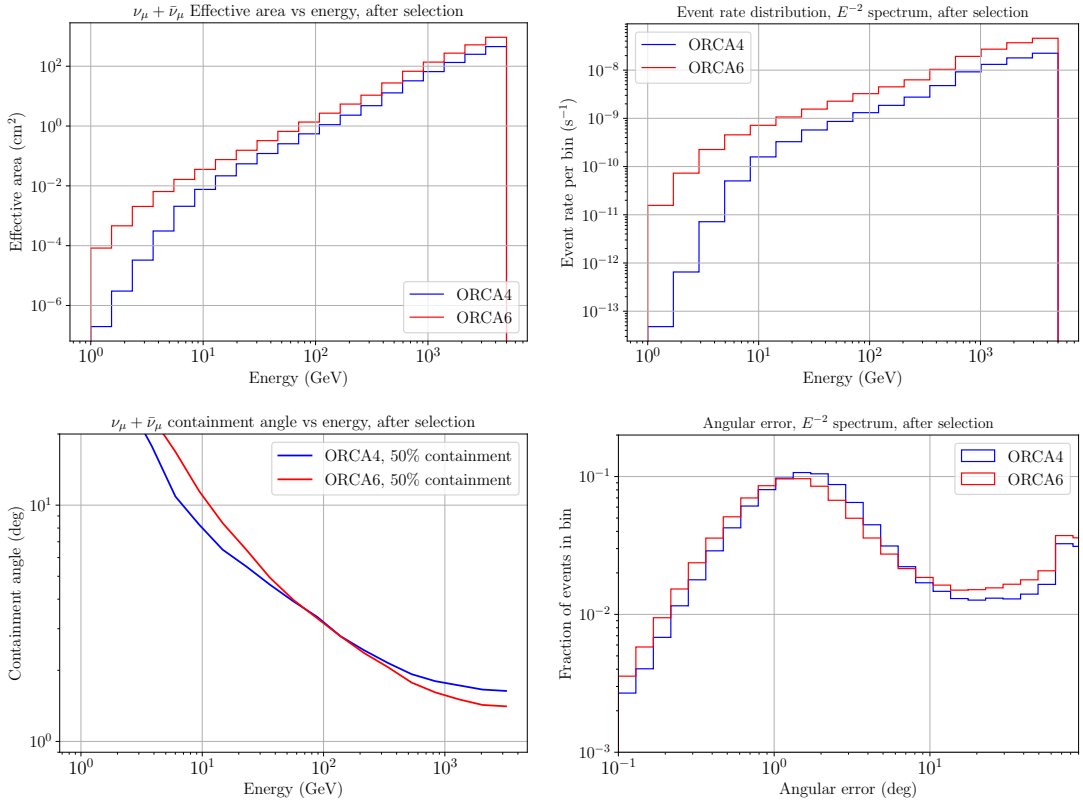

Figure 12.16.: Performance of the $\nu_\mu + \bar{\nu}_\mu$ search, after optimized score selection, in terms of effective area (top left), energy distribution (top right), median angular resolution (defined as the 50% containment angle, bottom left) and angular error (bottom right). These quantities are averaged over the set of GW events and shown for the two detector configurations. The two plots on the right assume an incoming neutrino flux $\Phi(E) = 10^{-4} \times E^{-2}\text{GeV}^{-1}\,\text{cm}^{-2}\,\text{s}^{-1}$.

We compute for every run the rate of events at a low-score level (score > 0.5). The assumption is that runs with similar rates at this level will also have similar rates at a higher selection score. We find a set of runs R whose rate is in an interval δ_{rate} that gives :

$$\begin{cases} \text{Rates}(R) \in \text{Rate}(\text{run}_{\text{GWevt}}) \pm \delta_{rate} \\ N_{\text{OFF}}(R) \approx 100 \end{cases} \tag{12.3}$$

The N_{OFF} here is the number of events in the RoI for the runs R. The estimated number of background events is mostly consistent with what was obtained during the cut optimization. The resulting sets of runs for each GW event are then used to compute the real N_{OFF} in the analysis.

12.3.5. ON/OFF search results

Table 12.8 and Table 12.9 show ON/OFF search results. In most GW events, no ON event was recorded. For the recorded ON events, we can compute the corresponding Poisson p-value p, that is the Poisson probability of observing at least N_{ON} events with the given expected background (neglecting the related statistical uncertainty for this computation). We find the lowest p-value to be 5% and associated with GW200115_042309. This value is fully compatible with background expectations when taking into account a trial factor on the number of GW events.

12.3.6. Flux upper limits

As no significant signal was detected, upper limits are computed using the JANG framework [249]. Fluence upper limits are shown for every GW event in Figure 12.17. Additionally, upper limits on the total energy emitted in neutrino assuming an isotropic flux $E^{\mathrm{iso}}_{\mathrm{tot},\nu}$ and this value scaled by the energy emitted in Gravitational Waves $f^{\mathrm{iso}}_{\nu} = E^{\mathrm{iso}}_{\mathrm{tot},\nu}/E_{\mathrm{GW}}$ are represented as a function of the estimated luminosity distance of the mergers in Figure 12.18. As we can see, the limits on the energy emitted in neutrinos are orders of magnitude larger than the energies emitted in gravitational waves. However, we should keep in mind that the assumption of an isotropic neutrino emission is made due to the fact that the inclinations of the merging binary systems are uncertain. Assuming that neutrinos are emitted in a jet instead would result in a significant reduction of that limit, but this is not possible without a precise estimation of the inclinations.

Event ID	90% CL region area (deg²)	Obs. probability	Min. score	Exp. Bkg	Exp.Signal	MRF
GW190706_222641	867.87	0.74	2.25	0.195	6.28E-07	4.15E+06
GW190707_093326	1148.99	0.69	2.32	0.205	8.56E-07	3.06E+06
GW190708_232457	14050.2	0.54	2.45	0.335	8.89E-07	3.06E+06
GW190719_215514	3119.97	0.53	2.34	0.215	7.38E-07	3.56E+06
GW190725_174728	2398.37	0.46	2.3	0.235	7.28E-07	3.63E+06
GW190727_060333	409.52	0.52	2.26	0.144	7.18E-07	3.57E+06
GW190728_064510	455.97	0.55	2.17	0.185	6.81E-07	3.82E+06
GW190731_140936	3518.74	0.64	2.28	0.185	8.96E-07	2.90E+06
GW190803_022701	1469.51	0.55	1.93	0.354	3.51E-07	7.81E+06
GW190805_211137	3804.05	0.7	2.3	0.245	8.27E-07	3.20E+06
GW190814	30.32	1	1.96	0.19	1.13E-06	2.30E+06
GW190828_063405	411.03	0.64	2.27	0.175	7.79E-07	3.33E+06
GW190828_065509	695.91	0.72	2.25	0.185	8.92E-07	2.91E+06
GW190909_114149	3975.16	0.56	2.27	0.255	7.64E-07	3.48E+06
GW190915_235702	400.4	0.84	1.83	0.194	5.39E-07	4.84E+06
GW190916_200658	4214.41	0.56	2.26	0.255	7.57E-07	3.51E+06
GW190917_114630	1916.68	0.69	2.34	0.215	8.31E-07	3.16E+06
GW190924_021846	336.67	0.3	2.03	0.143	4.47E-07	5.74E+06
GW190925_232845	877.44	1	2.22	0.205	1.11E-06	2.37E+06
GW190926_050336	2405.21	0.53	2.45	0.165	7.80E-07	3.31E+06
GW190929_012149	2090.63	0.63	2.28	0.225	8.31E-07	3.17E+06
GW190930_133541	1311.4	0.15	1.88	0.273	1.83E-07	1.46E+07
GW191103_012549	2519.77	0.46	2.32	0.205	5.72E-07	4.58E+06
GW191105_143521	728.97	0.82	2.3	0.185	8.08E-07	3.22E+06
GW191109_010717	1784.44	0.86	2.38	0.195	1.03E-06	2.53E+06
GW191113_071753	2993.6	0.69	2.28	0.225	7.82E-07	3.37E+06
GW191127_050227	1499.46	0.45	2.31	0.195	6.29E-07	4.15E+06
GW191129_134029	848.47	0.61	2.28	0.185	7.98E-07	3.26E+06
GW191204_110529	4747.78	0.45	2.26	0.265	6.27E-07	4.25E+06
GW191204_171526	345.13	0.81	2.35	0.144	9.48E-07	2.71E+06
GW191215_223052	596.16	0.62	2.34	0.145	7.72E-07	3.32E+06
GW191219_163120	2232.26	0.69	2.34	0.195	7.48E-07	3.49E+06
GW191222_033537	2299.47	0.71	2.44	0.165	8.05E-07	3.21E+06
GW191230_180458	1012.45	0.58	2.32	0.155	8.41E-07	3.06E+06
GW200105_162426	7882.02	0.53	2.3	0.375	7.48E-07	3.69E+06
GW200112_155838	4250.6	0.46	2.29	0.305	6.26E-07	4.31E+06
GW200115_042309	512.21	0.92	2.29	0.205	9.20E-07	2.84E+06

Table 12.6.: Cuts optimization results for GW events in the ORCA4 period. The "Exp. Bkg" and "Exp. signal" columns show the number of expected background and signal events in the ROI during the observation time window. Obs. probability is the probability of observing the GW event, and corresponds to the summed probability of every pixel located below horizon at the time of the GW event.

Event ID	90% CL region area (deg²)	Obs. probability	Min. score	Exp. Bkg	Exp.Signal	MRF
GW200128_022011	2677.66	0.59	2.16	0.29	1.63E-06	1.65E+06
GW200129_065458	80.5	0.11	1.95	0.20	5.75E-07	4.54E+06
GW200208_130117	37.69	0.99	1.59	0.12	2.77E-06	9.19E+05
GW200209_085452	924.69	0.46	2.01	0.35	9.75E-07	2.81E+06
GW200210_092254	1830.95	0.3	2.06	0.30	1.14E-06	2.38E+06
GW200219_094415	702.37	0.87	2.09	0.27	1.56E-06	1.72E+06
GW200220_061928	3484.96	0.6	1.99	0.24	1.60E-06	1.65E+06
GW200220_124850	3169.17	0.53	2.13	0.33	1.62E-06	1.68E+06
GW200302_015811	7010.99	0.61	2.21	0.42	1.51E-06	1.85E+06
GW200306_093714	4371.41	0.5	1.97	0.44	9.89E-07	2.83E+06
GW200308_173609	18705.76	0.55	2.26	0.40	1.69E-06	1.65E+06
GW200316_215756	410.54	0.08	1.94	0.26	7.71E-07	3.45E+06
GW200322_091133	31570.87	0.51	2.26	0.46	1.44E-06	1.96E+06

Table 12.7.: Cuts optimization results for GW events in the ORCA6.

GW event	Min. score	OFF zone LT(d)	N_{OFF}	N_{ON}	Exp. Bkg	p-value
GW190706_222641	2.25	21.49	92	0	0.063 +/- 0.007	-
GW190707_093326	2.32	18.24	87	0	0.041 +/- 0.004	-
GW190708_232457	2.45	10.55	100	0	0.11 +/- 0.011	-
GW190719_215514	2.34	14.48	80	0	0.084 +/- 0.008	-
GW190725_174728	2.3	17.79	90	0	0.07 +/- 0.007	-
GW190727_060333	2.26	28.78	113	0	0.065 +/- 0.007	-
GW190728_064510	2.17	26.55	114	0	0.052 +/- 0.005	-
GW190731_140936	2.28	17.4	85	0	0.075 +/- 0.008	-
GW190803_022701	1.93	11.01	97	0	0.079 +/- 0.008	-
GW190805_211137	2.3	15.39	93	0	0.054 +/- 0.005	-
GW190814	1.96	20.06	66	0	0.059 +/- 0.006	-
GW190828_063405	2.27	19.79	98	1	0.059 +/- 0.006	0.06
GW190828_065509	2.25	14.94	86	0	0.043 +/- 0.004	-
GW190909_114149	2.27	14.06	92	0	0.07 +/- 0.007	-
GW190915_235702	1.83	20.22	107	0	0.055 +/- 0.006	-
GW190916_200658	2.26	13.98	91	0	0.158 +/- 0.016	-
GW190917_114630	2.34	16.01	91	0	0.064 +/- 0.007	-
GW190924_021846	2.03	30.35	113	0	0.054 +/- 0.005	-
GW190925_232845	2.22	18.31	94	0	0.116 +/- 0.011	-
GW190926_050336	2.45	18.47	83	0	0.07 +/- 0.008	-
GW190929_012149	2.28	15.87	103	0	0.073 +/- 0.007	-
GW190930_133541	1.88	16.63	105	0	0.052 +/- 0.006	-
GW191103_012549	2.32	17	93	0	0.075 +/- 0.007	-
GW191105_143521	2.3	16.5	96	0	0.066 +/- 0.007	-
GW191109_010717	2.38	16.96	102	0	0.057 +/- 0.006	-
GW191113_071753	2.28	14.23	86	0	0.076 +/- 0.008	-
GW191127_050227	2.31	16.2	111	0	0.05 +/- 0.005	-
GW191129_134029	2.28	17.82	91	0	0.063 +/- 0.007	-
GW191204_110529	2.26	14.47	105	0	0.067 +/- 0.007	-
GW191204_171526	2.35	26.07	93	0	0.102 +/- 0.01	-
GW191215_223052	2.34	24.75	112	0	0.067 +/- 0.007	-
GW191219_163120	2.34	16.5	92	0	0.061 +/- 0.006	-
GW191222_033537	2.44	20.92	97	0	0.045 +/- 0.004	-
GW191230_180458	2.32	22.88	106	0	0.059 +/- 0.006	-
GW200105_162426	2.3	7.561	103	0	0.057 +/- 0.006	-
GW200112_155838	2.29	10.86	109	0	0.038 +/- 0.005	-
GW200115_042309	2.29	16.29	88	1	0.05 +/- 0.005	0.05

Table 12.8.: Results of the ON/OFF search in the ORCA4 period. The minimum score was found in the MRF minimization. The number of OFF/ON events, detected respectively outside/inside the +/- 500 s time window, are shown in columns N_{OFF}/N_{ON}. The expected background was computed from the OFF zone livetime and the number of OFF events. In the cases where an ON event was detected, a pre-trial indicative p-value is given. The OFF zone LT is the sum of runs livetimes selected in subsection 12.3.4.

GW event	Min. score	OFF zone LT(d)	N_{OFF}	N_{ON}	Exp. Bkg	p-value
GW200128_022011	2.16	4.414	97	0	0.255 +/- 0.026	-
GW200129_065458	1.95	5.449	82	0	0.175 +/- 0.019	-
GW200208_130117	1.59	8.854	97	0	0.127 +/- 0.013	-
GW200209_085452	2.01	4.869	150	0	0.357 +/- 0.029	-
GW200210_092254	2.06	4.239	94	0	0.257 +/- 0.027	-
GW200219_094415	2.09	4.141	76	0	0.213 +/- 0.024	-
GW200220_061928	1.99	3.29	82	0	0.289 +/- 0.032	-
GW200220_124850	2.13	3.093	76	0	0.285 +/- 0.033	-
GW200302_015811	2.21	3.747	160	1	0.496 +/- 0.039	0.39
GW200306_093714	1.97	2.322	73	0	0.366 +/- 0.043	-
GW200308_173609	2.26	2.817	81	1	0.334 +/- 0.037	0.28
GW200316_215756	1.94	4.54	102	1	0.261 +/- 0.026	0.23
GW200322_091133	2.26	3.373	109	0	0.375 +/- 0.036	-

Table 12.9.: Results of the ON/OFF search in the ORCA6 period.

Figure 12.17.: Upper limits on the incoming all-flavour neutrino flux $\phi = E^2 dn/dE$ for ORCA4+ORCA6, assuming E^{-2} spectrum. The different colors correspond to different ORCA configurations and GW catalogs.

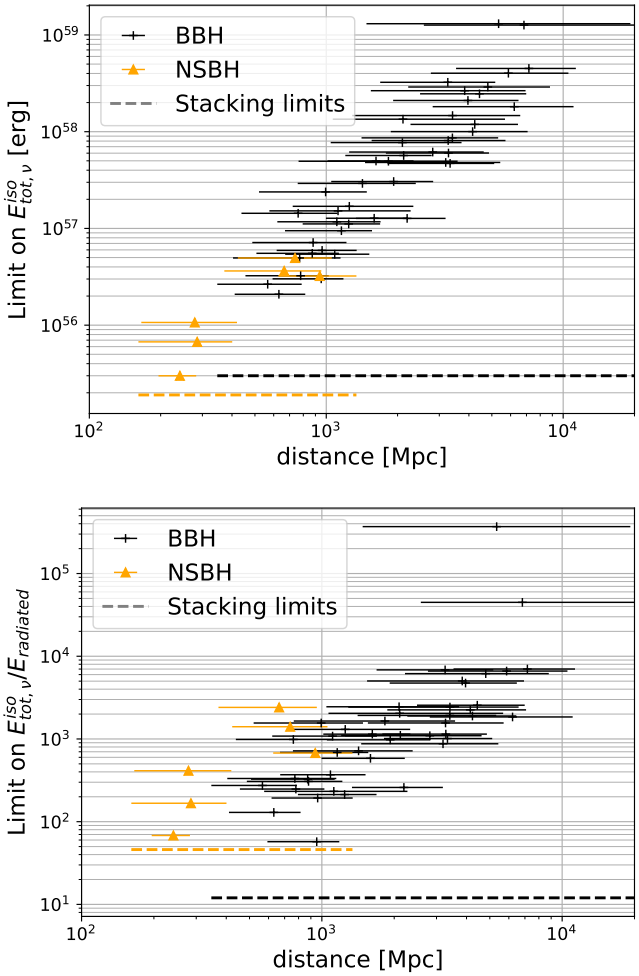

Figure 12.18.: 90% upper limits on the total energy $E^{\mathrm{iso}}_{\mathrm{tot},\nu}$ emitted in neutrinos of all flavors (top) and on $f^{\mathrm{iso}}_{\nu} = E^{\mathrm{iso}}_{\mathrm{tot},\nu}/E_{\mathrm{GW}}$ (bottom) as a function of the source luminosity distance, assuming E^{-2} spectrum and isotropic emission. The horizontal bars indicate the 5-95% range of the luminosity distance estimate, and the markers/colors correspond to the different source categories. The dashed bars correspond to the upper limits from the stacking analysis for BBH and NSBH categories.

A similar search was performed on MeV-scale neutrinos and the ranges of results of both ORCA analyses, in addition to several other searches from ANTARES, IceCube, and Super-Kamiokande are shown in Figure 12.19.

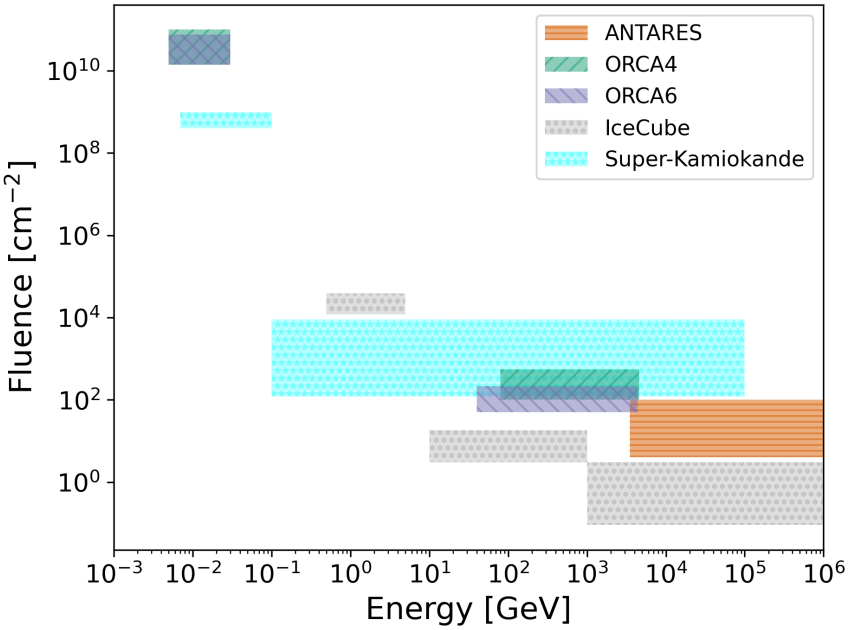

Figure 12.19.: Comparisons of the fluence upper limits ranges of several telescopes. In each case, the horizontal widths of the bands are the energy ranges of the respective analyses. The vertical width ranges from the lowest to the highest fluence upper limits in the studied catalog. ANTARES limits are reported in [250]. The IceCube results are extracted from [251], [252], and [253], from the lowest to the highest energy searches. The Super-Kamiokande results are obtained from [254].

13. KM3NeT Online analysis pipeline

The ANTARES telescope provided online follow-ups to external alerts between 2014 and the end of its data-taking period in 2022, as reviewed in [255]. Building upon the experience gained, a real-time external alert follow-up and internal alert generation system is under development for the KM3NeT detector. It aims to allow online data reconstruction, classification, and analysis in a reliable and automated way. In this section, we provide an overview of the system and its analysis methods.

13.1. High-level data processing procedure

A schematic of the Real-Time framework architecture can be found in Figure 13.1. It shows the global strategy of the online system. First, the data is sent from ORCA and ARCA into each of their shore stations from the Data Acquisition (DAQ) system where it is reconstructed as track-like and shower-like. The reconstruction is performed using similar algorithms to the standard, offline, data processing. Event classification is also performed using BDT and Graph-Neural Network (GNN) algorithms. This procedure is performed in real-time at a rate of approximately 7 events per second in the ARCA21 configuration and 20 events per second in the ORCA18 configuration. The total processing time is of the order of a few seconds. The reconstructed and classified events are then sent to a common platform noted as the Multi-messenger dispatcher in Figure 13.1 where they are stored in a database to be available for analysis.

An independent pipeline has been developed for the early detection and alert reporting for the next galactic Core-Collapse SuperNova (CCSN) and is described in [256]. The neutrino energy from such an event is expected to be in the MeV range, which is too low for the triggering of multiple DOMs and the occurrence of individual events. As such, a dedicated analysis strategy was designed that uses each individual DOM as a stand-alone detector by studying the number of coinciding hits in its PMTs.

13.2. Alert receiving and filtering

A subscription to the GCN Notices is implemented in the KM3NeT online system. While initially being conceived for alerting the community of GRB detections and reporting follow-ups, other types of transient alerts are now circulated with this system. Notably, the LIGO/Virgo/Kagra collaborations report the detections of GW events of the O4 run that started on May 24th, 2023.

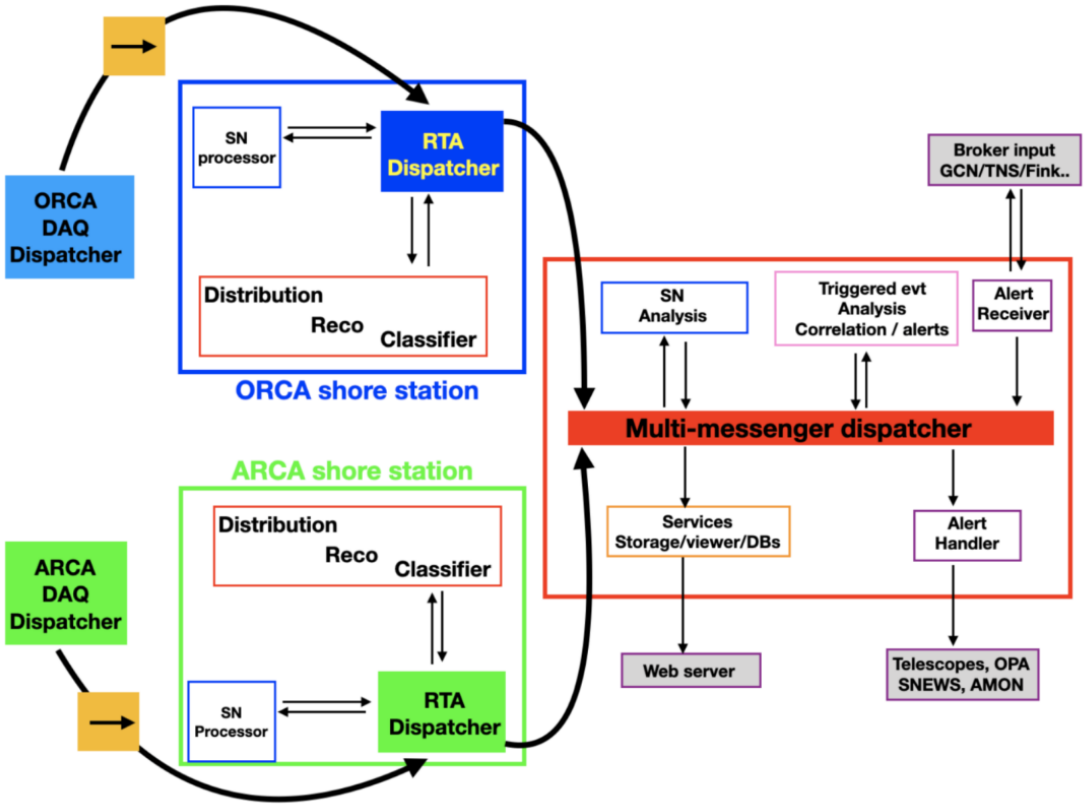

Figure 13.1.: Real Time framework architecture of KM3NeT

Different types of alerts are thus filtered to provide adapted analysis. The received alerts are tagged to the following types:

1. **GRB**: Alerts flagged as GRB from Fermi/GBM and LAT, Swift/BAT and its XRT follow-ups, and alerts from INTEGRAL.

2. **TRANSIENT**: Alerts from Swift and Fermi that are not flagged as GRB, HAWC observatory, and MAXI.

3. **GW**: Gravitational Wave alert from LIGO/Virgo/Kagra.

4. **NEUTRINO**: IceCube track alerts and IceCube Cascade coincidences through the AMON system.

5. **CCSN**: SuperNovae alerts from the SNEWS network or the SuperKamiokande facility.

Relevant pieces of information are extracted from the GCN message, saved in a database, and sent internally to trigger a follow-up analysis. Additionally, the parsed GCN is sent via e-mail and internal chat for human intervention or supervision. The microquasar monitoring, described in chapter 11, also triggers follow-up analyses.

At the time of writing, alert follow-ups from other platforms are being implemented in the system. It includes for example the Fink alert broker from the ZTF and LSST programs [257] and the Transient Name Server[1]. A schematic description of the alerts receiving strategy is shown in Figure 13.2.

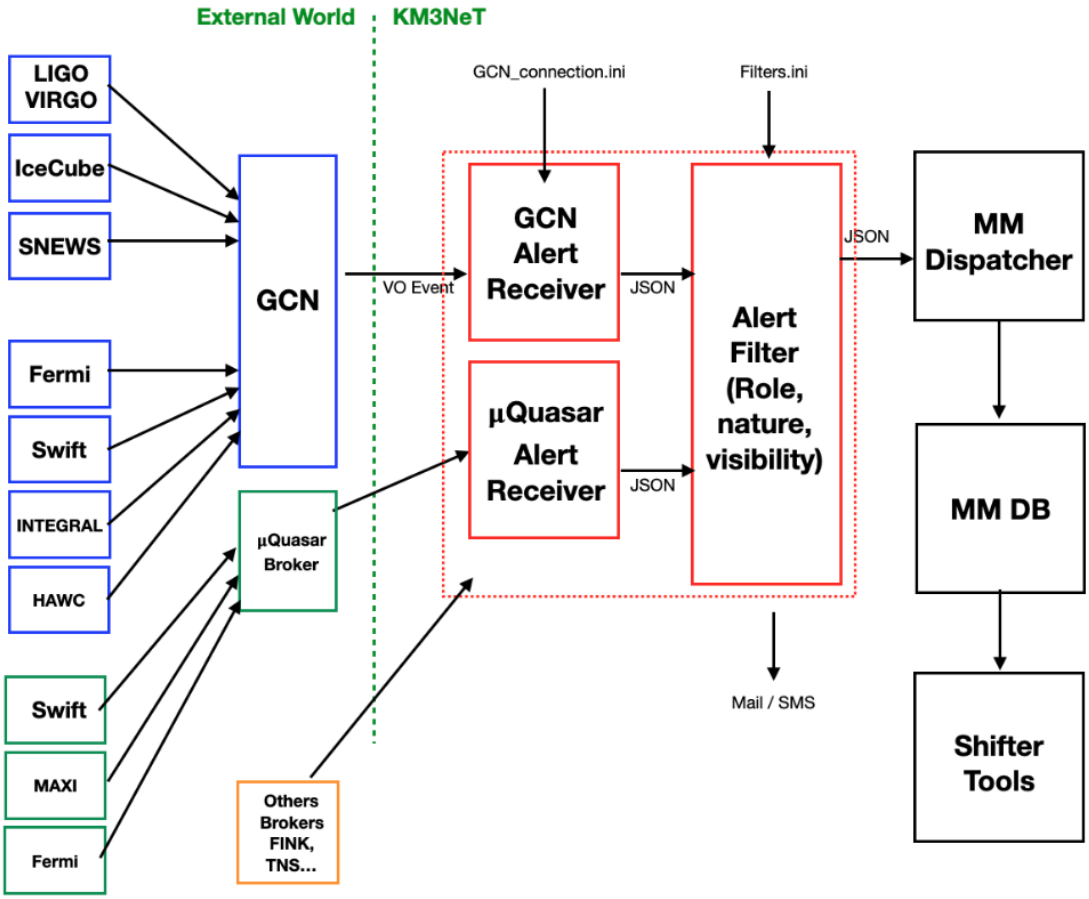

Figure 13.2.: Schematic of the alert receiver.

13.3. Follow-up analysis

The analysis scheme that is triggered depends on the type of the alert. At this time, three strategies have been put in place: a search of neutrino in correlation to well-localized short transient sources, well-localized long transient sources, and a search in correlation to sources with a large error region, mostly GW. The parameters of a well-localized follow-up analysis are the coordinates of the source, or the best-fit coordinates and its associated error radius, and is used for **GRB**, **TRANSIENT** and **NEUTRINO** alert types. On the other hand, the space correlation from a **GW** event

[1] www.wis-tns.org

necessitates that the search takes the probability skymap into account. In both cases, the analysis is performed using a binned ON/OFF method, similar to the one described in section 9.2,section 12.1 and section 12.2 for the point sources and section 12.3 for the GW events. The main differences from the analyses described in said sections reside in the fact that the selection cuts optimizations and the background estimation can be difficult to perform in real-time, in the absence of dedicated simulations and calibrations. The respective event selections were then chosen to keep the expected to a reasonable value, while performing a purely data-driven analysis, without relying on simulations.

The analysis pipelines are triggered independently for both ARCA and ORCA detectors, and are performed in multiple iterations with different time windows depending on the alert type:

- **GW** 2 iterations:
  - ± 500 seconds around the event, launched at alert reception
  - from 500 seconds before to 6 hours after the event
- **NEUTRINO** 2 iterations:
  - ± 1 hour around the event
  - ± 1 day around the event
- **GRB** and **TRANSIENT**: 4 iterations, each considering a time window starting 24h before the event to the last available data
  - At alert reception
  - 3h after the alert
  - 6h after the alert
  - 24h after the alert

At each iteration after the initial pipeline trigger, a check for any revision of the alert parameters is done to take into account coordinates refinements, improvement of error estimation, or possible retraction.

A commissioning phase of the KM3NeT Online analyses started in October 2022, and as of August 2023, it processed more than 300 alerts, with a rate that can reach 10 per day as seen in Figure 13.3. Around 170 follow-ups were performed after GRB candidates, mostly from the Fermi satellite; around 100 after GW alerts sent by the LIGO observatory; around 50 from neutrinos and 13 from other transients. Over this sample, no significant neutrino correlation to the received alert could be established.

At the time of writing, KM3NeT is not yet sending alerts and follow-up results to the community. This however is planned for mid-2024.

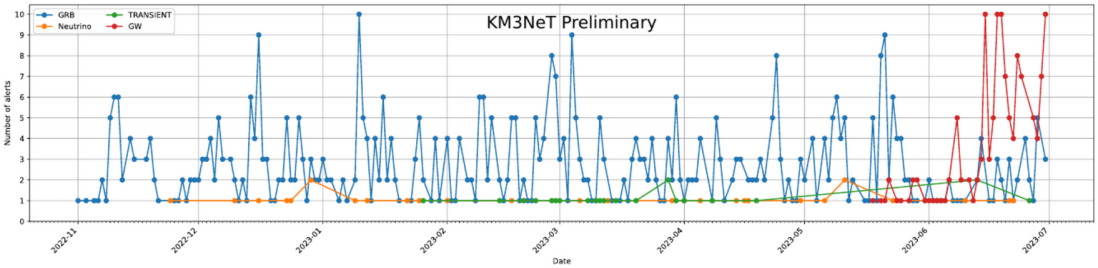

Figure 13.3.: Rate of alerts per day processed in the KM3NeT Online Framework from November 2022 to June 2023 [238].

13.4. GW Online Analysis

In order to provide a quick follow-up analysis and reduce the strain on the system caused by requests of reconstructed events to the database, the expected background is computed from events in the 2 weeks before the alert.

To ensure sufficient statistics for background estimation, the events are selected in the full sky and not in a region similar to the search region as it was chosen for the offline analysis in section 12.3. However, the background rate from atmospheric muons is highly dependent on the zenith angle. A simple rescaling of the solid angles of the ON and OFF regions might then introduce a bias if the ON region covers a large fraction of the sky. To correct for that effect, the sky is sliced in bands and the expected background in the ON region is computed as:

$$\text{Exp. Bkg} = \frac{t_{ON}}{t_{OFF}} \times \sum_i \frac{\Omega_{ON,i}}{\Omega_{OFF,i}} \cdot N_{OFF,i} \tag{13.1}$$

With t_{ON} and t_{OFF} the livetimes of the ON and OFF time windows, $\Omega_{ON,i}$ the solid angle of the search region included in the i-th band, $N_{OFF,i}$ the number of events recorded in this band and $\Omega_{OFF,i}$ the solid angle of the OFF region. If the ON and OFF time windows do not overlap, the OFF region is then the full sky and the solid angle of the band located between zenith angles θ_1 and θ_2 is simply

$$\Omega_{OFF,i} = 2\pi(\cos(\theta_1) - \cos(\theta_2)) \tag{13.2}$$

The event selection is then performed by selecting in each band a BDT score in order to reduce the overall expected background to around 2.7×10^{-3} events so that 1 event in the ON region gives a 3σ correlation.

An example is given in Figure 13.4 which is the second iteration of the ORCA follow-up analysis of GW event S230731an. We can see the ON region which is the region located inside the 90% confidence level contour, extended by an angle of 4°. We see an event recorded in the ON time window but outside the ON region, and no ON event.

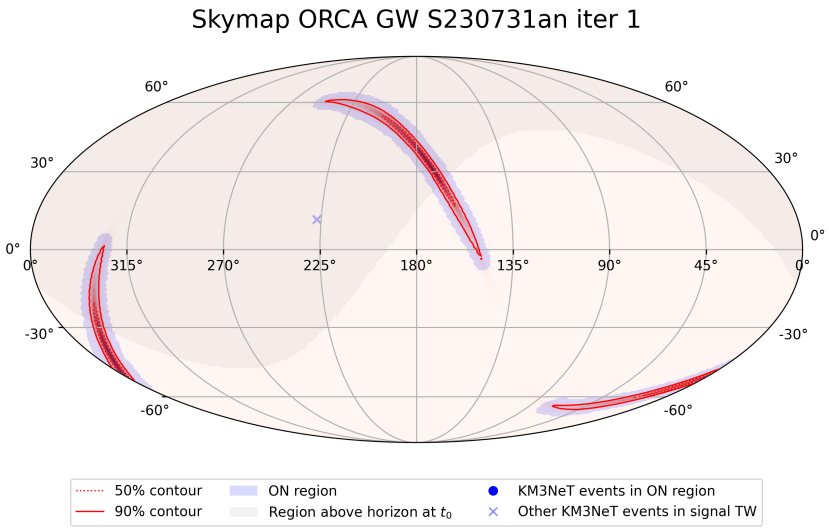

Figure 13.4.: Skymap of a GW event. The probability contours of the GW event are in red. The ORCA ON region is highlighted in blue.

Conclusion of Part III

In this part, we have discussed the follow-up analyses of neutrino, γ-ray, and GW alerts. While no significant signal was found, the analysis methods were implemented in the online system of KM3NeT. The analyses were performed in a detector that is still under construction, with only a fraction of the instrumented volumes. The ORCA analyses were then performed with 6 to 11 lines, with respect to the 115 lines planned to be integrated by 2028. At the time of writing, the ORCA site has 18 lines while the ARCA site has 28 lines, and 230 lines are planned also by 2028. The detector will then move toward better sensitivity and precision. In that sense, the angular resolution of the ARCA detector is foreseen to reach 0.1° which would be particularly relevant for the identification of steady and transient neutrino point sources. On the analysis methods, for the moment we have implemented binned "cut and count" type ON/OFF techniques. Unbinned, likelihood maximization types of methods are expected to provide better sensitivities. These however are not straightforward to implement in real-time, as they require a good understanding of our detectors which is difficult to obtain when they are quickly expanding with the implementation of new lines. From improvements in the analysis methods or growth of the detector size, the detector will keep increasing its capabilities, and with the complementarity of ORCA and ARCA, will provide interesting results on the follow-ups of future transient events, being GW detection of mergers, optical transients from LSST, or microquasar flares.

Acronyms

ADC Analog-to-Digital Converter. 60
AGN Active Galactic Nuclei. 27, 30, 42, 43, 49, 54

BDT Boosted Decision Tree. 148

DAQ Data Acquisition. 214
DOM Digital Optical Module. 78–81, 83
DU Detection Unit. 78, 80, 189

FAR False Alarm Rate. 182
FoV Field of View. 59, 66, 69, 71, 87, 89–91, 98, 109

GRB Gamma-Ray Burst. 28, 90, 188, 196
GW Gravitational Wave. 25–27, 188, 214, 216, 220

HE High Energy. 27, 56, 95, 185
HID Hardness Intensity Diagram. 45–47, 96, 123
HIMS Hard Intermediate State. 46
HMXB High-Mass X-Ray Binary. 39, 41, 50–52, 54, 56
HRV High Rate Veto. 80, 146
HS Hard State. 45, 47, 48, 52, 101, 105–108, 122–125, 132, 160

IACT Imaging Atmospheric Cherenkov Telescope. 52, 57, 59, 87, 105, 196
IRF Instrument Response Functions. 66, 67, 89, 113, 118, 127
ISCO Innermost Stable Circular Orbit. 42, 43
ISM Interstellar medium. 27, 34, 185

LMXB Low-Mass X-Ray Binary. 39, 41, 45, 49, 51, 54, 96

MC Monte-Carlo simulations. 62, 64, 65, 82, 85, 134, 140, 148, 152, 190, 203
MDF Model Discovery Factor. 190
MHD MagnetoHydroDynamic. 43, 44
MRF Model Rejection Factor. 151, 203
MWL Multi-Wavelength. 28, 43, 95, 105, 109, 189

NSB Night Sky Background. 61, 65

PDF Probability Density Function. 62, 86, 134, 136, 145, 147
PMT Photo-Multiplier Tube. 59–61, 63, 78, 80, 81, 83, 84, 86, 87, 140, 146, 147, 150, 203
PSF Point-Spread Function. 66, 89, 90, 136, 140

PWN Pulsar Wind Nebula. 27

QPO Quasi-Periodic Oscillation. 48–51

RMS Root Mean Square. 47, 48
RoI Region of Interest. 127, 147, 151, 190, 194, 195, 202
RWS Runwise Simulations. 62, 82, 114, 117–119

SED Spectral Energy Distribution. 35, 36, 54, 95, 99, 100, 103, 107, 108, 167, 185, 189, 191
SIMS Soft Intermediate State. 46, 48
SNR Supernova Remnant. 27, 35, 111
SS Soft State. 46–48, 52, 101, 105, 106, 122, 123, 125, 132
ST State transition. 46, 47, 49, 50, 52, 101, 105–108, 122, 123, 125, 132, 145, 160

ToO Target of Opportunity. 109, 111, 113, 119, 180, 183, 184
ToT Time over Threshold. 81, 83, 84, 147

UHE Ultra High Energy. 27, 28

VHE Very High Energy. 27, 28, 30, 35, 36, 53, 56, 57, 59, 64, 70, 87, 95, 105, 106, 183, 185, 196

XRB X-Ray Binary. 39, 56

Bibliography

[1] H Abe, S Abe, V A Acciari, et al. “Gamma-ray observations of MAXI J1820+070 during the 2018 outburst”. In: *Monthly Notices of the Royal Astronomical Society* 517.4 (Sept. 2022), pp. 4736–4751. DOI: 10.1093/mnras/stac2686. URL: https://doi.org/10.1093%2Fmnras%2Fstac2686 (cit. on pp. 3, 101, 102, 105–108, 164, 165, 175, 176).

[2] KM3NeT Collaboration, S. Aiello, A. Albert, et al. “Searches for neutrino counterparts of gravitational waves from the LIGO/Virgo third observing run with KM3NeT”. In: (2023). arXiv: 2311.03804 [astro-ph.HE] (cit. on p. 3).

[3] Gustavo E. Romero, M. Boettcher, S. Markoff, et al. “Relativistic Jets in Active Galactic Nuclei and Microquasars”. In: *Space Science Reviews* 207.1-4 (Jan. 2017), pp. 5–61. DOI: 10.1007/s11214-016-0328-2. URL: https://doi.org/10.1007%2Fs11214-016-0328-2 (cit. on pp. 9, 46).

[4] Andrea Palladino, Maurizio Spurio, and Francesco Vissani. “Neutrino Telescopes and High-Energy Cosmic Neutrinos”. In: *Universe* 6.2 (Feb. 2020), p. 30. DOI: 10.3390/universe6020030. URL: https://doi.org/10.3390%2Funiverse6020030 (cit. on pp. 11, 75).

[5] J. Palacios et al. “Refined neutrino follow-up of GRB 221009A with ARCA and ORCA detectors”. In: *PoS* ICRC2023 (2023), p. 1503 (cit. on pp. 16, 200, 201).

[6] Auger, Pierre, Maze, Roland, Ehrenfest, Paul, et al. “Les grandes gerbes de rayons cosmiques”. In: *J. Phys. Radium* 10.1 (1939), pp. 39–48. DOI: 10.1051/jphysrad:0193900100103900. URL: https://doi.org/10.1051/jphysrad:0193900100103900 (cit. on p. 25).

[7] C. Patrignani et al. “Review of Particle Physics”. In: *Chinese Physics C* 40.10 (Oct. 2016), p. 100001. DOI: 10.1088/1674-1137/40/10/100001. URL: https://dx.doi.org/10.1088/1674-1137/40/10/100001 (cit. on p. 26).

[8] B. P. Abbott, R. Abbott, T. D. Abbott, et al. “Multi-messenger Observations of a Binary Neutron Star Merger”. In: *The Astrophysical Journal* 848.2 (Oct. 2017), p. L12. DOI: 10.3847/2041-8213/aa91c9. URL: https://doi.org/10.3847%2F2041-8213%2Faa91c9 (cit. on pp. 25, 26).

[9] J. Ballet, T. H. Burnett, S. W. Digel, et al. *Fermi Large Area Telescope Fourth Source Catalog Data Release 2*. 2020. arXiv: 2005.11208 [astro-ph.HE] (cit. on pp. 27, 126).

[10] T. C. Weekes, M. F. Cawley, D. J. Fegan, et al. “Observation of TeV Gamma Rays from the Crab Nebula Using the Atmospheric Cerenkov Imaging Technique”. In: *The Astrophysical Journal* 342 (July 1989), p. 379. DOI: 10.1086/167599 (cit. on p. 27).

[11] D. Bose, V. R. Chitnis, P. Majumdar, et al. “Galactic and extragalactic sources of very high energy gamma rays”. In: *The European Physical Journal Special Topics* 231.1 (Jan. 2022), pp. 27–66. DOI: 10.1140/epjs/s11734-022-00434-8. URL: https://doi.org/10.1140%2Fepjs%2Fs11734-022-00434-8 (cit. on p. 27).

[12] and H. Abdalla, F. Aharonian, F. Ait Benkhali, et al. “Revealing x-ray and gamma ray temporal and spectral similarities in the GRB 190829A afterglow”. In: *Science* 372.6546 (June 2021), pp. 1081–1085. DOI: 10.1126/science.abe8560. URL: https://doi.org/10.1126%2Fscience.abe8560 (cit. on p. 28).

[13] and F. Aharonian, F. Ait Benkhali, E. O. Angüner, et al. “Time-resolved hadronic particle acceleration in the recurrent nova RS Ophiuchi”. In: *Science* 376.6588 (Apr. 2022), pp. 77–80. DOI: 10.1126/science.abn0567. URL: https://doi.org/10.1126%2Fscience.abn0567 (cit. on p. 28).

[14] Mathieu de Naurois. “The Making of Catalogues of Very-High-Energy γ-ray Sources”. In: *Universe* 7.11 (Nov. 2021), p. 421. DOI: 10.3390/universe7110421. URL: https://doi.org/10.3390%2Funiverse7110421 (cit. on p. 28).

[15] Zhen Cao, F. A. Aharonian, Q. An, et al. “Ultrahigh-energy photons up to 1.4 petaelectronvolts from 12 γ-ray Galactic sources”. In: *Nature* 594.7861 (June 2021), pp. 33–36. DOI: 10.1038/s41586-021-03498-z (cit. on p. 28).

[16] Adam Burrows and James M. Lattimer. “Neutrinos from SN 1987A”. In: *Astrophysical Journal Letters* 318 (July 1987), p. L63. DOI: 10.1086/184938 (cit. on p. 28).

[17] E.N. Alexeyev, L.N. Alexeyeva, I.V. Krivosheina, et al. “Detection of the neutrino signal from SN 1987A in the LMC using the INR Baksan underground scintillation telescope”. In: *Physics Letters B* 205.2 (1988), pp. 209–214. ISSN: 0370-2693. DOI: https://doi.org/10.1016/0370-2693(88)91651-6. URL: https://www.sciencedirect.com/science/article/pii/0370269388916516 (cit. on p. 28).

[18] Maurizio Spurio. *Particles and astrophysics : a multi-messenger approach*. eng. Astronomy and astrophysics library. Heidelberg: Springer, 2015 - 2015. ISBN: 9783319345390 (cit. on pp. 28, 33).

[19] R. Abbasi, M. Ackermann, J. Adams, et al. “Improved Characterization of the Astrophysical Muon–neutrino Flux with 9.5 Years of IceCube Data”. In: *The Astrophysical Journal* 928.1 (Mar. 2022), p. 50. DOI: 10.3847/1538-4357/ac4d29. URL: https://dx.doi.org/10.3847/1538-4357/ac4d29 (cit. on pp. 28, 29).

[20] Icecube Collaboration, R. Abbasi, M. Ackermann, et al. “Observation of high-energy neutrinos from the Galactic plane”. In: *Science* 380.6652 (June 2023), pp. 1338–1343. DOI: 10.1126/science.adc9818. URL: https://doi.org/10.1126%2Fscience.adc9818 (cit. on pp. 28, 37).

[21] A. Albert, S. Alves, M. André, et al. “Hint for a TeV neutrino emission from the Galactic Ridge with ANTARES”. In: *Physics Letters B* 841 (June 2023), p. 137951. DOI: 10.1016/j.physletb.2023.137951. URL: https://doi.org/10.1016%2Fj.physletb.2023.137951 (cit. on p. 28).

[22] Mark Aartsen, Markus Ackermann, Jenni Adams, et al. “Neutrino emission from the direction of the blazar TXS 0506+056 prior to the IceCube-170922A alert”. In: *Science* 361.6398 (July 2018), pp. 147–151. DOI: 10.1126/science.aat2890. URL: https://doi.org/10.1126%2Fscience.aat2890 (cit. on pp. 29, 189).

[23] R. Abbasi, M. Ackermann, J. Adams, et al. “Evidence for neutrino emission from the nearby active galaxy NGC 1068”. In: *Science* 378.6619 (Nov. 2022), pp. 538–543. DOI: 10.1126/science.abg3395. URL: https://doi.org/10.1126%2Fscience.abg3395 (cit. on p. 29).

[24] ENRICO Fermi. “On the Origin of the Cosmic Radiation”. In: *Phys. Rev.* 75 (8 Apr. 1949), pp. 1169–1174. DOI: 10.1103/PhysRev.75.1169. URL: https://link.aps.org/doi/10.1103/PhysRev.75.1169 (cit. on p. 31).

[25] E. Fermi. “Galactic Magnetic Fields and the Origin of Cosmic Radiation.” In: *Astrophysical Journal* 119 (Jan. 1954), p. 1. DOI: 10.1086/145789 (cit. on p. 31).

[26] Matthew G. Baring. *Diffusive Shock Acceleration: the Fermi Mechanism*. 1997. arXiv: astro-ph/9711177 [astro-ph] (cit. on p. 31).

[27] Malcolm S. Longair. *High Energy Astrophysics*. 2011 (cit. on pp. 31, 32, 44).

[28] George B. Rybicki and Alan P. Lightman. *Radiative Processes in Astrophysics*. 1986 (cit. on pp. 32, 42).

[29] O. Klein and T. Nishina. “Uber die Streuung von Strahlung durch freie Elektronen nach der neuen relativistischen Quantendynamik von Dirac”. In: *Zeitschrift fur Physik* 52.11-12 (Nov. 1929), pp. 853–868. DOI: 10.1007/BF01366453 (cit. on p. 33).

[30] Gabriele Ghisellini. *Radiative Processes in High Energy Astrophysics*. Springer International Publishing, 2013. DOI: 10.1007/978-3-319-00612-3. URL: https://doi.org/10.1007%2F978-3-319-00612-3 (cit. on p. 33).

[31] Matteo Cerruti. “Leptonic and Hadronic Radiative Processes in Supermassive-Black-Hole Jets”. In: *Galaxies* 8.4 (Oct. 2020), p. 72. DOI: 10.3390/galaxies8040072. URL: https://doi.org/10.3390%2Fgalaxies8040072 (cit. on p. 33).

[32] S. Hümmer, M. Rüger, F. Spanier, et al. “SIMPLIFIED MODELS FOR PHOTOHADRONIC INTERACTIONS IN COSMIC ACCELERATORS”. In: *The Astrophysical Journal* 721.1 (Aug. 2010), pp. 630–652. DOI: 10.1088/0004-637x/721/1/630. URL: https://doi.org/10.1088%2F0004-637x%2F721%2F1%2F630 (cit. on p. 34).

[33] Francis Halzen and Ali Kheirandish. *IceCube and High-Energy Cosmic Neutrinos*. 2022. arXiv: 2202.00694 [astro-ph.HE] (cit. on p. 34).

[34] S. R. Kelner, F. A. Aharonian, and V. V. Bugayov. “Energy spectra of gamma rays, electrons, and neutrinos produced at proton-proton interactions in the very high energy regime”. In: *Physical Review D* 74.3, 034018 (Aug. 2006), p. 034018. DOI: 10.1103/PhysRevD.74.034018. arXiv: astro-ph/0606058 [astro-ph] (cit. on pp. 34, 161).

[35] F. Acero, F. Aharonian, A. G. Akhperjanian, et al. “First detection of VHE γ-rays from SN 1006 by HESS”. In: *Astronomy and Astrophysics* 516 (June 2010), A62. DOI: 10.1051/0004-6361/200913916. URL: https://doi.org/10.1051%2F0004-6361%2F200913916 (cit. on p. 35).

[36] F. L. Villante and F. Vissani. “How precisely can neutrino emission from supernova remnants be constrained by gamma ray observations?” In: *Physical Review D* 78.10 (Nov. 2008). DOI: 10.1103/physrevd.78.103007. URL: https://doi.org/10.1103%2Fphysrevd.78.103007 (cit. on pp. 37, 159).

[37] Francesco Vissani, Felix Aharonian, and Narek Sahakyan. “On the detectability of high-energy galactic neutrino sources”. In: *Astroparticle Physics* 34.10 (May 2011), pp. 778–783. DOI: 10.1016/j.astropartphys.2011.01.011. URL: https://doi.org/10.1016%2Fj.astropartphys.2011.01.011 (cit. on p. 37).

[38] Alexander Kappes, Jim Hinton, Christian Stegmann, et al. “Potential Neutrino Signals from Galactic γ-Ray Sources”. In: *The Astrophysical Journal* 656.2 (Feb. 2007), pp. 870–878. DOI: 10.1086/508936. arXiv: astro-ph/0607286 [astro-ph] (cit. on p. 37).

[39] G. E. Romero and G. S. Vila. “The proton low-mass microquasar: high-energy emission”. In: *Astronomy and Astrophysics* 485.3 (July 2008), pp. 623–631. DOI: 10.1051/0004-6361:200809563. arXiv: 0804.4606 [astro-ph] (cit. on pp. 37, 54).

[40] Claire Guépin, Kumiko Kotera, and Foteini Oikonomou. *High-energy neutrino transients and the future of multi-messenger astronomy*. 2022. arXiv: 2207.12205 [astro-ph.HE] (cit. on p. 37).

[41] A. Neronov, D. Semikoz, J. Aublin, et al. *Hadronic nature of high-energy emission from the Galactic Ridge*. 2023. arXiv: 2307.07978 [astro-ph.HE] (cit. on p. 37).

[42] Vittoria Vecchiotti, Francesco L. Villante, and Giulia Pagliaroli. *Unveiling the nature of galactic TeV sources with IceCube results*. 2023. arXiv: 2307.07451 [astro-ph.HE] (cit. on p. 37).

[43] Riccardo Giacconi, Herbert Gursky, Frank R. Paolini, et al. "Evidence for x Rays From Sources Outside the Solar System". In: *Physical Review Letters* 9.11 (Dec. 1962), pp. 439–443. DOI: 10.1103/PhysRevLett.9.439 (cit. on p. 38).

[44] B. Louise Webster and Paul Murdin. "Cygnus X-1-a Spectroscopic Binary with a Heavy Companion ?" In: *Nature* 235.5332 (Jan. 1972), pp. 37–38. DOI: 10.1038/235037a0 (cit. on p. 38).

[45] J. E. Pringle and M. J. Rees. "Accretion Disc Models for Compact X-Ray Sources". In: *Astronomy and Astrophysics* 21 (Oct. 1972), p. 1 (cit. on p. 38).

[46] C. T. Bolton. "Orbital elements and an analysis of models for HDE 226868 = Cygnus X-1." In: *The Astrophysical Journal* 200 (Sept. 1975), pp. 269–277. DOI: 10.1086/153785 (cit. on p. 38).

[47] B. Margon, H. C. Ford, J. I. Katz, et al. "The bizarre spectrum of SS 433." In: *The Astrophysical Journal Letters* 230 (May 1979), pp. L41–L45. DOI: 10.1086/182958 (cit. on p. 38).

[48] A. C. Fabian and M. J. Rees. "SS 433: a double jet in action?" In: *Monthly Notices of the Royal Astronomical Society* 187 (Apr. 1979), 13P–16. DOI: 10.1093/mnras/187.1.13P (cit. on p. 38).

[49] R. M. Hjellming and K. J. Johnston. "Structure, strength and polarization changes in radio source SS 433." In: *Nature* 290 (Mar. 1981), pp. 100–107. DOI: 10.1038/290100a0 (cit. on p. 38).

[50] R. M. Hjellming and K. J. Johnston. "An analysis of the proper motions of SS 433 radio jets." In: *The Astrophysical Journal Letters* 246 (June 1981), pp. L141–L145. DOI: 10.1086/183571 (cit. on p. 38).

[51] B. J. Geldzahler, E. B. Fomalont, and N. L. Cohen. "SCORPIUS-X-1 the Microquasar - New VLA and VLBI Results". In: *Two Topics in X-Ray Astronomy, Volume 1: X Ray Binaries. Volume 2: AGN and the X Ray Background*. Ed. by J. Hunt and B. Battrick. Vol. 1. ESA Special Publication. Nov. 1989, p. 415 (cit. on p. 38).

[52] E. B. Fomalont and B. J. Geldzahler. "The Radio Lobes of Scorpius X-1 Are Unrelated Background Sources". In: *The Astrophysical Journal* 383 (Dec. 1991), p. 289. DOI: 10.1086/170785 (cit. on p. 38).

[53] I. F. Mirabel, L. F. Rodriguez, B. Cordier, et al. "A double-sided radio jet from the compact Galactic Centre annihilator 1E1740.7-2942". In: *Nature* 358.6383 (July 1992), pp. 215–217. DOI: 10.1038/358215a0 (cit. on p. 39).

[54] I. F. Mirabel and L. F. Rodriguez. "A superluminal source in the Galaxy". In: *Nature* 371.6492 (Sept. 1994), pp. 46–48. DOI: 10.1038/371046a0 (cit. on pp. 39, 48).

[55] I. F. Mirabel and L. F. Rodriguez. “Microquasars in our Galaxy”. In: *Nature* 392.6677 (Apr. 1998), pp. 673–676. DOI: 10.1038/33603 (cit. on p. 40).

[56] Thomas M. Tauris and Ed van den Heuvel. *Formation and Evolution of Compact Stellar X-ray Sources*. 2003. arXiv: astro-ph/0303456 [astro-ph] (cit. on p. 41).

[57] N. I. Shakura and R. A. Sunyaev. “Black holes in binary systems. Observational appearance.” In: *Astronomy and Astrophysics* 24 (Jan. 1973), pp. 337–355 (cit. on p. 41).

[58] I. F. Mirabel and L. F. Rodriguez. “Sources of Relativistic Jets in the Galaxy”. In: *Annual Review of Astronomy and Astrophysics* 37.1 (Sept. 1999), pp. 409–443. DOI: 10.1146/annurev.astro.37.1.409. URL: https://doi.org/10.1146%2Fannurev.astro.37.1.409 (cit. on p. 42).

[59] R. A. Sunyaev and L. G. Titarchuk. “Comptonization of X-Rays in Plasma Clouds - Typical Radiation Spectra”. In: *Astronomy and Astrophysics* 86 (June 1980), p. 121 (cit. on p. 42).

[60] G. Miniutti and A. C. Fabian. “A light bending model for the X-ray temporal and spectral properties of accreting black holes”. In: *Monthly Notices of the Royal Astronomical Society* 349.4 (Apr. 2004), pp. 1435–1448. DOI: 10.1111/j.1365-2966.2004.07611.x. URL: https://doi.org/10.1111%2Fj.1365-2966.2004.07611.x (cit. on p. 42).

[61] F. Frontera, L. Amati, A. A. Zdziarski, et al. “Spectral and Temporal Behavior of the Black Hole Candidate XTE J1118+480 as Observed with BeppoSAX”. In: *The Astrophysical Journal* 592.2 (Aug. 2003), p. 1110. DOI: 10.1086/375809. URL: https://dx.doi.org/10.1086/375809 (cit. on p. 42).

[62] Ferreira, J., Petrucci, P.-O., Henri, G., et al. “A unified accretion-ejection paradigm for black hole X-ray binaries - I. The dynamical constituents”. In: *Astronomy and Astrophysics* 447.3 (2006), pp. 813–825. DOI: 10.1051/0004-6361:20052689. URL: https://doi.org/10.1051/0004-6361:20052689 (cit. on p. 42).

[63] Chris Done, Marek Gierliński, and Aya Kubota. “Modelling the behaviour of accretion flows in X-ray binaries”. In: *The Astronomy and Astrophysics Review* 15.1 (Aug. 2007), pp. 1–66. DOI: 10.1007/s00159-007-0006-1. URL: https://doi.org/10.1007%2Fs00159-007-0006-1 (cit. on p. 42).

[64] Andrzej A. Zdziarski and Marek Gierliń ski. “Radiative Processes, Spectral States and Variability of Black-Hole Binaries”. In: *Progress of Theoretical Physics Supplement* 155 (2004), pp. 99–119. DOI: 10.1143/ptps.155.99. URL: https://doi.org/10.1143%2Fptps.155.99 (cit. on p. 43).

[65] T.P. Ray and J. Ferreira. “Jets from young stars”. In: *New Astronomy Reviews* 93 (Dec. 2021), p. 101615. DOI: 10.1016/j.newar.2021.101615. URL: https://doi.org/10.1016%2Fj.newar.2021.101615 (cit. on p. 43).

[66] Deanne L. Coppejans and Christian Knigge. “The case for jets in cataclysmic variables”. In: *New Astronomy Reviews* 89 (2020), p. 101540. ISSN: 1387-6473. DOI: https://doi.org/10.1016/j.newar.2020.101540. URL: https://www.sciencedirect.com/science/article/pii/S1387647320300178 (cit. on p. 43).

[67] R. D. Blandford and R. L. Znajek. “Electromagnetic extraction of energy from Kerr black holes”. In: *Monthly Notices of the Royal Astronomical Society* 179.3 (July 1977), pp. 433–456. ISSN: 0035-8711. DOI: 10.1093/mnras/179.3.433. eprint: https://academic.oup.com/mnras/article-pdf/179/3/433/9333653/mnras179-0433.pdf. URL: https://doi.org/10.1093/mnras/179.3.433 (cit. on p. 43).

[68] R. D. Blandford and D. G. Payne. “Hydromagnetic flows from accretion disks and the production of radio jets.” In: *Monthly Notices of the Royal Astronomical Society* 199 (June 1982), pp. 883–903. DOI: 10.1093/mnras/199.4.883 (cit. on p. 43).

[69] David L. Meier, Shinji Koide, and Yutaka Uchida. “Magnetohydrodynamic Production of Relativistic Jets”. In: *Science* 291.5501 (2001), pp. 84–92. DOI: 10.1126/science.291.5501.84. eprint: https://www.science.org/doi/pdf/10.1126/science.291.5501.84. URL: https://www.science.org/doi/abs/10.1126/science.291.5501.84 (cit. on pp. 43, 44).

[70] Julien Malzac. *Radiation processes and models*. 2018. arXiv: 1804.03451 [astro-ph.HE] (cit. on p. 45).

[71] R. P. Fender, T. M. Belloni, and E. Gallo. “Towards a unified model for black hole X-ray binary jets”. In: *Monthly Notices of the Royal Astronomical Society* 355.4 (Dec. 2004), pp. 1105–1118. DOI: 10.1111/j.1365-2966.2004.08384.x. arXiv: astro-ph/0409360 [astro-ph] (cit. on p. 45).

[72] T.M. Belloni. “States and Transitions in Black Hole Binaries”. In: *The Jet Paradigm*. Springer Berlin Heidelberg, Oct. 2009, pp. 53–84. DOI: 10.1007/978-3-540-76937-8_3. URL: https://doi.org/10.1007%2F978-3-540-76937-8_3 (cit. on p. 45).

[73] S. Corbel, M. A. Nowak, R. P. Fender, et al. “Radio/X-ray correlation in the low/hard state of GX 339-4”. In: *Astronomy and Astrophysics* 400 (Mar. 2003), pp. 1007–1012. DOI: 10.1051/0004-6361:20030090. arXiv: astro-ph/0301436 [astro-ph] (cit. on p. 47).

[74] Stéphane Corbel, Stéphane Corbel, Mickael Coriat, et al. “The ’universal’ radio/X-ray flux correlation : the case study of the black hole GX 339-4”. In: *Monthly Notices of the Royal Astronomical Society* 428 (2012), pp. 2500–2515. URL: https://api.semanticscholar.org/CorpusID:119182032 (cit. on pp. 47, 123).

[75] Rob Fender and Tomaso Belloni. “GRS 1915+105 and the Disc-Jet Coupling in Accreting Black Hole Systems”. In: *Annual Review of Astronomy and Astrophysics* 42.1 (Sept. 2004), pp. 317–364. DOI: 10.1146/annurev.astro.42.053102.134031. arXiv: astro-ph/0406483 [astro-ph] (cit. on p. 47).

[76] E. Gallo, R. P. Fender, and G. G. Pooley. “A universal radio-X-ray correlation in low/hard state black hole binaries”. In: *Monthly Notices of the Royal Astronomical Society* 344.1 (Sept. 2003), pp. 60–72. DOI: 10.1046/j.1365-8711.2003.06791.x. arXiv: astro-ph/0305231 [astro-ph] (cit. on p. 47).

[77] Rob Fender and Teo Muñ oz-Darias. “The Balance of Power: Accretion and Feedback in Stellar Mass Black Holes”. In: *Astrophysical Black Holes*. Springer International Publishing, 2016, pp. 65–100. DOI: 10.1007/978-3-319-19416-5_3. URL: https://doi.org/10.1007%2F978-3-319-19416-5_3 (cit. on p. 47).

[78] P. Casella, T. Belloni, and L. Stella. “The ABC of Low-Frequency Quasi-periodic Oscillations in Black Hole Candidates: Analogies with Z Sources”. In: *The Astrophysical Journal* 629.1 (Aug. 2005), p. 403. DOI: 10.1086/431174. URL: https://dx.doi.org/10.1086/431174 (cit. on p. 48).

[79] Floriane Cangemi. “Approche multi-diagnostique des émissions de haute énergie des microquasars à trous noirs”. Theses. Université Paris Cité, Oct. 2020. URL: https://theses.hal.science/tel-03114988 (cit. on p. 48).

[80] J. S. Bright, R. P. Fender, et al. “An extremely powerful long-lived superluminal ejection from the black hole MAXI J1820+070”. In: *Nature Astronomy* 4.7 (Mar. 2020), pp. 697–703. DOI: 10.1038/s41550-020-1023-5 (cit. on pp. 49, 50, 107).

[81] Jeroen Homan, Joe Bright, Sara E. Motta, et al. “A Rapid Change in X-Ray Variability and a Jet Ejection in the Black Hole Transient MAXI J1820+070”. In: *The Astrophysical Journal* 891.2 (Mar. 2020), p. L29. DOI: 10.3847/2041-8213/ab7932. URL: https://doi.org/10.3847%2F2041-8213%2Fab7932 (cit. on p. 51).

[82] F. Carotenuto, S. Corbel, E. Tremou, et al. “The black hole transient MAXI J1348–630: evolution of the compact and transient jets during its 2019/2020 outburst”. In: *Monthly Notices of the Royal Astronomical Society* 504.1 (2021), pp. 444–468. DOI: 10.1093/mnras/stab864. URL: https://hal.science/hal-03191134 (cit. on p. 49).

[83] M. Cadolle Bel, P. Sizun, A. Goldwurm, et al. “The broad-band spectrum of Cygnus X-1 measured by INTEGRAL”. In: *Astronomy and Astrophysics* 446.2 (Jan. 2006), pp. 591–602. DOI: 10.1051/0004-6361:20053068. URL: https://doi.org/10.1051%2F0004-6361%3A20053068 (cit. on p. 51).

[84] M. Revnivtsev, M. Gilfanov, E. Churazov, et al. “Super-Eddington outburst of V4641 Sgr”. In: *Astronomy and Astrophysics* 391.3 (Aug. 2002), pp. 1013–1022. DOI: 10.1051/0004-6361:20020865. URL: https://doi.org/10.1051%2F0004-6361%3A20020865 (cit. on p. 51).

[85] Andrzej A. Zdziarski, Juri Poutanen, Joanna Mikolajewska, et al. “Broad-band X-ray/γ-ray spectra and binary parameters of GX 339–4 and their astrophysical implications”. In: *Monthly Notices of the Royal Astronomical Society* 301.2 (Dec. 1998), pp. 435–450. DOI: 10.1046/j.1365-8711.1998.02021.x. URL: https://doi.org/10.1046%2Fj.1365-8711.1998.02021.x (cit. on p. 52).

[86] J. Rodriguez, M. Cadolle Bel, J. Alfonso-Garzó n, et al. “Correlated optical, X-ray, and gamma-ray flaring activity seen with INTEGRAL during the 2015 outburst of V404 Cygni”. In: *Astronomy and Astrophysics* 581 (Sept. 2015), p. L9. DOI: 10.1051/0004-6361/201527043. URL: https://doi.org/10.1051%2F0004-6361%2F201527043 (cit. on p. 52).

[87] F. Cangemi, J. Rodriguez, T. Belloni, et al. “INTEGRAL study of MAXI J1535-571, MAXI J1820+070, and MAXI J1348 - 630 outbursts”. In: *Astronomy and Astrophysics* 669 (Jan. 2023), A65. DOI: 10.1051/0004-6361/202243564. URL: https://doi.org/10.1051%2F0004-6361%2F202243564 (cit. on pp. 52, 163–166).

[88] Zanin, R., Fernández-Barral, A., de Oña Wilhelmi, E., et al. “Gamma rays detected from Cygnus with likely jet origin”. In: *A&A* 596 (2016), A55. DOI: 10.1051/0004-6361/201628917. URL: https://doi.org/10.1051/0004-6361/201628917 (cit. on p. 52).

[89] Denys Malyshev, Andrzej A. Zdziarski, and Maria Chernyakova. “High-energy gamma-ray emission from Cyg X-1 measured by Fermi and its theoretical implications”. In: *Monthly Notices of the Royal Astronomical Society* 434.3 (Sept. 2013), pp. 2380–2389. DOI: 10.1093/mnras/stt1184. arXiv: 1305.5920 [astro-ph.HE] (cit. on p. 52).

[90] Fermi LAT Collaboration, A. A. Abdo, M. Ackermann, et al. “Modulated High-Energy Gamma-Ray Emission from the Microquasar Cygnus X-3”. In: *Science* 326.5959 (Dec. 2009), p. 1512. DOI: 10.1126/science.1182174 (cit. on p. 52).

[91] S. Corbel, G. Dubus, J. A. Tomsick, et al. “A giant radio flare from Cygnus X-3 with associated gamma-ray emission”. In: *Monthly Notices of the Royal Astronomical Society* 421.4 (Feb. 2012), pp. 2947–2955. DOI: 10.1111/j.1365-2966.2012.20517.x. URL: https://doi.org/10.1111%2Fj.1365-2966.2012.20517.x (cit. on p. 52).

[92] A. Loh, S. Corbel, G. Dubus, et al. “High-energy gamma-ray observations of the accreting black hole V404 Cygni during its 2015 June outburst”. In: *Monthly Notices of the Royal Astronomical Society: Letters* 462.1 (July 2016), pp. L111–L115. DOI: 10.1093/mnrasl/slw142. URL: https://doi.org/10.1093%2Fmnrasl%2fFslw142 (cit. on p. 52).

[93] Max Harvey, Cameron B Rulten, and Paula M Chadwick. “V404 Cygni with Fermi-LAT”. In: *Monthly Notices of the Royal Astronomical Society* 506.4 (July 2021), pp. 6029–6038. ISSN: 0035-8711. DOI: 10.1093/mnras/stab2097. URL: https://doi.org/10.1093/mnras/stab2097 (cit. on p. 52).

[94] J. Albert, E. Aliu, H. Anderhub, et al. “Very High Energy Gamma-Ray Radiation from the Stellar Mass Black Hole Binary Cygnus X-1”. In: *The Astrophysical Journal* 665.1 (July 2007), pp. L51–L54. DOI: 10.1086/521145. URL: https://doi.org/10.1086%2F521145 (cit. on p. 52).

[95] M. L. Ahnen, S. Ansoldi, L. A. Antonelli, et al. “Search for very high-energy gamma-ray emission from the microquasar Cygnus X-1 with the MAGIC telescopes”. In: *Monthly Notices of the Royal Astronomical Society* 472.3 (Aug. 2017), pp. 3474–3485. DOI: 10.1093/mnras/stx2087. arXiv: 1708.03689 [astro-ph.HE] (cit. on p. 52).

[96] J. Albert, E. Aliu, H. Anderhub, et al. “Variable Very-High-Energy Gamma-Ray Emission from the Microquasar LS I +61 303”. In: *Science* 312.5781 (June 2006), pp. 1771–1773. DOI: 10.1126/science.1128177. URL: https://doi.org/10.1126%2Fscience.1128177 (cit. on p. 52).

[97] F. Aharonian, A. G. Akhperjanian, K.-M. Aye, et al. “Discovery of Very High Energy Gamma Rays Associated with an X-ray Binary”. In: *Science* 309.5735 (July 2005), pp. 746–749. DOI: 10.1126/science.1113764. URL: https://doi.org/10.1126%2Fscience.1113764 (cit. on p. 52).

[98] G. Dubus. “Gamma-ray binaries: pulsars in disguise?” In: *Astronomy & Astrophysics* 456.3 (Sept. 2006), pp. 801–817. DOI: 10.1051/0004-6361:20054779. URL: https://doi.org/10.1051%2F0004-6361%3A20054779 (cit. on p. 52).

[99] G. E. Romero, A. T. Okazaki, M. Orellana, et al. “Accretion vs. colliding wind models for the gamma-ray binary LS I +61 303: an assessment”. In: *Astronomy and Astrophysics* 474.1 (Oct. 2007), pp. 15–22. DOI: 10.1051/0004-6361:20078035. arXiv: 0706.1320 [astro-ph] (cit. on p. 53).

[100] F. Aharonian, F. Ait Benkhali, J. Aschersleben, et al. “Acceleration and transport of relativistic electrons in the jets of the microquasar SS 433”. In: *Science* 383.6681 (Jan. 2024), pp. 402–406. ISSN: 1095-9203. DOI: 10.1126/science.adi2048. URL: http://dx.doi.org/10.1126/science.adi2048 (cit. on p. 53).

[101] A. U. Abeysekara, A. Albert, R. Alfaro, et al. “Very-high-energy particle acceleration powered by the jets of the microquasar SS 433”. In: *Nature* 562.7725 (Oct. 2018), pp. 82–85. DOI: 10.1038/s41586-018-0565-5 (cit. on p. 53).

[102] Omar Tibolla and on behalf of HAWC collaboration. “Recent results from the HAWC experiment”. In: *Journal of Physics: Conference Series* 2429.1 (Feb. 2023), p. 012017. DOI: 10.1088/1742-6596/2429/1/012017. URL: https://dx.doi.org/10.1088/1742-6596/2429/1/012017 (cit. on p. 53).

[103] G. E. Romero, D. F. Torres, M. M. Kaufman Bernadó, et al. “Hadronic gamma-ray emission from windy microquasars”. In: *Astronomy and Astrophysics* 410.2 (Nov. 2003), pp. L1–L4. DOI: 10.1051/0004-6361:20031314-1. URL: https://doi.org/10.1051%2F0004-6361%3A20031314-1 (cit. on p. 54).

[104] Justin D. Finke, Charles D. Dermer, and Markus Böttcher. “Synchrotron Self-Compton Analysis of TeV X-Ray-Selected BL Lacertae Objects”. In: *The Astrophysical Journal* 686.1 (Oct. 2008), p. 181. DOI: 10.1086/590900. URL: https://dx.doi.org/10.1086/590900 (cit. on p. 54).

[105] Greg Salvesen and Supavit Pokawanvit. “Origin of spin–orbit misalignments: the microblazar V4641 Sgr”. In: *Monthly Notices of the Royal Astronomical Society* 495.2 (Apr. 2020), pp. 2179–2204. DOI: 10.1093/mnras/staa1094. URL: https://doi.org/10.1093%2Fmnras%2Fstaa1094 (cit. on p. 54).

[106] E. Massaro, A. Tramacere, M. Perri, et al. “Log-parabolic spectra and particle acceleration in blazars”. In: *Astronomy & Astrophysics* 448.3 (Mar. 2006), pp. 861–871. DOI: 10.1051/0004-6361:20053644. URL: https://doi.org/10.1051%2F0004-6361%3A20053644 (cit. on pp. 54, 159).

[107] F Aharonian, L Anchordoqui, D Khangulyan, et al. “Microquasar LS 5039: a TeV gamma-ray emitter and a potential TeV neutrino source”. In: *Journal of Physics: Conference Series* 39.1 (May 2006), p. 408. DOI: 10.1088/1742-6596/39/1/106. URL: https://dx.doi.org/10.1088/1742-6596/39/1/106 (cit. on p. 54).

[108] Amir Levinson and Eli Waxman. “Probing Microquasars with TeV Neutrinos”. In: *Physical Review Letters* 87.17 (Oct. 2001). DOI: 10.1103/physrevlett.87.171101. URL: https://doi.org/10.1103%2Fphysrevlett.87.171101 (cit. on pp. 55, 144).

[109] C. Distefano, D. Guetta, E. Waxman, et al. “Neutrino Flux Predictions for Known Galactic Microquasars”. In: *The Astrophysical Journal* 575.1 (Aug. 2002), pp. 378–383. DOI: 10.1086/341144. URL: https://doi.org/10.1086%2F341144 (cit. on pp. 55, 144, 145).

[110] M. M. Reynoso and G. E. Romero. “Magnetic field effects on neutrino production in microquasars”. In: *Astronomy and Astrophysics* 493.1 (Nov. 2008), pp. 1–11. DOI: 10.1051/0004-6361:200811004. URL: https://doi.org/10.1051%2F0004-6361%3A200811004 (cit. on p. 55).

[111] Hugo R. Christiansen, Mariana Orellana, and Gustavo E. Romero. “High-energy neutrino emission from x-ray binaries”. In: *Physical Review D* 73.6 (Mar. 2006). DOI: 10.1103/physrevd.73.063012. URL: https://doi.org/10.1103%2Fphysrevd.73.063012 (cit. on p. 55).

[112] Matías M. Reynoso and Agustín M. Carulli. “On the possibilities of high-energy neutrino production in the jets of microquasar SS433 in light of new observational data”. In: *Astroparticle Physics* 109 (2019), pp. 25–32. ISSN: 0927-6505. DOI: https://doi.org/10.1016/j.astropartphys.2019.02.003. URL: https://www.sciencedirect.com/science/article/pii/S0927650518301166 (cit. on p. 55).

[113] J. F. Zhang, Y. G. Feng, M. C. Lei, et al. “High-energy neutrino emission from low-mass microquasars”. In: *Monthly Notices of the Royal Astronomical Society* 407.4 (Sept. 2010), pp. 2468–2474. ISSN: 0035-8711. DOI: 10.1111/j.1365-2966.2010.17072.x. eprint: https://academic.oup.com/mnras/article-pdf/407/4/2468/3212353/mnras0407-2468.pdf. URL: https://doi.org/10.1111/j.1365-2966.2010.17072.x (cit. on p. 56).

[114] A. Albert, M. André, G. Anton, et al. “Time-dependent search for neutrino emission from X-ray binaries with the ANTARES telescope”. In: *Journal of Cosmology and Astroparticle Physics* 2017.04 (Apr. 2017), p. 019. DOI: 10.1088/1475-7516/2017/04/019. URL: https://dx.doi.org/10.1088/1475-7516/2017/04/019 (cit. on pp. 56, 134, 145).

[115] R. Abbasi, M. Ackermann, J. Adams, et al. “Search for High-energy Neutrino Emission from Galactic X-Ray Binaries with IceCube”. In: *The Astrophysical Journal Letters* 930.2, L24 (May 2022), p. L24. DOI: 10.3847/2041-8213/ac67d8. arXiv: 2202.11722 [astro-ph.HE] (cit. on p. 56).

[116] Karri I I Koljonen, Konstancja Satalecka, Elina J Lindfors, et al. “Microquasar Cyg X-3 – a unique jet-wind neutrino factory?” In: *Monthly Notices of the Royal Astronomical Society: Letters* 524.1 (June 2023), pp. L89–L93. DOI: 10.1093/mnrasl/slad081. URL: https://doi.org/10.1093%2Fmnrasl%2Fslad081 (cit. on p. 56).

[117] S. Heinz and R. Sunyaev. “Cosmic rays from microquasars: A narrow component to the CR spectrum?” In: *Astronomy & Astrophysics* 390.2 (July 2002), pp. 751–766. DOI: 10.1051/0004-6361:20020615. URL: https://doi.org/10.1051%2F0004-6361%3A20020615 (cit. on p. 56).

[118] Robert Marcus Wagner. “Measurement of very high energy gamma-ray emission from four blazars using the MAGIC telescope and a comparative blazar study”. PhD thesis. Max-Planck-Institute for Physics, Munich, Jan. 2006 (cit. on p. 58).

[119] P. A. Čerenkov. “Visible Radiation Produced by Electrons Moving in a Medium with Velocities Exceeding that of Light”. In: *Phys. Rev.* 52 (4 Aug. 1937), pp. 378–379. DOI: 10.1103/PhysRev.52.378. URL: https://link.aps.org/doi/10.1103/PhysRev.52.378 (cit. on p. 58).

[120] Aharonian, F., Akhperjanian, A. G., Bazer-Bachi, A. R., et al. “Observations of the Crab nebula with HESS”. In: *A&A* 457.3 (2006), pp. 899–915. DOI: 10.1051/0004-6361:20065351. URL: https://doi.org/10.1051/0004-6361:20065351 (cit. on pp. 59, 63).

[121] J. Michael Davies and E. S. Cotton. “Design of the quartermaster solar furnace”. In: *Solar Energy* 1 (1957), pp. 16–22. URL: https://api.semanticscholar.org/CorpusID:121644127 (cit. on p. 59).

[122] K BERNLOHR. “The optical system of the H.E.S.S. imaging atmospheric Cherenkov telescopes. Part I: layout and components of the system”. In: *Astroparticle Physics* 20.2 (Nov. 2003), pp. 111–128. DOI: 10.1016/s0927-6505(03)00171-3. URL: https://doi.org/10.1016%2Fs0927-6505%2803%2900171-3 (cit. on p. 59).

[123] Baiyang Bi, Miquel Barcelo, Christian Bauer, et al. “Performance of the new FlashCam-based camera in the 28m telescope of H.E.S.S.” In: *Proceedings of 37th International Cosmic Ray Conference — PoS(ICRC2021)*. Sissa Medialab, July 2021. DOI: 10.22323/1.395.0743. URL: https://doi.org/10.22323%2F1.395.0743 (cit. on p. 59).

[124] S. Funk, G. Hermann, J. Hinton, et al. “The trigger system of the H.E.S.S. telescope array”. In: *Astroparticle Physics* 22.3-4 (Nov. 2004), pp. 285–296. DOI: 10.1016/j.astropartphys.2004.08.001. URL: https://doi.org/10.1016%2Fj.astropartphys.2004.08.001 (cit. on p. 59).

[125] F. Aharonian, A.G. Akhperjanian, K.-M. Aye, et al. “Calibration of cameras of the H.E.S.S. detector”. In: *Astroparticle Physics* 22.2 (Nov. 2004), pp. 109–125. DOI: 10.1016/j.astropartphys.2004.06.006. URL: https://doi.org/10.1016%2Fj.astropartphys.2004.06.006 (cit. on p. 60).

[126] R. Chalme-Calvet, M. de Naurois, and J. -P. Tavernet. *Muon efficiency of the H.E.S.S. telescope*. 2014. arXiv: 1403.4550 [astro-ph.IM] (cit. on p. 61).

[127] G. Mohanty, S. Biller, D.A. Carter-Lewis, et al. “Measurement of TeV gamma-ray spectra with the Cherenkov imaging technique”. In: *Astroparticle Physics* 9.1 (1998), pp. 15–43. ISSN: 0927-6505. DOI: https://doi.org/10.1016/S0927-6505(98)00005-X. URL: https://www.sciencedirect.com/science/article/pii/S092765059800005X (cit. on p. 61).

[128] J. Hahn, R. de los Reyes, K. Bernlöhr, et al. “Impact of aerosols and adverse atmospheric conditions on the data quality for spectral analysis of the H.E.S.S. telescopes”. In: *Astroparticle Physics* 54 (Feb. 2014), pp. 25–32. DOI: 10.1016/j.astropartphys.2013.10.003. URL: https://doi.org/10.1016%2Fj.astropartphys.2013.10.003 (cit. on p. 61).

[129] M.P. Kertzman and G.H. Sembroski. “Computer simulation methods for investigating the detection characteristics of TeV air Cherenkov telescopes”. In: *Nuclear Instruments and Methods in Physics Research Section A: Accelerators, Spectrometers, Detectors and Associated Equipment* 343.2 (1994), pp. 629–643. ISSN: 0168-9002. DOI: https://doi.org/10.1016/0168-9002(94)90247-X. URL: https://www.sciencedirect.com/science/article/pii/016890029490247X (cit. on p. 62).

[130] Julien Guy. “Premiers résultats de l’expérience HESS et étude du potentiel de détection de matière noire supersymétrique”. Theses. Université Pierre et Marie Curie - Paris VI, May 2003. URL: https://theses.hal.science/tel-00003488 (cit. on p. 62).

[131] D. Heck, J. Knapp, J. N. Capdevielle, et al. “CORSIKA: A Monte Carlo code to simulate extensive air showers”. In: (Feb. 1998) (cit. on p. 62).

[132] Konrad Bernlöhr. “Simulation of imaging atmospheric Cherenkov telescopes with CORSIKA and sim_telarray”. In: *Astroparticle Physics* 30.3 (Oct. 2008), pp. 149–158. DOI: 10.1016/j.astropartphys.2008.07.009. URL: https://doi.org/10.1016%2Fj.astropartphys.2008.07.009 (cit. on p. 62).

[133] M. Holler, Jean-Philippe Lenain, M. de Naurois, et al. “A Run-Wise Simulation and Analysis Framework for Imaging Atmospheric Cherenkov Telescope Arrays”. In: *Astroparticle Physics* 123 (Dec. 2020), p. 102491. DOI: 10.1016/j.astropartphys.2020.102491. URL: https://hal.science/hal-03371643 (cit. on p. 62).

[134] A. M. Hillas. “Cerenkov Light Images of EAS Produced by Primary Gamma Rays and by Nuclei”. In: *19th International Cosmic Ray Conference (ICRC19), Volume 3*. Vol. 3. International Cosmic Ray Conference. Aug. 1985, p. 445 (cit. on p. 62).

[135] Mathieu de Naurois and Loïc Rolland. “A high performance likelihood reconstruction of γ-rays for imaging atmospheric Cherenkov telescopes”. In: *Astroparticle Physics* 32.5 (Dec. 2009), pp. 231–252. DOI: 10.1016/j.astropartphys.2009.09.001. URL: https://doi.org/10.1016%2Fj.astropartphys.2009.09.001 (cit. on pp. 62, 65, 67).

[136] M. Holler, A. Balzer, R. Chalmé-Calvet, et al. *Photon Reconstruction for H.E.S.S. Using a Semi-Analytical Shower Model*. 2015. arXiv: 1509.02896 [astro-ph.IM] (cit. on pp. 62, 67).

[137] R.D. Parsons and J.A. Hinton. “A Monte Carlo template based analysis for air-Cherenkov arrays”. In: *Astroparticle Physics* 56 (2014), pp. 26–34. ISSN: 0927-6505. DOI: https://doi.org/10.1016/j.astropartphys.2014.03.002. URL: https://www.sciencedirect.com/science/article/pii/S0927650514000231 (cit. on p. 64).

[138] T. -P. Li and Y. -Q. Ma. “Analysis methods for results in gamma-ray astronomy.” In: *The Astrophysical Journal* 272 (Sept. 1983), pp. 317–324. DOI: 10.1086/161295 (cit. on pp. 70, 110).

[139] Wolfgang A. Rolke, Angel M. López, and Jan Conrad. “Limits and confidence intervals in the presence of nuisance parameters”. In: *Nuclear Instruments and Methods in Physics Research Section A: Accelerators, Spectrometers, Detectors and Associated Equipment* 551.2-3 (Oct. 2005), pp. 493–503. DOI: 10.1016/j.nima.2005.05.068 (cit. on pp. 73, 112).

[140] Agata Trovato. “Development of reconstruction algorithms for large volume neutrino telescopes and their application to the KM3NeT detector”. PhD thesis. Catania U., SSC, 2014 (cit. on p. 74).

[141] Bettina Hartmann. *Reconstruction of Neutrino-Induced Hadronic and Electromagnetic Showers with the ANTARES Experiment*. 2006. arXiv: astro-ph/0606697 [astro-ph] (cit. on pp. 74, 77).

[142] Sheldon L. Glashow. “Resonant Scattering of Antineutrinos”. In: *Phys. Rev.* 118 (1 Apr. 1960), pp. 316–317. DOI: 10.1103/PhysRev.118.316. URL: https://link.aps.org/doi/10.1103/PhysRev.118.316 (cit. on p. 74).

[143] T. Chiarusi and M. Spurio. “High-energy astrophysics with neutrino telescopes”. In: *The European Physical Journal C* 65.3-4 (Jan. 2010), pp. 649–701. DOI: 10.1140/epjc/s10052-009-1230-9. URL: https://doi.org/10.1140%2Fepjc%2Fs10052-009-1230-9 (cit. on pp. 76, 79).

[144] “ANTARES: the first undersea neutrino telescope”. In: *Nucl. Instrum. Meth. A* 656 (2011), pp. 11–38. DOI: 10.1016/j.nima.2011.06.103. arXiv: 1104.1607 [astro-ph.IM] (cit. on p. 77).

[145] S. Adrian-Martinez et al. “Letter of intent for KM3NeT 2.0”. In: *J. Phys. G* 43.8 (2016), p. 084001. DOI: 10.1088/0954-3899/43/8/084001. arXiv: 1601.07459 [astro-ph.IM] (cit. on p. 77).

[146] P Amram, M Anghinolfi, S Anvar, et al. “The ANTARES optical module”. In: *Nuclear Instruments and Methods in Physics Research Section A: Accelerators, Spectrometers, Detectors and Associated Equipment* 484.1 (2002), pp. 369–383. ISSN: 0168-9002. DOI: https://doi.org/10.1016/S0168-9002(01)02026-5. URL: https://www.sciencedirect.com/science/article/pii/S0168900201020265 (cit. on p. 78).

[147] KM3NeT Collaboration. *The KM3NeT multi-PMT optical module*. 2022. arXiv: 2203.10048 [astro-ph.IM] (cit. on p. 78).

[148] A. Zwart, E. Heine, J. Hogenbirk, et al. “A TDC for the characterization of KM3NeT PMTs”. In: *Nuclear Instruments and Methods in Physics Research Section A: Accelerators, Spectrometers, Detectors and Associated Equipment* 725 (2013). VLVnT 11, Erlangen, Germany, 12 - 14 October, 2011, pp. 170–174. ISSN: 0168-9002. DOI: https://doi.org/10.1016/j.nima.2012.12.101. URL: https://www.sciencedirect.com/science/article/pii/S0168900212016579 (cit. on p. 81).

[149] D. Bailey. “Monte Carlo tools and analysis methods for understanding the ANTARES experiment and predicting its sensitivity to dark matter”. PhD thesis. Oxford U., 2002 (cit. on p. 82).

[150] S. Aiello, A. Albert, S. Alves Garre, et al. “gSeaGen: The KM3NeT GENIE-based code for neutrino telescopes”. In: *Computer Physics Communications* 256 (2020), p. 107477. ISSN: 0010-4655. DOI: https://doi.org/10.1016/j.cpc.2020.107477. URL: https://www.sciencedirect.com/science/article/pii/S0010465520302241 (cit. on p. 82).

[151] G. Carminati, M. Bazzotti, A. Margiotta, et al. “Atmospheric MUons from PArametric formulas: a fast GEnerator for neutrino telescopes (MUPAGE)”. In: *Computer Physics Communications* 179.12 (2008), pp. 915–923. ISSN: 0010-4655. DOI: https://doi.org/10.1016/j.cpc.2008.07.014. URL: https://www.sciencedirect.com/science/article/pii/S001046550800266X (cit. on p. 82).

[152] René Brun, F Bruyant, Federico Carminati, et al. *GEANT: Detector Description and Simulation Tool; Oct 1994*. CERN Program Library. Long Writeup W5013. Geneva: CERN, 1993. DOI: 10.17181/CERN.MUHF.DMJ1. URL: https://cds.cern.ch/record/1082634 (cit. on p. 82).

[153] C. Colnard. “Ultra-high energy neutrino simulations”. In: 2009. URL: https://api.semanticscholar.org/CorpusID:56133430 (cit. on p. 82).

[154] R. Le Breton, M. Billault, C. Boutonnet, et al. “The calibration units of KM3NeT”. In: *Journal of Instrumentation* 16.09 (Sept. 2021), p. C09004. DOI: 10.1088/1748-0221/16/09/C09004. URL: https://dx.doi.org/10.1088/1748-0221/16/09/C09004 (cit. on p. 83).

[155] S Adrian-Martinez, M Ageron, J A Aguilar, et al. “The positioning system of the ANTARES Neutrino Telescope”. In: *Journal of Instrumentation* 7.08 (Aug. 2012), T08002–T08002. DOI: 10.1088/1748-0221/7/08/t08002. URL: https://doi.org/10.1088%2F1748-0221%2F7%2F08%2Ft08002 (cit. on pp. 83, 141).

[156] Riccobene, Giorgio. “The Positioning system for KM3NeT”. In: *EPJ Web Conf.* 207 (2019), p. 07005. DOI: 10.1051/epjconf/201920707005. URL: https://doi.org/10.1051/epjconf/201920707005 (cit. on p. 83).

[157] J.A. Aguilar, I. Al Samarai, A. Albert, et al. “Time calibration of the ANTARES neutrino telescope”. In: *Astroparticle Physics* 34.7 (Feb. 2011), pp. 539–549. DOI: 10.1016/j.astropartphys.2010.12.004. URL: https://doi.org/10.1016%2Fj.astropartphys.2010.12.004 (cit. on p. 83).

[158] Rosa Coniglione, Alexandre Creusot, Irene Di Palma, et al. “KM3NeT Time Calibration”. In: *Proceedings of 36th International Cosmic Ray Conference — PoS(ICRC2019)*. Vol. 358. 2019, p. 868. DOI: 10.22323/1.358.0868 (cit. on p. 83).

[159] M. Ageron, J.A. Aguilar, A. Albert, et al. “The ANTARES optical beacon system”. In: *Nuclear Instruments and Methods in Physics Research Section A: Accelerators, Spectrometers, Detectors and Associated Equipment* 578.3 (Aug. 2007), pp. 498–509. DOI: 10.1016/j.nima.2007.05.325. URL: https://doi.org/10.1016%2Fj.nima.2007.05.325 (cit. on p. 83).

[160] S. Aiello, A. Albert, M. Alshamsi, et al. “Nanobeacon: A time calibration device for the KM3NeT neutrino telescope”. In: *Nuclear Instruments and Methods in Physics Research Section A: Accelerators, Spectrometers, Detectors and Associated Equipment* 1040 (Oct. 2022), p. 167132. DOI: 10.1016/j.nima.2022.167132. URL: https://doi.org/10.1016%2Fj.nima.2022.167132 (cit. on p. 83).

[161] Bruny Baret. *Charge Calibration of the ANTARES high energy neutrino telescope*. 2009. arXiv: 0908.0810 [astro-ph.IM] (cit. on p. 83).

[162] Aart Heijboer. “Track reconstruction and point source searches with ANTARES”. PhD thesis. Amsterdam U., 2004 (cit. on p. 84).

[163] J.A. Aguilar, I. Al Samarai, A. Albert, et al. “A fast algorithm for muon track reconstruction and its application to the ANTARES neutrino telescope”. In: *Astroparticle Physics* 34.9 (Apr. 2011), pp. 652–662. DOI: 10.1016/j.astropartphys.2011.01.003. URL: https://doi.org/10.1016%2Fj.astropartphys.2011.01.003 (cit. on p. 84).

[164] S. Adrián-Martínez, I. Al Samarai, A. Albert, et al. *First search for neutrinos in correlation with gamma-ray bursts with the ANTARES neutrino telescope*. 2013. arXiv: 1302.6750 [astro-ph.HE] (cit. on p. 85).

[165] Fabian Schüssler. “Energy reconstruction in neutrino telescopes”. In: *33rd International Cosmic Ray Conference*. 2013, p. 0421 (cit. on p. 85).

[166] The ANTARES Collaboration. *Neutrino Point Source Search including Cascade Events with the ANTARES Neutrino Telescope)*. 2015. arXiv: 1510.04508 [astro-ph.HE] (cit. on p. 85).

[167] A. Albert, M. André, M. Anghinolfi, et al. “An Algorithm for the Reconstruction of Neutrino-induced Showers in the ANTARES Neutrino Telescope”. In: *The Astronomical Journal* 154.6 (Dec. 2017), p. 275. DOI: 10.3847/1538-3881/aa9709. URL: https://dx.doi.org/10.3847/1538-3881/aa9709 (cit. on p. 85).

[168] A. Albert, M. André, M. Anghinolfi, et al. “An algorithm for the reconstruction of high-energy neutrino-induced particle showers and its application to the ANTARES neutrino telescope”. In: *The European Physical Journal C* 77.6 (June 2017). DOI: 10.1140/epjc/s10052-017-4979-2. URL: https://doi.org/10.1140%2Fepjc%2Fs10052-017-4979-2 (cit. on p. 86).

[169] Karel Melis, Aart Heijboer, and Maarten De Jong. “KM3NeT/ARCA Event Reconstruction Algorithms”. In: *Proceedings of 35th International Cosmic Ray Conference — PoS(ICRC2017)*. Vol. 301. 2017, p. 950. DOI: 10.22323/1.301.0950 (cit. on pp. 86, 87).

[170] Jannik Hofestädt. “Shower reconstruction with the KM3NeT/ORCA detector”. In: *PoS* ICRC2015 (2016), p. 1083. DOI: 10.22323/1.236.1083 (cit. on p. 87).

[171] W. B. Atwood, A. A. Abdo, M. Ackermann, et al. “THE LARGE AREA TELESCOPE ON THE FERMI GAMMA-RAY SPACE TELESCOPE MISSION”. In: *The Astrophysical Journal* 697.2 (May 2009), p. 1071. DOI: 10.1088/0004-637X/697/2/1071. URL: https://dx.doi.org/10.1088/0004-637X/697/2/1071 (cit. on p. 87).

[172] Keith C. Gendreau, Zaven Arzoumanian, and Takashi Okajima. “The Neutron star Interior Composition ExploreR (NICER): an Explorer mission of opportunity for soft x-ray timing spectroscopy”. In: *Space Telescopes and Instrumentation 2012: Ultraviolet to Gamma Ray*. Ed. by Tadayuki Takahashi, Stephen S. Murray, and Jan-Willem A. den Herder. Vol. 8443. International Society for Optics and Photonics. SPIE, 2012, p. 844313. DOI: 10.1117/12.926396. URL: https://doi.org/10.1117/12.926396 (cit. on p. 89).

[173] Scott D. Barthelmy, Louis M. Barbier, Jay R. Cummings, et al. “The Burst Alert Telescope (BAT) on the SWIFT Midex Mission”. In: *Space Science Reviews* 120.3-4 (Oct. 2005), pp. 143–164. DOI: 10.1007/s11214-005-5096-3. URL: https://doi.org/10.1007%2Fs11214-005-5096-3 (cit. on p. 90).

[174] H. A. Krimm, S. T. Holland, R. H. D. Corbet, et al. “THE SWIFT/BAT HARD X-RAY TRANSIENT MONITOR”. In: *The Astrophysical Journal Supplement Series* 209.1 (Oct. 2013), p. 14. DOI: 10.1088/0067-0049/209/1/14. URL: https://dx.doi.org/10.1088/0067-0049/209/1/14 (cit. on pp. 90, 98).

[175] Masaru Matsuoka, Kazuyoshi Kawasaki, Shiro Ueno, et al. “The MAXI Mission on the ISS: Science and Instruments for Monitoring All-Sky X-Ray Images”. In: *Publications of the Astronomical Society of Japan* 61.5 (Oct. 2009), pp. 999–1010. DOI: 10.1093/pasj/61.5.999. URL: https://doi.org/10.1093%2Fpasj%2F61.5.999 (cit. on p. 90).

[176] H. V. Bradt, R. E. Rothschild, and J. H. Swank. “X-ray timing explorer mission”. In: *Astronomy and Astrophysics Supplement Series* 97.1 (Jan. 1993), pp. 355–360 (cit. on p. 91).

[177] N. Iyer, A. Nandi, and S. Mandal. “DETERMINATION OF THE MASS OF IGR J17091–3624 FROM “SPECTRO-TEMPORAL” VARIATIONS DURING THE ONSET PHASE OF THE 2011 OUTBURST”. In: *The Astrophysical Journal* 807.1 (July 2015), p. 108. DOI: 10.1088/0004-637x/807/1/108. URL: https://doi.org/10.1088%2F0004-637x%2F807%2F1%2F108 (cit. on p. 96).

[178] Jerome A. Orosz, James F. Steiner, Jeffrey E. McClintock, et al. “AN IMPROVED DYNAMICAL MODEL FOR THE MICROQUASAR XTE J1550–564”. In: *The Astrophysical Journal* 730.2 (Mar. 2011), p. 75. DOI: 10.1088/0004-637x/730/2/75. URL: https://doi.org/10.1088%2F0004-637x%2F730%2F2%2F75 (cit. on p. 96).

[179] Rachel K. D. MacDonald, Charles D. Bailyn, Michelle Buxton, et al. “THE BLACK HOLE BINARY V4641 SAGITARII: ACTIVITY IN QUIESCENCE AND IMPROVED MASS DETERMINATIONS”. In: *The Astrophysical Journal* 784.1 (Feb. 2014), p. 2. DOI: 10.1088/0004-637x/784/1/2. URL: https://doi.org/10.1088%2F0004-637x%2F784%2F1%2F2 (cit. on p. 96).

[180] C. A. L. Bailer-Jones, J. Rybizki, M. Fouesneau, et al. “Estimating Distance from Parallaxes. IV. Distances to 1.33 Billion Stars in Gaia Data Release 2”. In: *The Astronomical Journal* 156.2 (July 2018), p. 58. DOI: 10.3847/1538-3881/aacb21. URL: https://doi.org/10.3847%2F1538-3881%2Faacb21 (cit. on p. 96).

[181] E. Kalemci, T. J. Maccarone, and J. A. Tomsick. “A Dust-scattering Halo of 4U 1630–47 Observed with Chandra and Swift: New Constraints on the Source Distance”. In: *The Astrophysical Journal* 859.2 (May 2018), p. 88. DOI: 10.3847/1538-4357/aabcd3. URL: https://doi.org/10.3847%2F1538-4357%2Faabcd3 (cit. on p. 96).

[182] M. J. Reid and J. C. A. Miller-Jones. *On the Distances to the X-ray Binaries Cygnus X-3 and GRS 1915+105*. 2023. arXiv: 2309.15027 [astro-ph.HE] (cit. on p. 96).

[183] Juthika Khargharia, Cynthia S. Froning, and Edward L. Robinson. “NEAR-INFRARED SPECTROSCOPY OF LOW-MASS X-RAY BINARIES: ACCRETION DISK CONTAMINATION AND COMPACT OBJECT MASS DETERMINATION IN V404 Cyg AND Cen X-4”. In: *The Astrophysical Journal* 716.2 (May 2010), pp. 1105–1117. DOI: 10.1088/0004-637x/716/2/1105. URL: https://doi.org/10.1088%2F0004-637x%2F716%2F2%2F1105 (cit. on p. 96).

[184] J. C. A. Miller-Jones, P. G. Jonker, V. Dhawan, et al. “THE FIRST ACCURATE PARALLAX DISTANCE TO A BLACK HOLE”. In: *The Astrophysical Journal* 706.2 (Nov. 2009), pp. L230–L234. DOI: 10.1088/0004-637x/706/2/l230. URL: https://doi.org/10.1088%2F0004-637x%2F706%2F2%2Fl230 (cit. on p. 96).

[185] James F. Steiner, Jeffrey E. McClintock, and Mark J. Reid. “THE DISTANCE, INCLINATION, AND SPIN OF THE BLACK HOLE MICROQUASAR H1743-322”. In: *The Astrophysical Journal* 745.1 (Dec. 2011), p. L7. DOI: 10.1088/2041-8205/745/1/l7. URL: https://doi.org/10.1088%2F2041-8205%2F745%2F1%2Fl7 (cit. on p. 96).

[186] M. Heida, P. G. Jonker, M. A. P. Torres, et al. “The Mass Function of GX 339–4 from Spectroscopic Observations of Its Donor Star”. In: *The Astrophysical Journal* 846.2 (Sept. 2017), p. 132. DOI: 10.3847/1538-4357/aa85df. URL: https://doi.org/10.3847%2F1538-4357%2Faa85df (cit. on p. 96).

[187] M. A. P. Torres, J. Casares, F. Jimé nez-Ibarra, et al. “The Binary Mass Ratio in the Black Hole Transient MAXI J1820+070”. In: *The Astrophysical Journal* 893.2 (Apr. 2020), p. L37. DOI: 10.3847/2041-8213/ab863a. URL: https://doi.org/10.3847%2F2041-8213%2Fab863a (cit. on pp. 96, 165).

[188] Tolga Dinçer. “The near-infrared counterpart of X-ray transient MAXI J1535-571”. In: *The Astronomer’s Telegram* 10716 (Sept. 2017), p. 1 (cit. on p. 96).

[189] Raj Kumar, Subir Bhattacharyya, Nilay Bhatt, et al. “Estimation of spin and mass of the black hole in MAXI J1348-630 from the soft state using NICER and NuSTAR observations”. In: *Monthly Notices of the Royal Astronomical Society* 513.4 (July 2022), pp. 4869–4874. DOI: 10.1093/mnras/stac1170 (cit. on p. 96).

[190] Lian Tao, John A. Tomsick, Jinlu Qu, et al. “The Spin of the Black Hole GRS 1716-249 Determined from the Hard Intermediate State”. In: *The Astrophysical Journal* 887.2 (Dec. 2019), p. 184. DOI: 10.3847/1538-4357/ab5282. URL: https://dx.doi.org/10.3847/1538-4357/ab5282 (cit. on p. 96).

[191] M. della Valle, I. F. Mirabel, and L. F. Rodriguez. “The optical and radio counterpart of the X-ray Nova Ophiuchi 1993”. In: *Astronomy and Astrophysics* 290 (Oct. 1994), pp. 803–806 (cit. on p. 96).

[192] V. Tudose, R. P. Fender, M. Linares, et al. “The disc–jet coupling in the neutron star X-ray binary Aquila X-1”. In: *Monthly Notices of the Royal Astronomical Society* 400.4 (Dec. 2009), pp. 2111–2121. ISSN: 0035-8711. DOI: 10.1111/j.1365-2966.2009.15604.x. eprint: https://academic.oup.com/mnras/article-pdf/400/4/2111/5660687/mnras0400-2111.pdf. URL: https://doi.org/10.1111/j.1365-2966.2009.15604.x (cit. on p. 96).

[193] Megumi Shidatsu, Satoshi Nakahira, Katsuhiro L. Murata, et al. “X-Ray and Optical Monitoring of State Transitions in MAXI J1820+070”. In: *The Astrophysical Journal* 874.2 (Apr. 2019), p. 183. DOI: 10.3847/1538-4357/ab09ff (cit. on pp. 101, 102, 105, 175).

[194] C. B. Adams, W. Benbow, A. Brill, et al. “Observation of the Gamma-Ray Binary HESS J0632+057 with the H.E.S.S., MAGIC, and VERITAS Telescopes”. In: *The Astrophysical Journal* 923.2, 241 (Dec. 2021), p. 241. DOI: 10.3847/1538-4357/ac29b7. arXiv: 2109.11894 [astro-ph.HE] (cit. on p. 106).

[195] Marta A Dziełak, Barbara De Marco, and Andrzej A Zdziarski. “A spectrally stratified hot accretion flow in the hard state of MAXI J1820+070”. In: *Monthly Notices of the Royal Astronomical Society* 506.2 (June 2021), pp. 2020–2029. ISSN: 0035-8711. DOI: 10.1093/mnras/stab1700. eprint: https://academic.oup.com/mnras/article-pdf/506/2/2020/39116809/stab1700.pdf. URL: https://doi.org/10.1093/mnras/stab1700 (cit. on pp. 107, 163).

[196] Wolfgang A. Rolke and Angel M. López. “Confidence intervals and upper bounds for small signals in the presence of background noise”. In: *Nuclear Instruments and Methods in Physics Research Section A: Accelerators, Spectrometers, Detectors and Associated Equipment* 458.3 (Feb. 2001), pp. 745–758. DOI: 10.1016/s0168-9002(00)00935-9 (cit. on pp. 110, 154).

[197] and H. Abdalla, A. Abramowski, F. Aharonian, et al. “A search for new supernova remnant shells in the Galactic plane with H.E.S.S.” In: *Astronomy &amp Astrophysics* 612 (Apr. 2018), A8. DOI: 10.1051/0004-6361/201730737. URL: https://doi.org/10.1051%2F0004-6361%2F201730737 (cit. on p. 111).

[198] T Bassi, M Del Santo, A D’Aì, et al. “The long outburst of the black hole transient GRS 1716–249 observed in the X-ray and radio band”. In: *Monthly Notices of the Royal Astronomical Society* 482.2 (Oct. 2018), pp. 1587–1601. ISSN: 0035-8711. DOI: 10.1093/mnras/sty2739. eprint: https://academic.oup.com/mnras/article-pdf/482/2/1587/26288794/sty2739.pdf. URL: https://doi.org/10.1093/mnras/sty2739 (cit. on p. 113).

[199] Lian Tao, YuPeng Chen, Can GÜNGÖR, et al. “Swift observations of the bright uncatalogued X-ray transient MAXI J1535-571”. In: *Monthly Notices of the Royal Astronomical Society* 480.4 (Aug. 2018), pp. 4443–4454. ISSN: 0035-8711. DOI: 10.1093/mnras/sty2157. eprint: https://academic.oup.com/mnras/article-pdf/480/4/4443/25539467/sty2157.pdf. URL: https://doi.org/10.1093/mnras/sty2157 (cit. on p. 113).

[200] Arghajit Jana, Dipak Debnath, Debjit Chatterjee, et al. “Accretion Flow Evolution of a New Black Hole Candidate MAXI J1348–630 during the 2019 Outburst”. In: *The Astrophysical Journal* 897.1 (June 2020), p. 3. DOI: 10.3847/1538-4357/ab9696. URL: https://doi.org/10.3847%2F1538-4357%2Fab9696 (cit. on p. 119).

[201] A. A. Abdo, M. Ackermann, M. Ajello, et al. “FERMI/LARGE AREA TELESCOPE BRIGHT GAMMA-RAY SOURCE LIST”. In: *The Astrophysical Journal Supplement Series* 183.1 (June 2009), pp. 46–66. DOI: 10.1088/0067-0049/183/1/46. URL: https://doi.org/10.1088%2F0067-0049%2F183%2F1%2F46 (cit. on p. 126).

[202] S. S. Wilks. “The Large-Sample Distribution of the Likelihood Ratio for Testing Composite Hypotheses”. In: *The Annals of Mathematical Statistics* 9.1 (1938), pp. 60–62. DOI: 10.1214/aoms/1177732360. URL: https://doi.org/10.1214/aoms/1177732360 (cit. on p. 126).

[203] W. Atwood, A. Albert, L. Baldini, et al. *Pass 8: Toward the Full Realization of the Fermi-LAT Scientific Potential*. 2013. arXiv: 1303.3514 [astro-ph.IM] (cit. on p. 127).

[204] A. Albert, M. André, M. Anghinolfi, et al. “ANTARES Neutrino Search for Time and Space Correlations with IceCube High-energy Neutrino Events”. In: *The Astrophysical Journal* 879.2 (July 2019), p. 108. DOI: 10.3847/1538-4357/ab253c. URL: https://dx.doi.org/10.3847/1538-4357/ab253c (cit. on p. 134).

[205] S. Adrian-Martinez, I. Al Samarai, A. Albert, et al. “SEARCH FOR COSMIC NEUTRINO POINT SOURCES WITH FOUR YEARS OF DATA FROM THE ANTARES TELESCOPE”. In: *The Astrophysical Journal* 760.1 (Nov. 2012), p. 53. DOI: 10.1088/0004-637x/760/1/53. URL: https://doi.org/10.1088%2F0004-637x%2F760%2F1%2F53 (cit. on p. 140).

[206] C. Distefano, D. Guetta, E. Waxman, et al. “Neutrino Flux Predictions for Known Galactic Microquasars”. In: *The Astrophysical Journal* 575.1 (Aug. 2002), pp. 378–383. DOI: 10.1086/341144. URL: https://doi.org/10.1086%2F341144 (cit. on p. 144).

[207] Sonia Karkar. “Détection de microquasars et calibration en temps du télescope à neutrinos Antares”. Theses. Université de la Méditerranée - Aix-Marseille II, June 2004. URL: https://theses.hal.science/tel-00008240 (cit. on pp. 144, 145).

[208] Tianqi Chen and Carlos Guestrin. “XGBoost: A Scalable Tree Boosting System”. In: *CoRR* abs/1603.02754 (2016). eprint: 1603.02754 (cit. on p. 148).

[209] Gary C. Hill and Katherine Rawlins. “Unbiased cut selection for optimal upper limits in neutrino detectors: the model rejection potential technique”. In: *Astroparticle Physics* 19.3 (June 2003), pp. 393–402. DOI: 10.1016/s0927-6505(02)00240-2. URL: https://doi.org/10.1016%2Fs0927-6505%2802%2900240-2 (cit. on p. 151).

[210] Andrea Tramacere. *JetSeT: Numerical modeling and SED fitting tool for relativistic jets*. Astrophysics Source Code Library, record ascl:2009.001. Sept. 2020. ascl: 2009.001 (cit. on p. 159).

[211] A. Tramacere, P. Giommi, M. Perri, et al. “Swift observations of the very intense flaring activity of Mrk 421 during 2006. I. Phenomenological picture of electron acceleration and predictions for MeV/GeV emission”. In: *Astronomy & Astrophysics* 501.3 (Apr. 2009), pp. 879–898. DOI: 10.1051/0004-6361/200810865. URL: https://doi.org/10.1051%2F0004-6361%2F200810865 (cit. on p. 159).

[212] A. Tramacere, E. Massaro, and A. M. Taylor. “STOCHASTIC ACCELERATION AND THE EVOLUTION OF SPECTRAL DISTRIBUTIONS IN SYNCHRO-SELF-COMPTON SOURCES: A SELF-CONSISTENT MODELING OF BLAZARS’ FLARES”. In: *The Astrophysical Journal* 739.2 (Sept. 2011), p. 66. DOI: 10.1088/0004-637x/739/2/66. URL: https://doi.org/10.1088%2F0004-637x%2F739%2F2%2F66 (cit. on p. 159).

[213] J. Rodi, A. Tramacere, F. Onori, et al. “A Broadband View on Microquasar MAXI J1820+070 during the 2018 Outburst”. In: *The Astrophysical Journal* 910.1 (Mar. 2021), p. 21. DOI: 10.3847/1538-4357/abdfd0. URL: https://doi.org/10.3847%2F1538-4357%2Fabdfd0 (cit. on pp. 161–166).

[214] Andrzej A. Zdziarski, Julien Malzac, and W. Bednarek. “A model of the TeV flare of Cygnus X-1: electron acceleration and extended pair cascades”. In: *Monthly Notices of the Royal Astronomical Society: Letters* 394.1 (Mar. 2009), pp. L41–L45. DOI: 10.1111/j.1745-3933.2008.00605.x. URL: https://doi.org/10.1111%2Fj.1745-3933.2008.00605.x (cit. on pp. 162, 163).

[215] Marek Gierliński, Chris Done, and Kim Page. “X-ray irradiation in XTE J1817-330 and the inner radius of the truncated disc in the hard state”. In: *Monthly Notices of the Royal Astronomical Society* 388.2 (Aug. 2008), pp. 753–760. DOI: 10.1111/j.1365-2966.2008.13431.x. URL: https://doi.org/10.1111%2Fj.1365-2966.2008.13431.x (cit. on p. 162).

[216] Marek Gierliński, Chris Done, and Kim Page. “Reprocessing of X-rays in the outer accretion disc of the black hole binary XTE J1817-330”. In: *Monthly Notices of the Royal Astronomical Society* 392.3 (Jan. 2009), pp. 1106–1114. DOI: 10.1111/j.1365-2966.2008.14166.x. URL: https://doi.org/10.1111%2Fj.1365-2966.2008.14166.x (cit. on p. 162).

[217] C. R. Kaiser. “The flat synchrotron spectra of partially self-absorbed jets revisited”. In: *Monthly Notices of the Royal Astronomical Society* 367.3 (Apr. 2006), pp. 1083–1094. DOI: 10.1111/j.1365-2966.2006.10030.x. URL: https://doi.org/10.1111%2Fj.1365-2966.2006.10030.x (cit. on p. 163).

[218] Yanting Dong, Zhu Liu, Youli Tuo, et al. “Analysis of the reflection spectra of MAXI J1535-571 in the hard and intermediate states”. In: *Monthly Notices of the Royal Astronomical Society* 514.1 (May 2022), pp. 1422–1432. DOI: 10.1093/mnras/stac1466. URL: https://doi.org/10.1093%2Fmnras%2Fstac1466 (cit. on pp. 163, 166).

[219] J. M. Miller, K. Gendreau, R. M. Ludlam, et al. “A NICER Spectrum of MAXI J1535-571: Near-maximal Black Hole Spin and Potential Disk Warping”. In: *The Astrophysical Journal* 860.2 (June 2018), p. L28. DOI: 10.3847/2041-8213/aacc61. URL: https://doi.org/10.3847%2F2041-8213%2Faacc61 (cit. on p. 163).

[220] A. J. Tetarenko, G. Petitpas, G. R. Sivakoff, et al. “(Sub)-millimetre Observations of MAXI J1820+070 (ASASSN-18ey) Suggest Jet Quenching on July 6”. In: *The Astronomer’s Telegram* 11831 (July 2018), p. 1 (cit. on p. 164).

[221] P. Casella, V. Testa, D. M. Russell, et al. “Declining near-infrared flux from the black-hole candidate MAXI J1820+070 (ASASSN-18ey) in transition”. In: *The Astronomer’s Telegram* 11833 (July 2018), p. 1 (cit. on p. 164).

[222] T D Russell, M Lucchini, A J Tetarenko, et al. “Rapid compact jet quenching in the Galactic black hole candidate X-ray binary MAXI J1535-571”. In: *Monthly Notices of the Royal Astronomical Society* 498.4 (Sept. 2020), pp. 5772–5785. DOI: 10.1093/mnras/staa2650. URL: https://doi.org/10.1093%2Fmnras%2Fstaa2650 (cit. on pp. 164, 165, 167).

[223] T. D. Russell, A. J. Tetarenko, J. C. A. Miller-Jones, et al. “Disk-Jet Coupling in the 2017/2018 Outburst of the Galactic Black Hole Candidate X-Ray Binary MAXI J1535-571”. In: *The Astrophysical Journal* 883.2 (Oct. 2019), p. 198. DOI: 10.3847/1538-4357/ab3d36. URL: https://doi.org/10.3847%2F1538-4357%2Fab3d36 (cit. on p. 165).

[224] P Atri, J C A Miller-Jones, A Bahramian, et al. “A radio parallax to the black hole X-ray binary MAXI J1820+070”. In: *Monthly Notices of the Royal Astronomical Society: Letters* 493.1 (Jan. 2020), pp. L81–L86. DOI: 10.1093/mnrasl/slaa010. URL: https://doi.org/10.1093%2Fmnrasl%2Fslaa010 (cit. on p. 165).

[225] Navin Sridhar, Sudip Bhattacharyya, Sunil Chandra, et al. “Broad-band reflection spectroscopy of MAXI J1535–571 using AstroSat: estimation of black hole mass and spin”. In: *Monthly Notices of the Royal Astronomical Society* 487.3 (May 2019), pp. 4221–4229. DOI: 10.1093/mnras/stz1476. URL: https://doi.org/10.1093%2Fmnras%2Fstz1476 (cit. on p. 165).

[226] C M Wood, J C A Miller-Jones, J Homan, et al. “The varying kinematics of multiple ejecta from the black hole X-ray binary MAXI J1820 + 070”. In: *Monthly Notices of the Royal Astronomical Society* 505.3 (May 2021), pp. 3393–3403. DOI: 10.1093/mnras/stab1479. URL: https://doi.org/10.1093%2Fmnras%2Fstab1479 (cit. on p. 165).

[227] Joanna Mikołajewska, Andrzej A. Zdziarski, Janusz Ziółkowski, et al. “The Donor of the Black Hole X-Ray Binary MAXI J1820+070”. In: *The Astrophysical Journal* 930.1 (Apr. 2022), p. 9. DOI: 10.3847/1538-4357/ac6099. URL: https://doi.org/10.3847%2F1538-4357%2Fac6099 (cit. on p. 175).

[228] Andrzej A. Zdziarski, Alexandra J. Tetarenko, and Marek Sikora. “Jet Parameters in the Black Hole X-Ray Binary MAXI J1820+070”. In: *The Astrophysical Journal* 925.2 (Feb. 2022), p. 189. DOI: 10.3847/1538-4357/ac38a9. URL: https://doi.org/10.3847%2F1538-4357%2Fac38a9 (cit. on p. 175).

[229] J. Swinbank. “Comet: A VOEvent broker”. In: *Astronomy and Computing* 7-8 (2014). Special Issue on The Virtual Observatory: I, pp. 12–26. ISSN: 2213-1337. DOI: https://doi.org/10.1016/j.ascom.2014.09.001. URL: https://www.sciencedirect.com/science/article/pii/S2213133714000407 (cit. on p. 182).

[230] M.G. Aartsen, M. Ackermann, J. Adams, et al. “The IceCube realtime alert system”. In: *Astroparticle Physics* 92 (June 2017), pp. 30–41. DOI: 10.1016/j.astropartphys.2017.05.002. URL: https://doi.org/10.1016%2Fj.astropartphys.2017.05.002 (cit. on p. 189).

[231] A. Acharyya, C. B. Adams, A. Archer, et al. *Multiwavelength Observations of the Blazar PKS 0735+178 in Spatial and Temporal Coincidence with an Astrophysical Neutrino Candidate IceCube-211208A*. 2023. arXiv: 2306.17819 [astro-ph.HE] (cit. on pp. 189, 191).

[232] S. Abdollahi, M. Ajello, L. Baldini, et al. “The Fermi-LAT Lightcurve Repository”. In: *The Astrophysical Journal Supplement Series* 265.2, 31 (Apr. 2023), p. 31. DOI: 10.3847/1538-4365/acbb6a. arXiv: 2301.01607 [astro-ph.HE] (cit. on p. 190).

[233] G. C. Hill, J. Hodges, B. Hughey, et al. “Examining the Balance Between Optimising an Analysis for Best Limit Setting and Best Discovery Potential”. In: *Statistical Problems in Particle Physics, Astrophysics and Cosmology*. Ed. by Louis Lyons and Müge Karagöz Ünel. Jan. 2006, p. 108. DOI: 10.1142/9781860948985_0025 (cit. on p. 190).

[234] F. Filippini, G. Illuminati, A. Heijboer, et al. “Search for neutrino counterpart to the blazar PKS0735+178 potentially associated with IceCube-211208A and Baikal-GVD-211208A with the KM3NeT neutrino detectors.” In: *The Astronomer’s Telegram* 15290 (Mar. 2022), p. 1 (cit. on p. 192).

[235] Alexander Plavin, Yuri Y. Kovalev, Yuri A. Kovalev, et al. “Observational Evidence for the Origin of High-energy Neutrinos in Parsec-scale Nuclei of Radio-bright Active Galaxies”. In: *The Astrophysical Journal* 894.2 (May 2020), p. 101. DOI: 10.3847/1538-4357/ab86bd. URL: https://doi.org/10.3847%2F1538-4357%2Fab86bd (cit. on p. 192).

[236] A. V. Plavin, Y. Y. Kovalev, S. V. Troitsky, et al. “The flaring radio-bright blazar PKS 0215+015 coincident with the high energy neutrino alert IceCube-220225A”. In: *The Astronomer’s Telegram* 15247 (Feb. 2022), p. 1 (cit. on p. 192).

[237] Matthias Kadler, Talvikki Hovatta, Sebastian Kiehlmann, et al. “TELAMON and OVRO detection of an inverted spectrum and radio flare of TXS0310+022 coincident with IceCube-220304A”. In: *The Astronomer’s Telegram* 15266 (Mar. 2022), p. 1 (cit. on p. 192).

[238] J. Palacios et al. “Follow-up of multimessenger alerts with KM3NeT ARCA and ORCA”. In: *PoS* ICRC2023 (2023), p. 1521 (cit. on pp. 194, 218).

[239] LHAASO Collaboration*†, Zhen Cao, F. Aharonian, et al. “A tera–electron volt afterglow from a narrow jet in an extremely bright gamma-ray burst”. In: *Science* 380.6652 (2023), pp. 1390–1396. DOI: 10.1126/science.adg9328. eprint: https://www.science.org/doi/pdf/10.1126/science.adg9328. URL: https://www.science.org/doi/abs/10.1126/science.adg9328 (cit. on p. 196).

[240] Andrey Romanov and Piotr Kalaczyński. “Comparison of the atmospheric muon flux measured by the KM3NeT detectors with the CORSIKA simulation using the Global Spline Fit model”. In: *Proceedings of 38th International Cosmic Ray Conference — PoS(ICRC2023)*. Vol. 444. 2023, p. 338. DOI: 10.22323/1.444.0338 (cit. on p. 199).

[241] R. Abbasi, M. Ackermann, J. Adams, et al. “Limits on Neutrino Emission from GRB 221009A from MeV to PeV Using the IceCube Neutrino Observatory”. In: *The Astrophysical Journal, Letters* 946.1, L26 (Mar. 2023), p. L26. DOI: 10.3847/2041-8213/acc077. arXiv: 2302.05459 [astro-ph.HE] (cit. on p. 199).

[242] Shigeo S. Kimura, Kohta Murase, Imre Bartos, et al. “Transejecta high-energy neutrino emission from binary neutron star mergers”. In: *Phys. Rev. D* 98.4 (2018), p. 043020. DOI: 10.1103/PhysRevD.98.043020. arXiv: 1805.11613 [astro-ph.HE] (cit. on p. 201).

[243] Shigeo S. Kimura, Kohta Murase, Peter Mészáros, et al. “High-Energy Neutrino Emission from Short Gamma-Ray Bursts: Prospects for Coincident Detection with Gravitational Waves”. In: *Astrophys. J. Lett.* 848.1 (2017), p. L4. DOI: 10.3847/2041-8213/aa8d14. arXiv: 1708.07075 [astro-ph.HE] (cit. on p. 201).

[244] Kumiko Kotera and Joseph Silk. “Ultrahigh Energy Cosmic Rays and Black Hole Mergers”. In: *Astrophys. J. Lett.* 823.2 (2016), p. L29. DOI: 10.3847/2041-8205/823/2/L29. arXiv: 1602.06961 [astro-ph.HE] (cit. on p. 201).

[245] R. Abbott et al. “GWTC-2: Compact Binary Coalescences Observed by LIGO and Virgo During the First Half of the Third Observing Run”. In: *Phys. Rev. X* 11 (2021), p. 021053. DOI: 10.1103/PhysRevX.11.021053. arXiv: 2010.14527 [gr-qc] (cit. on p. 201).

[246] R. Abbott et al. *GWTC-2.1: Deep Extended Catalog of Compact Binary Coalescences Observed by LIGO and Virgo During the First Half of the Third Observing Run*. Aug. 2021. arXiv: 2108.01045 [gr-qc] (cit. on p. 201).

[247] R. Abbott et al. *GWTC-3: Compact Binary Coalescences Observed by LIGO and Virgo During the Second Part of the Third Observing Run*. Nov. 2021. arXiv: 2111.03606 [gr-qc] (cit. on p. 201).

[248] Bruny Baret et al. “Bounding the Time Delay between High-energy Neutrinos and Gravitational-wave Transients from Gamma-ray Bursts”. In: *Astropart. Phys.* 35 (2011), pp. 1–7. DOI: 10.1016/j.astropartphys.2011.04.001. arXiv: 1101.4669 [astro-ph.HE] (cit. on p. 202).

[249] M. Lamoureux. *Joint Analysis of Neutrinos and Gravitational waves*. https://github.com/mlamo/jang. 2021 (cit. on p. 206).

[250] A. Albert et al. “Search for neutrino counterparts to the gravitational wave sources from LIGO/Virgo O3 run with the ANTARES detector”. In: *JCAP* 04 (2023), p. 004. DOI: 10.1088/1475-7516/2023/04/004. arXiv: 2302.07723 [astro-ph.HE] (cit. on p. 213).

[251] R. Abbasi et al. “Probing neutrino emission at GeV energies from compact binary mergers with the IceCube Neutrino Observatory”. In: *arXiv* (May 2021). arXiv: 2105.13160 [astro-ph.HE] (cit. on p. 213).

[252] Rasha Abbasi et al. “Gravitational Wave Follow-Up Using Low Energy Neutrinos in IceCube DeepCore”. In: *PoS* ICRC2021 (2021), p. 939. DOI: 10.22323/1.395.0939. arXiv: 2107.11285 [astro-ph.HE] (cit. on p. 213).

[253] R. Abbasi et al. “IceCube Search for Neutrinos Coincident with Gravitational Wave Events from LIGO/Virgo Run O3”. In: *Astrophys. J.* 944.1 (2023), p. 80. DOI: 10.3847/1538-4357/aca5fc. arXiv: 2208.09532 [astro-ph.HE] (cit. on p. 213).

[254] K. Abe et al. “Search for neutrinos in coincidence with gravitational wave events from the LIGO-Virgo O3a Observing Run with the Super-Kamiokande detector”. In: *Astrophys. J.* 918.2 (2021), p. 78. DOI: 10.3847/1538-4357/ac0d5a. arXiv: 2104.09196 [astro-ph.HE] (cit. on p. 213).

[255] A. Albert, S. Alves, M. André, et al. *Review of the online analyses of multi-messenger alerts and electromagnetic transient events with the ANTARES neutrino telescope*. 2022. arXiv: 2211.07551 [astro-ph.HE] (cit. on p. 214).

[256] S. Aiello, A. Albert, M. Alshamsi, et al. “Implementation and first results of the KM3NeT real-time core-collapse supernova neutrino search”. In: *The European Physical Journal C* 82.4 (Apr. 2022). DOI: 10.1140/epjc/s10052-022-10137-y. URL: https://doi.org/10.1140%2Fepjc%2Fs10052-022-10137-y (cit. on p. 214).

[257] Anais Möller, Julien Peloton, Emille E O Ishida, et al. “fink, a new generation of broker for the LSST community”. In: *Monthly Notices of the Royal Astronomical Society* 501.3 (Nov. 2020), pp. 3272–3288. DOI: 10.1093/mnras/staa3602. URL: https://doi.org/10.1093%2Fmnras%2Fstaa3602 (cit. on p. 216).

APPENDICES

A. X-Ray flaring periods

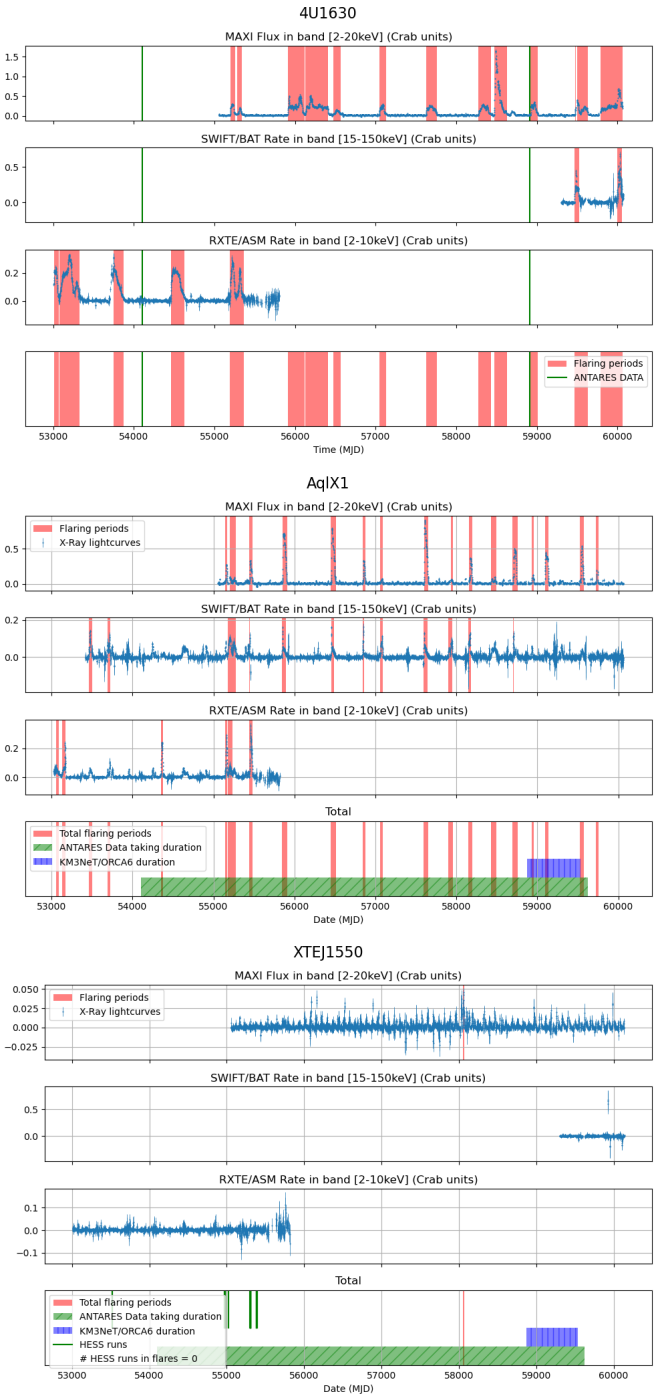

Figure 1.: X-Ray lightcurves and associated flares.

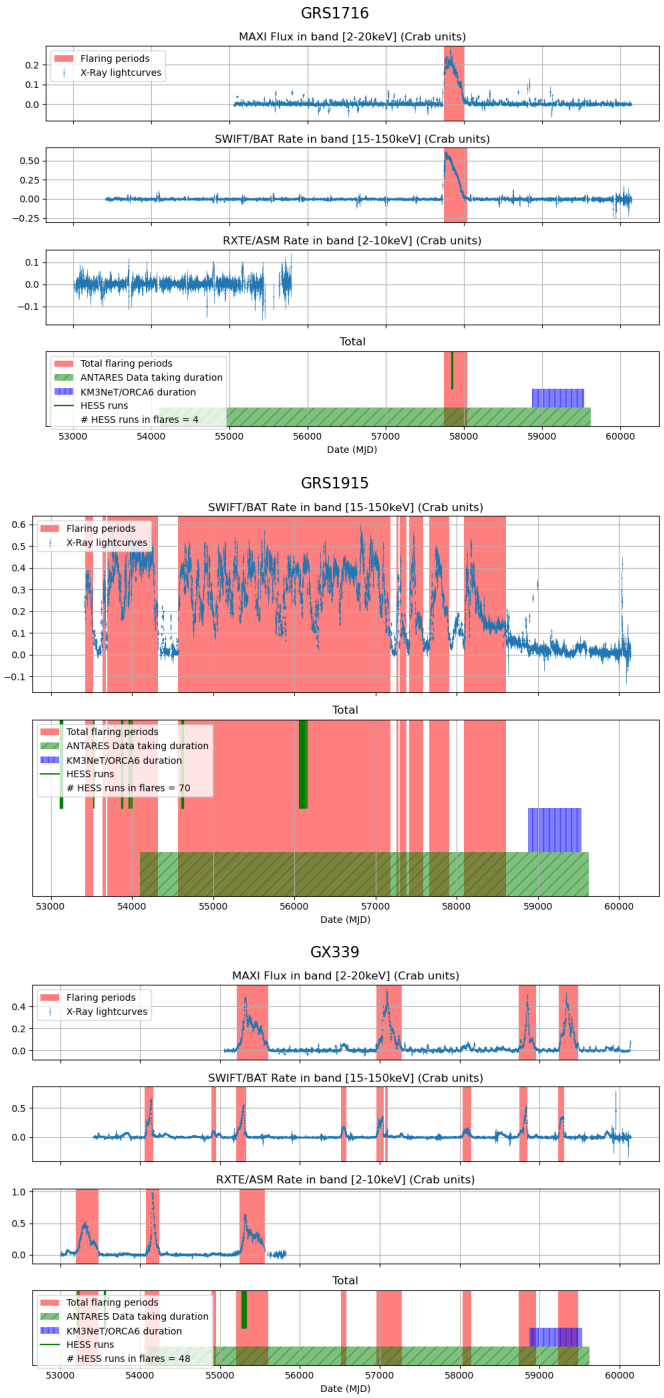

Figure 1: X-Ray lightcurves and associated flares. (cont.)

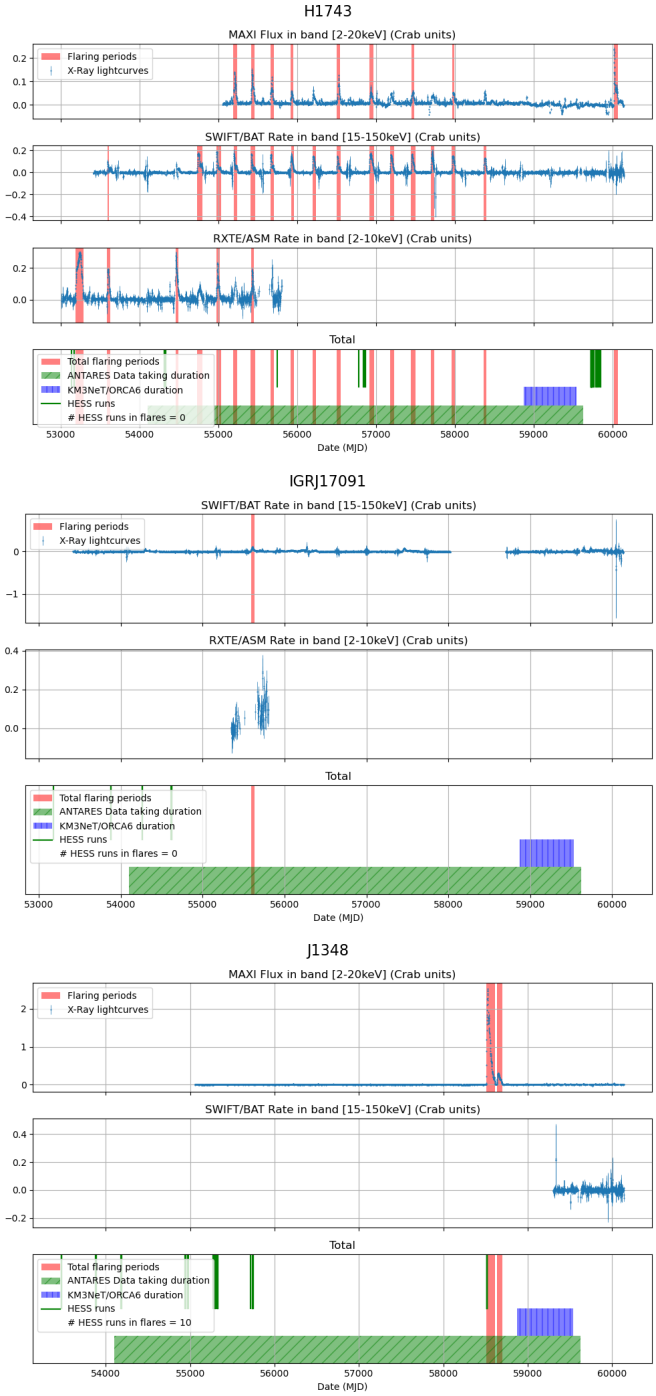

Figure 1: X-Ray lightcurves and associated flares. (cont.)

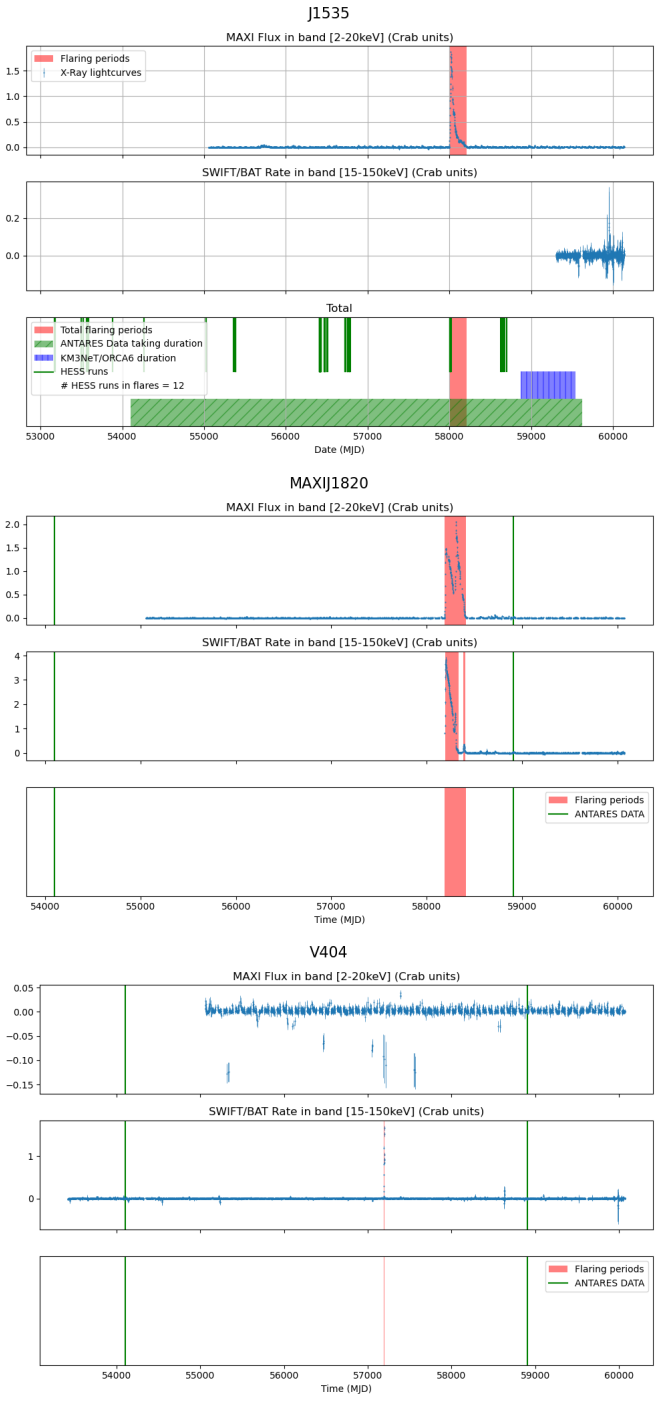

Figure 1: X-Ray lightcurves and associated flares. (cont.)

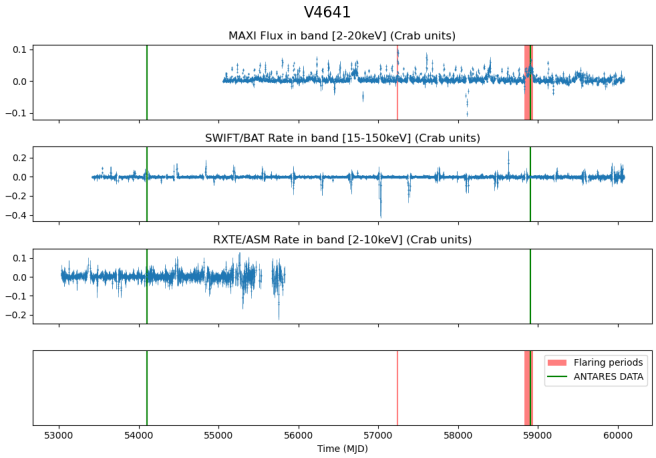

Figure 1: X-Ray lightcurves and associated flares. (cont.)

B. GX339-4 Spectral states definitions

Figure 2.: Spectral states of GX339-4 as shown by the lightcurves and hardness ratios during flares. Upper subplots: Hard X-Ray (Swift/BAT), Middle subplots: Soft X-Rays (MAXI/GSC and RXTE/ASM), Lower subplots: MAXI/GSC and RXTE/ASM hardness ratios. Periods corresponding to each state are highlighted with the following colors: Red for the Hard states, Blue for the Soft States and Yellow for the State Transitions.

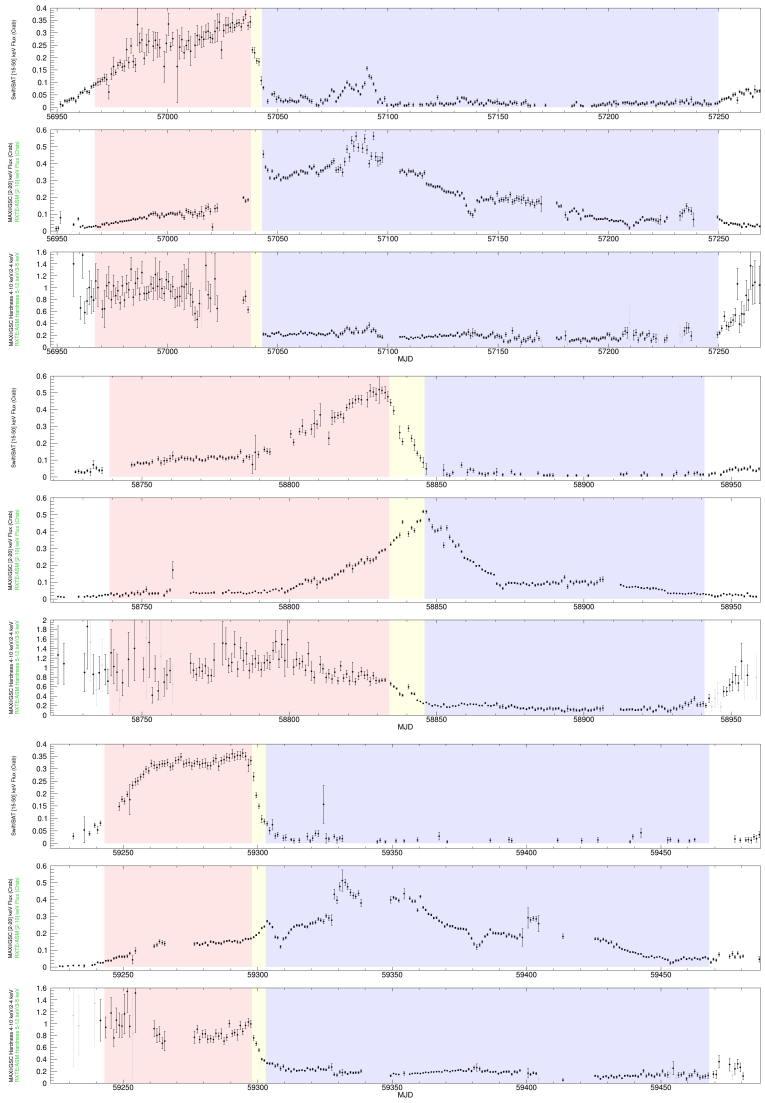

Figure 2: Spectral states of GX339-4 (cont.)

C. Search for neutrino counterpart to the blazar PKS0735+178 potentially associated with IceCube-211208A and Baikal-GVD-211208A with the KM3NeT neutrino detectors.

ATel #15290; F. Filippini, G. Illuminati (Univ. Bologna, INFN Bologna), A. Heijboer, C. Gatius, R. Muller (Nikhef), D. Dornic, F. Huang, S. Le Stum (CPPM, Aix-Marseille Univ.), J. Palacios Gonzalez (IFIC), S. Celli, A. Zegarelli (Univ. La Sapienza, INFN Roma), R. Coniglione (INFN LNS), D. Samtleben (Nikhef, Leiden Univ.), Y. Y. Kovalev, A. Plavin (ASC Lebedev) on behalf of the KM3NeT Collaboration on 21 Mar 2022; 10:54 UT

Using data from the KM3NeT neutrino detectors, we have performed a follow-up analysis of the potential correlation between one track event IceCube-211208A (GCN #31191>) and a flare of the blazar PKS0735+178. This blazar was observed during a strong flare in gamma rays (ATel #15099, ATel #15129), X-rays (ATel #15102, ATel #15108, ATel #15109, ATel #15113, ATel #15130), optical (ATel #15098, ATel #15100, ATel #15132, ATel #15136, ATel #15148) and radio (ATel #15105) bands. This flare covers the full month of December 2021. No additional neutrino events from the direction of the alert have been reported by IceCube (GCN #31195) and ANTARES (ATel #15106). Baikal-GVD has also reported an observation of a high-energy cascade neutrino in coincidence with this flaring blazar and IceCube-211208A (ATel #15112). Baksan has also reported one muon neutrino in spatial coincidence on December 4, 2021 (ATel #15143). During a +/- 1 day time-window centered on the IceCube event time, no up-going muon neutrino candidate was recorded by the ARCA detector within an MDP optimized search cone of 1.4 deg radius centered on the blazar coordinates. During this time window, the source remains 42.3% visible [2021/12/08T08h19 - 18h29 and 2021/12/09T08h15 - 18h25]. An additional search over an extended time window covering the full month of December 2021 has yielded one up-going muon neutrino candidate in coincidence in ARCA with an estimated neutrino energy of 18 TeV, at Dec 15 08h51 31.6 from the direction (RA=113.5 deg, DEC=17.6 deg, Error (50 %) = 1.8 deg). The p-value of this association is 0.14. The 5 - 95% neutrino energy range where this search is sensitive is 9 TeV - 11 PeV. A similar approach has been performed using the ORCA data sensitive to lower energy events (200 GeV - 5 TeV). In both search time windows, no up-going muon neutrino candidate has been recorded (search cones of 4.2 / 2.3 deg for the short and extended search time windows). KM3NeT is a large undersea (Mediterranean Sea) infrastructure hosting two neutrino detectors, sensitive to astrophysical neutrinos in the GeV-PeV energy range: ARCA at high energy and ORCA at low energy. 8 and 10 detection units are in operation in ARCA and ORCA, respectively.

D. GCN CIRCULAR 32741: GRB 221009A: search for neutrinos with KM3NeT

The KM3NeT Collaboration (https://www.km3net.org/) reports:

Using the data from the online fast processing chain, the KM3NeT Collaboration has performed a dedicated search for track-like muon neutrino events arriving from the direction of GRB 221009A (Dichiara et al. GCN 32632 (Swift); Veres et al. GCN 32636 (Fermi-GBM)). The search covers the time range of [T0-50s, T0+5000s], with T0 being the trigger time reported by Fermi-GBM (T0=2022-10-09 13:16:59.00 UTC), during which both KM3NeT detectors were collecting good quality data. However, the GRB location was above the KM3NeT horizon (mean elevation of about ~ 40deg) during the search time window, significantly reducing the point-like source sensitivity. In both detectors, zero events were observed in the search window, while o(0.1) were expected from the background. The online fast processing uses preliminary calibrations and detector alignment, which will be superseded in a future elaborated analysis.

A parallel search has been performed in the MeV range (Eur.Phys.J.C 82 (2022) 4, 317) without any significant neutrino coincidence.

KM3NeT is a large undersea (Mediterranean Sea) infrastructure hosting two neutrino detectors, sensitive to burst of supernova neutrinos in the MeV range and to astrophysical neutrinos in the GeV-PeV energy range: ARCA at high energy and ORCA at low energy. A total of 21 and 11 detection lines are currently in operation in ARCA and ORCA, respectively.